UNIVERSITY of BRADFORD Library

University of Bradford eThesis

This thesis is hosted in Bradford Scholars – The University of Bradford Open Access repository. Visit the repository for full metadata or to contact the repository team

© University of Bradford. This work is licenced for reuse under a Creative Commons Licence.

MICRO-INJECTION MOULDED MICRONEEDLES FOR DRUG DELIVERY

Karthik Jayan NAIR

BPharm PGDip MSc

Submitted for the degree of

Doctor of Philosophy

School of Engineering and Informatics

UNIVERSITY OF BRADFORD

2014

Abstract

Karthik Jayan Nair

Micro-injection moulded microneedles for drug delivery

Keywords: Micro-injection moulding, Microneedles, Bovine serum albumin, Plasma treatment, Surface energy and Optical coherence tomography.

The emergence of microneedle (MN) technologies offers a route for a pain free, straightforward and efficient way of transdermal drug delivery, but technological barriers still exist which pose significant challenges for manufacture of MN systems with high volume outputs at low cost. The main aim of this research was to develop new ways for MN manufacture primarily using micro-injection moulding processes with high performance engineering thermoplastics.

During the moulding process these polymeric melts will be subjected to extreme stress and temperature gradients and detailed material characterisation combined with in-line monitoring is desirable to optimise the moulding parameters and will help in achieving sharp microneedles with acceptable quality. Hence high shear rheology of these selected materials was performed at wall shear rates carried out in excess of 10^7 s^{-1} over a range of temperatures to predict the flow behaviour of polymer melts at such high shear strain rates. This information was fed into injection moulding simulation software tools (Moldflow) to assist the MN production process design. The optimal design was then used to produce a full 3D solid model of the injection mould and mould insert.

Furthermore various design of experiments were conducted considering input parameters such as injection pressure, injection speed, melt temperature, filling time and mould cavity temperature. Response variables including product quality and data acquired from the cavity pressure and temperature transducers were used to optimise the manufacturing process. The moulded MNs were geometrically assessed using a range of characterisation techniques such as atomic force microscopy, confocal microscopy and scanning electron microscopy. An attempt to make hollow MNs was performed and encountered many challenges like partial cavity filling and part ejection during processing. Studies were carried out to understand the problem and identified the major problem was in tool design and improvements to the moulding tool design were recommended.

Plasma treatment and mechanical abrasion were employed to increase the surface energy of the moulded polymer surfaces with the aim of enhancing protein adsorption. Sample surface structures before and after treatment were studied using AFM and surface energies have been obtained using contact angle measurement and calculated using Owens-Wendt theory. Adsorption performance of bovine serum albumin and release kinetics for each sample set was assessed using a Franz diffusion cell. Results indicate that plasma treatment significantly increases the surface energy and roughness resulting in better adsorption and release of BSA.

To assist design-optimisation and to assess performance, a greater understanding of MN penetration behaviour is required. Contact stiffness, failure strength and creep behaviour were measured during compression tests of MN against a steel surface, and *in-vitro* penetration of MNs into porcine skin. The

MN penetration process into porcine skin was imaged using optical coherence tomography. Finally, a finite element model of skin was established to understand the effect of tip geometry on penetration.

The output of findings from this research will provide proof of concept level development and understanding of mechanisms of MN penetration and failure, facilitating design improvements for micro-injection moulded polymeric MNs.

Acknowledgements

Undertaking this PhD has been a truly life-changing experience for me and it would not have been possible to do without the support and guidance that I received from many people.

First and foremost I want to thank my supervisors Dr Benjamin Whiteside and Prof Anant Paradkar. I appreciate all their contributions of time and ideas. Working with them over the past few years has been both a privilege and an absolute pleasure.

I would like to extend a special appreciation to Ben for the generous funding which allowed me to undertake this research and also for giving me the opportunity to attend conferences and meet many interesting people. Ben also has been extremely supportive and has given me the freedom to pursue various microneedle projects and collaborate with different universities without any objection.

The members of the Polymer IRC group (led by Prof Phil Coates) have contributed immensely to my personal and professional time at Bradford. The group has been the source of friendship as well as good advice and collaboration. I am very much grateful to Mr Keith Norris and I very much appreciate his enthusiasm, intensity, witty character and willing to do frequent injection moulding experiments with me. I hope that I could be as lively, enthusiastic, and energetic as Keith and to someday be able to please an audience as well as he can.

During the initial stages of my work regarding rheology, I am particularly indebted to Dr Adrian Kelly who helped me with capillary rheology experiments

and Dr Raj Patel for all his support relating to the contact angle and surface energy calculations. In regards to the AFM work, I thank Dr Collin Grant, the surface characterisation work done in this thesis would not have been possible without his contribution. I would also like to thank him for the patience and support he gave to teach me the Igor Software. For the Skin penetration work I thank Dr Pete Twigg and Dr Paul Spencer for the microneedle simulation studies.

A person deserving a special mention during my PhD is Dr Cristina Tuinea-Bobe, she has always been a constant point of support, advice and guidance. I will never forget the many wonderful parties and fun we had at her place.

A good friend is always important to survive the lengthy PhD life, I was lucky to have Mr Maksims Babenko as my friend and formed the core of my research time in Ben's MNT lab. I would also like to thank him for all the CAD drawings which he drew for me for the completion of this thesis.

Several other colleagues and collaborators have been very helpful during this research. I would like to use this opportunity to express my appreciation. They include Mr John Wyborn, Mr Glen Thompson, Miss Bushra Parveen, Mr Sachin Korde, Mr Newsun Jose, Mr Ken Howell, Mr Rohan Amardekar, Dr Dimitrious Vgenopoulos, Mr Hassan Saeed and Dr Simon Todd of Renephra Ltd.

Lastly, I would like to thank my family for all their love and encouragement. For my parents who raised me with a love of science and supported me in all my pursuits. And most of all for my loving, supportive, encouraging, and patient wife Chaitrali whose faithful support during Ph.D is so appreciated. Thank you.

Table of Contents

List of Figures

List of Tables

Abbreviations

API	=	Active pharmaceutical ingredient	p/T	=	Pressure/temperature
ANOVA	=	Analysis of Variance	PC	=	Polycarbonate
AIDS	=	Acquired immunodeficiency syndrome	PEEK	=	Polyether ether ketone
AFM	=	Atomic force microscopy	PBS	=	Phosphate buffer solution
BSA	=	Bovine serum albumin	PDMS	=	Polydimethylsiloxane
BSE	=	Back scattered electrons	POM	=	Poly oxy methylene
CCD	=	charge-coupled device	PPS	=	Polyphenylene sulfide
CMOS	=	Complementary metal–oxide–semiconductor	PBT	=	Polybutylene terephthalate
CAD	=	Computer aided design	RSM	=	Response surface methodology
CLSM	=	Confocal laser scanning microscopy	RF	=	Radio frequency
DNA	=	Deoxyribonucleic acid	RMS	=	Root mean square
DRIE	=	Deep reactive-ion etching	RNA	=	Ribonucleic acid

DOE	=	Design of experiments	RIE	=	Reactive-ion etching
DO	=	Design order	SMNs	=	Silicon microneedles
DAQ	=	Data Acquisition	SC	=	Stratum corneum
DLC	=	Diamond like carbon	STL	=	Standard Tessellation Language
DC	=	Direct current	SEM	=	Scanning electron microscope
EDM	=	Electric discharge machining	SLD	=	Super luminescent diode
FEA	=	Finite element analysis	SE	=	Secondary electrons
FDC	=	Franz diffusion cell	TiN	=	Titanium nitride
FDA	=	Food and drug administration	TDDS	=	Transdermal drug delivery system
HN	=	Hypodermic needle	TFA	=	Trifluoroacetic acid
HPLC	=	High-performance liquid chromatography	TEWL	=	Transepidermal water loss
KrF	=	Krypton fluoride laser	XPS	=	X-ray photoelectron spectroscopy
LIGA	=	Lithography, electroplating and moulding	XeF_2	=	Xenon difluoride
LCP	=	Liquid-crystal polymer	XeCl	=	Xenon monochloride
MN	=	Microneedles	UV	=	Ultraviolet
MEMS	=	Micro-electro-mechanical systems	µIM	=	Micro-injection moulding
MW	=	Molecular weight	µCT	=	X-ray microtomography
OCT	=	Optical coherence tomography			

Symbols

E_B	=	Binding energy
E_K	=	Kinetic energy
h_c	=	Contact depth (nm)
R_a	=	Average roughness, (nm)
R_q	=	Root mean square roughness, (nm)
kV	=	Kilovolts
T*g*	=	Glass transition temperature
MPa	=	Mega pascal
GPa	=	Giga pascal
N	=	Newton
rpm	=	Rotation per minute
psi	=	Per square inch
kHz	=	Kilo hertz
E_r	=	Reduced modulus
h_{max}	=	Penetration depth (nm)

h_f	=	Final depth (nm)
S	=	Unloading stiffness
H	=	Hardness
θ	=	Contact angle (degree)
λ	=	Wavelength (nm)
kDa	=	Kilo dalton
W	=	Watts
eV	=	Electron volt (J)
σ_S	=	Overall Surface free energy
σ_L^P	=	Polar component of the surface energy of the liquid (mJ/m^2)
σ_L^D	=	Dispersive component of the surface energy of the liquid (mJ/m^2)
σ^P	=	Polar component of the surface energy of the solid (mJ/m^2)
σ^D	=	Dispersive component of the surface energy of the solid (mJ/m^2)

Chapter 1 Introduction, Aim and Outline of the Thesis

1.0 Introduction

Puncturing human skin with hypodermic needles (HNs), which is an invasive medical procedure for injecting or collecting biological samples has been universally accepted for many decades (Donnelly *et al*., 2010 and McAllister *et al.,* 2000). Despite the widespread use, HN mediated injections cause pain, related infections and sometimes bleeding (Arduino, 1997 and Ebah, 2012). It is estimated that over 15% of the world's adult population suffer from trypanophobia (fear of hypodermic needles) (Hamilton, 1995). For diabetic patients who are dependent on multiple insulin injections on a daily basis, drug delivery using conventional syringes is the most accepted route (Al-Tabakha *et al*., 2008). Patch-based transdermal drug delivery offers an alternative way to administer drugs without the drawbacks of the HNs, but the conventional transdermal drug delivery is limited to those drugs which can diffuse the skin barrier. The outermost layer of the skin stratum corneum (SC) provides a significant barrier and only drugs with low molecular weight <500 Da and adequate lipophilicity can be successfully administered. So delivery of hydrophilic drugs and macromolecular agents like peptides, DNA and interfering RNA is cumbersome (Barry *et al*., 2001). Therefore, facilitation of drug penetration through these biological membranes can only be achieved by reversible disruption of molecular structure of the barrier membranes (Birchall, 2012 and Barry *et al*., 2001). However, current advances in micromanufacturing technologies offer a number of advantages over HNs and guided the formulation scientists to design micron-sized needles called

Microneedles (MNs) (Cleary *et al*., 2011 and Jiang, 2006). The increasing number of promising therapeutic agents and their limited ability to reach the systemic circulation due to the exceptional barrier properties of biological membranes such as the SC of the skin has made MN drug delivery an exciting platform for many researchers and among the more prominent has been Mark Prausnitz from Georgia Institute of Technology.

MNs consist of a plurality of micro-projections, ranging from 10-1800 µm in height and various shapes which are attached to a base support produced from number of different techniques like etching, lithographic and moulding techniques to produce sharp, high aspect ratio, solid or hollow features in materials such as plastics, silicon, ceramics and metals (Attia *et al*., 2009). MNs, when used to puncture skin will create a transient aqueous transport pathways of micron dimensions and improve permeability (Donnelly *et al.,* 2010). These microchannels are orders of magnitude larger than molecular dimensions and should readily allow transport of hydrophilic macromolecules and supramolecular complexes (Prausnitz, 2004 and Shakeel *et al*., 2011). MNs in addition could be also used for sampling body fluid for applications such as measuring glucose level in the blood or used for diagnostics such as bio-chemical sensing and physiological signal monitoring like electrocardiography and electromyography (Bora *et al.,* 2009 and Mahony *et al*., 2011). Further more MNs are not sufficiently tall to cause pain by stimulating the nerve endings which lie deep within the skin (typically 1.5 mm in human skin) which is in contrast to conventional HNs (Barry *et al*., 2001). There is a significant potential for this technology in the future as MNs are targeted to $25 billion global vaccine, $3.6 billion syringe and $120 billion global biologics market while the

MN drug delivery market was evaluated at $400 million globally for 2012 (Herman *et al.,* 2012 and Greystone Associates, 2012). However, before MNs find widespread use, researchers must rationalise the techniques for optimally and reproducibly inserting them into the skin and complete the integration of MNs into full diagnostic, monitoring or drug delivery systems (Birchall *et al*., 2011 and Rattanapak *et al*., 2013).

The design of the microneedle can impact how quickly drugs can be delivered through them (Coulman *et al*., 2009) and depending on their specific application, microneedles may vary in materials, fabrication processes, geometry and size (Maaden *et al*., 2012) while length and tip sharpness are two key factors that have to be taken into account in their designs (Rattanapak *et al.,* 2013).

Given that MNs are microscopic drug delivery systems it is important that skin biomechanics are considered for optimised device design. The viscoelastic nature of skin often makes microneedle insertion ineffective leading to sub-optimal and variable drug dosage (Birchall *et al*., 2011 and Groves *et al*., 2012). For some applications it is beneficial to deposit a depot of material within the skin, which can release a drug slowly (Barry *et al*., 2001). One such example is the delivery of vaccines to the skin and it is receiving growing attention due to the presence of immune-processing Langerhans cells in the epidermis and dermis (Birchall, 2012 and Pearton *et al*., 2010).

In general terms, MNs could be used for extended delivery of drugs, macromolecules for systemic or local effect and offers significant advantage by avoiding the peaks and troughs of non-controlled delivery (Urquhart, 2000, Tiwari *et al*., 2012 and Rattanapak et *al*., 2013).

Despite offering several advantages, technological barriers still remain which pose significant challenges for manufacture of microneedle systems with high volume outputs at low cost to be adapted by pharmaceutical companies at a large scale. The price of microneedle arrays also have to be competitive with the price range of current drug delivery techniques and devices available today (Coulman *et al*., 2009 and Donnelly *et al.,* 2010).

Over the past two decades, several manufacturing solutions that mainly use wet and dry etching of silicon substrates to produce MN patches for medical applications have been reported (Attia *et al*., 2009 and Donnelly *et al.,* 2010). Patches made out of silicon oxide and titanium have also been machined. By applying etching technologies, especially by etching silicon wafers, precise MNs can be produced (Zhao *et al*., 2009). However, these manufacturing technologies are slow, costly and a limited choice of materials is available, thus creating a major impediment to large scale manufacturing and commercialising of MNs. In addition, silicon is not an ideal material for producing MNs as it is brittle and hence not approved by FDA for use where it is in direct contact with human tissues. (Song *et al*., 2010)

Injection moulding is a well-established manufacturing process which offers several advantages in terms of bulk manufacturability, range of materials and precise replication. It is also a very cost effective replication method for the mass production of macro and micro polymer components and is seen as the manufacturing process of choice for producing affordable MN patches (Steglich *et al*., 2010, Trichur *et al*., 2002 and Yung *et al*., 2011).

1.1. Aim

The principle aim of this thesis is to study the application of micro injection moulding (µIM) technology and advanced tooling solutions for high volume, low cost production of microneedle devices for optimised drug delivery using high performance engineering thermoplastics. In order to achieve this, understanding of the requirements of the material selection, design and manufacturing, penetration and delivery from MNs needs to be acquired. Therefore several sub-aims needed to be formulated.

- *to optimise the manufacturing process for solid and hollow MNs using µIM technology*
- *to investigate and understand the influence of various surface modifications on the polymer surfaces and protein adsorption behaviour*
- *to enable optimal characterisation and to assess the performance of these MNs*

1.2. Thesis outline

In **Chapter 2** the literature regarding transcutaneous drug delivery, introduction to MNs and µIM is reviewed, with a focus on the tooling techniques and process parameters in µIM. A critical view on importance of surface modifications on polymer surfaces are mentioned. Different surface characterisation techniques used in evaluation and optimisation of MNs are also discussed.

The research described in the thesis is divided into four parts: solid microneedle manufacturing using µIM (Part I), surface energetics and protein adsorption (Part II), performance, prediction of insertion and delivery of solid MN arrays

(Part III) and hollow microneedle manufacturing using µIM (Part IV).

Part I: *Solid polymeric microneedles manufacturing using µIM*

Manufacturing of solid MN arrays using µIM is discussed in **Chapter 3**. A range of candidate materials were selected based on their processing characteristics, mechanical properties and regulatory requirements. High shear rheology of these selected materials was carried out at different temperatures to predict the flow behaviour of polymer melts at high shear strain rates experienced during µIM process. The design of the MN array was performed using 3D solid modelling tools and candidate designs/material combinations were optimised using injection moulding simulation software tools (Moldflow). The optimal design was then used to produce a full 3D solid model of the injection mould.

MNs were manufactured using existing state of the art microinjection moulding facilities at Bradford University. The primary focus of this work was to validate and optimise a process suitable for low cost, bulk manufacture of the MNs. Parameters such as injection pressure, injection speed, melt temperature, filling time and mould cavity temperature are key parameters that were assessed. Various design of experiments along with in-line data acquisition measurement were used to optimise the fabrication process. The MNs produced were then geometrically assessed using a range of characterisation techniques such as atomic force microscopy (AFM), confocal microscopy and scanning electron microscopy (SEM).

Part II: *Influence of surface modification of polymer surfaces and protein adsorption*

This part focuses on surface modification by plasma and mechanical roughening on µIM polymeric surfaces and the resulting influence on protein adsorption. In **Chapter 4** three high performance engineering grade thermoplastics were selected. Moulded specimens of each material have been manufactured using µIM and samples from each production batch have been subsequently subjected to a range of plasma treatment and mechanical abrasion. These samples were coated with BSA (bovine serum albumin) to study the protein adsorption on these treated polymer surfaces. Sample surface structures before and after treatment were studied using AFM and surface energies have been obtained using contact angle measurement and calculated using Owens-Wendt theory. Finally adsorption performance and BSA release kinetics for each sample set was assessed.

Part III: *Performance and predication of penetration forces and drug delivery of polymeric solid MNs*

To enable optimal characterisation and to assess the performance of these MNs, a greater understanding of the penetration behaviour is required. In **Chapter 5** the forces required for the mechanical failure, contact stiffness, creep behaviour and mechanisms for MN penetration into porcine skin were studied. A finite element model of the skin and MNs were established to understand the effect of tip geometry on penetration. Moreover passive diffusion of BSA from the polymeric solid MN arrays across dermatomed abdominal neonatal porcine skin was investigated *in vitro* using Franz diffusion cells. Here, the utility of OCT in studying MN insertion depth and position in porcine skin *in vitro* were also studied.

Part IV: *Hollow polymeric microneedles manufacturing using µIM*

With the knowledge obtained from manufacturing solid MNs an attempt to design and manufacture of hollow MN is discussed in Chapter **6**. Materials selected and information obtained from **Chapter 3** were used to design the hollow MN mould. Various design of experiments were conducted to optimise the parameters and encountered many challenges like partial cavity filling and part ejection during processing. To find out the exact cause of these problems MN inserts were visualised using SEM and confocal microscopy and further improvements to moulding tool were suggested and discussed in this chapter.

1.3. References

1. Attia UM, Marsona S and Alcock JR, Micro-injection moulding of polymer microfluidic devices, *Microfluidics and nano fluidics* **7** (2009) 1-28.

2. Al-Tabakha MM and Arida AL, Recent challenges in insulin *delivery* systems: A Review, *Indian Journal of Pharmaceutical Sciences* **3** (2008) 278-288.

3. Arduino MJ, Bland LA, Danzig LE, McAllister SK and Aguero SM, Microbiologic evaluation of needleless and needle-access devices, *American Journal of Infect Control* **25** (1997) 377–380.

4. Bora P, Kumar L and Bansal KA, Microneedle technology for advanced drug delivery: Evolving vistas, *CRIPS*. **9** (2009) 7-10.

5. Barry BW, Novel mechanism and devices to enable successful transdermal drug delivery, *European Journal of Pharmaceutical Sciences* **14** (2001) 101-114.

6. Birchall JC, Overcoming the stratum corneum barrier: microneedle delivery of macromolecules and vaccines, *International Journal of Cosmetic Science* **4** (2012) 361-372.

7. Birchall JC, Clemo R, Anstey A and John DN. Microneedles in clinical practice -an exploratory study into the opinions of healthcare professionals and the public. *Pharm Res.* **28** (2011) 95-106.

8. Cleary GW, Microneedles for Drug Delivery, *Pharmaceutical Research* **28** (2011) 1–6.

9. Coulman S, Anstey AV, Gateley C, Morrissey A, McLoughlin P, Allender CJ, and Birchall JC, Microneedle mediated delivery of nanoparticles into human skin, *International Journal of Pharmaceutics* **366** (2009) 190-200.

10. Donnelly RF, Raj Singh TR and Woolfson DA, Microneedle-based drug delivery systems: Microfabrication, drug delivery and safety, *Drug Delivery* **4** (2010) 187–207.

11. Ebah LM, Extraction and analysis of interstitial fluid and characterisation of the interstitial compartment in kidney disease, A Thesis submitted to

the University of Manchester for the degree of Doctor of Philosophy in the Faculty of Medical and Human Sciences, (2012).

12. Greystone Associates, Microneedles in Medicine: Technology, Devices, Markets and Prospects, Greystone Associates, Amherst, NH (2012).

13. Groves RB, Coulman S, Birchall JC and Evans SL, Quantifying the mechanical properties of human skin to optimise future microneedle device design, *Computer Methods in Biomechanics and Biomedical Engineering* **15** (2012) 73-82.

14. Hamilton J, Needle Phobia - A Neglected Diagnosis, *Journal of Family Practice* **2** (1995) 169–175.

15. Herman WA and Devey GB, Future trends in medical device technologies: A Ten-Year Forecast US Food and Drug administration (2012).

16. Jiang N, Ocular drug delivery using microneedles, Thesis. Georgia Institute of Technology (2006).

17. Maaden KV, Jiskoot W and Bouwstra J, Microneedle technologies for transdermal drug and vaccine delivery, *Journal of Controlled Release* **161** (2012) 645–655.

18. McAllister DV, Allen MG and Prausnitz MR, Microfabricated microneedles for gene and drug delivery, *Annual Review of Biomedical Engineering* **2** (2000) 289–313.

19. Mahony CO, Pini F, Blake A, Webster C and McCarthy KG, Microneedle-based electrodes with integrated through-silicon via for bio potential recording, *Sensors and Actuators A: Physical* **186** (2011) 130-136

20. Prausnitz MR, Microneedle for transdermal drug delivery, *Advanced Drug Delivery Reviews* **5** (2004) 581-587.

21. Pearton M, Kang SM, Song JM, Kim YC, Quan FS, Anstey A, Ivory M, Prausnitz MR, Compans RW, Birchall JC. Influenza virus-like particles coated onto microneedles can elicit stimulatory effects on Langerhans cells in human skin. *Vaccine* **28** (2010) 6104-6113.

22. Rattanapak T, Birchall JC, Young K, Ishii M, Meglinski I, Rades T and Hook S, Transcutaneous immunization using microneedles and cubosomes: Mechanistic investigations using Optical Coherence Tomography and Two-Photon Microscopy, *Journal of Controlled Release* **10** (2013) 894-903.

23. Shakeel M, Pathan DN, Ziyaurrrahman AR, Bagwan A and Sayed B, Microneedle as novel drug delivery system: A review, *International Research Journal of Pharmacy* **2** (2011) 72-77.

24. Steglich D, Lacan F, Dessors S, Eigenbro H, Moguedet M and Bambury E, Optimising the replication quality of polymer injection-moulded microneedles on the impress platform (2010) www.impress-fp7.eu.

25. Song JM, Kim YC, Lipatov AS, Pearton M, Davis CT, Yoo DG, Park KM, Chen LM, Quan FS, Birchall JC, Donis RO, Prausnitz MR, Compans RW and Kang S-M. Microneedle Delivery of H5N1 Influenza Virus-Like Particles to the Skin Induces Long-Lasting B- and T-Cell Responses in Mice. *Clin. Vacc. Immunol* **17** (2010) 1381-1389.

26. Tiwari G, Tiwari R, Sriwastawa B, Bhati L, Pnadey S and Bannerjee SK, Drug delivery systems: An updated review, *International Journal of Pharmaceutical Investigation* **2** (2012) 2–11.

27. Trichur R, Kim S, Zhu X, Suk JW, Hong C-C, Choi J-W and Ahn CH, Development of plastic microneedles for transdermal interfacing using injection moulding techniques, *Micro Total Analysis Systems* **1** (2002)1395–397.

28. Urquhart J, Controlled drug delivery: therapeutic and pharmacological aspects, *Journal of Internal Medicine* **248** (2000) 357-376

29. Yung K L, Yan X, Kang C, Liu H, Tam KF, Ko SM, Kwan FY and Lee MH, Sharp tipped plastic hollow microneedle array by microinjection moulding, *Journal of Micromechanics and Microengineering* **22** (2011) 1317-1322

30. Zhao G, Li W, Tang G and Chen J, Fabrication of bulk titanium out-of-plane microneedles, *Proceedings of the 2009, 4th IEEE International Conference on Nano/Micro Engineered and Molecular Systems* (2009) 428-431.

Chapter 2 Background

2.0. Drug delivery

The most common route of drug administration for many decades is oral delivery because it is painless and can be self-administered. Unfortunately many drugs delivered in this manner are degraded within the gastrointestinal tract or not absorbed in sufficient quantity to be effective (Kuno *et al*., 2011). Historically to ensure high efficacy and to achieve a therapeutic dose, these drugs must be administered by intravenous, intramuscular or subcutaneous injection. Recently, a variety of other modes of administration less common than oral or injection methods have evolved (Hoffman, 2008 and Saltzman, 2001) because of the specific advantages for particular agents or certain diseases. Figure 2.1 illustrates common routes of drug administration.

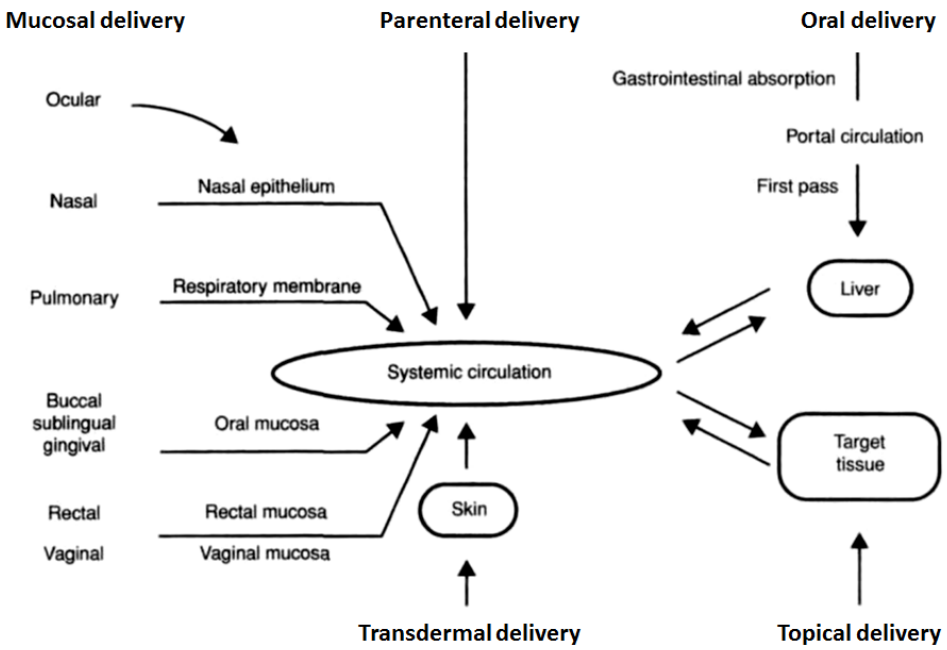

Figure 2.1 Common routes of drug administration (Kewal, 2008).

The route and method of drug administration will influence the kinetics of bio-distribution and elimination and therefore the effectiveness of the therapy (Jiang *et al*., 2007). Delivery of identical amounts of drug to tissue sites differing in local anatomy and physiology (e.g. injection into a muscle vs injection to a subcutaneous space) can result in measurable differences in the pattern of delivery. For regions of the body with a significant barrier to drug permeation, such as the tight junctions in the eye and brain and the stratum corneum of skin, great care should be taken to deliver drugs appropriately as these organs are highly selective for permeability of drugs (Kuno *et al*., 2011).

New drug delivery systems form one of the fastest growing health care sectors and it is estimated that this sector will climb to $250 billion by 2015 (Herman, 2012 and Greystone Associates 2012). New drug delivery technologies also help the life cycle of a product when its patent expires. Patent expiration can mean a rapid loss of millions of dollars in annual sales, as makers of generic versions enter the market (Eisenstein, 2011). It is estimated that by 2015 over 50 blockbuster products (drugs generating more than $1billion of revenue each year) worth $73 billion will lose patent protection and almost over 100 drug patents worth $53 billion will expire (Frost and Sullivan, 2011). Pharmaceutical companies are replacing these revenues by adding improved delivery packages (Nair *et al*., 2013). A superior drug delivery system can make a product more attractive than a generic competitor (Borshell, and Ahmed, 2012; Kuno *et al.,* 2011).

There are more than 300 drug delivery companies working on 35 drug delivery systems to deliver APIs more effectively and conveniently (Nair *et al.*, 2013) The most significant of these today are transdermal delivery systems with a

current market of $ 2.2 billion and 700 million sales each year respectively (Paudel *et al*., 2010; Frost and Sullivan, 2011). However this platform of drug delivery can offer difficulties for certain therapeutic treatments due to the barrier properties of skin (Eisenstein, 2011). A detailed review of transdermal drug delivery is discussed below.

2.1. Anatomy of skin

The skin is the body's largest organ, covering the entire body. In addition to serving as a protective shield against heat, light, injury, and infection, the skin also regulates body temperature and stores water and fat (Barry, 2002). The skin is made up of the following layers (Figure 2.2 and 2.3)

1. Epidermis
2. Dermis
3. Hypodermis or Subcutaneous fat layer (subcutis)

EPIDERMIS	The epidermis is the thin outer layer of the skin which consists of the following three parts: **Stratum corneum** (horny layer Figure 2.3.) This layer consists of fully mature keratinocytes which contain fibrous proteins (keratins). The outermost layer is continuously shed. The stratum corneum (Figure 2.4) prevents the entry of most foreign substances as well as the loss of fluid from the body (Cevc, 1997). **Keratinocytes** (squamous cells) This layer, just beneath the stratum corneum, contains living keratinocytes, which mature and form the stratum corneum. **Basal layer** The basal layer is the deepest layer of the epidermis, containing basal cells. Basal cells continually divide, forming new keratinocytes, replacing the old ones that are shed from the skin's surface. The epidermis also contains melanocytes, which are cells that produce melanin (skin pigment) (Saltzman, 2001).
DERMIS	The dermis is the middle layer of the skin. The dermis contains the following: Blood vessels, lymph vessels, hair follicles, sweat glands, collagen bundles, fibroblasts and nerves. The dermis is held together by a protein called collagen, made by fibroblasts. This layer gives skin flexibility and strength. It also contains pain and touch receptors (Cevc, 1997).
SUBCUTIS	The subcutis is the deepest layer of skin. The subcutis, consisting of a network of collagen and fat cells, helps conserve the body's heat and protects the body from injury by acting as a shock absorber. (Barry, 2002 and Saltzman, 2001)

Table 2.1 Details of the different layers of the skin.

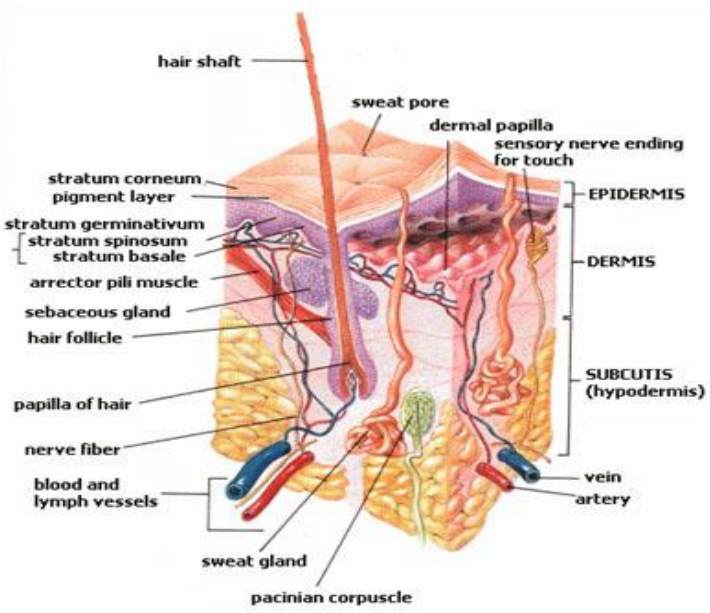

Figure 2.2 Cross-section showing different layers of skin (www.skinqd.com).

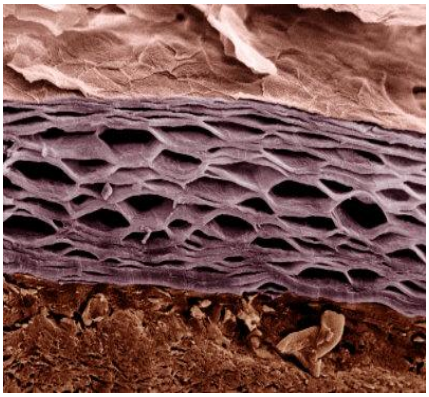

Figure 2.3 Cross section of human skin showing the stratum corneum layer of the epidermis (www.skinqd.com).

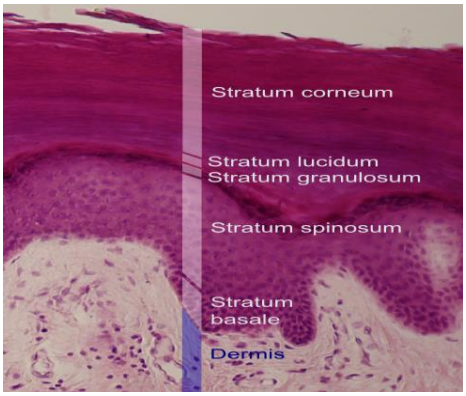

Figure 2.4 Histological section showing the different layers of the skin (www.oucom.ohiou).

2.2. Why transdermal drug delivery?

A drug delivery system in which drugs are administered through the skin for systemic or local pharmacological response is called a transdermal drug delivery system (TDDS). Transdermal delivery has a variety of advantages compared with the oral route in particular, where there is a significant first-pass effect of the liver that can prematurely metabolize drugs (Prausnitz, 2008). Transdermal delivery also has advantages over hypodermic injections, which are painful, generate dangerous medical waste and pose the risk of disease transmission by needle re-use, especially in developing countries (Frost and Sullivan, 2011). In contrast, transdermal systems are non-invasive, can be self-administered and they can provide drug release for long periods of time, up to one week (Jiang *et al*., 2007). TDDS also improve patient compliance and the systems are generally inexpensive. In addition to avoiding hypodermic needles, transdermal vaccine delivery could improve immune responses by targeting delivery to immunogenic langerhans cells and dermal dendritic cells (Figure 2.5) that may generate a strong immune response at much lower doses than deeper injection in the skin so giving rise to an improved vaccine administration (Prausnitz, 2008). Although vaccines are typically macromolecules, viral particles, or other large supramolecular constructs, their small (microgram) doses facilitate the possibility of transdermal delivery. In a world where needle reuse kills at least 1.3 million people per year from hepatitis B and AIDS, needle-free, patch-based vaccination could have large impact (Jiang *et al*., 2007). In addition, the possibility of administering vaccine patches by minimally trained personnel or patients themselves could not only facilitate compliance with routine, seasonal and pandemic vaccination needs, but could also expedite

vaccination campaigns in developing countries where medical personnel are in short supply (Donnelly *et al*., 2010 and Eisenstein, 2011).

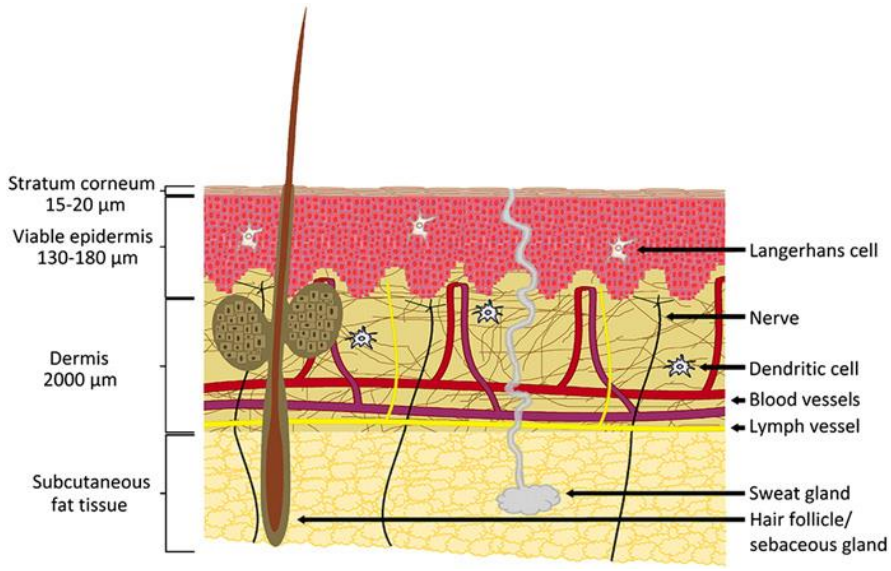

Figure 2.5 Representation of the skin microanatomy (Maaden *et al*., 2012).

2.2.1. Challenges in TDDS

When we have poor drug adsorption or enzymatic degradation by oral administration of drugs and painful parenteral drug delivery, an alternative approach of drug delivery across the skin is more appealing. However, transdermal delivery is severely limited by the inability of the large majority of drugs to cross skin at therapeutic rates due to the great barrier imposed by skin's outer stratum corneum layer (Paudel *et al*., 2010). With current delivery methods, successful transdermal drugs have molecular masses that are only up to a few hundred daltons and it has been difficult to exploit the transdermal route to deliver hydrophilic drugs; peptides and macromolecules, including new genetic treatments employing DNA (Eisenstein, 2011).

There are two important layers in skin: the dermis and the epidermis. The outermost layer, the epidermis, is approximately 100 to 150 micrometers thick, has no blood flow and includes the stratum corneum (SC). This is the most

influential layer for transdermal delivery as its composition allows it to keep water within the body and foreign substances out. As the SC is considered dead, there is no active transport and no difference between in vitro or in vivo permeation (Paudel *et al*., 2010). Once the drug molecule crosses the SC, molecules permeate rapidly and sweep into the blood stream either by transcellular or intracellular pathways (Miyano *et al*., 2005). The dermal papillary is so rich with blood capillaries that most penetrates clear within minutes (Jiang *et al*., 2007).

2.2.2. Existing transdermal drug delivery technologies

To overcome the main limitation of transdermal drug delivery and increase skin permeation, various ingenious technologies (Figure 2.6) have been established ranging from chemical/lipid enhancers, to electric fields employing iontophoresis and electroporation, to pressure waves generated by ultrasound or photo acoustic effects. Although these second generation mechanisms are all different but share the common goal to disrupt stratum corneum structure in order to create holes big enough for molecules to pass through (Kendall *et al*., 2010). The size of the disruptions generated by each of these methods are believed to be of dimension large enough to permit transport of small drugs and, in some cases, macromolecules, but probably small enough to prevent causing damage of clinical significance (Prausnitz, 2004).

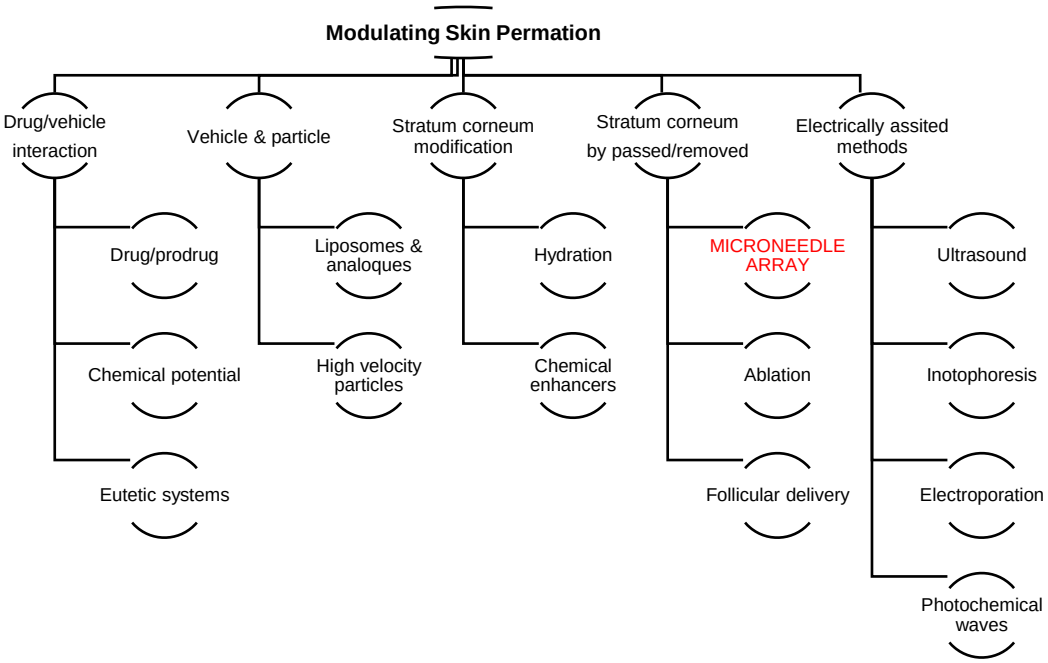

Figure 2.6 Various methods of enhancing transdermal drug delivery (adapted from Barry *et al*., 2001).

Recently a third generation approach that involves use of micron-scale needles (Microneedles) for creating larger transport pathways of micron dimensions and subsequently increasing the skin permeability has been developed. These pathways are order of magnitude larger than molecular dimensions and therefore, should readily permit transport of macromolecules (Kendall *et al*., 2010). Microneedles in addition could be also used for sampling body fluid like measuring glucose level in the blood (Bora *et al*., 2009). Despite their very large size relative to drug adminstration on a clinical scale they are not sufficiently tall to cause pain by stimulating the nerve endings which lie deep within the skin or eye (typically 1.5 mm in human skin) which is in contrast to conventional hypodermic needles. Therefore MNs offer a route for a completely pain free and minimal tissue damage platform for drug delivery (Jiang *et al*., 2007). Although the concept of MNs was patented in late 1970's by Alza Corp, the potential was not exploited until 1998 where Prausnitz *et al* publishes the first paper on use of

microfabricated MNs to enhace calcein delivery across skin. A schematic showing different ways MNs can be used to administer drugs is shown in Figure 2.7.

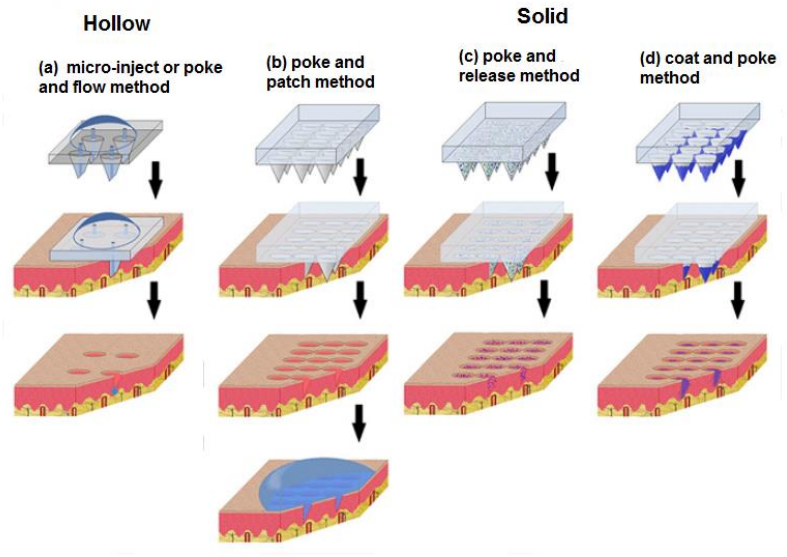

Figure 2.7 Schematic representation of different methods of MN application across the skin (a) Hollow MNs for continuous drug delivery (*micro-inject method or poke and flow method*) or body fluid sampling (b) Solid MNs applied and removed to create micro pores followed by the application of a traditional transdermal patch also called as *poke with patch* (c) Polymeric MNs which remain in skin and dissolve over time to deliver the drug within the MNs *(poke and release method)* (d) Solid MNs coated with drug molecules applied for instant delivery also called as *coat and poke method* (Maaden *et al*., 2012).

2.3. Microneedles

The first MNs where developed by Alza Corp in 1970 using silicon but many other materials such as stainless steel, dextrin, glass, ceramic, maltose, galactose and various other thermoplastic polymers are being used for the fabrication of microneedles (Donnelly *et al*., 2010 and Piotter, 2007). The creation of MNs for TDDS is been thought to be originated by combining the benefits of both conventional hypodermic needle injection and transdermal patches. Over the past decade, various designs of MNs have been developed

(Figure 2.8 and Table 2.2) using tools from the micro-electronics industry. Exploitation of these micro-electro-mechanical systems (MEMS) techniques has led to potential application in biomedical fields (called BioMEMS) which are used in drug delivery, bio sensors, DNA sequencing and chemical analysis systems. MNs have been fabricated in different range of sizes, shapes and materials, including solid spikes, biodegradable polymer, and hollow microneedles. Usually MNs are 25-1800 µm in length and 50-400 µm at the base and have a sharp tip with 5-40 µm radius (Lee et *al*., 2010 and Donnelly *et al*., 2010).

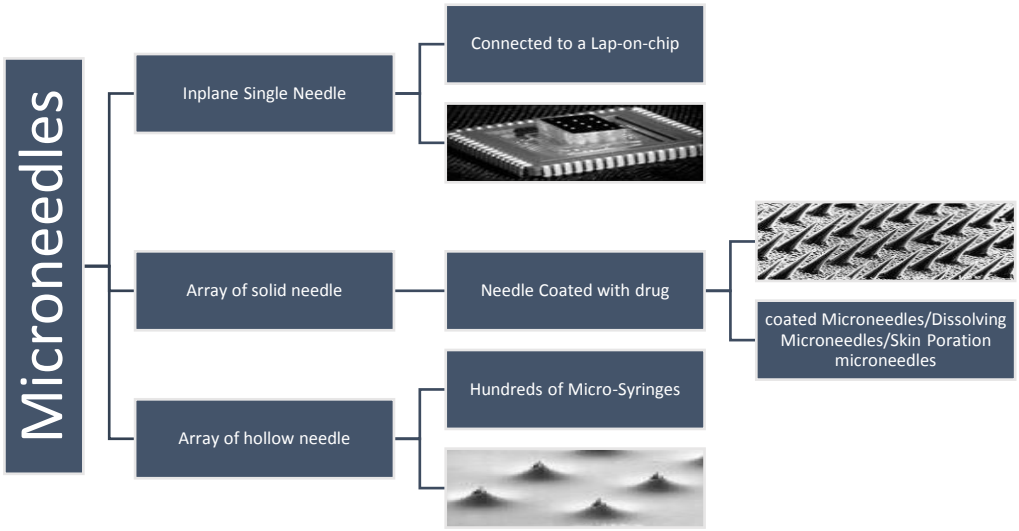

Figure 2.8 Types of Microneedles.

Name of the Technology	Manufacturer	Available drug product	Drug Products in developments
Macroflux	Alza	none	PTH patch, Vaccines, Proteins
h-patch	Valeritas	Bolus insulin delivery	-
Microinfusor	BD	none	Vaccines, Macromolecules
Micro-Trans	Valeritas	none	Fluid sensing of glucose and hormones
Microstructured Transdermal system	3M	none	Hydrophilic molecules
Micropiles	Texmac-Nanodes	10% Lidocaine and Indomethacin	
Microneedle Therapy System	Clinical resolution lab	Microneedle Dermaroller	

Table 2.2 List of advanced microneedle based drug delivery technologies (Bora.P. *et al*., 2007).

2.3.1. Types and materials used for microneedles

2.3.1.1. Solid microneedles

These were first designed to create micron-size pores on the skin which then acts as direct pathways allowing drug molecules to travel deep into the tissue. These MNs have usually sharp tips and good mechanical strength and are either made of silicon, metal or polymers.

2.3.1.2. Silicon microneedles (SMNs)

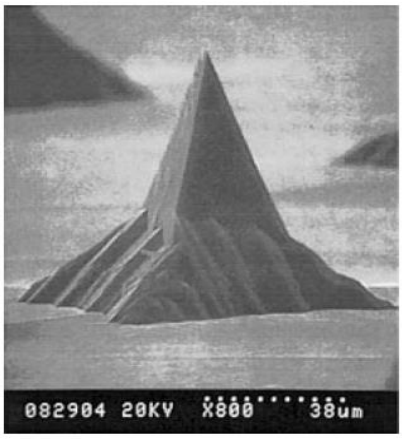

Figure 2.9 A single silicon microprobe fabricated by anisotropic silicon etching and used to deliver genes to plant and mammalian cells (Trimmer *et al*., 1995).

These are the simplest form of solid microneedle and usually spiked (Figure 2.9). The unique unifying characteristics are its simple fabrication schemes; using a deep-reactive ion etching method (Figure 2.10) we can manufacture them. This manufacturing step also includes depositing chromium masking layer onto a silicon wafer, patterning it using photolithography into dots with the size of the desired needle base. The wafer is then dry etched to create a high aspect ratio silicon microneedle. Prausnitz *et al* published the first study on SMNs (Figure 2.11) where it was demonstrated to increase the permeability of in vitro human epidermis by four times. A similar study conducted by McAllister *et al* showed that epidermis permeability of fluorescently-tagged bovine serum albumin (BSA) can be increased up to 1000 fold after treatment with SMNs (Jiang, 2006).

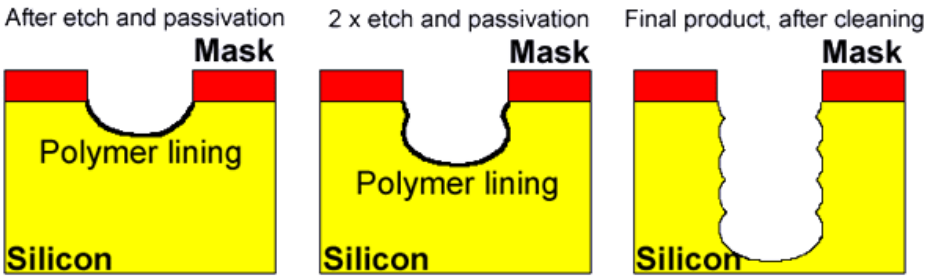

Figure 2.10 Diagram above illustrates how the process Deep Reactive Ion Etching (DRIE) incorporates alternate stages of etching to produce deep, vertical features (www.ukmig.com).

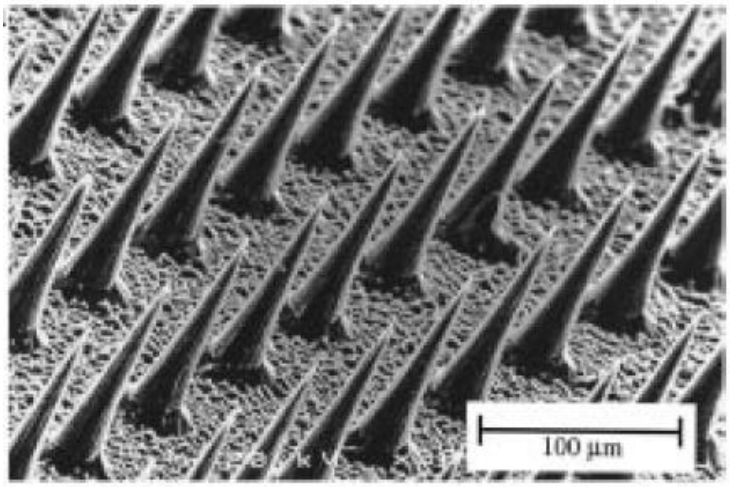

Figure 2.11 Arrays of solid silicon microneedles used in transdermal drug delivery study and demonstrated enhancement of dermal permeability (Prausnitz *et al*., 1998).

2.3.1.3. Metal microneedles

Although silicon is a commonly used substrate in microelectronics with extensive process development for more than 35 years, it is relatively expensive and requires clean room processing (Jiang, 2006). Metals are considered as better alternative materials for MNs and have very good mechanical strength and can be fabricated with ease. Various metals like stainless steel, titanium, palladium-cobalt alloys and nickel have been used as structural material for MNs fabrication. Metal SMs are fabricated using electroplating (palladium), photochemical etching (titanium), and laser cutting (stainless steel). *In vivo*

studies conducted by Martanto *et al* showed SMNs coated with insulin decreased the blood glucose level by 80% as compared to the control subjects.

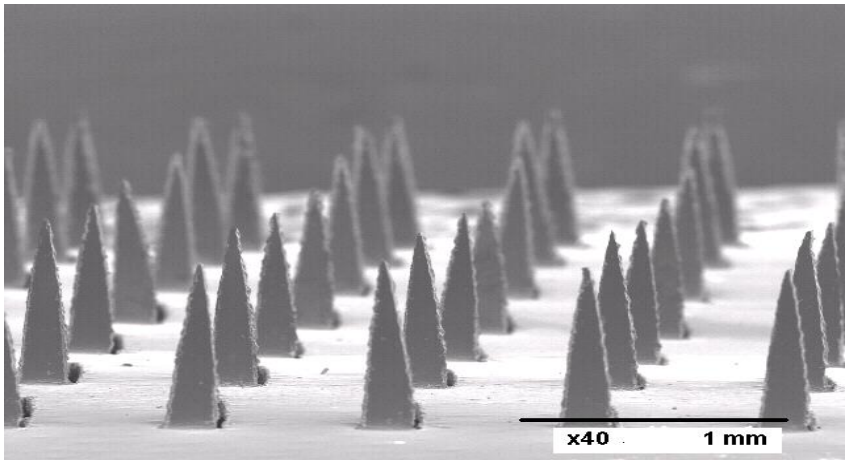

Figure 2.12 Solid stainless steel microneedle arrays used in an insulin delivery test using diabetic rats in vivo (Davis *et al*., 2004).

Solid metal microneedles (Figure 2.12 and 2.13) are generally formulated by coating the drug solution onto the shafts to single needle or arrays of needles, after application into the skin the coating dissolves off the MNs shaft and creates drug depots within the tissue to provide sustained release (Jiang, 2006)

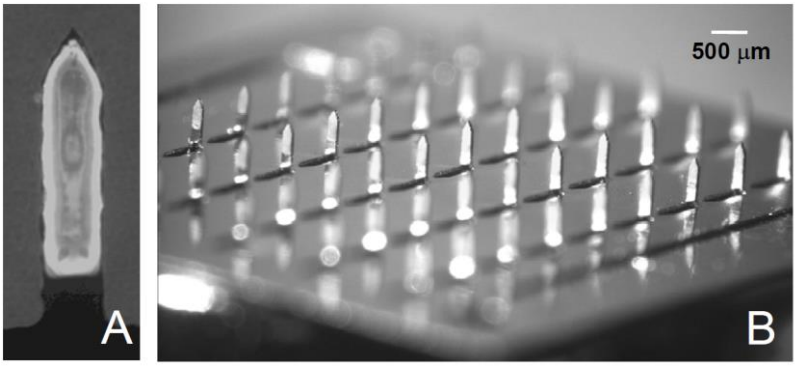

Figure 2.13 Images of coated solid metal microneedles (A) shows a fluorescent image of a single microneedle coated with sodium fluorescein, NaFl, and (B) shows a multi-array of microneedles coated with calcein (Gill and Prausnitz, 2007).

2.3.1.4. Hollow microneedles

Solid MNs increase the skin permeation by creating holes; however it is sometimes necessary to have more controlled transport pathways to delivery drugs to underlying tissue. This can be achieved by using hollow MNs (Figure 2.14). Hollow MNs are created by inclusion of a hollow lumen to the solid MNs, this capability substantially increases the drug loading of large molecules and deliver it in a pressure driven-convective transport (Jiang, 2006).

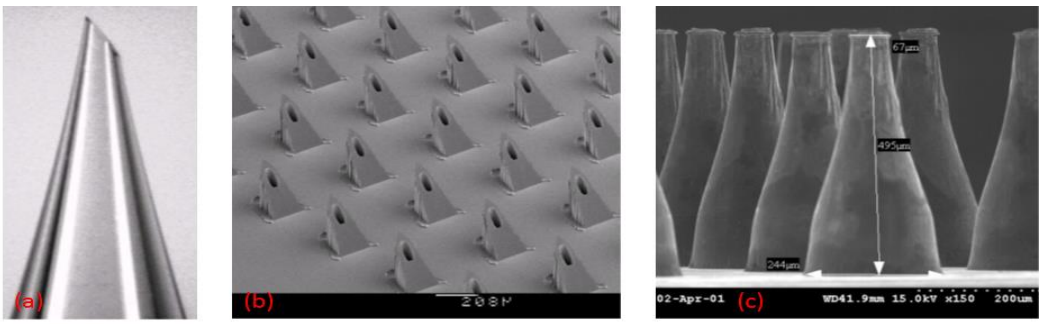

Figure 2.14 SEM images of different types of hollow microneedles (a) single, bevelled-tip, hollow glass microneedle used in micro infusion within human cadaver skin (Martanto, Moore *et al*., 2006) (b) arrays of hollow silicon microneedles used for transdermal liquid transport (Gardnier *et al*., 2002) (c) array of hollow, metallic microneedles used for skin insertion test (Davis, 2003).

2.3.1.5. Polymeric microneedles

Polymeric MNs have been fabricated using materials including engineering thermoplastics, biodegradable polymers, poly-silicon and sugars (Donnelly et *al*., 2010). Such polymeric MNs are gaining much attention because of the flexibility of the raw materials and the wide range of properties which they offer, such as biocompatibility, strength, toughness and optical clarity. When compared to other MEMS processes, fabrication of polymeric MNs can be considerably more cost effective (Piotter, 2006). To accurately manufacture

them to micro-scale tolerances, a variety of mould based techniques are used such as casting, hot embossing, injection moulding and investment moulding (Attia *et al*., 2009) Polymeric MNs can be loaded with molecules like drugs, DNA or vaccines and unlike solid and hollow MNs polymeric MNs acts as drug implants after insertion into the tissue (Jiang, 2006).

2.4. Why polymers?

Several materials have been used to date for manufacturing micro-featured structures for example glass and silicon. Polymers show superior properties over glass and silicon for many reasons (Fiorini and Chiu, 2005). Polymers are very cost effective; especially for mass production of disposable MNs. Polymers have a wide variety of characteristic material properties like mechanical strength, optical properties, chemical stability and biocompatibility (Attia *et al*., 2009). So they are relatively easy to tailor and to achieve required properties for processing and applications. Because of the viscoelastic nature of the polymers, increasing the shear rate and maintaining the polymer temperature above its T*g* (glass transition temperature) will allow the polymer to fill the smallest mould details (Hill S, 1995). There are many examples in the literature available where (*μ*IM) have been successfully used to replicate sub-micron features and surfaces with nano patterns (Attia *et al*., 2009; Demir, 2013; Whiteside *et al*., 2003; Martyn, 2004). A comparison between polymers and glass properties with respect to their use for microneedle applications is shown in Table 2.3.

	Polymers	Glass
Manufacturing Cost	Low in cost relative to glass, especially for mass-production.	Higher in cost, especially for relatively large-area substrates. Higher costs are also associated with clean-room facilities
Fabrication complexity	Fabrication steps are simpler than glass, and no wet chemistry is needed.	Time consuming and expensive, and wet chemistry is used.
Clean room Facilities	Clean-room facilities are necessary for applications where avoiding contamination with dust is critical. In certain cases, particles may become pressed into the polymer during processing without having an effect on device functionality.	Clean-room facilities are needed to avoid contamination.
Properties	Wide selection of polymers, hence mechanical, optical, chemical and biological properties can be tailored.	Less variability in available properties relative to polymers.
Operation temperature	Limited for polymers because of relatively low Tg compared to glass.	Wider range of operation temperature (1050-1200°C) relative to polymers.
Optical properties and fluorescence	Optical transparency is lower than glass. Except for special grades, polymers also have higher auto fluorescence relative to glass	Excellent optical properties; auto fluorescence levels do not affect detection capabilities.
Bonding	Different bonding options are available, for example: adhesives, thermal fusion, ultrasonic welding and mechanical clamping.	Time consuming relative to polymers. Bonding options include thermal, adhesive and anodic bonding.
Surface treatment	Surface treatment methods are available for polymers, but routine, well-established derivatisation techniques are not available.	Established chemical modification procedures for glass are available using organosilanes
Compatibility with organic solvents or strong acids	Except for some special grades, polymers are generally not compatible with most organic solvents and in some cases, strong bases or acids.	Good resistance to organic solvents and acids.
Geometrical flexibility	Polymer processing techniques offer more flexibility for geometrical designs, including for example different cross-	Limited to 2½-D designs. Due to the isotropic nature of the etching process, only shallow, low aspect ratio, mainly semi-circular channel

	section (curved, vertical or V-groove), high aspect ratio square channels, channels with a defined but arbitrary wall angle, or channels with different heights.	cross-sections are possible in glass substrates.
Permeability to gasses	Higher gas permeability relative to glass.	Glass does not have the gas permeability required for some biological applications, such as living mammalian cells.

Table 2.3 Comparisons between polymers and glass properties with respect to their use for microneedle applications (Attia *et al*., 2009).

2.5. Polymer selection for MN application

Selecting the appropriate polymer to micro-inject MN components is one of the challenging tasks in process design for MNs, because several considerations have been taken into account (Donnelly *et al*., 2010). These include the effect of polymer on achievable part tolerance, costs and meeting material property requirements. In the case of micro features like MNs, understanding the thermal properties are important, especially when the MN device is subject to elevated temperatures while processing. In order to avoid softening of the device, and subsequent deformation in features, glass transition temperature (T*g*), melt temperature (T_m) and thermal expansion coefficient will be critical (Hill, 1995 and Attia *et al*., 2009). During the processing of the polymer, dimensional stability and accuracy are key properties for MN polymers which are dependent on consistency of material and tendency to shrinkage (Heckele, 2004).

Micro-injection moulding is a process that exposes thermoplastics to severe operating conditions in terms of temperatures (up to few hundred degrees) and pressures (up to tens of mega-Pascals). In addition, being a pseudoplastic material, polymeric melts experience shear-thinning, i.e. a decrease in viscosity with increase in shear rate. Thus, radical changes in the material properties are

expected due to high shear-rates resulting from flow in to micro cavities (Attia *et al*., 2009). Therefore, the polymer selected should be appropriate for micro-injection moulding (Whiteside *et al*., 2003 and Fiorini, 2005).

Generally speaking, all standard thermoplastic materials suitable for conventional injection moulding can be used for micro-injection moulding, provided that some manufacturing conditions are met (Niggemann, 1998). Most of the materials used today in micro-injection moulding are low-viscosity formulations of standard polymers (Yao, 2002). For example, the polymer should possess low viscosity and hence good flow properties (Donnelly *et al*., 2010 and Attia *et al*., 2009). High mechanical strength is also recommended in order for the moulded part to resist mechanical stresses associated with demoulding friction or ejector forces. This is especially important for high-aspect-ratio structures, where a larger surface of contact between the mould and the polymer imposes higher frictional resistance while demoulding. Thus, small structures are often torn off at high-aspect ratios (Yao, 2002 and Attia *et al*., 2009). Taking into consideration the radical temperature changes in the variotherm process (heating the mould's surface prior to injection of the plastic, followed by cooling the mould as quickly as possible after the cavity has been filled), it is recommended that the polymer has a narrow temperature interval between free-flowing and rapid solidification (Weber, 1998 and Attia *et al*., 2009). Many researchers have reported mouldability of engineering plastics. Table 2.4 summarises polymers that have been reported as mouldable by the micro-injection moulding process. Most of the known engineering plastics appear on this list. Among the listed materials, some polymers such as POM, PPS, PBT and LCP have been specifically recommended for medical

applications, because they comply with the approval criteria of the European regulatory agencies (Attia *et al*., 2009).

Some challenges still exist with respect to polymer selection. Designed experiments show that a single polymer can have different filling quality for different part shapes or aspect ratios (Whiteside *et al*., 2003 and Hill, 1995). In addition, for a specific geometrical shape, using different polymers results in different part qualities in terms of filling and shrinkage (Martyn, 2003). This interaction between the type of polymer moulded and the quality of the part produced makes it a challenging task to determine a specific material for a certain application without testing it under different conditions (Martyn, 2003; Attia *et al*., 2009 and Yoon, 2007).

Class	Polymer	Full Name
Amorphous	PMMA :Acrylic	Polymethylmethacrylate
	PC	Polycarbonate
	PSU	Polysulfon
	PS	Polystyrene
	COC	Cyclic Olefin Copolymer
	COP	Cyclic Olefin Polymer
	PPE(PPO)	Polyphenylene Oxide
	PEI	Polyetherimide
	PAI	Polyamide imide
	MABS	Methylmethacrylate Acrylonitrile-Butadiene-Styrene
	SAN	Styrene Acrylonitrile
	SBS	Styrene-Butadiene-Styrene
	ABS	Acrylonitrile-Butadiene-Styrene
Semi-crystalline	LCP	Liquid Crystal Polymer
	PP	Polypropylene
	PE	Polyethylene
	POM :Acetal	Polyoxymethylene
	POM-C	Polyoxymethylene (Carbon-filled)
	PBT:Polyester	Polybutylene Terephthalate
	PBT-HI	Polybutylene Terephthalate (filled with 15% glass fibre)
	PA6:Nylon	Polyamide 6
	PA 12	Polyamide 12
	PA 12-C	Polyamide 12 (Carbon-filled)
	PVDF	Polyvinylidene Fluoride
	PFA:Teflon	Perfluoroalkoxy
	PEEK	Polyetheretherketone
	PLA:Polyester	Polylactic Acid (Polylactide)

Table 2.4 Polymers for micro injection moulding (Attia *et al*., 2009).

2.5.1. Patent search

US Patent Number	Topic	Date of the Patent	Main Inventor	Claim
US3964482	Drug delivery device	22/6/1976	Martin.S.Gerstel Alza Corporation, California	First drug delivery device comprising projections for penetrating Stratum corneum
US6924087B2	Polymer Microneedles	2/8 /2005	Yeshurun et al Nano Pass Technology	Method to produce an inexpensive, robust, sharp hollow and solid MN array for drug delivery from radiation sensitive material
US6899838	Method of forming a mold and molding a micro-device	7/52005	Becton, Dickinson and Company (Franklin Lakes, NJ, US)	A method of forming a device including a plurality of micron or sub-micron sized using injection molding, compression molding, embossing or any other compatible technique.
US7497980	Microneedles and Microneedle Fabrication	3/3/2009	Xu, Yuan .Agency for Science,technology and Research (Centros, Singapore)	The method of forming moulds for hollow microneedle array.
US6749792	Micro-needles and methods of manufacture and use thereof	15/6/2004	Olson, Lorin LifeScan, Inc. (Milpitas, CA)	Method of manufacturing Microneedles using lithograghy and how to give tip angle for increase insertion
US20030135161	Microneedle devices and methods of manufacture	17/7/2003	Fleming, Patrick R. 3M INNOVATIVE PROPERTIES COMPANY	Manufacturing methods of microneedle using simultaneous application of pressure and ultrasonic energy.
US 6551849	Method for fabricating arrays of micro-needles	22/4/2003	Kenney, Christopher J. University of Hawaii	Method of manufacturing Silicon hollow and solid Microneedle using etching techniques.
US 5658515	Polymer micromold and fabrication process	19/8/1997	Lee, Abraham P.	Fabrication of mould assembly for a micronozzle or microneedle, and plastic parts, such as microballoons for angioplasty, polymer microparts, and microactuators, etc
US7918814	Method for drug delivery to ocular tissue using microneedle	05/4/2011	Prausnitz, Mark R. Georgia Tech Research Corporation (Atlanta, GA, US) Emory University (Atlanta, GA, US)	Delivery drugs to the posterior segment of the eye using array of multiple microneedles.

US20100312191	Microneedle Devices and Methods of Manufacture and Use Thereof	9/12/2010	Prausnitz, Mark R. Georgia Tech Research Corporation (Atlanta, GA, US)	Method of manufacturing hollow and porous microneedles using etching and electroplating techniques.

Table 2.5 List of patents related to microneedle technology.

So on the basis of literature available (Table 2.4 and 2.5) three candidate materials for microneedle manufacture have been shortlisted based on their mechanical properties, rheological behaviour and biocompatibility – PC (Lexan HPX8REU), PEEK (Optima LT-3) and LCP (Vectra B230).

2.5.2. Polycarbonate (PC)

PC are long-chain linear polyesters of carbonic acid and dihydric phenols, such as bisphenol A. Lexan HPX8REU polycarbonate offers an outstanding balance of high strength, toughness, clarity, processability, and bondability for medical device components. (CES Edupack 2010, Polycarbonate specs sheet)

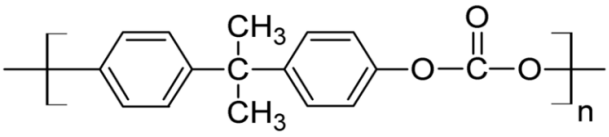

Figure 2.15 Chemical structure of polycarbonate (www.omnexus.com).

Lexan HPX8REU is designated as medical-grade and has met the requirements of the FDA-Modified ISO 10993. Polycarbonate has a melting point at 220°C and glass transition temperature of about 150°C, so it softens gradually above this point and flows above about 300°C. The mould must be held at high temperatures, generally above 80°C to make strain- and stress-free products

(Howdeshell *et al.,* 2006). Table 2.6 shows the typical injection moulding parameters for PC.

Typical Injection Moulding Conditions	
Barrel Temperatures	
Rear	241- 266^{o}C
Middle	268-288 ^{o}C
Front	279-302 ^{o}C
Nozzle	268-307 ^{o}C
Melt Temperature	282-302 ^{o}C
Mould Temperature	65-105 ^{o}C
Injection Pressure	10000-20000 psi
Hold Pressure	50-70 % injection pressure
Back Pressure	50-100 psi
Screw Pressure	50-75 rpm
Injection Speed	Moderate to fast
Cushion	1/8-14 in
Clamp	3-5 tin/in^{2}

Table 2.6 Injection moulding parameters for polycarbonate (www.valueplastics.com).

2.5.3. Poly ether ether ketone (PEEK)

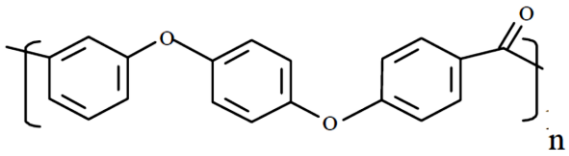

Figure 2.16 Chemical structure of PEEK (www.engineersedge.com).

PEEK (poly (oxy-1, 4-phenyleneoxy-1, 4-phenylencarbonyl-1, 4-phenylene) is an organic semi crystalline thermoplastic with excellent mechanical and chemical resistance properties that are retained to high temperatures. The Young's modulus is 3.6 GPa and its tensile strength 90 to 100 MPa. PEEK has a glass transition temperature at around 143°C and melts around 343°C. The thermal conductivity increases nearly linearly versus temperature between room temperature and solidus temperature. It is highly resistant to thermal

degradation as well as attack by both organic and aqueous environments. It is attacked by halogens and strong acids as well as some halogenated compounds and aromatic hydrocarbons at high temperatures. It dissolves completely in concentrated sulfuric acid at room temperature. Because of its robustness, PEEK is used to fabricate items used in demanding applications, including bearings, piston parts, pumps, HPLC columns, compressor plate valves, and cable insulation. It is one of the few plastics compatible with ultra-high vacuum applications. PEEK is considered an advanced biomaterial used in medical implants. (CES Edupack 2010, Poly ether ether ketone specs sheet) Table 2.7 shows the typical injection moulding parameters for PEEK.

Parameter	Unfilled Grades
Mould Temperature	177–204°C
Rear Zone Temperature	354°C
Middle Zone Temperature	365°C
Front Zone Temperature	371°C
Nozzle Temperature	374°C
Injection Speed	Moderate
Injection Pressure	10–20 (690–1380) kpsi (bar)
Hold Pressure	5–10 (340–690) kpsi (bar)
Back Pressure	500 (35) psi (bar)
Screw Speed	75 rpm

Table 2.7 Injection moulding Parameters for PEEK.

2.5.4. Liquid crystal polymer (LCP)

Liquid crystal polymers (aromatic polyester polymer) are a family of high performance plastics. They are distinguished from semi-crystalline plastics by their special molecular structure, which consists of rigid, rod-like macromolecules that are ordered in the melt phase to form liquid crystal structures (Figure 2.17).The characteristic property profile and behaviour of

liquid crystal polymers are so different from those of other resins, that LCPs are treated as a separate class of polymer (Table 2.9). Even so, they can be processed by all conventional methods used for thermoplastics, including injection moulding, extrusion, co- extrusion, blow moulding, etc. Table 2.6 shows the typical injection moulding parameters for LCP.

Parameter	Unfilled Grades
Mould Temperature	70-120°C
Rear Zone Temperature	270-280°C
Middle Zone Temperature	275-285°C
Front Zone Temperature	280-290°C
Nozzle Temperature	300-310°C
Injection Speed	Moderate-low
Injection Pressure	10–20 (690–1380) kpsi (bar)
Hold Pressure	5–10 (340–690) kpsi (bar)
Back Pressure	500 (35) psi (bar)
Screw Speed	60 rpm

Table 2.8 Injection moulding Parameters for LCP.

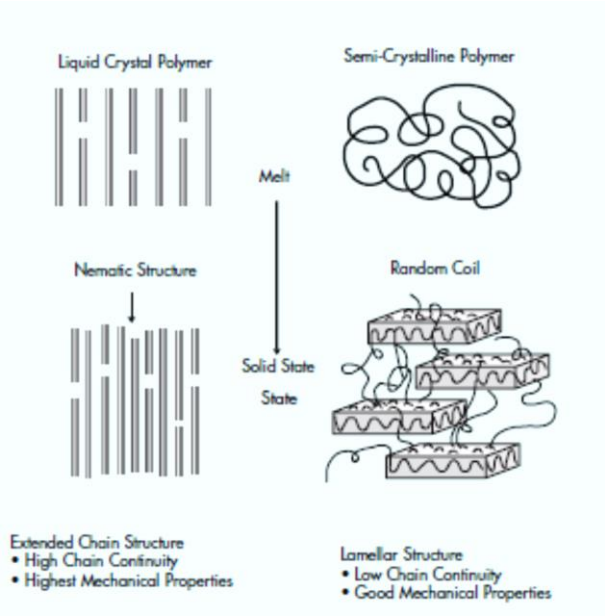

Figure 2.17 Representation of structural difference between LCP and conventional semi-crystalline polymers (www.ticona.co.uk/vectra).

Amorphous Polymers	Semi-Crystalline Polymers	Liquid Crystal Polymers
No sharp melting point/soften gradually	Relatively sharp melting point	Melt over a range of temperatures; low heat of fusion
Random chain orientation in both solid and melt phase	Ordered arrangement of chains of molecules and regular recurrence of crystalline structure only in solid phase	High chain continuity; extremely ordered molecular structure in both melt phase and solid phase
Do not flow as easily as semi-crystalline polymers in moulding process	Flow easily above melting point	Flow extremely well under shear within melting range
Fiber glass and/or mineral reinforcement only slightly improves Deflection Temperature under Load (DTUL)	Reinforcement increases load bearing capabilities and DTUL considerably, particularly with highly crystalline polymers	Reinforcement reduces anisotropy and increases load bearing capability and DTUL
Can give a transparent part	Part is usually opaque due to the crystal structure of semi-crystalline resin	Part is always opaque due to the crystal structure of liquid crystal resin
Examples: cyclic olefinic copolymer, acrylonitrile-butadiene-styrene (ABS), polystyrene (PS), polycarbonate (PC), polysulfone (PSU), and polyetherimide (PEI)	Examples: polyester (Impet® and Celanex® thermoplastic polyesters, Duranex™ PBT), polyphenylene sulfide (Fortron® PPS), polyamide (Celanese® nylon), polyacetal copolymer (Celcon® POM, Hostaform® POM, Duracon™ POM)	Examples: Vectra® LCP

Table 2.9 Comparison of amorphous, semi crystalline and liquid crystal polymers (www.ticona.co.uk/vectra).

2.6. Methods of manufacturing MNs

The first MNs were manufactured from silicon (Hashmi *et al*., 1995 and Henry *et al*., 1998), but many other materials have also been used in MN fabrication, such as stainless steel dextrin, glass, ceramic, maltose, galactose and various other thermoplastics (Donnelly *et al*., 2010). Over the last decade, investigators have used different methods in the manufacture of a wide range of MNs, such

as physical and chemical vapour deposition, chemical isotropic etching, injection moulding, reactive ion etching, surface micromachining, lithography-electroforming-replication and laser drilling (Trichur *et al*., 2002; Kolli and Banga, 2008; Stoeber and Liepmann, 2005; Yang and Zahn, 2004). The most common method of MN manufacture used by many leading researchers in microneedle community is by casting, etching or hot embossing techniques. These techniques still pose a great challenge for bulk manufacturing for low cost microneedles. The only group to date capable of producing commercial MNs at low cost is the 3M innovative microneedle team lead by Patrick R and Hansen K. They use injection moulding techniques to successfully manufacture solid MNs (composed of 1260 needles) and hollow MNs (composed of 16 needles).

2.6.1. Why micro-injection moulding

MN devices have extensive applications in the fields of medicine and biotechnology many researchers are currently focusing on manufacturing of MN devices on a mass production scale with relatively low costs (Sammoura *et al*., 2007; Attia *et al*., 2009 and Donnelly *et al*., 2010). This is especially important if the purpose of application is for disposable use (Yung, 2011). Among the different micro-moulding techniques available (reaction injection moulding/ hot embossing/thermo forming), micro-injection moulding (*μ*IM) is one of the most promising techniques for manufacturing polymeric MNs (Trichur *et al*., 2002 and Liepmann, 2005). For mass market applications polymers possess advantages over other materials. With short cycle times, full automation, accurate replication, high productivity of complex geometry parts (Yung, 2011 and

Whiteside *et al*., 2004) and dimensional control *μ*IM is considered to be the best manufacturing technique for MNs (Steglich *et al*.,2012). A schematic of a conventional injection moulding machine is shown in Figure 2.18 while Figure 2.19 shows the drawing of the hot embossing process and Figure 2.20 schematic drawing of the injection moulding process.

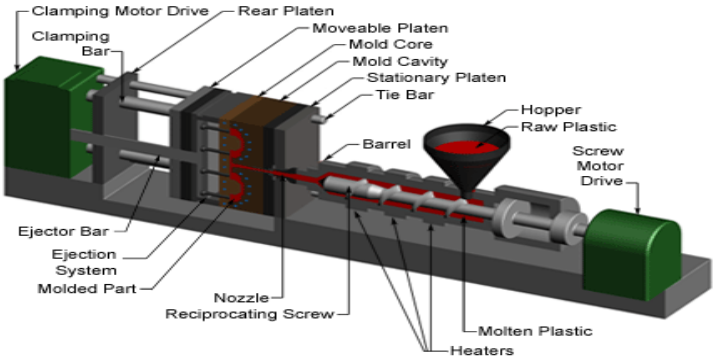

Figure 2.18 Injection moulding machine (www.custompartnet.com).

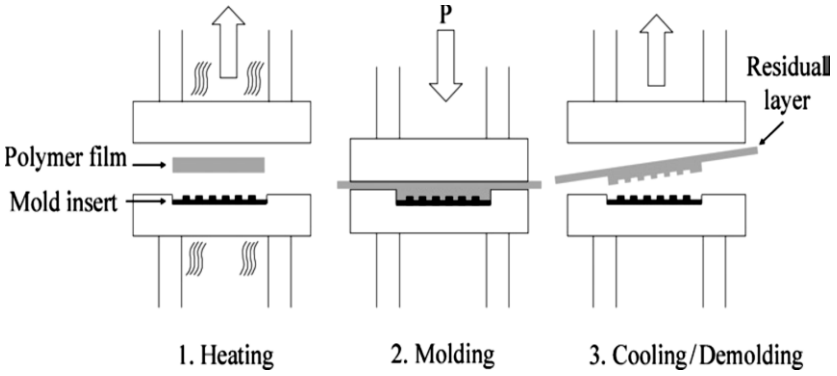

Figure 2.19 Schematic drawing of the hot embossing process (Giboz *et al*., 2007).

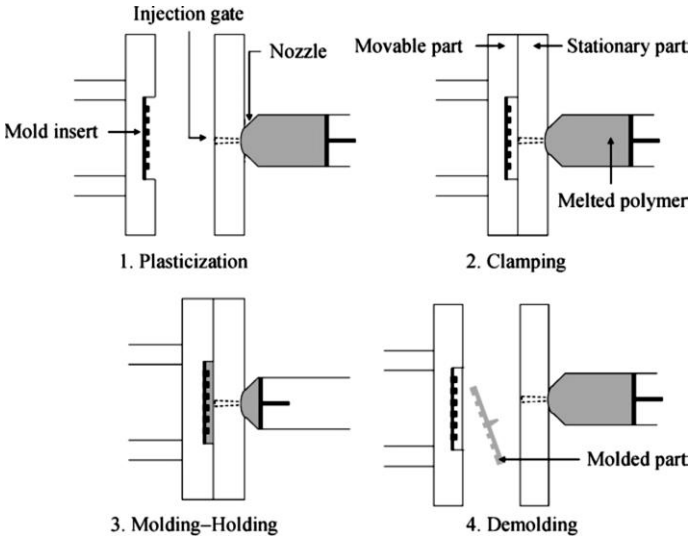

Figure 2.20 Schematic drawing of the injection moulding process (Giboz *et al*., 2007).

2.6.2. What is (*μ*IM)?

Micro injection moulding is an extension of injection moulding capable of developing a more efficient, and cost effective process for manufacturing parts with micro features. It is a process of transferring micron precision of micro structured metallic moulds to moulded products. Here, thermoplastic material in the form of granules is transferred to a hopper to a heated barrel where it becomes molten. This material is then forced under pressure inside a mould cavity where it is subjected to holding time for a specific time so as to compensate material shrinkage. After sufficient time the material solidifies into mould shape and gets ejected, and the cycle repeats (Wang, 1987)

Many researchers have mentioned different definition of a micro-moulded part. Whiteside *et al* explains a micro-moulded part should weigh in the range of few milligrams and features should be in the micrometer range (Whiteside *et al*., 2004).

2.6.3. Tooling techniques and process parameters

Process cycle

The sequence of events during the injection moulding of a plastic part is called the injection moulding cycle. The cycle begins by

Stage 1 *(Feeding)*

Thermoplastic powdered or granulated thermoplastic is fed from a hopper into the Injection Moulding machine.

Stage 2 *(Heating)*

The Injection Moulding machine consists of a hollow steel barrel, containing a rotating screw which carries the plastic along the barrel to the mould. Heaters surround the barrel melt the plastic as it travels along the barrel.

Stage 3 *(Clamping)*

Two halves of the mould should be securely closed by clamping unit prior to the injection of the material into the mould. Each half of the mould attached to the machine is allowed to slide and when the hydraulics pushes the mould halves together and exerts sufficient force to keep it closed while the material is injected.

Stage 4 *(Injection)*

During this process the fed raw plastic is melted by heat and pressure and the molten plastic is injected into the mould very quickly and the build-up of the pressure packs and holds the material. The amount of the material injected into the mould is called the shot.

Stage 5 *(Hold/Pack pressure)*

Injection phase ends when 95-99 % of the cavity is filled and moves to holding pressure and the point at which this happens is called switch over point. The

need of holding pressure is to replace the volume of the part during the cooling down phase and without this pressure the moulded part may crimp.

Stage 6 *(Cooling)*

Following the holding pressure the next phase is cooling, where the molten plastic inside the mould begins to cool as soon as it makes contact with interior mould surfaces. As this process occurs the plastic solidifies into the shape of the desired part.

Stage 7 *(Ejection)*

After the cooling cycle the last stage is ejection of the moulded part from the mould. When the mould is opened an ejector mechanism is usually used to push the part out of the mould. The time required to open the mould and to eject the part is called as dry cycle time of the machine. Once the part is ejected the mould can be clamped shut for the next shot to be injected (Fenner, 1979). After the injection moulding cycle some post processing is required like excess material along with any flash that has occurred should be trimmed (Figure 2.21)

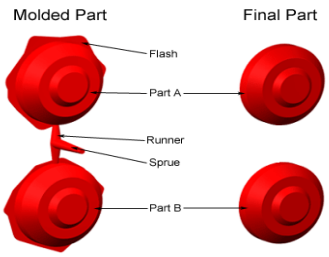

Figure 2.21 Schematic of an injection moulded part (www.custompartnet.com).

2.6.4. Equipment

The machine unit comprises of many components which are available in various configurations (horizontal/vertical) but the fundamental systems comprising a machine are:

a) Injection unit
b) Clamping unit

The Injection unit

The first part of this unit is a hopper where raw plastic is kept. The hopper has opening in the bottom which allows the entry of the poured plastic pellets into the heated barrel (Weber, 1998). The injection unit is responsible for heating and injecting the material into the mould. The microinjection machine utilises a plasticising and injection system different from the conventional in-line reciprocating screw system. Unlike the in-line reciprocating screw system (Figure 2.22), the microinjection machine employs a stationary plasticising screw which prevents axial wear (Cabrera, 2010). Axial wear is present because the reciprocating screw has two functions: plasticising and injection, thus it must travel back and forth between shots. Furthermore, the reciprocating movement of the screw leads to inconsistent thermal distributions. As a consequence, the density of the metered material, and shot volumes are inconsistent (Niggemann, 1998).

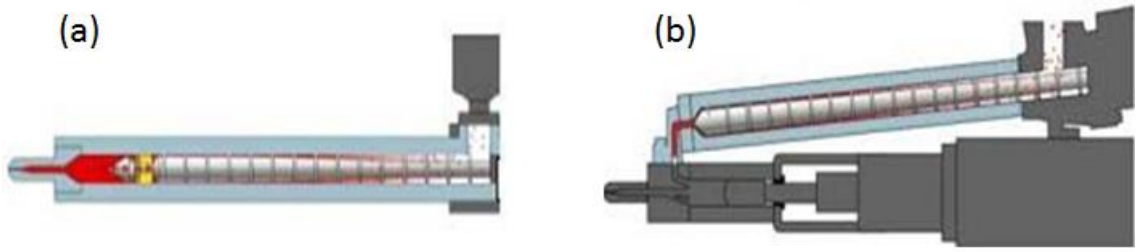

Figure 2.22 Different types of injection units (a) reciprocating screw system (b) V-Line two stage system (Cabrera, 2010).

Clamping unit

Each half of the mould is fixed to a large plate called platen and the front mould which has the mould cavity is mounted to a stationary platen and aligns with

nozzle of the injection unit. The rear half of the mould core is mounted to a movable platen which slides along the bars (Potsch *et al*., 2008). The electrically or pneumatically powered clamping motor actuates clamping bars that rotates the movable platen towards the stationary platen and exert sufficient force to keep the mould securely closed while the material is injected and subsequently cools. After sufficient cooling time the mould is opened by the clamping motor and an ejector device which is attached to the rear half of the mould is actuated which releases the moulded part (Cabrera, 2010). A list of micro-moulding machines commercially available and their characteristics are shown in Table 2.10.

Manufacturer	Model	Clamp force (kN)	Injection capacity (cm^3)	Injection pressure (Bars)	Plasticization (screw or plunger)	Injection speed (mm s^{-1})
Lawton	Sesame Nanomolder	13.6	0.082	3500	10 mm plunger	1200
APM	SM-5EJ	50	1	2450	14 mm screw	800
Battenfeld	Microsystem 50	56	1.1	2500	14 mm screw	760
Nissei	AU3	30	3.1	–	14 mm screw	–
Babyplast	Babyplast 6/10	62.5	4	2650	10 mm plunger	–
Sodick	TR05EH	49	4.5	1970	14 mm screw	300
Rondol	High Force 5	50	4.5	1600	20 mm screw	–
Boy	12/AM 129-11	129	4.5	2450	12 mm screw	–
Toshiba	EC5-01.A	50	6	2000	14 mm screw	150
Fanuc	Roboshot S2000-I 5A	50	6	2000	14 mm screw	300
Sumimoto	SE7M	69	6.2	1960	14 mm screw	300
Milacron	Si-B17 A	147	6.2	2452	14 mm screw	–
MCP	12/90 HSE	90	7	1728	16 mm screw	100
Nissei	EP5 Real Mini	49	8	1960	16 mm screw	250
Toshiba	NP7	69	10	2270	16 mm screw	180

Table 2.10 List of micro-moulding machines commercially available and their characteristics (Giboz *et al*., 2007).

2.6.5. Tooling

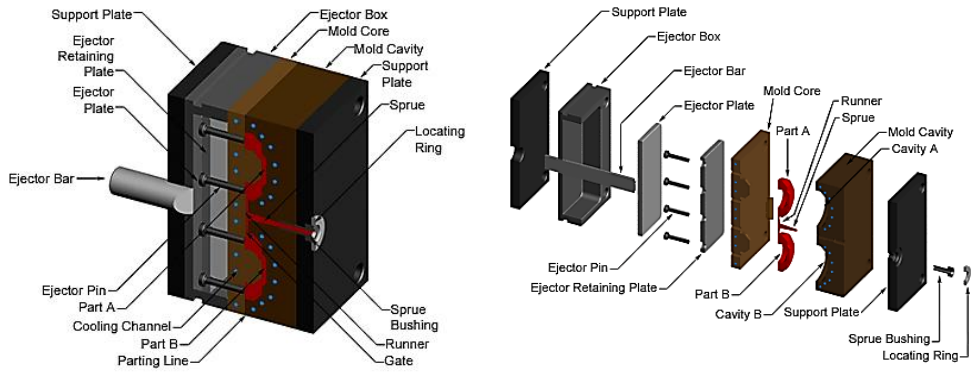

Figure 2.23 Showing mould closed and mould - exploded view (www.custompartnet.com/wu/InjectionMolding).

The *μ*IM process uses moulds which are typically made from various grades of steel or aluminium. The mould can be split into two halves and has many components. One half is stationary and rear half is movable and can be opened. The two main components of the mould are the mould cavity and mould core (Potsch *et al*., 2008). When the mould is closed the mould core and mould cavity form the part cavity, which will be filled with molten plastic shown in Figure 2.23 (Cabrera, 2010).

Mould base

The mould core and mould cavity are mounted to mould base which is then fixed to the platens inside the *μ*IM machine the front half of the mould base (Figure 2.24) includes a support plate to which mould cavity is attached. It also accommodate sprue brushing and locating ring in order to align the mould base to the nozzle. The rear half accommodates the ejector pins to which the mould core is attached. During the process when the clamping unit separates the

ejector bars pushes ejector plate forward inside the ejector box which in turn pushes the ejector pins into the moulded parts (Potsch *et al*., 2008).

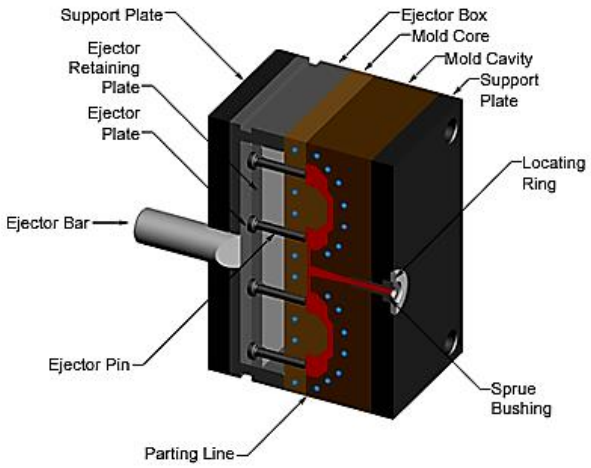

Figure 2.24 Showing the mould base (www.custompartnet.com).

Mould channels

For the molten plastic to flow into the mould cavities several channels are integrated into the mould design. The first part of the molten plastic that enters the mould through a sprue (Potsch *et al*., 2008). Some additional channels (Figure 2.25) called runners carry the molten plastic from sprue to all the cavities that must be filled (Robert, 1994). At each runner the molten plastic enters the cavity through a gate which gives direction for the flow (Attia *et al*., 2009).

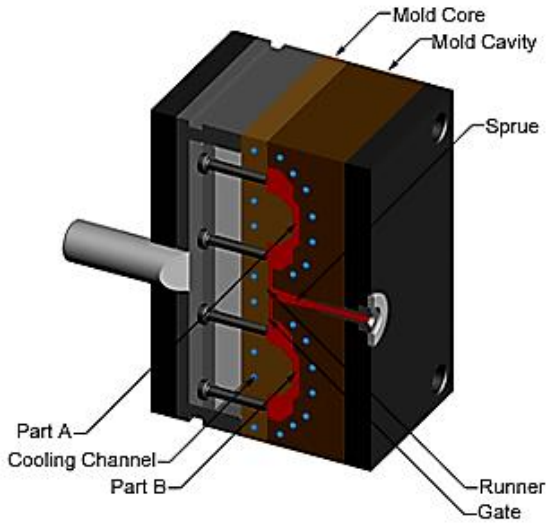

Figure 2.25 Mould showing mould channels (www.custompartnet.com).

Moulds made for micro-injection moulding of Microneedles are similar to moulds made for conventional injection moulding. However, moulds made for microinjection moulding have special features. For example, moulds can be controlled by the variotherm process one has to also consider about the evacuation procedure of the microneedles which can be done using air evacuation systems. Due to the size of the mould cavity and features, adapted mould sensors are used, because conventional sensors are not always suitable to micro-features. Special ejector/withdrawal design is important, so that microneedles are not deformed due to the induced friction between the mould and the part (Robert, 1994 and Attia *et al*., 2009).

Moulds used specially for microneedle applications are usually produced on an insert, which is then fitted in the main mould body. While the mould is made of steel, as in conventional injection moulding, inserts can be manufactured of other materials, depending on the technology used. This is because hardened steel, which is the commonly used material for mould-making, requires

specialised, and hence expensive, tools for machining micro-sized channels and features (Robert, 1994). The use of insert moulds also reduces the over-all cost of process set up where the finalised mould design is produced by a number of iterative steps in which parts are moulded and the mould design is then changed (Potsch *et al*., 2008 and Attia *et al*., 2009).

2.6.6. Difference between conventional injection moulding (IM) and micro-injection moulding (µIM)

The µIM is moulding process (Figure 2.26) supposed to provide the precision of micron or even submicron for the products, which is difficult to be produced using a traditional IM machine. In the traditional reciprocating IM process, polymer is melted and injected into the cavity through the screw barrel system. So the main difference between µIM and conventional IM process is separation of plasticisation and polymer melt injection phase (Bellantone *et al*., 2013).

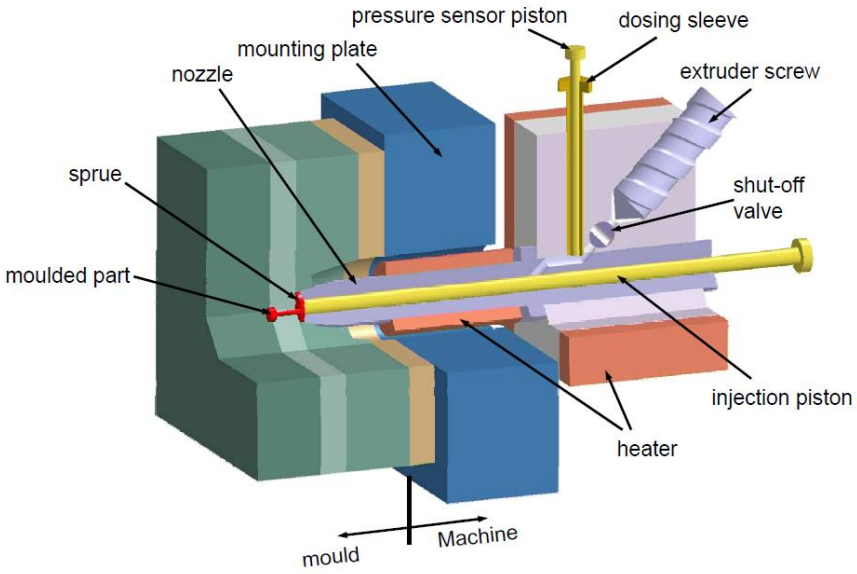

Figure 2.26 Micro-injection moulding process (www.mamk.fi).

In a conventional IM (also called as single step system as shown in Figure 2.27) plasticising, metering and injection happens in the same barrel. With the screw

diameters in range of 16-32mm it is very difficult to control small shot size (Bellantone *et al.*, 2013).

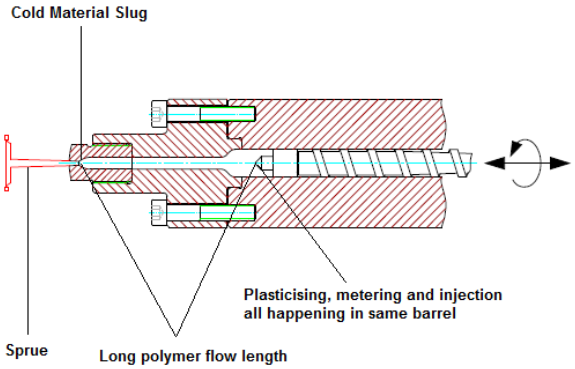

Figure 2.27 Single step standard injection technology (www.mamk.fi).

A conventional IM system with 14 mm screw diameter will require 0.0056 mm stroke to produce a shot weight of 1mg which is extremely difficult to obtain. Other issues with this technology include a large melt cushion (extra material in the barrel to ensure the part is packed during the hold time), cold material slug (the polymer melt that is initially pushed to the nozzle which in contact with a cold mould) and long polymer flow length. This shows that to manufacture micro dimensions we need a specialised system or refinements in IM, leading to the development of micro-injection moulding systems.

µIM uses two or three step technology, where in a two-step process (Figure 2.28) plasticisation and metering occurs in the same barrel and then the metered dose is transferred to the injection unit where a small piston injects the shot into the mould cavity.

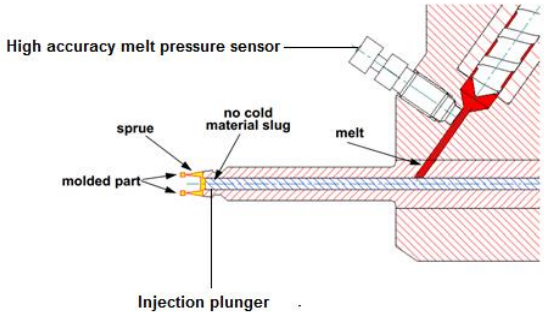

Figure 2.28 Two-step split plasticising injection technology (www.mamk.fi).

Where as in the three step process (Figure 2.29) shot preparation is separated into plasticisation phase where the polymer pellets are melted down in the extrusion screw and in the next step this polymer melt is extruded into the metering chamber where a servo-driven plunger prepares a dose of material and a shut of valve closes to stop material flowing back into metering chamber. Then a predetermined volume of polymer melt is transferred to the injection chamber to be injected into the mould cavity.

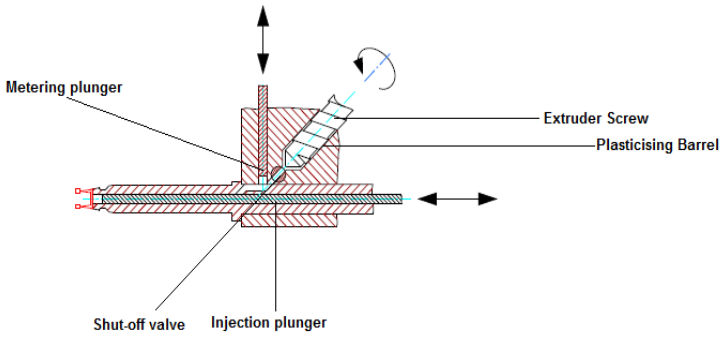

Figure 2.29 Three step split plasticising, dosing and injection technology (www.mamk.fi).

2.7. Surface modification

Polymers are widely used in many fields like aeronautics, engineering, electronics, automobiles, pharmaceuticals and medical devices. Despite the huge use, its hydrophobic nature makes polymers difficult to coat with medicaments which is important for solid coated MN drug delivery systems. A well-established solution to this problem is surface modification of the polymer surface to increase the surface free energy and wettability. Research conducted by Labat *et al*, showed the effect of low power plasma treatment on polypropylene for improved ketoprofen release. Vasilev, studied the potential of plasma polymerisation to modify the surface of the polymer films to enhance drug delivery and Kusuya *et al*, prepared controlled release tablets of theophylline using plasma techniques. Table 2.11 shows various methods of surface treatment available in the literature.

Technique	Process	Types	Technology Status	Comments
Abrasion	Mechanical	Dry or wet blasting, hand or machine sanding	Obsolete	Labour intensive, must deal with residuals
Chemical Etching	Chemical	Immersion, brushing, rinsing and spraying	Obsolete	Safety issues due to use of corrosive, toxic materials and hazardous-waste disposal problems
Corona Discharge	Electrical and Chemical	Available for both conductive and dielectric substrates	Contemporary	Applicable to films and webs
Gas Plasma	Electrical and Chemical	Available for film or three dimensional applications	Contemporary	Convenient and cost effective, nontoxic materials
UV	Electrical and Chemical	For distinct parts in batch systems	Developmental Contemporary	Generally only in batch format and requires longer residence time

Table 2.11 Various methods of surface treatments (Tillmann and Vogli, 2006).

2.7.1. Mechanical surface roughening (abrasive technique)

This process is considered to be the easy and most inexpensive surface modification technique since the cost of the equipment is very low. Among conventional surface treatment techniques, mechanical abrasion serves only to increase the surface area of the material by "roughening" the exposed areas prior to coating or adhesive bonding. Mechanical abrasion can be achieved through dry blasting, wet blasting or hand/machine sanding. These processes can be very operator sensitive, labour-intensive, dirty, and difficult to perform on the high-production volumes. Davies *et al* (1991) showed that surface roughening of PEEK 450G increased bond strength to values 4.6 times as high as without roughening (Comyn and Mascia, 1996).

2.7.2. Surface etching

In this process surface material is removed by immersing the polymer in a liquid bath containing a chemical etchant. Etching by wet chemistry is least preferred because it requires disposal of chemical used. The etchants attack the material such as oxide, nitride, aluminium, poly silicon, gold and silicon. In dry etching is carried out in the presence of inert or reactive gases. It is categorised into two main types reactive ion etching (RIE) which involves chemical process, and ion-beam milling, which involves purely physical processes. Davis *et al* demonstrated the etching of carbon fibre filled PEEK where he used a composition of 7 g $K_2Cr_2O_7$ + 12g H_2O + 150g H_2SO_4 and achieved bond strength 12 times as high as without etching (Davies *et al*., 1991).

2.7.3. Corona treatment

Corona treatment, also called as air plasma is a surface modification technique that uses a low temperature corona discharge (electrical discharge brought on by the ionization of a fluid surrounding a conductor that is electrically energized) plasma to impart changes in the properties of a surface. Corona treatment is a widely used surface treatment method in the plastic film, extrusion, and converting industries. The corona plasma is generated by the application of a low-frequency (10-20 kHz) generator and a step up transformer which provides high voltage sharp electrode tips which forms plasma at the ends of the sharp tips (Figure 2.30). Zeilier *et al* found that PEEK after corona treatment increased the surface free energy by from 30.2 dynes/cm^2 to 50 dynes/cm^2 (Zeiler *et al*., 1997).

Figure 2.30 Electrical discharge during corona discharge (www.dynetechnology.co.uk).

2.7.4. Laser treatment

In this process either a gas or a solid is excited to emit light of a particular wavelength. For gases like XeF (351 nm), XeCl (308 nm), KrF (248 nm) and XeF_2 (157 nm) corresponding wavelengths are used. Wavelengths smaller than 175 nm produce ozone so extractor chambers are necessary. Sardas *et al* tested PEEK with laser XeCl (308 nm) and the resulting PEEK surface was accompanied by surface roughening and ablation. In this case the lap shear strength (standard test method for *strength* properties of adhesives) with PEEK was increased from 3 MPa to 18 MPa (Laurens, 1998 and Sadras, 1989).

2.7.5. UV-light

UV treatment employs light bulbs emitting light at wavelength between 170nm and 308nm. Studies by Comyn *et al* sowed increase oxygen content and decreasing contact angle which both are indicative for improved bonding properties (Comyn, 1996).

2.7.6. Plasma treatment

This process is an important technology for surface modification which alters the surface chemistry of a polymer by exposing a polymer to a low temperature, low pressure glow discharge (i.e. plasma). The resulting plasma is partially ionised gas consisting of large concentration of excited atomic, molecular, ionic and free radical species. Plasma is also referred as the fourth state of matter. (Bauman *et al*., 2002).

2.7.6.1. Creating plasma

The principle components of a plasma system are the vacuum chamber, the vacuum pump and the high-frequency generator. When energy is continuously applied to matter its total heat content increases and undergoes state transformation from solid to gaseous state shown in the Figure 2.32. Carrying on applied energy the existing shell of the atom breaks up and electrically charged and excited particles and molecule fragments are formed (negatively charged electron and positively charged ions, radicals). This mixture is called plasma (Figure 2.31) (Mcintyre *et al*., 1995). Figure 2.33 and 2.34 shows how the plasma equipment works.

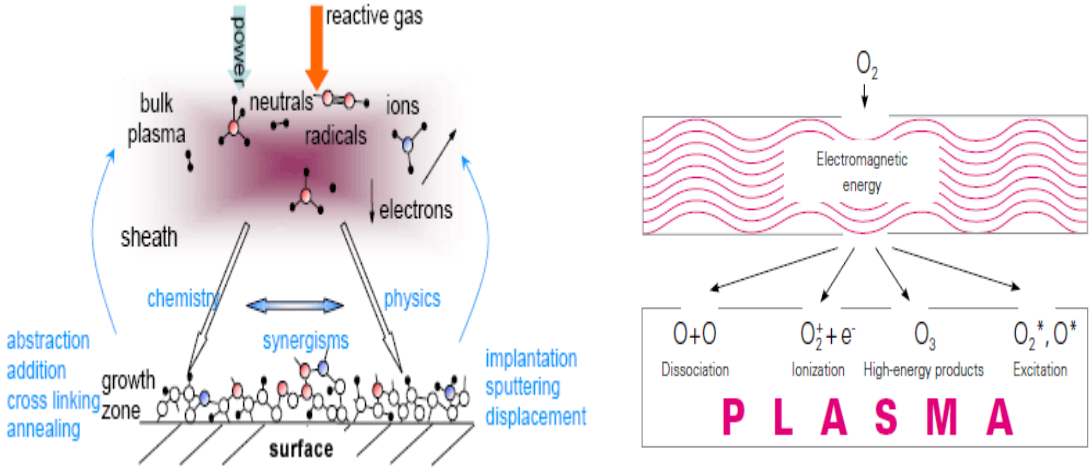

Figure 2.31 Showing Plasmas are a mixture of reactive species (Introduction to plasma technology published by Diener electronic Germany).

Solid State ⟶ Liquid ⟶ Gas ⟶ Plasma

Figure 2.32 Changes of the aggregate state under applied energy.

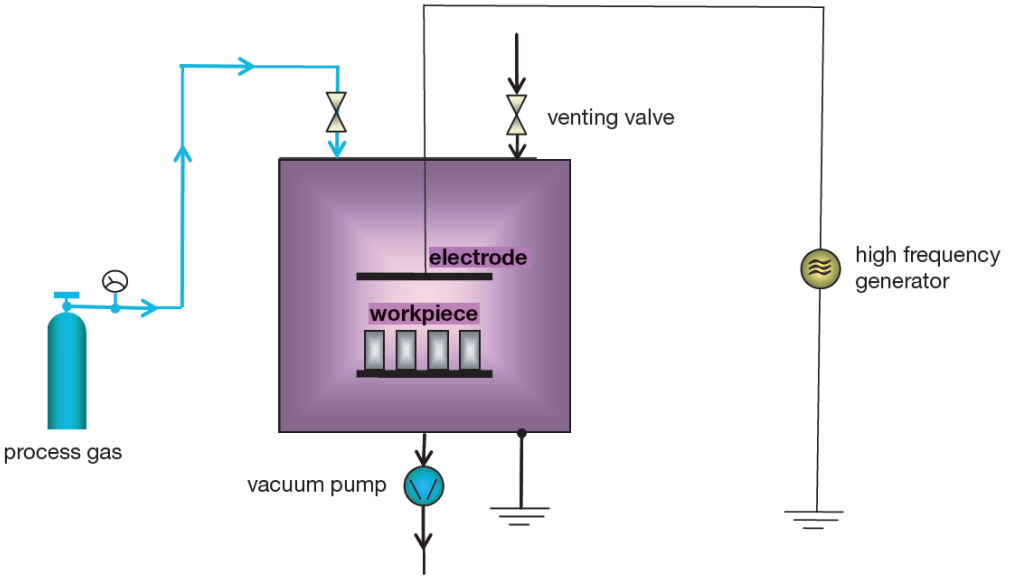

Figure 2.33 Schematic of kHz and MHz plasma systems (Introduction to plasma technology published by Diener electronic Germany).

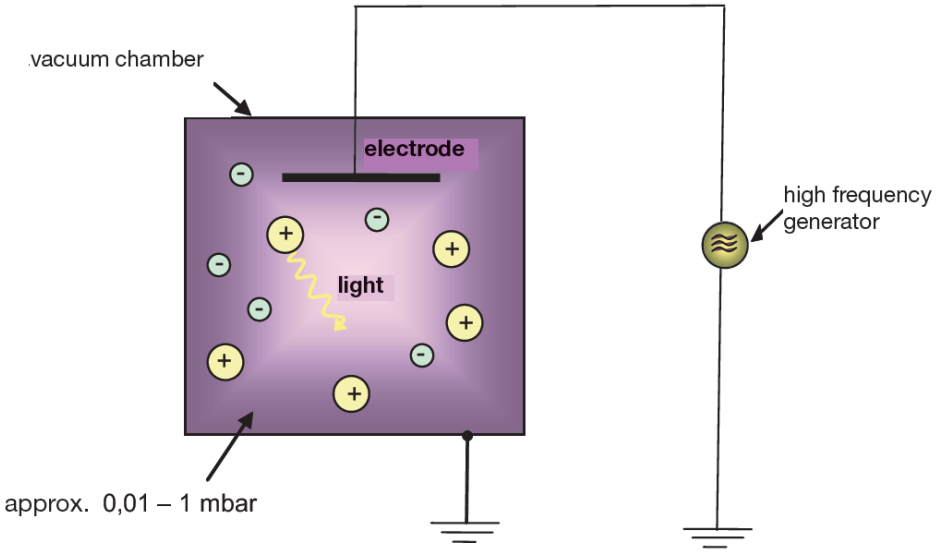

Figure 2.34 Schematic of a plasma chamber (Introduction to plasma technology published by Diener electronic Germany).

Ionisation starts by collision of an electron with a molecule of the residual gas, a further electron is ejected from the molecule which becomes a positively charged ion and migrates to the cathode as the ejected electron moves towards the anode and meets further molecules. These accelerated cations release numerous electrons from the cathode and this process continues like an avalanche until entire gas in the chamber is ionised. Typically for activation of polymers air oxygen, nitrogen helium, argon and ammonia are used (Mcintyre *et al*., 1995).

2.7.6.2. Plasma activation

Most of the engineering thermoplastics are homo-polar in structure and needs to be pre-treated before printing or gluing. The strength of activation can be tested using contact angle measurements. Figure 2.35 shows the schematic of the surface changes that occur during plasma treatment. The better the activation, the more flattened is the water droplet on the surface (decrease in contact angle Figure 2.36 a & b). This can also be verified by using test inks (example shown in Figure 2.36c & d) (Finson *et al*., 1995). Plasma activation can be characterized by five steps: production by ionization, transfer of chemistry to precursors, transport of radicals to the surface, surface interactions with deposition, recirculation and generation of new monomers. Plasma surface interactions of arriving radicals with a surface lead in first instance to the formation of a chemically bounded surface layer and thus to a (nearly) totally passivated surface. Subsequent-arriving hard radicals will still stick to this surface, whereas intermediate radicals may diffuse across the surface. By finding a vacant site or by reaction they may contribute to deposition and cross-linking (Comyn J 1996).

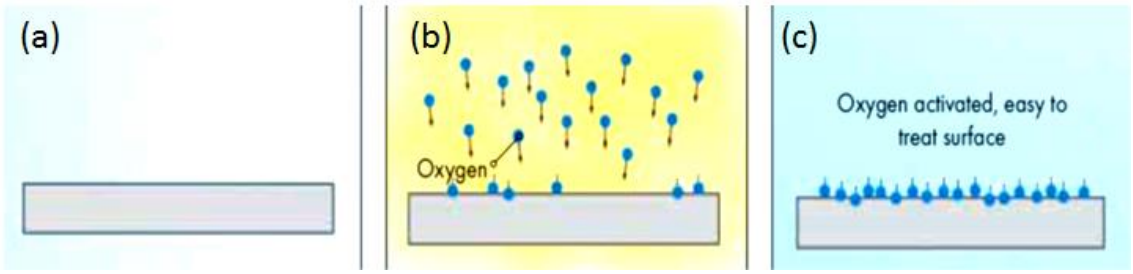

Figure 2.35 Schematic of the surface changes that occur during plasma treatment (a) before plasma treatment (b) during plasma and (c) after plasma treatment (www.dynetechnology.co.uk).

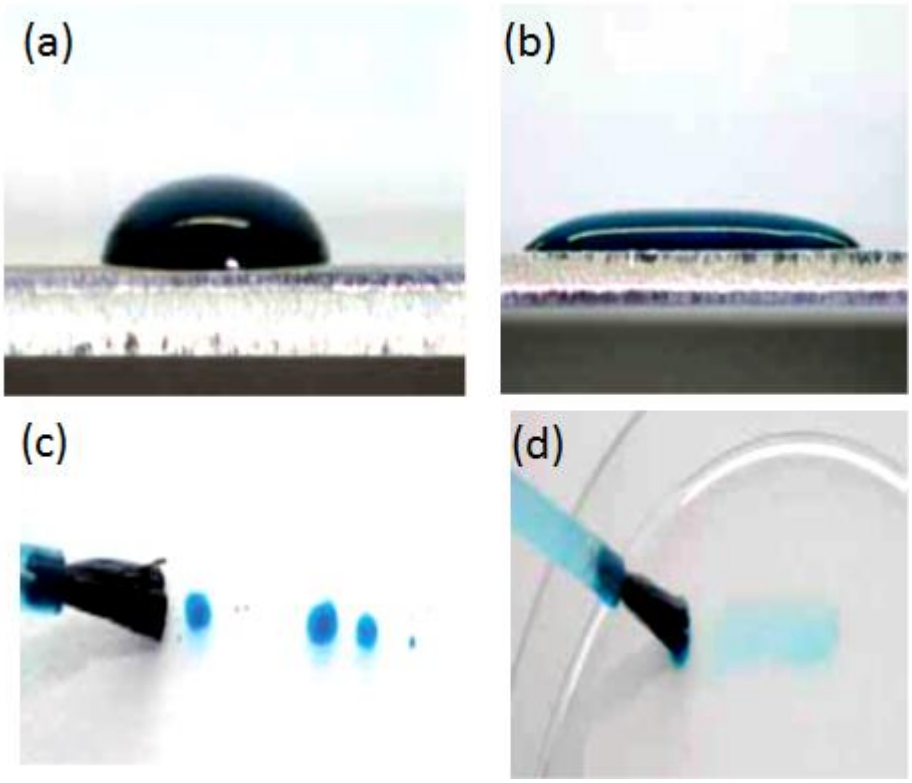

Figure 2.36 effect of plasma on wettability and surface energy (a) Untreated Surface (b) plasma activated surface (c) Untreated Surface (< 28mN/m) (d). Activated Surface (< 72mN/m) (Introduction to plasma technology published by Diener electronic Germany).

To determine the efficiency of the surface activation process and to estimate the bonding potential it is very important to measure the surface energy of the polymers surface. Measuring the surface energy of a liquid is relatively straightforward. However, determining the surface energy of solid surfaces is a

little more difficult and cumbersome. The measurements are not made directly and instead calculated from a set of liquid/solid contact angles, developed by bringing various liquids in contact with the solid surface. To measure the surface energy of the polymer surfaces knowledge of surface tension values for the test liquids used is required and moreover to make matter more difficult it is not possible to choose a universal set of liquids for use in determining surface energy for polymer surfaces (Finn, 2007). Even when an acceptable set of test liquids has been chosen to determine the contact angle on the polymer surfaces, the surface energy of the polymer surfaces is still not fixed as there is no universally agreed definition for surface energy. Rather there are several widely used theories for converting contact angle data into solid surface energy values (Heimenz, 1997).

2.8. Surface characterisation techniques

2.8.1. Contact angle and surface energy

Material selection of polymers for medical devices and disposables is determined by various properties such as physical/optical properties, cost, and biocompatibility etc. However, due to low surface energy (non-wetting) characteristics many challenges are faced during coating and bonding drugs to polymeric medical devices (Finn, 2007). In order to improve the wetting and adhesion properties of the polymer surfaces, they are often subjected to various surface modification and treatment for example plasma or corona treatment where polar groups are introduced to the surface which increases the overall surface energy. Thorough understanding of the surface free energy of the polymers surfaces before and after treatment is thus of crucial importance when

producing coatable polymers devices (Khan *et al*., 2009; Rulison, 2003 and Finn, 2007)

What is contact angle and how do we measure it?

Contact angle is a measure of the ability of a liquid to spread on to a given surface. It is the angle between the outline tangent of the deposited drop and the surface of this solid as shown in Figure 2.37 (Khan *et al*., 2009).

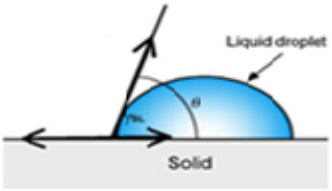

Figure 2.37 diagram illustrating the contact angle of a liquid sample (www.face-kyowa.com).

The measured contact angle of the liquid on the solid surface is linked to the surface energy and so one can calculate the surface energy of the solid and discriminate between the polar and non-polar interaction (Rulison, 2003). Young's equation (Equation 2.1 and Figure 2.38) was first used to describe the interactions between the forces of cohesion and adhesion and was referred to as surface energy (Khan *et al*., 2009).Figure 2.39 shows the typical evaluations of contact angle on hydrophilic and hydrophobic surfaces.

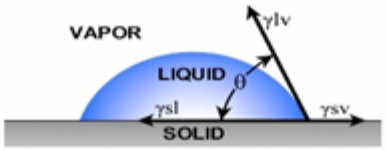

$$\gamma^{sv} = \gamma^{sl} + \gamma^{lv} \cos\theta \quad (2.1)$$

Where θ is the contact angle
γ^{sl} is the solid/liquid interfacial free energy
γ^{sv} is the solid surface free energy
γ^{lv} is the liquid surface free energy

Figure 2.38 Diagram explaining Young's equation (www.face-kyowa.com).

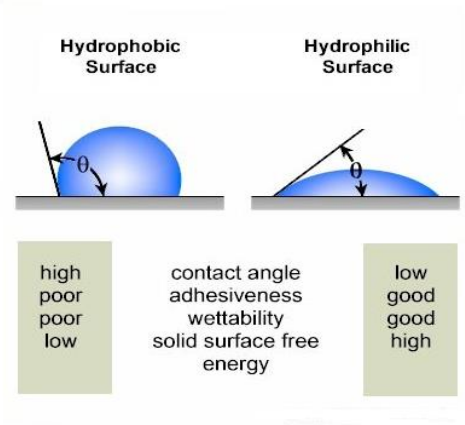

Figure 2.39 Diagram explaining typical evaluations of contact angle (www.face-kyowa.com).

Contact angle measurements give some important information:

1. The affinity of the liquid to the solid surface
2. If a set of reference liquids are used, the surface energy of the solid can be determined by discriminating the polar and dispersive components. The most common models are Goods or Owens and Wendt model (Rulison, 2003).
3. The measure of hysteresis between the advancing angles gives information about surface contamination and rugosity.

Surface energy calculations

Three most important parameters that define the shape of the drop created at the solid surface are:

1. Solid- liquid interfacial tensionγ_{sl}
2. Solid-vapour interfacial tensionγ_{sv} (γ_S)
3. Liquid-vapour interfacial tensionγ_{lv} (γ_L)

With the help of young's equation all three parameters can be linked with the contact angle.

$$-\gamma_{sv} + \gamma_{sl} + \gamma_{lv} cos\theta = 0 \quad (2.2)$$

In equation 2.2 γ_{lv} and θ are measurable so various additional theories and equation have been developed to determine γ_{sl} and γ_{sv}

Different theories to measure surface free energy

Many theories exist which enable the measure of surface free energies. The most commonly used are:

1. Neumann theory
2. Zisman theory (one component model for solid surface energy)
3. Owens/Wendt theory (two component model for solid surface energy)
4. Fowkes theory (two component model for solid surface energy).
5. Van Oss theory (three component model for solid surface energy)

Neumann theory: this model does not distinguish between the various components of surface energy and it also does not relate the material physico-chemical properties. The contact angle equation is written as

$$\cos\theta = \frac{(0.015\gamma_S - 2)\sqrt{\gamma_S}\,\gamma_L + \gamma_L}{\gamma_L(0.015\sqrt{\gamma_S}\gamma_L - 1)} \quad (2.3)$$

This equation is limited to low polar components like fluorinated surface and it is difficult to compare values obtained with different liquids.

Zisman theory: Zisman defines the surface energy of a solid as equal to the surface tension of the highest surface tension liquid (real or imaginary) that will completely wet the solid, with a contact angle of 0°. This comes from the widely observed tendency of contact angle to decrease as liquid surface tension decreases on the same solid sample (Mittal, 1993). In the Zisman model contact angle is plotted in the form of liquid surface tension versus cosine of contact angle (cos θ and extrapolated to cos θ =1 (θ=0°), and a surface tension value is obtained for the highest surface tension liquid that will completely wet the solid surface, with a contact angle of 0° as shown in Figure 2.40 (Rulison, 2003).

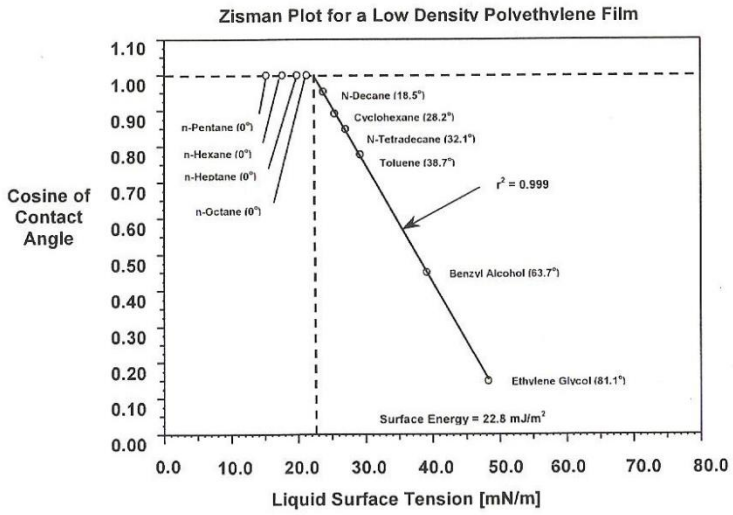

Figure 2.40 Zisman Plot for a low Density Polyethylene film (Rulison, 2003).

The limitation of this theory is that it only works best with non-polar surfaces such as polyethylene and polypropylene. The Zisman theory becomes inadequate with polymers which have heteroatom content like polyamides, polyesters, polyacrylates and polycarbonates. It is inadequate for surfaces like

glasses, ceramics and metals because it is a single-parameter model and ignores specific liquid/solid surface interactions (Rulison, 2003).

Owens/Wendt theory: This is also called the harmonic mean theory and it is based on a two component models which determine the dispersive and polar components of surface energy (Owens and Wendt, 1969). The dispersive component accounts for vander-waals and site specific interactions (Mittal, 1993). The polar component accounts for dipole-dipole, dipole-induced dipole and hydrogen bonding interactions which a surface may have with applied liquids. Based on this Owens/Wendt developed a two parameter model that mathematically is based on Good's and Young's equations, which describe interaction between solid surfaces and liquids (Rulison, 2003). The equations are as follows

Good's Equation

$$\sigma_{SL} = \sigma_S + \sigma_L - 2(\sigma_L^D \times \sigma_s^D)^{1/2} - 2(\sigma_L^P \times \sigma_s^P)^{1/2} \quad (2.4)$$

Young's Equation

$$\sigma_S = \sigma_{Sl} + \sigma_L \cos\theta \quad (2.5)$$

σ_L	*surface tension of the wetting liquid*
σ_L^D	*dispersive component of surface tension of the liquid*
σ_L^P	*polar component of surface tension of the liquid*
σ_S	*overall surface energy of the test solid*
σ_s^D	*dispersive component of the surface energy of the solid*
σ_s^P	*polar component of the surface energy of the solid*
σ_{sL}	*interfacial tension between solid and liquid*
(θ)	*contact angle*

Owens/Wendt combined both Good's and Young's equation to produce the following equation.

$$\frac{\sigma_L(cos\theta+1)}{2(\sigma_L^D)^{1/2}} = (\sigma_S^P)^{1/2}\frac{(\sigma_L^P)^{1/2}}{(\sigma_L^D)^{1/2}} + (\sigma_S^D)^{1/2} \quad (2.6)$$

Results and Graph showing Owens/Wendt plot for poly methyl methacrycrylate is shown in Figure 2.41 and Figure 2.42.

Liquid	Room Temperature Surface Tension (mN/m)	Contact Angle on PTFE (degrees)	Dispersive Component (mN/m)	Polar Component (mN/m)
n-hexane	18.4	12.0	18.4	0.0
n-heptane	19.9	25.6	19.9	0.0
n-octane	21.3	33.0	21.3	0.0
n-decane	23.8	42.3	23.8	0.0
cyclohexane	25.5	47.1	25.5	0.0
n-tetradecane	26.4	49.4	26.4	0.0
toluene	28.4	58.2	26.1	2.3
nitromethane	36.5	84.8	22.0	14.5
methyl benzoate	37.2	79.3	27.0	10.2
benzyl alcohol	39.0	78.6	30.3	8.7
ethylene glycol	47.7	94.9	26.4	21.3
formamide	57.0	107.2	22.4	34.6
glycerol	63.4	100.7	37.0	26.4
water	72.8	113.7	26.4	46.4

Figure 2.41 Results for the probe liquids used to test poly methyl methacrycrylate (Rulison, 2003).

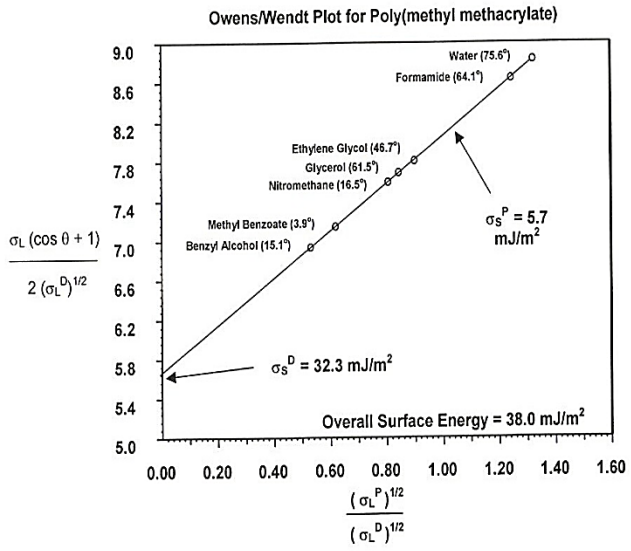

Figure 2.42 Owens/Wendt plot for poly (methyl methacrycrylate) (Rulison, 2003).

Once all the contact angle data for a set of probe liquids on a solid is obtained we can determine the surface tension values (overall, polar and dispersive) for the liquid used, which provides all the information necessary to plot contact angle data on Owens/Wendt format and once the graph is plotted the slope of the line is used to calculate the dispersive component of the surface energy of the solid using equation given above. Since the Owens/Wendt theory is two component model for solid surface energy, it is also two –component model for liquid surface tension. The overall surface tension of each probe liquid must be separated into polar and dispersive component as well. This is done using a standard reference surface. The accepted standard reference surface for two-component liquid surface tension determination is poly (tetrafluoroethylene) (PTFE). Pure untreated PTFE is assumed to have a surface energy of 18.0mJ/m^2 and is assumed to be capable of no polar interactions. (Owens and Wendt, 1969)

In other words, $\sigma_S = \sigma_S^D = 18.0$ mJ/m^2 and σ_S^P = 0 mJ/m^2 for PTFE. Substituting these values into primary Owens/Wendt theory equation we get

$$\sigma_L^D = \frac{(\sigma_L{}^2 cos\theta_{PTFE} + 1)^2}{72} \quad (2.7)$$

Where θ_{PTFE} = the contact angle measured between PTFE and the probe liquid Therefore the dispersive surface tension component (σ_L^D) can be determined for any liquid for which the overall surface tension (σ_L) is known, simply by measuring the contact angle between the liquid and PTFE (θ_{PTFE}) and using the equation (2.7). The polar surface energy component for the liquid is then determined by difference ($\sigma_L^P = \sigma_L - \sigma_L^D$).

Fowkes theory: Owens/Wendt theory works well for surfaces of moderate polarity; it is also usually fair amount of work. Many probe liquids need to tested for contact angle against the solid being calculated.

Fowke's theory works using the contact angle data from two liquids and most recommended liquids are Di-iodomethane and water. Di-iodomethane has overall surface tension of 50.8 mN/m. (Di-iodomethane has no polar component so $\sigma_L = \sigma_L^D = 50.8$ mN/m). So Di-iodomethane is used as the probe liquid for the step 1 and water which has $\sigma_L^P = 46.4$ mN/m and $\sigma_L^D = 26.4$ mN/m is then used in step 2 and overall surface energy is calculated using the equation

Overall surface energy $\sigma_S = \sigma_S^P + \sigma_S^D$ (2.8)

Van Oss theory: the surface energy in this model is written as

$$\gamma_S = \gamma_S^D + 2\sqrt{\gamma_S^+}\,\gamma_{\bar{S}} \quad (2.9)$$

Where γ_S^D = dispersive component (Lifshitz-van der Waals interactions)

$\gamma_S^- \gamma_S^+$ = polar components (polar interactions, Lewis acid-base)

This theory focuses on separating the surface energy of a solid into three components (a dispersive, an acid component and a base component)

2.8.2. Atomic force microscope (AFM)

In order to determine the extent of plasma activation and to understand the surface morphology of polymers atomic force microscopy is widely used. Since its invention in 1986 by Binnig, Quate, and Gerber the atomic force microscope (AFM) has become an indispensable tool for investigators studying physical chemical, tribological and surface properties of biological, biomechanical and electromechanical materials (Xiaodong *et al*., 2002). Atomic force microscopy is the most widely used subset of Scanning Probe Microscopy (SPM), which can be used in ambient conditions with minimum sample preparation. Figure 2.43 shows the general classification of the SPM. AFM is able to measure three-dimensional topography information from the angstrom level to the micron scale with unprecedented resolution (Oraby *et al*., 2010).

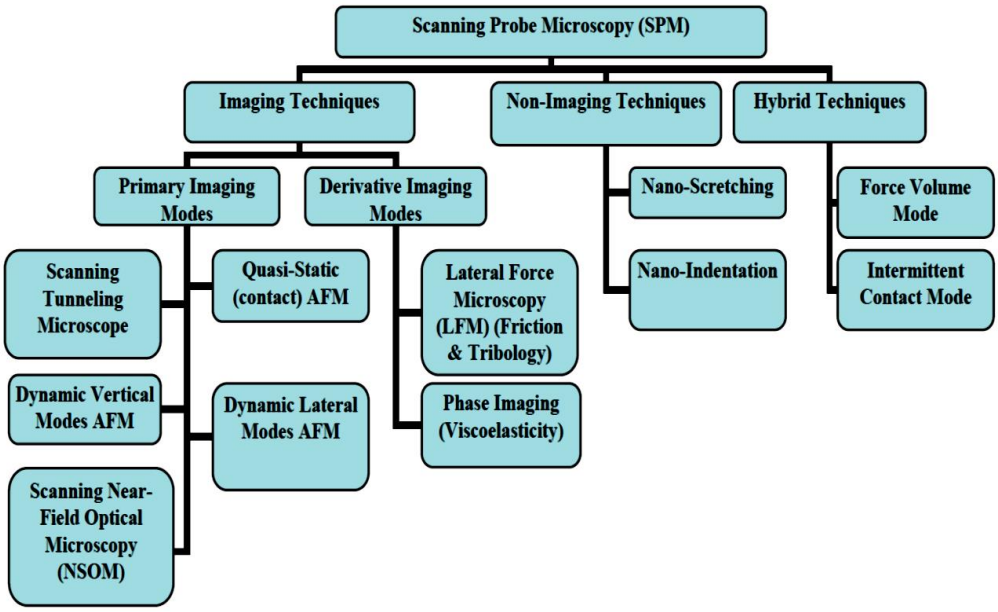

Figure 2.43 General classification of Scanning Probe Microscopy (SPM) (Clemente, 2008).

The AFM consists of a cantilever with a sharp tip (probe) at its end that is used to scan the specimen surface. The cantilever is typically silicon or silicon nitride with a tip radius in order of nanometers (Xiaodong *et al*., 2002). When the tip is brought into proximity of a sample surface, forces between the tip and the sample lead to a deflection of the cantilever according to Hooke's law. The sample is mounted on a piezoelectric tube that can move the sample in the *z* direction for maintaining a constant force, and the *x* and *y* directions for scanning the sample (Lal, 1994). Alternatively a 'tripod' configuration of three piezo crystals may be employed, with each responsible for scanning in the x, y and z directions. In newer designs, the tip is mounted on a vertical piezo scanner while the sample is being scanned in X and Y using another piezo block (Clemente, 2008). The resulting map of the area $z = f(x, y)$ represents the topography of the sample. An AFM image is typically comprised of a signal representing some Z distance of cantilever motion per X, Y point on the scan raster. These signals can be from various measurement points in the instrument: the voltage to move the Z piezo actuator in response to the feedback loop; the closed loop sensor monitoring the movement of the top plate of the optical lever detector; the amplitude, phase or deflection signal from the position sensitive detector; or some kind of error in the feedback loop. All signals are typically read as a voltage in the MFP3D system Figure 2.44 (Fuierer, 2009).

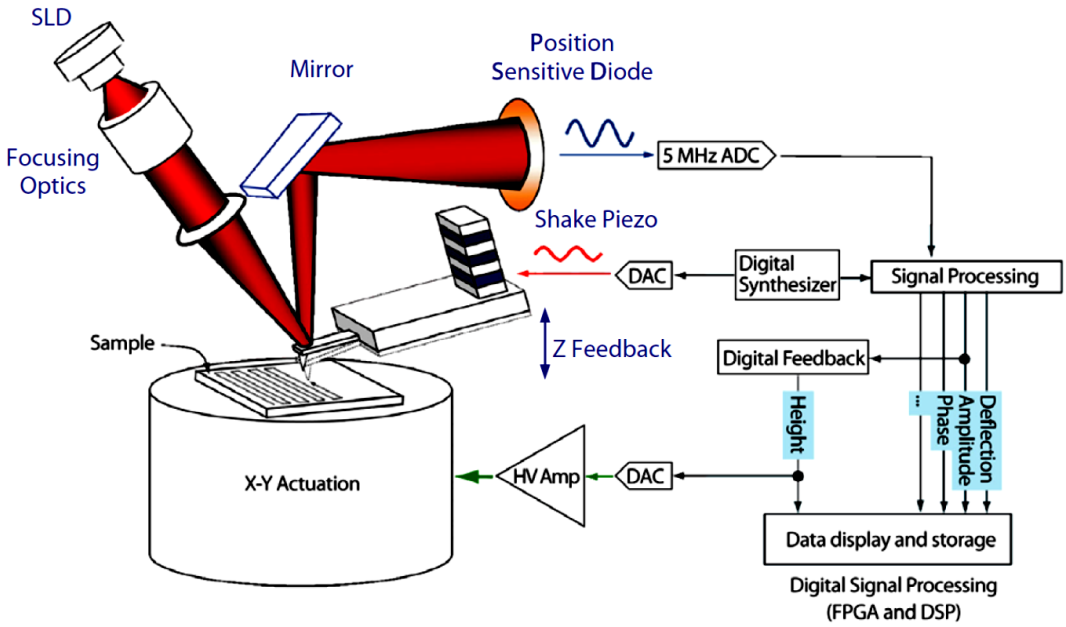

Figure 2.44 Simplified schematic allowing a better understand of the instrument. A super luminescent diode (SLD) provides columnised light that is reflected off the back of the cantilever to a position sensitive diode (PSD), which sends a voltage value to a feedback loop that is trying to maintain some user defined set point- this is typically a deflection or amplitude (voltage) signal from the PSD, depending on the imaging mode employed (AC or Contact mode) (Fuierer, Asylum Research procedural operation manual for MFP-3D version 2009).

AFM imaging modes

Contact mode

In this mode, the tip is in full contact with the surface as the sample is moved in a XY pattern while maintaining a user defined deflection voltage (i.e., force) to keep a positive deflection on the cantilever (bows towards surface shown in Figure 2.45). Depending on how soft the sample is, and what forces are being applied, the technique can be destructive. However, this technique is great for hard surfaces, or imaging cells in fluid at very low set point forces (Fuierer, 2009).

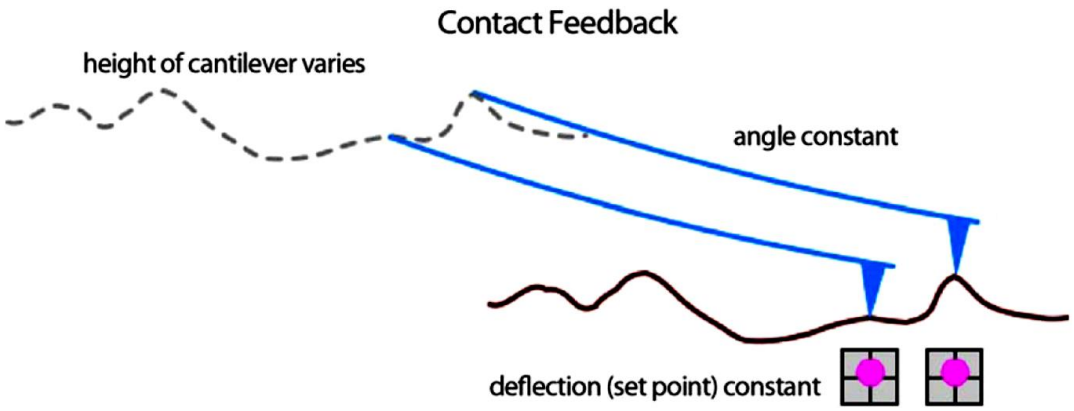

Figure 2.45 Showing the Contact mode of the AFM (Fuierer, Asylum Research procedural operation manual for MFP-3D Version 2009).

Non-contact mode

In this mode, the tip of the cantilever does not contact the sample surface. The cantilever is instead oscillated at a frequency slightly above its resonant frequency where the amplitude of oscillation is typically a few nanometers (<10 nm) (Magonov, 1997). The van der Waals forces, which are strongest from 1 nm to 10 nm above the surface, or any other long range force which extends above the surface acts to decrease the resonance frequency of the cantilever (Lal, 1994). This decrease in resonant frequency combined with the feedback loop system maintains a constant oscillation amplitude or frequency by adjusting the average tip-to-sample distance. Measuring the tip-to-sample distance at each (x, y) data point allows the scanning software to construct a topographic image of the sample surface (Fuierer, 2009).

Tapping mode (AC mode or intermittent contact mode)

This technique drives the cantilever just off its fundamental resonant frequency at some user defined amplitude set point, typically some dampened value of the

'Free Air' amplitude of the cantilever (i.e., not being dampened by the sample). This set point is read as a voltage off the PSD (Scalf, 2006) The feedback loop maintains this set point amplitude (voltage) as the tip is scanning across the surface, retracting the Z piezo when the amplitude gets dampened over (bumps); or extending the Z piezo when/if it oscillates at a larger amplitude than the amplitude set point (over holes). The latter is why the set point must be a dampened amplitude ratio of the 'Free Air' ratio (Fuierer, 2009 and Vansteenkiste *et al*., 2000).

The roughness parameters are determined on each image obtained in tapping mode (height image) and are defined as R_q which is the standard deviation of the Z values within a given area and is calculated by

$$R_q = [\Sigma(Z_i - Z_{ave})^2/N]^{0.5} \quad 2.10$$

Where, Z_{ave} is the average of the Z values within the given area, Z_i is the current Z value, and N the number of points within the given area.

2.8.3. Nanoindentation

The AFM can also be operated in a non-imaging mode, called force mode, to perform indentation tests. A force curve is produced, which is a plot of tip deflection as a function of the vertical motion of the scanner. This curve can be analysed to provide information on the local mechanical response. Also, the spring constant of the cantilever probe can be chosen such that small differences in response can be detected between polymers that have a certain range of stiffness. AFM indentation measurements are relative measurements, largely due to the lack of information regarding the tip shape of the probes (Xiaodong, 2002). A large portion of the current polymer nanoindentation

literature focuses on the measurement of material properties such as Young's modulus or elastic modulus (E_r) and indentation hardness (H) from indentation data. Modulus can be extracted from load-displacement curves following the method of Field and Swain. These methods have been thoroughly reviewed, along with limitations and necessary instrument calibrations, in many recent publications. While *Er* (reduced modulus) and *H* (hardness) are the most commonly reported nanoindentation parameters; they are not always the most relevant properties for all materials characterisation (Fuierer, 2009).

In nanoindenter, displacement is typically monitored by capacitance or inductance, while force actuation is provided through electrostatic force generation, magnetic coils, or expansion of a piezoelectric element. A schematic of a nanoindenter system using a three-plate capacitor for displacement sensing is shown in Figure 2.46. The tip is mounted directly onto the middle plate of the capacitor and a load is applied to move the tip into the sample (Xiaodong, 2002). Load and displacement are monitored continuously during the indentation process, resulting in a load-displacement curve, as shown in Figure 2.47(a).

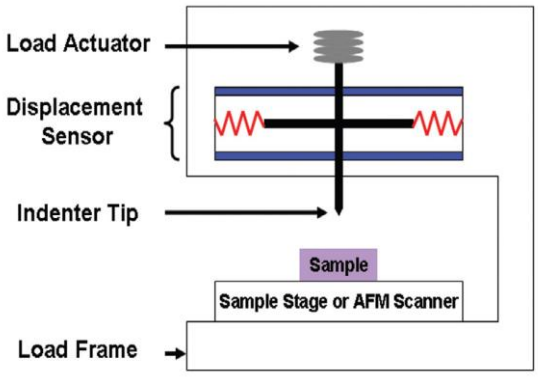

Figure 2.46 Schematic of a nanoindenter system (www.nanotechweb.org).

During indentation, the indentation depth versus time and the load versus time are recorded simultaneously. After the data is recorded, it can be displayed as a standard load/depth curve. Hardness and modulus can be determined from the load/depth curve and the tip contact area versus contact depth function. The interaction between the tip and the sample during the indentation process is illustrated in Figure 2.48(b) and in this study h_c (contact depth) was measured instead of h_{max} (penetration depth or displacement).

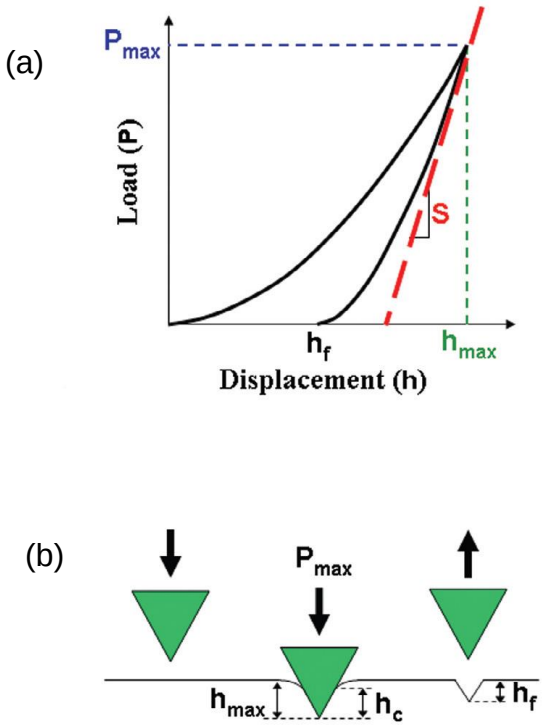

Figure 2.47 Schematic of (a) a typical load-displacement curve and (b) the indentation process. P_{max} = maximum load applied; h_{max} = penetration depth; h_c = contact depth (the height of the contact between the tip and the sample); h_f = final depth; S = unloading stiffness (TriboScope® User Manual).

In a typical depth sensing nanoindentation hardness apparatus, the position of the indenter relative to the surface of the specimen (depth of an indent) during an indentation process is monitored. The measured displacements are the sum

of the indentation depth in the specimen and the displacement associated with the measuring instrument, termed as the load-frame compliance. It is important that we measure the load-frame compliance, since at large indentation depths with high modulus, the load-frame displacement can be a significant fraction of the total displacement. The relationship for the compliance (inverse of stiffness) of the contact between any axisymmetric indenter and an elastically isotropic half-space is given by

$$C_c = \frac{dh}{dP} = \frac{\sqrt{\pi}}{2}\frac{1}{\sqrt{A}}\frac{1}{E_r} \quad 2.11$$

Where, *Er* is the reduced modulus described by the relationship

$$\frac{1}{E_r} = \left(\frac{1-\upsilon^2}{E}\right)_{specimen} + \left(\frac{1-\upsilon^2}{E}\right)_{indenter}$$

2.12

and *E* and *υ* are Young's modulus and Poisson's ratio respectively.

Here 'h' is the displacement of the indenter relative to the specimen, P is the load, and 'A' is the projected area of contact between the specimen and the indenter. The hardness of a sample is given by the relationship

$$H = \frac{P_{max}}{A}$$

2.13

Where *H* is the hardness, P_{max} is the maximum applied force, and A is the projected contact area (TriboScope® User Manual).

2.8.4. Confocal laser scanning microscopy (CLSM or LSCM)

To obtain information from the inner structure of the samples using conventional transmitted-light microscope specimens needs to be very thin and translucent.

To satisfy these kind of problems, changes where brought into the conventional light microscopy and thus the invention of confocal microscope in 1955 by Marvin Minsky (Minsky, 1988).

A CLSM is technique of obtaining sharp optical images of specimens with depth selectivity. This is achieved by a process called as optical sectioning where in focus images are acquired from selected depth, in other words CLSM works by point-by-point illumination of the specimen and rejection of out-of-focus light by spatial filtering techniques (Figure 2.48). Thus getting better observation and fine details it is possible to generate 3D reconstructions of a volume of the specimen by overlaying a series of this slices taken along the vertical axis using a computer (Semwogerere, 2005).

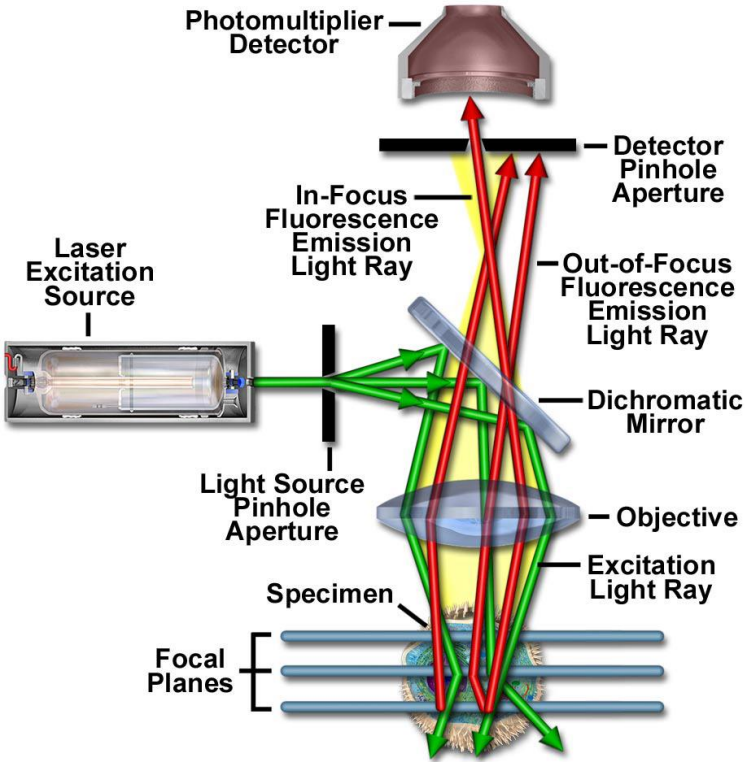

Figure 2.48 Schematic diagram of the optical pathway and principal components in a laser scanning confocal microscope (www.zeisscampus.magnet.fsu.edu).

A laser is used to provide the coherent light (excitation source) and reflects off a dichroic mirror. Then the laser hits two mirrors which scans the laser across the specimen in defined focal plane, secondary fluorescence emitted gets de-scanned by the same mirrors that are used to scan the excitation light from the laser. The emitted light passes through the dichroic and is focused as a confocal point at the detector pinhole aperture (Corle and Kino, 1996). So in CSLM there is never a complete image of the specimen at any given instant only one point is seen. Therefore a detector system is attached to a microcomputer which constructs the image pixel by pixel. The information obtained from a series of optical sections at regular intervals are used to create the complete image. The software then can combine all these 2D images to form a 3D rendition (Claxton, 2006).

2.8.5. Scanning electron microscope (SEM)

Is a type of electron microscope that generates images of the specimen by scanning using focused beam of electrons. A typical SEM instrument (Figure 2.49) comprises of a vacuum system, electronic console and the electronic optical column (consists of beam generation/electron gun, condenser lens, deflection coil, objective lens or beam interaction system and secondary electron detector) (Xin and Muller, 2010).

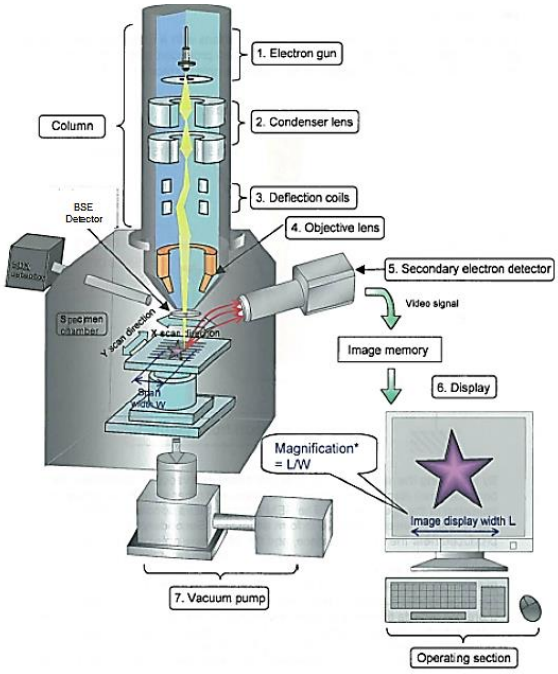

Figure 2.49 Configuration of the scanning electron microscopy. (www.engr.uvic.camechelectronmicroscopy).

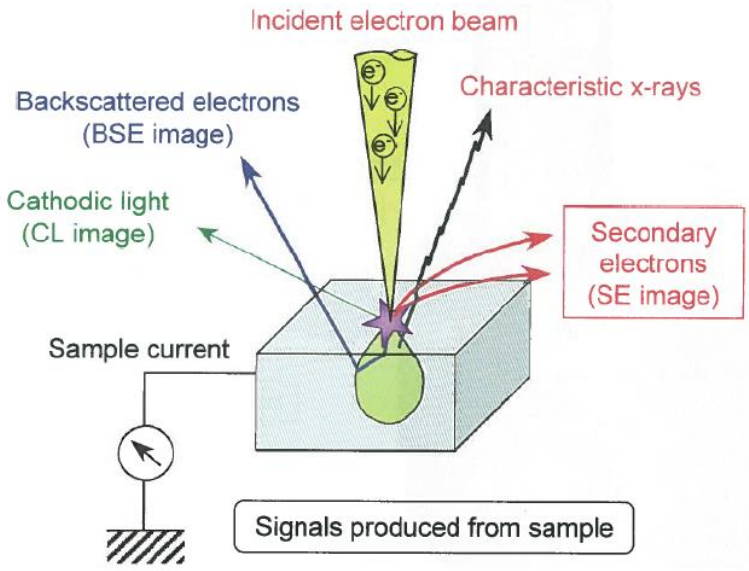

Figure 2.50 Signals that result from electron beam-specimen interaction (www.engr.uvic.ca).

When the electron beam produced by the electron gun in vacuum is converged via the electromagnetic lens (condenser and objective lens) and irradiated to the specimen, it generates secondary electrons (SE) and back scattered electrons (BSE) (Figure 2.50) (SanAgustin *et al*., 2009).

SE are created near the sample surface because of the result of inelastic collision and scattering of incident electrons with the specimen electrons and reflects the topographical structure of the sample with a resolution of ≈ 10nm while BSE are generated further from the sample surface due to elastic collision and scattering events between incident electrons and specimen nuclei and electrons and reflects the compositional distribution on the sample surface. Sometimes an X-ray detector may be fitted on SEM for conducting elemental analysis. The SEM primarily uses SE or BSE signals from the respective detector to produce an image (Egerton, 2009).

2.8.6. Optical coherence tomography (OCT)

Is a non-invasive optical signal acquisition device, which is used to obtain high resolution cross sectional images. It is similar to ultrasound imaging except that OCT uses light instead of sound. It is widely used in medical imaging for diagnosis of ocular and vascular diseases. Figure 2.51 shows the comparison of resolution of OCT with other imaging techniques. Modern OCTs are recently used in non-destructive industrial applications like material thickness, surface roughness characterisation and volume loss measurements (Jakob *et al*., 2010).

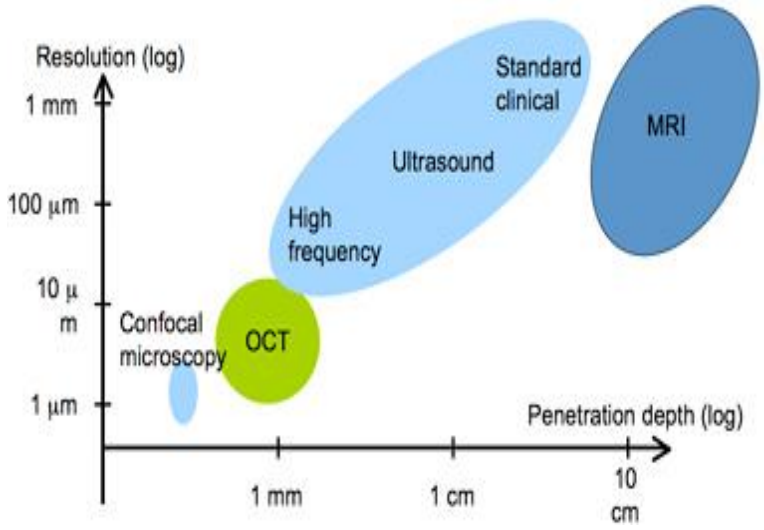

Figure 2.51 Comparison of resolution of OCT with other imaging techniques (www.zmpbmt.meduniwien.ac.at).

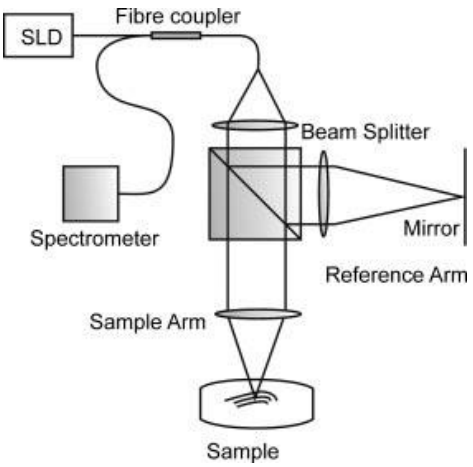

Figure 2.52 Schematic setup of the fibre-based OCT system. The light source is a super luminescent diode (SLD) that has a large spectral bandwidth. After travelling through the beam splitter, the light scattered back from the sample is superimposed on the reference beam an travels back to the fibre coupler to give an interference pattern in the spectrometer, which is evaluated after Fourier transformation (Jakob *et al*., 2010).

OCT works on the principle of white light interferometry and uses a special light source such as a super luminescent diode (SLD) or ultra-short pulse lasers with coherence length in the range of several microns (Nemeth *et al*., 2013).

OCT uses low coherence interferometry to generate 2D- images through optical back scattering. A SLD which serves as the light source is split into beams in a Michelson interferometer where one beam is focused on to the sample while

other one is (reference beam) is terminated at the mirror (Figure 2.52). While the sample beam penetrates to the specimen the backscattered light from the sample is passed through the same lens and optical path used for emission (Fercher *et al*., 2003). As this is an interferometry technique the sample beam is then recombined with the reference beam. The combined beam of light travels through the fibre optics and its interference pattern is analysed in the spectrometer. A greater interference will be created from the areas of the sample which reflects more light and any light that is outside the short coherence length will not interfere. This generates a depth profile known as A-scan and acquiring these scans in a line across the specimen creates a 2D transverse image called as B-scan. By assembling series of this 2D scans 3D-images are created (Huang *et al*., 1991). Recently there has been significant interest in the microneedle community to use OCT for a real time penetrating measurements. Figure 2.53 shows a modified OCT image showing the MN penetration.

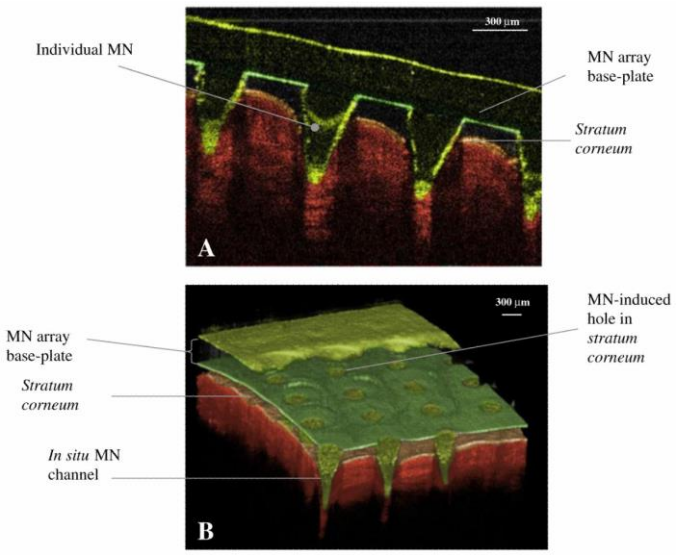

Figure 2.53 Example of a 3D-OCT image showing Microneedle insertion depth and position in human skin in vivo (Donnelly *et al*., 2010).

2.8.7. X-ray photo electron spectroscopy (XPS)

Also known as electron spectroscopy for chemical analysis (ESCA) is widely used quantitative spectrometric technique that measures the elemental composition, empirical formula, chemical state and electronic state of the elements that exist within outermost atomic layers of the solid (2-10 nm). A typical XPS consists of an X-ray generator, ultrahigh vacuum chamber, an electron collection system (which includes electron collection lens and electron energy analyser) and vacuum sample introduction chamber.

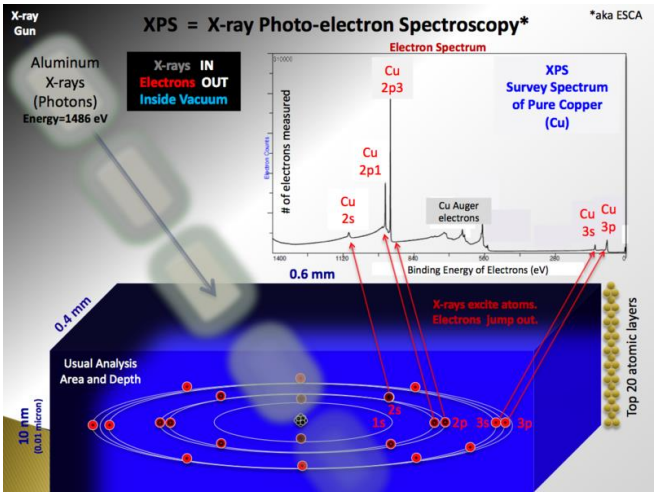

Figure 2.54 Representation of the XPS process showing the emission of an electron from the shell of an atom (Briggs and Grant, 2003).

The XPS process fundamentally works using the photoelectric effect where electrons are made to eject from an at the sample's surface using an X-ray photon mostly from monochromatic Aluminum Kα or non-monochromatic Magnesium Kα x-rays and the energy of the liberated photoelectron is analysed using a spectrometer by measuring the electron's kinetic energy, which gives

information of the nature of the elements present in the specimen as shown in Figure 2.54 (Watts, 1990).

The kinetic energy of the ejected electrons is named Ek, and it is determined by the following equation.

$$E_B = hv - E_K - \phi$$

Where E_B *and* E_K *are respectively the binding and the kinetic energy of the emitted photoelectron, hv is the photon energy, and* ϕ *is the spectrometer work function (the minimum energy needed to remove an electron from solid).*

By collecting the emitted photoelectrons with an electron analyser, counting them and studying the spectrum of the number of electrons versus its distribution of kinetic or binding energy (using the equation), it is possible to recognize the material they come from. The analysis of a wide range of E_B will provide unique signatures of the elements as a function of their atomic number and also enables to relate peak intensity to an amount of element present in the sample (Watts and Wolstenholme, 2003).

2.9. References

1. Attia UM, Marsona S and Alcock JR, Micro-injection moulding of polymer microfluidic devices, *Microfludics and Nano Fludics* **7** (2009) 1-28.

2. Barry BW, Drug delivery routes in skin: a novel approach, *Advanced Drug Delivery Reviews* **1** (2002) 31–40.

3. Bauman BD, Surface-modified polymer particles: performance additives for epoxy and cast polyurethane, *Thermoset Technology/Epoxy Resin Formulators Division Technology Conference*, Florida, (2002).

4. Bellantone V, Surace R, Trotta G and Fassi I, Replication capability of microinjection moulding process for polymeric parts manufacturing, *International Journal of Manufacturing Technology* **67** (2013) 1407-1421.

5. Bora P, Kumar L, and Bansal KA, Microneedle technology for advanced drug delivery: Evolving vistas, *Current Research & Information on Pharmaceutical Sciences* **9** (2009) 7-10.

6. Borshell N and Ahmed T, Approaches to valuation of pharmaceutical licensing deals, Pharma Deals, Imprint of Pharma Ventures Ltd (2012) Oxford, www.pharmaventures.com

7. Briggs D and Grant JT, Surface analysis by Auger and X-ray photoelectron spectroscopy, IM publications and surface spectra limited (2003).

8. Cabrera ED, Evaluation of the capabilities of microinjection moulding to produce deformable membrane mirrors, Thesis, (2010).

9. Cevc G, Drug delivery across the skin, *Expert Opinion on Investigational Drugs* **12** (1997) 1887-937.

10. Chen X, Prow T, Crichton ML, Jenkins DW, Roberts MS, Frazer IH, Fernando GJ and Kendall F, Dry-coated micro projection array patches for targeted delivery of immuno therapeutics to the skin, *Journal of* ControlledRelease,**139**(2010)212-220.

11. Claxton NS, Fellers TJ, and Davidson MW, Confocal microscopy *Encyclopedia of Medical Devices and Instrumentation,* (2006).

12. Clemente AV, Principles of Atomic Force Microscopy (AFM). *Physics of Advanced Materials Winter School*, (2008).

13. Comyn J, Mascia L, Xiao G and Parker BM, Plasma-treatment of polyetheretherketone (PEEK) for adhesive bonding, *International Journal of Adhesion and Adhesives* **16** (1996) 97-104.

14. Corle TR and Kino GS, *Confocal scanning optical microscopy and related imaging systems*, New York: Academic Press, (1996).

15. Davies P, Courty C, Xanthopoulos N and Mathieu HJ, Surface treatment for adhesive bonding oncarbon fibre-poly (etherether ketone) composites, *Journal of Materials Science Letters* **10** (1991) 335-338.

16. Demir YK, Akan Z and Kerimoglu O, *Characterization of polymeric microneedle arrays for transdermal drug delivery, Public Library of Science One* **8** (2013) 1-9.

17. Donnelly RF, Majithiya R, Singh TR, Morrow DI, Garland MJ, Demir YK, Migalska K, Ryan E, Gillen D, Scott CJ and Woolfson AD, Design, optimisation and characterisation of polymeric microneedle arrays prepared by novel laser-based micromoulding technique, *Pharmaceutical Res*earch **2** (2010) 169-178.

18. Donnelly RF, Raj Singh TR and Woolfson DA, Microneedle-based drug delivery systems: microfabrication, drug delivery, and safety, *Drug Delivery* **4** (2010) 187–207.

19. Dupret F, Couniot A, Mal O, Vanderschuren L and Verhoyen O, Modelling and simulation of injection moulding in Advances in the Flow and Rheology of Non-Newtonian Fluids, Rheology Series, *Elsevier* (1998) 939-1010.

20. Egerton RF, Physical principles of electron microscopy: an introduction to TEM, SEM, and AEM, *Springer Science Business Media, Inc* (2009) 125-132.

21. Eisenstein M, Something new under the skin, *Nature Biotechnology* **29** (2011) 107-109.

22. Fenner RT, Principles of polymer processing, The macmillan press ltd, London, (1979).

23. Fercher AF, Drexler W, Hitzenberger CK and Lasser T, Optical coherence tomography—principles and Applications, *Reports on Progress in Physics* **66** (2003) 239–303.

24. Finn K H, The measurement of surface energy of polymer by means of contact angles of liquids on solid surfaces, Thesis Submitted University of Oslo, (2007).

25. Finson ES, Kaplan L and Wood L, Plasma treatment of webs and films, *38th annual Technical Conference Proceedings for the Society of Vacuum Coaters*, Chicago, (1995).

26. Fiorini GS and Chiu DT, Disposable microfluidic devices: fabrication, function and application, *Bio-techniques* **38** (2005) 429-446.

27. Frost and Sullivan, World pharmaceutical frontiers providing a global perspective on the pharmaceutical industry, (2011) 107-111.

28. Fuierer R, Procedural Operation Manual for MFP-3D Version 10.5, *Asylum Research* (2009).

29. Garcia T, Plasma processes as a cleaner alternative for cleaning, corrosion resistance, and functionalization of metallic surfaces, *2nd International Workshop Advances in Cleaner Production* (2009) 21-27.

30. Giboz J, Copponnex T and Mele P, Microinjection moulding of thermoplastic polymers: a review, *Journal of Micromechanics and Micro engineering* **17** (2007) 96-109.

31. Gill HS and Prausnitz MR, Coated microneedles for transdermal delivery, *Journal of Controlled Release* **117** (2007) 227-237.

32. Heckele M and Schomburg W, Review on micro moulding of thermoplastic polymers, *Journal of Micromechanics and Micro engineering* **14** (2004) 1-14.

33. Heimenz P, Principles of colloid and surface chemistry (Undergraduate Chemistry: A series of textbooks) Marcel Dekker, New York (1997) ISBN 0-8247-7476-0.

34. Henry S, McAllister DV, Allen MG and Prausnitz MR, Microfabricated microneedles: a novel approach to transdermal drug delivery, *Journal of Pharmaceutical Science* **8** (1998) 922–925.

35. Herman WA and Devey GB, Future trends in medical device technologies: A ten-year forecast US Food and Drug administration (2012).

36. Hill S, Kämper K, Dasbach U, Döpper J, Ehrfeld W and Kaupert M, An investigation of computer modelling for micro-injection moulding, *Proceedings of Microsym'95*, September 1995.

37. Hoffman AS, The origins and evolution of “controlled” drug delivery systems, *Journal of Controlled Release* **132** (2008)153–163.

38. Howdeshell KL, Peterman PH, Judy BM, Taylor JA, Orazio CE, Ruhlen RL, Saal FSVS and Welshons WV, Bisphenol A is released from used polycarbonate animal cages into water at room temperature, *Environmental Health Perspectives* **111**, (2003) 1180-1187.

39. Huang D, Swanson EA, Lin CP, Schuman JS, Stinson WG, Chang W, Hee MR, Flotte T, Gregory K and Puliafito CA, Optical coherence tomography, *Science* **254** (1991) 1178–1181.

40. Jain KK, Drug delivery systems Humana Press, *Springer Science* (2008) 9-16.

41. Jiang J, Gill HS, Ghate D, McCarey BE, Patel SR, Edelhauser HF and Prausnitz MR, Coated microneedles for drug delivery to the eye, *Investigative Ophthalmology & Visual Science* **48** (2007) 4038-4043.

42. Jiang N, Ocular drug delivery using microneedles, Thesis, Georgia Institute of Technology, (2006).

43. Khan MI and Nasef MM, Spreading behaviour of silicone oil and glycerol drops on coated papers, *Leonardo Journal of Sciences* **8** (2009) 18 - 30.

44. Kim S, Polyetheretherketone surface functionalization by low-energy ion-beam irradiation under a reactive O_2 environment and its effect on the PEEK/copper adhesives, *Langmuir* **20** (2004) 157-163.

45. Kuzuya M, Kondo S and Sasai Y, Plasma techniques for preparation of controlled drug release systems. *Plasmas and Polymers*, **6** (2001) 145-162.

46. Kolli CS, Banga AK. Characterization of solid maltose microneedles and their use for transdermaldelivery. *Pharm Res*. **14** (2008) 104–13.

47. Kuno N and Shinobu F, (2011) Recent Advances in Ocular Drug Delivery Systems, *Polymers* **3** (2011) 193-221.

48. Vasilev K, Nanoengineered Plasma Polymer Films for Biomaterial Applications, *Plasma Chem Plasma Process* (2013) 90-103.

49. Kurtz SM and Devine JN, Polyetheretherketone biomaterials in trauma, orthopedic and spinal implants, *Biomaterials* **28** (2007) 4845-4869.

50. Lal R and John SA. Biological applications of atomic-force microscopy, *American Journal of Physiology* **266** (1994) 1-21.

51. Laurens P, Sadras B, Decobert F, Arefi-Khonsari F and Amouroux J, Enhancement of the adhesive bonding properties of PEEK by excimer laser treatment, *International Journal of Adhesion & Adhesives* **18** (1998) 19-27.

52. Lee HJ, Jeon HY, Park SJ, Lee HW and Bae S, Micro needle array fabrication for drug delivery and drug delivery evaluation test using

optical inspection module, *International Conference on Nanotechnology and Biosensors* **2** (2010) 100-104.

53. Lippmann JM, Geiger EJ, Pisano AP. Polymer investment molding: Method for fabricating hollow, microscale parts. *Sensors and Actuators A*: *Physical.* **134** (2007) 2–10.

54. Labay C, Canal C and Garcia-Celma MJ, Influence of Corona Plasma Treatment on Polypropylene and Polyamide 6.6 on the Release of a Model Drug, *Plasma Chem Plasma Process* **30** (2010) 885-896.

55. Maaden KV, Jiskoot W and Bouwstra J, Microneedle technologies for transdermal drug and vaccine delivery, *Journal of Controlled Release* **161** (2012) 645–655.

56. Magonov SN, Characterization of polymer surfaces with atomic force microscopy, *Annual Review of Materials Science* **27** (1997) 175–222.

57. Martanto W, Davis SP, Holiday NR, Wang J, Gill HS and Prausnitz MR, Transdermal delivery of insulin using microneedles in vivo, *Pharmaceutical Research* **6** (2004) 946-952.

58. Martyn M, Whiteside B, Coates P, Allan P, Greenway G and Hornsby P, Aspects of Micromoulding Polymers for Medical Applications. Proceedings of the Annual Technical Conference, Chicago, 2004.

59. Martyn M, Whiteside B, Coates P, Allan P, Greenway G and Hornsby P, Micromoulding: consideration of processing effects on medical materials, Proceedings of the Annual Technical Conference, Nashville, TN, (2003).

60. Mauritz JMA, Morrisby RS, Hutton, Coulton HL and Clemens FK. Imaging Pharmaceutical Tablets with Optical Coherence Tomography, *Journal of Pharmaceutical Sciences*, **99** (2010) 385-391.

61. Mcintyre NS and MJ Walzak, New UV/ozone treatment improves adhesiveness of polymer surfaces, *Modern Plastics* (1995) 79-81.

62. Minsky M, Memoir on inventing the confocal scanning microscope *Journal of Scanning Microscopies* **10** (1988) 128–138.

63. Mittal KL, Contact angle wettability and Adhesion, *VSP* Utrecht (1993).

64. Miyano T, Tobinaga Y, Kanno T, Matsuzaki Y, Takeda H, Wakui M and Hanada K, Sugar micro needles as transdermic drug delivery system, *Biomed Micro devices* **7** (2005) 185-188.

65. Nair AKK, Sankaraiah J, Narasimha DK and Mallu UR, Novel drug delivery technologies-a changing and challenging global scenario, *The Experiment* 8 (2013) 468-482.

66. Nemeth A, Hannesschlager G, Leiss-Holzinger E, Wiesauer K and Leitner M, Optical coherence tomography – applications in non-destructive testing and evaluation, *INTECH* **9** (2013) 161-185.
67. Niggemann M, Ehrfeld W and Weber L, Fabrication of miniaturized biotechnical devices< Proceedings of SPIE - The International Society for Optical Engineering; 21 September 1998 through 22 September 1998; Santa Clara, CA.

68. Oraby SE and Alaskari AM, Atomic Force Microscopy (AFM) topographical surface characterization of multilayer-coated and uncoated carbide inserts, World Academy of Science, Engineering and Technology, (2010).

69. Owens DK and Wendt RC, Estimation of the surface free energy of polymers, *Journal of Applied Polymer Science* **13** (1969) 1741–1747.

70. Paudel KP, Milewski M, Swadley CL, Brogden NK, Ghosh P, Stinchcomb AL, Challenges and opportunities in dermal/transdermal delivery, *Therapeutic Delivery* **1** (2010) 109-131.

71. Piotter V, Micro-injection moulding for the manufacturing of medical devices, *Medical Device Manufacturing & Technology* (2006) 23-27.

72. Potsch G and Michaeli W, Injection moulding: an introduction, Carl Hanser Publishers, 2008.

73. Prausnitz MR and Langer R, Transdermal drug delivery, *Nature Biotechnology* **11** (2008) 1261–1268.

74. Prausnitz MR, Mitragotri S and Langer R, Current status and future potential of transdermal drug delivery*, Nature Review Drug Discovery* **2** (2004)115-24.

75. Robert AM, Plastic part design for Injection Moulding: An Introduction Hanser Publishers, 1994

76. Rulison C, So you what to measure surface energy? Technical Note Kruss GmbH, Hamburg, **306** (2003) 1-16.

77. Sadras B, Decobert F, Arefi F and Amouroux J, Enhancement of adhesion on polyether etherketone (PEEK) by excimer laser treatments, *SPIE* 2789 (1989) 305-313.

78. Saltzman MW, Drug Delivery: Engineering Principles for Drug Therapy. Oxford University Press New York, (2001).

79. Sammoura F, Kang JJ, Heo YM, Tae SJ, Liwei L. Polymeric microneedle fabrication using a microinjection moulding technique. *Microsyst Technol*. **13** (2007)517–22.

80. SanAgustin JT, Follit JA, Hendricks G and Pazour GJ, Scanning electron microscopy to examine cells and organs, *Methods in Cell Biology* **91** (2009) 81–87.
81. Scalf J, Introduction to Nanoparticle Characterization with AFM Pacific Nanotechnology, Inc. Santa Clara, (2006)

82. Semwogerere D and Weeks ER, Confocal Microscopy, *Encyclopedia of Biomaterials and Biomedical Engineering*, Taylor & Francis (2005).

83. Steglich D, Lacan F, Dessors S, Eigenbro H, Moguedet M and Bambury E, Optimising the replication quality of polymer injection-moulded microneedles on the IMPRESS platform, (2010)

84. Stoeber B, Liepmann D. Arrays of hollow out-of-plane micro-needles for drug delivery. *J Microelectromech Syst*. **14** (2005) 472–9.

85. Tillmann W and Vogli E, Selecting surface-treatment technologies © 2006 WILEY-VCH Verlag GmbH & Co. KGaA.

86. Trimmer W, Ling P, Chin CK, Orton P, Gaugler R, Hashmi S, Hashmi G, Brunette B and Reed M, Injection of DNA into plant and animal tissues with micromechanical piercing structures, *Micro Electro Mechanical Systems* 8th Workshop Amsterdam, (1995) 111-115.

87. Trichur R, Kim S, Zhu X, Suk JW, Hong C-C, Choi J-W, Ahn CH. Development of plasticmicroneedles for transdermal interfacing using injection moulding techniques. *Micro Total Anal Syst*. **1** (2002) 395–7.

88. Vansteenkiste SO, Corneillie SI, Schacht EH, Chen X, Davies MC, Moens M, Vaeck LV, Direct measurement of protein adhesion at biomaterial surfaces by scanning force microscopy, *Langmuir* **16** (2000) 3330-3336.

89. Wang KK, Injection and compression moulding fundamentals, *Marcel Dekker*, New York, 1987.

90. Watts JF and Wolstenholme J, An introduction to surface analysis by XPS and AES, Published by Wiley & Sons, Chichester, UK, 2003.

91. Watts JF, An Introduction to surface analysis by electron spectroscopy, Oxford University Press, Oxford, 1990.

92. Weber L and Ehrfeld W, Micro-moulding- processes, moulds, applications, Kunsts Plast Eur Munich, Germany **88** (1998) 60-63.

93. Whiteside B, Martyn M, Coates P, Allan P, Hornsby P and Greenway G, Micromoulding: process characteristics and product properties, *Plastics Rubbers Composites* **32** (2003) 231-239.

94. Whiteside B, Martyn M and Coates P, In-process monitoring of micromoulding-assessment of process variation, *International Polymer Processing* **20** (2004) 162-169.

95. Xiaodong L and Bhushan B, A review of nanoindentation continuous stiffness measurement technique and its applications, *Materials Characterization* **48** (2002) 11 – 36.

96. Xin HL and Muller DA, Electron microscopy: A new spin on electron beams, *Nature Nanotechnology* **5** (2010) 764-765.

97. Yao D and Kim B, High aspect ratio micro features injection moulding, *Journal of Injection Moulding Technology* **6** (2002) 11-17.

98. Yoon SH, Alabran M, Lee J, Mead J, Barry C and Carter D, Micro-injection molding of high aspect ratio features with thermoplastic polyurethanes, Proceedings of the Annual Technical Conference, (2007).

99. Yung KL, Xu Y, Kang C, Liu H, Tam KF, Ko SM, Kwan FY and Lee MH, Sharp tipped plastic hollow microneedle array by microinjection moulding, *Journal of Micromechanics and Micro engineering* **22** (2011) 1317-1322.

100. Yang M, Zahn JD. Microneedle insertion force reduction using vibratory actuation. *Biomed Microdevices*. **6** (2004)177–82.

101. Zeiler T, Surface modification of thermoplastic polymer materials in view of the Improve their bondability, Thesis Erlangen (1997).

Accessed websites

1. Images of Cross-section showing different layers of skin and Cross Section of Human Skin Showing the Stratum Corneum Layer of the Epidermis were copied from http://skinqd.com/how-it-works/clinical-studies and this site was accessed on 16/08/2013.

2. Image of the histological section showing the different layers of the skin was copied from http://www.oucom.ohiou.edu/dbmswitmer/Downloads/Basic%20Skin%20Histology2-21-01.pdf and this site was accessed on 20/03/2013.

3. The diagram of Deep Reactive Ion Etching (DRIE) was copied from http://www.ukmig.com/page.php?id=14&PHPSESSID=f9089d822d82b8c65deef53c35f8ea5c and this site was accessed on 18/01/2011.

4. Chemical structure of PEEK was copied from http://www.engineersedge.com/plastic/plastic_material/polyetheretherketone-peek-plastic.htm and this site was accessed on 24/03/2012.

5. Image showing the structural Difference between LCP and conventional Semi-crystalline polymers was taken from http://www.celanese.com/engineered-materials/Technical-Information.aspx and this site was accessed on 24/03/2012.

6. Comparison of amorphous, semi crystalline and liquid crystal polymers table was adapted from http://www.celanese.com/cn-cn/ /media/Engineered%20Materials/Files/Brochures/Cware-001_VectraIndCwareBro_AM_0613.pdf and this site was accessed on 24/03/2012.

7. Injection moulding machine pics was copied from http://www.custompartnet.com/wu/InjectionMolding and this site was accessed on 29/06/2014.

8. Images of Micro-injection moulding process and single step standard injection technology were copied from https://www.mamk.fi/instancedata/prime_product_julkaisu/mamk/embeds/mamkwwwstructure/20224_Wittmann_Battenfeld_Kirsch.pdf this site was accessed on 29/06/2014.

9. Image of Electrical discharge during corona discharge http://www.dynetechnology.co.uk/applications/corona/ this site was accessed on 13/07/2012.

10. Diagram illustrating the contact angle of a liquid sample was copied from http://www.facekyowa.co.jp/english/en_science/en_theory/en_what_contact_angle/ this site was accessed on 23/08/2012

Chapter 3 Micro-injection moulding of solid microneedles

Graphical abstract

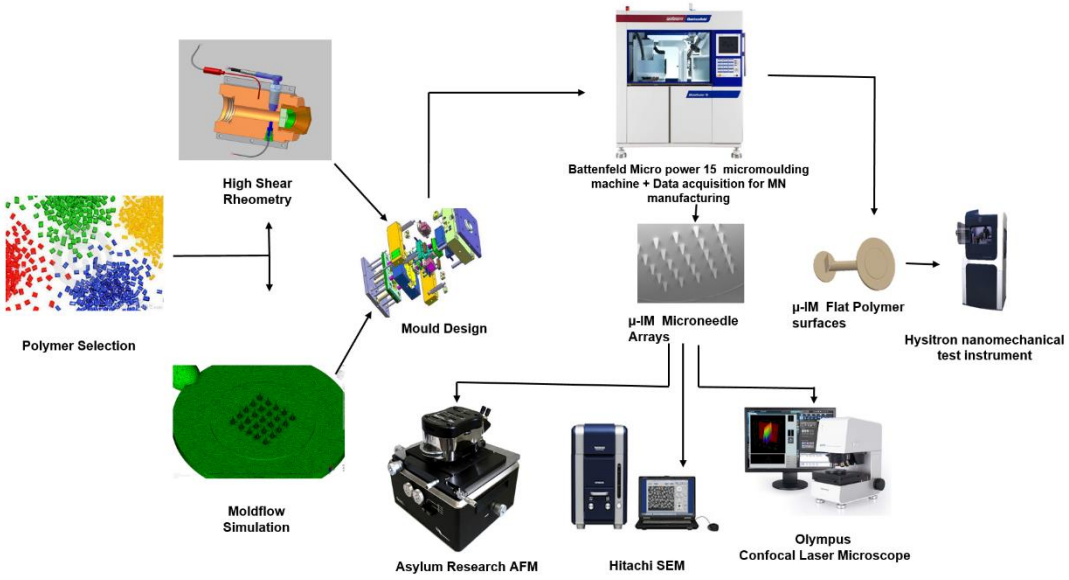

Figure 3.1 Schematic representation of the Chapter 3.

3.0. Introduction

The number of applications of polymeric materials for medical use has seen a significant increase over the last decade as they are very cost effective; especially for mass production of disposable medical devices such as catheters, syringes, tubing etc. Micro-injection moulding (µIM) is considered to be the most widely used manufacturing technology in the plastic industry for production of devices like optical grating elements, biochips and artificial organs which may contain micro scale features with bespoke properties which are not possible using conventional moulding techniques (Jeng, 2010 and Piotter, 2006). Despite the fast growth of µIM manufacturing technology, both experimental and modelling data regarding the process characterisation are scarce (Whiteside, 2005 and Chu, 2008).

Our aim here is to develop and fabricate polymeric solid microneedle arrays using micro- injection moulding. For such small polymeric components, subjected to the extreme stress, strain rate and temperature gradients encountered in the micro-moulding process, detailed material characterisation combined with process monitoring is desirable to highlight variations in moulding conditions and this will assist in creating a viable manufacturing process with acceptable quality products. Furthermore, off line tests of the resulting products allow investigation of the most statistically important process parameters which influence the resulting mechanical performance of the component. In this chapter micromoulding process dynamics along with in-line temperature-pressure monitoring system required for accurate monitoring and evaluation of moulding conditions for each MN produced was characterised. This chapter is divided into following sections.

Polymer processability: measurements at various temperatures have been performed to predict the flow behaviour of polymer melts at very high shear strain rates and this information was fed into Autodesk Moldflow® software to assist the MN production process design.

Design of the mould: with the feedback from the initial rheological and simulation data a mould and mould-insert were designed. Careful attention was given to the thermal characteristics and evacuation of the mould insert is done by vacuum. To exactly monitor the filling of MNs in the cavity, a pressure and temperature transducer was located opposite to the insert.

Manufacturing and process characterisation: a range of sensors were installed onto the µIM machine in order to record parameters such as injection pressure, injection speed, melt temperature, filling time, melt cushion, part weight, mould cavity temperature and pressure. A design of experiments (DOE) combined with data acquired (especially from the cavity pressure and temperature transducers) were used to optimise the manufacturing process.

Mechanical testing: it is very important that polymeric MNs have good mechanical strength to sustain the insertion force to pierce the human skin and delivery the drugs. So contact depth, hardness and modulus of the selected materials were carried using a nanoindenter.

Product evaluation: the scale of micro moulded products causes problems when considering assessment of dimensional properties. Most commonly calibrated optical microscopy is the preferred method but the high aspect ratio and complex geometry of MNs can be difficult to image using optical scanning

systems. Here techniques like SEM, AFM and Confocal laser microscope were utilised for MN characterisation.

3.1. Experimental

3.1.1. High shear strain rheometry

Experiments were performed using a Fanuc Roboshot S2000-*i*100a injection moulding machine, with screw diameter 22 mm. The operation mode on the machine was set to air-mode and front end of the nozzle was removed and replaced by a capillary die as show in the Figure 3.2a.Two pressure transducers (Dynisco PT435 and Kistler 4015A) were used to measure the pressure at the entrance to the capillary die. Each polymer was injected at a range of speeds (0.3; 0.5; 0.8; 1.3; 2; 3.2; 5.1; 8.1; 12.9; 20.4; 32.3; 51.2 and 81.4 mm/s) to obtain high shear rate, first through a long die (0.5 mm orifice diameter with 8 mm length) and the experiments were repeated using a short die (0.5 mm orifice diameter with 0 mm length). Polymer was melted in the screw of the injection moulding machine at a rotation speed of 20 rpm with a back pressure of 10 MPa. Injection was initiated following a dwell time of 30 seconds. Process data was recorded using a LabView SC2345 data acquisition unit triggered by a 24 V signal from the moulding machine at the start of the each injection. Four polymers were characterised at different temperatures as listed in the Table 3.1.

Polymer Type	Trade Name	Grade	Manufacturer	Test Temperatures°C		
Polycarbonate (PC)	Lexan ®	HPX8REU	Sabic Innovative Plastics	280	300	320
Polycarbonate (PC)	Makrolon ®	RX2258	Bayer AG	280	300	320
Polycarbonate(PC)	Makrolon ®	RX2430	Bayer AG	280	300	320
Poly ether ether ketone (PEEK)	PEEK	LT-3	Invibio Inc.	380	400	420

Table 3.1 Details of the polymers studied.

(a) (b)

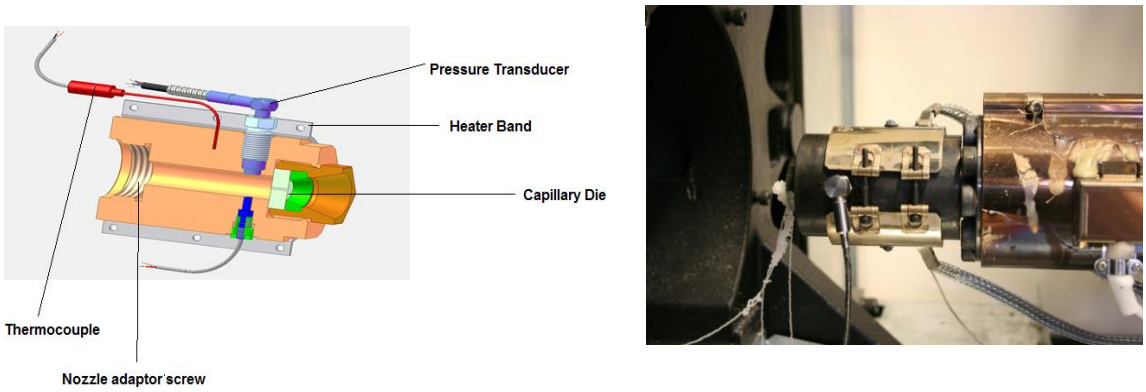

Figure 3.2 (a) Schematic of cross-section of the nozzle adapter with the location of pressure adaptor and capillary die (b) Photograph of the high shear rheometry adaptor in the Injection moulding machine.

3.1.2. Modelling and simulation

In order to study the simulation of the MNs a 3D CAD model from Autodesk Inventor® was imported as a STL format. The initial step was to create a mesh, which breaks down the model into small triangular elements so the software can use the principle of finite element analysis for the study. A 3D mesh solver was used to mesh the MN model, and once the meshing was created the software shows the amount of the triangular elements the model consists. The next step was to locate the injection point (where the polymer injection would place during the moulding process) followed by selecting the manufacturer and grade of the material selected from the material database. The last step was to configure the injection moulding parameters shown in Table 3.2.

Polymer	Mould temperature (°C)	Melt temperature(°C)	Flow rate cm^3/s
PEEK	220	420	992.5
LEXAN	120	320	331

Table 3.2 Simulation input parameter.

3.1.3. Nanoindentation

The indentations were performed using a nano-indenter Figure 3.3 (Hysitron TI 950 TriboIndenter equipped with a diamond berkowich conical probe with tip radius 107.64 µm) to obtain a load versus displacement output.

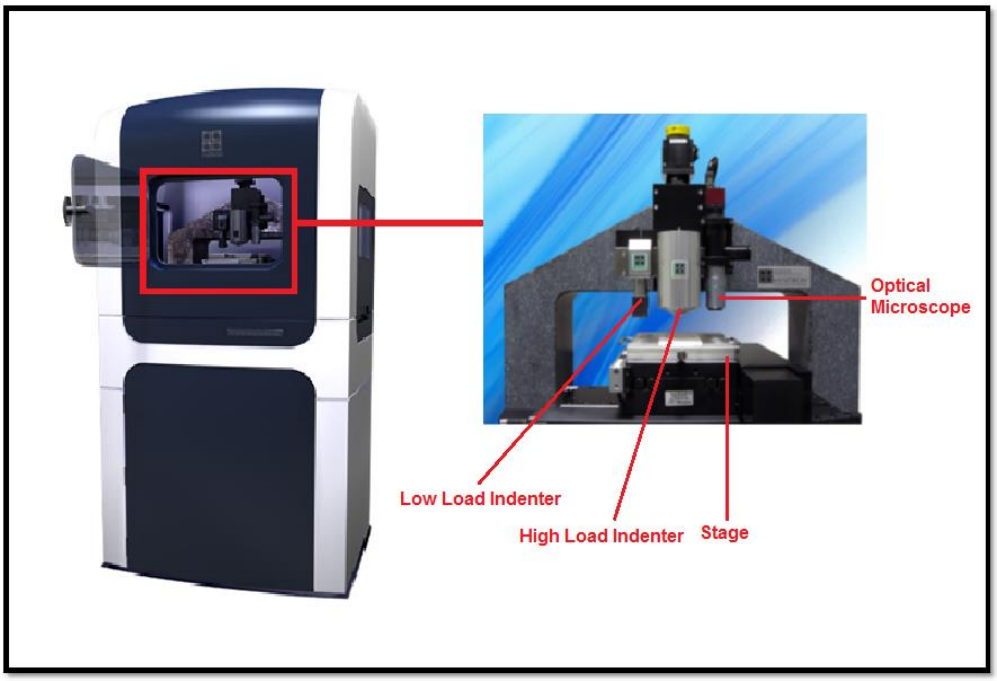

Figure 3.3 Image of the Hysitron TriboIndenter.

The micro-injection moulded polymer discs of PEEK, LCP and PC as shown in the Figure 3.4 were carefully loaded to the indenter. Once the sample discs were secured in place, the optical microscope which is integral with the indenter unit was used to identify all possible areas on the sample surface that needs indentation.

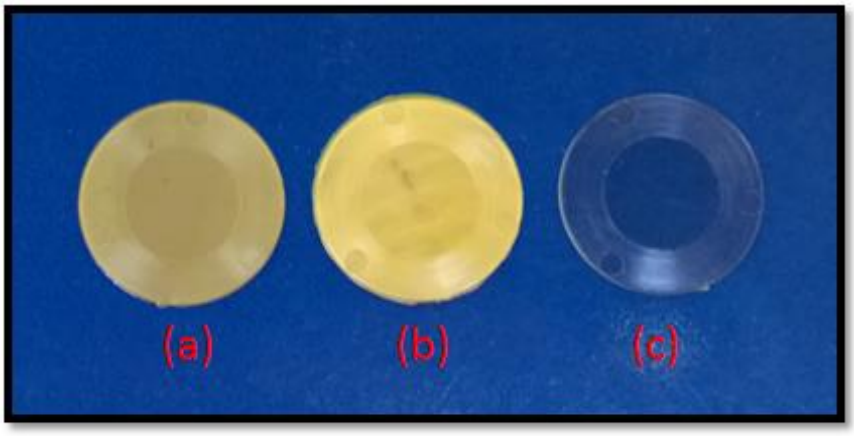

Figure 3.4 Photographic images of micro-injection moulded specimen used for characterisation (a) PEEK, (b) LCP and (c) PC.

The area function describing the real indenter used for the indentation experiments requires a precise calibration, especially at the tip. The tip defect, which is always present due to technological limitations in the manufacture of the indenter, may greatly affect the evaluation of the mechanical properties of the tested surface at the first material layers. Tip shape calibration was therefore performed by analysing a set of 100 load-penetration curves on fused silica with maximum loads of between 100 μN and 10000 μN. This calibration allows the displacement of the load frame to be removed from the total measured displacement so that only displacement due to penetration of the tip into the sample remains. Tip-shape calibration is based on determining the area function. The method is based on the assumption that Young's modulus of elasticity is independent of indentation depth. The area function calibration procedure utilizes a reference material; fused silica with Young's modulus of 69.6GPa is used as a standard sample for calibration purpose. A series of 500 indents were conducted on each polymer disc (Figure 3.4) with the indent load varying from 1 mN to 10 mN. All these 500 indents were carried out at 5 different locations at a separation distance of 100 μm. This same procedure

was carried out using a high load indenter (Berkovich conical probe with tip radius µm) with forces from 100 mN to 1 N at 5 different locations in the polymer disc 200 µm apart.

During an indentation, the indenter probe is driven into the sample surface and then withdrawn by decreasing the applied load. Both the applied load (P) and depth of penetration into the sample surface (h) were continuously monitored and a load versus displacement plot is obtained. The hardness and reduced modulus was calculated at each load from the resulting load versus displacement curve, and provided as an output by the data acquisition unit of the machine. The values of reduced modulus (E_r) and hardness were obtained from the unloading curve using the Oliver and Pharr method.

3.1.4. Manufacturing of solid microneedles

3.1.4.1. Micro-injection moulding hardware

There are many µIM manufacturers such as Battenfeld, Sodick, Ferromatic Milacron and Boy, but the Battenfeld Microsystem 50 has been most widely used by many researchers for µIM research (Sha, 2007; Pirskanen, 2005; Whiteside, *et al*., 2005; Chu *et al*., 2008 and Piotter, 2002). This machine offers high repeatability, accurate dosing, high injection and back pressure, clean room facility and a robotic hand for inspecting and picking the micro-parts. In this work all the replication studies of the MN insert were performed on Battenfeld Micro-Power 15 micromoulding machine as shown in the Figure 3.5. Micro-power 15 is the latest micromoulding machine from Battenfeld and has some significant changes from Microsystem 50, particularly the clamping and injection unit which are all new. The machine maximum clamping force and

injection speed are 150 KN and 1200 mm/s respectively. A servo drive controller in the machine has closed loop functionality to switchover from injection to hold phases in sub 100 µs based on settings for time, displacement or pressure. Of these settings, Battenfeld strongly recommend the use of pressure-controlled switchover to provide the most repeatable products as the process is not dependent on accuracy of dosing and any small variations will simply manifest themselves as subtle variations in the size of the melt cushion. As shown in Figure 3.6 a 14 mm diameter extrusion screw plasticises the polymer pellets using combination of mechanical and thermal energy and accurately feeds the pre-set volume into the injection barrel. A 4.95 mm injection plunger transfers polymer melt directly to the split plane of the mould. The injection plunger can travel into the split plane and guarantees a short flow path with high pressure for an extremely precise injection process. A data acquisition system was enabled for process monitoring and data recording. Three thermocouples located on the extruder, central distributor and nozzle for controlling the melt temperature. In this study the temperature at the nozzle is considered to be the melt temperature. Figure 3.7 shows the internal components of the Micro-power 15 injection-moulding machine. Figure 3.8 and 3.9 shows the exact location of the injection drive shaft and location of the displacement sensor in the Micropower 15 injection unit respectively.

Figure 3.5 Image of the Battenfeld MicroPower 15.

Figure 3.6 Injection unit of the MicroPower and regarded as the benchmark in micro system technology. It is able to inject thermally homogeneous melt with minimal flow paths.

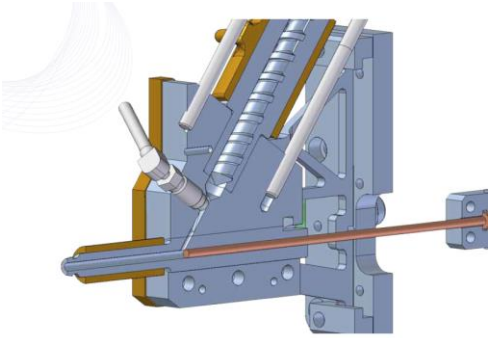

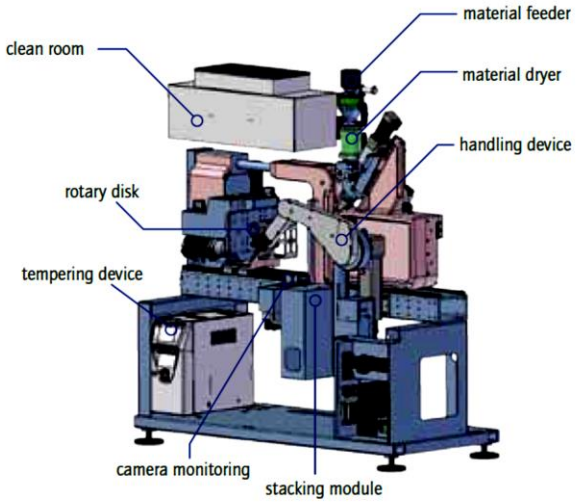

Figure 3.7 Internal units of MicroPower 15.

Figure 3.8 MicroPower 15 with injection unit cover removed exposing internal workings.

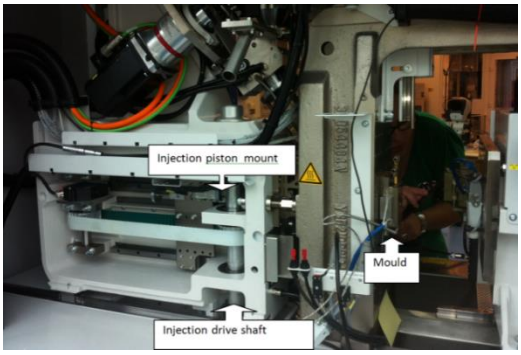

Figure 3.9 Location of the displacement sensor in the MicroPower 15 injection unit.

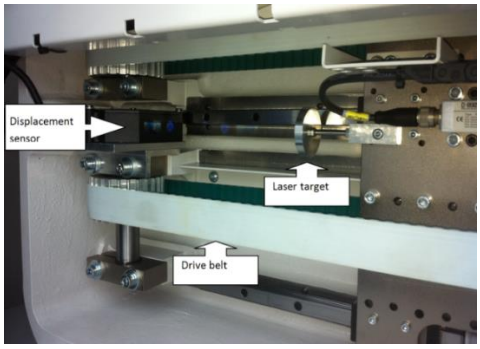

3.1.4.2. Mould design and fabrication

Moulds made for micro-injection moulding of MNs are similar to moulds made for conventional injection moulding However, moulds made for microinjection moulding are significantly smaller and have some special features. For example some features include, vacuum, heating and cooling of the mould and special ejection systems. Due to the size of the mould cavity and features, adapted mould sensors are used, because conventional sensors are not always suitable to micro-features a special ejector/withdrawal design is important, so that microneedles are not deformed due to the induced friction between the mould and the part (Robert, 1994 and Attia *et al*., 2009)**.** The two plate mould components were customised and ordered from Hasco Ltd. The cavity and core plates, ejector pins, cartridge heater housing and venting were machined in University of Bradford. A technical drawing with detailed dimension and components of the mould is shown in Figure 3.10, 3.11 and 3.12. High grade steel (Mould steel 1.1730/ 1.2311 and tool mould steel P20) was selected as mould components is subjected to high wear and tear, and to prevent it from corrosion. Moreover cavity plates and core plates are subjected to high forces, therefore hardened steel was used.

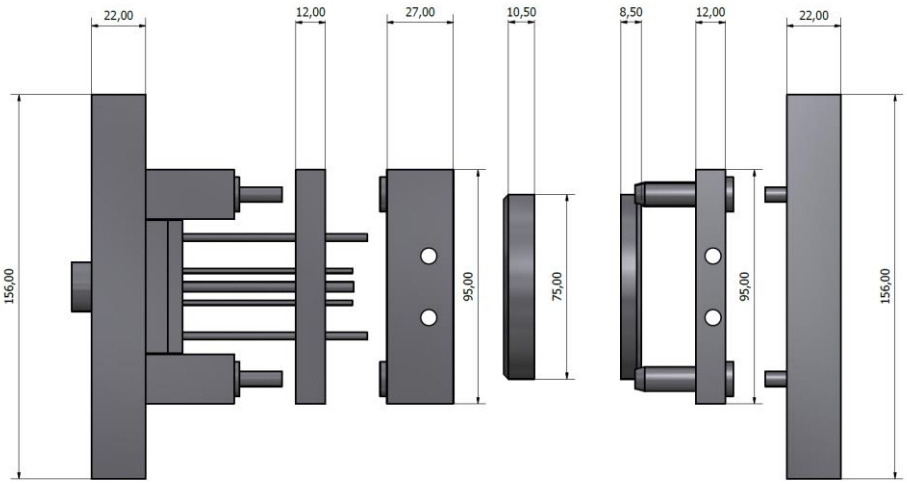

Figure 3.10 2D drawing of the mould with the dimensions.

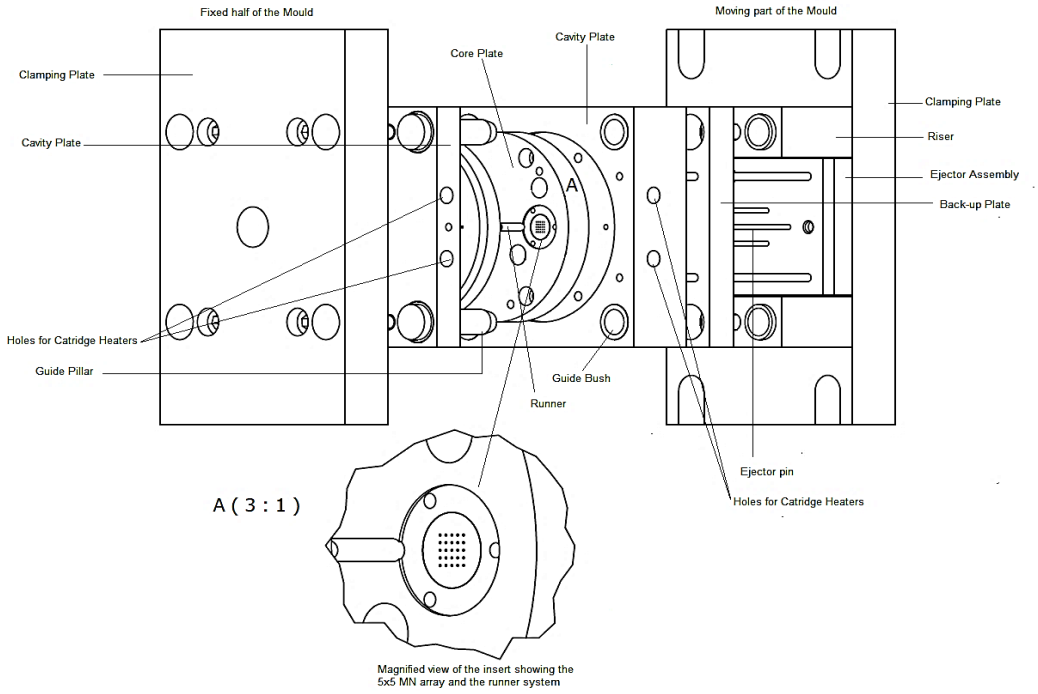

Figure 3.11 Technical drawing of the 2-plate mould showing the MN insert.

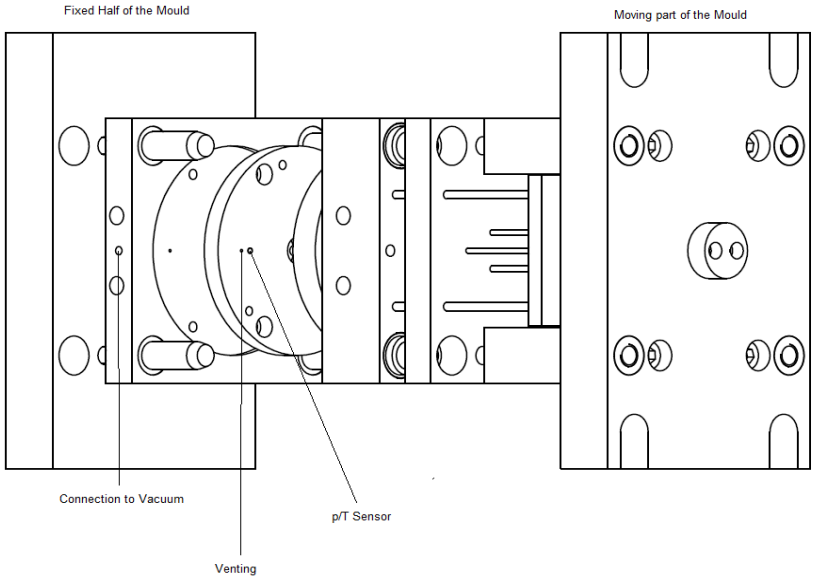

Figure 3.12 Technical drawing of the 2-plate mould showing the p/T sensor and venting system.

Mould surface temperature is of paramount importance in plastic injection moulding. With higher mould temperature, the surface quality of the moulded part will be better but the cooling time will be also high (Jeng, 2010). So optimised mould temperature allowing solidification of the part without compromising the finish quality is very crucial. There are many methods of mould heating like electric cartridge, electromagnetic induction coil, oil, hot air and infrared. Whichever type of heating used, rapid heating cycle improves product quality in injection moulding. In this work mould heating is done by using electric cartridge heaters, which are easy to install and use. Four Watflow Firerod cartridge heaters (2 on each side of the mould) were used. These heaters have a maximum operating temperature above 500ºC.

3.1.4.3. MN mould inserts and part geometry

Moulds used specifically for microneedle applications are usually produced on an insert, which is then fitted in the main mould body. While the mould is made of steel, as in conventional injection moulding, inserts can also be manufactured of other materials, depending on the technology used. Silicon or metals are usually used, however silicon is not as durable and long lasting as metals and hence silicon is only used for small production runs which doesn't need long lifetimes. Use of metal like hardened steel is the suitable alternative but requires specialised micro-machining techniques to create micro features into the mould inserts. Common methods include LIGA, micro-milling, micro grinding, laser and electric-discharge machining (EDM).

The use of insert moulds also reduces the overall cost of process set up where the finalised mould design is produced by a number of iterative steps in which parts are moulded and the mould design is then changed (Potsch *et al*., 2008 and Attia *et al*., 2009). The MN mould insert which is shown in Figure 3.13 was made out of Stavax ESR (Bohler-Uddeholm Corp, USA). The sink EDM was used to create negative MN features into the insert and was outsourced to Isometric tool and design USA.

An important factor to consider while designing microneedles is the skin anatomy. The main objective of the MNs is to facilitate pain free drug delivery. The human skin is made of three layers where the outer is the dead stratum corneum (10-20 µm), middle viable epidermis (90-150 µm) and underlying dermis (Figure 2.3) (detailed anatomy discussed in Chapter 2). The main consideration is that the needle length should long enough to pierce deep into

the subcutaneous region but not penetrating into capillaries, blood vessels and nerve endings.

Another important factor which is important is the tip radius, sharper the needle tip less force is required for insertion and less pain. But one also need to consider sharper the tip reduced strength at the tip so chances of needle tip breaking off while insertion might occur. Based on this microneedle with shaft length 600 µm and 300 µm base and tip radius 10-15 µm width were designed for this study. Figure 3.14 and 3.15 gives a clear view of the 3D model of the moulded MN part and schematic of the MN part geometry.

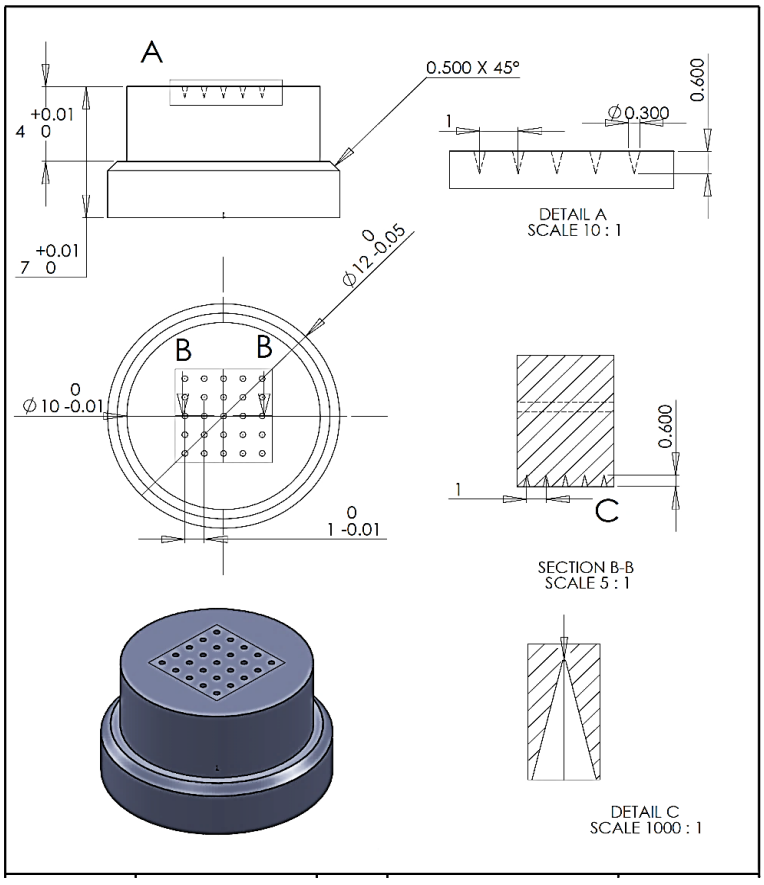

Figure 3.13 2D drawing of the MN insert with dimension created using Solid-works CAD software.

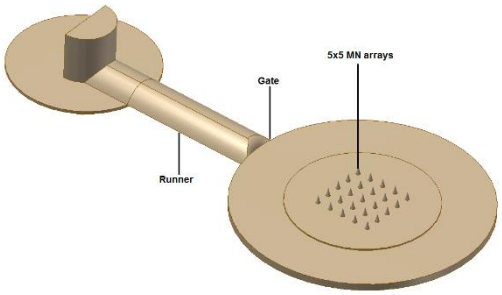

Figure 3.14 3D view of the moulded MN part, modelled using CAD software.

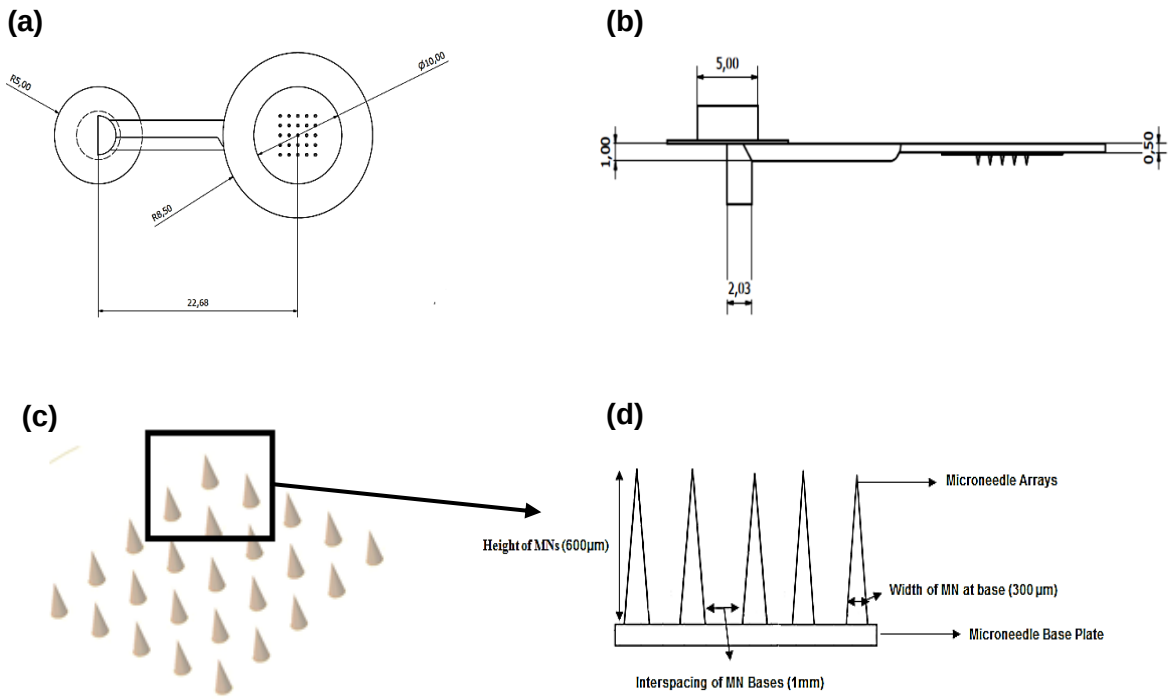

Figure 3.15 (a) 2D-view of the MN part with dimensions (b) side-view of the part with dimensions; (c) schematic representation of a microneedle array (d) schematic representation of a microneedle array showing its geometrical parameters like height of MNs in array, interspacing of MN bases and width of MN at base.

3.1.4.4. Materials

The following materials were selected for the MN manufacturing. All the polymers selected were based on the mechanical strength and melt flow index. Lexan ® HPX8REU, Makrolon ® RX2258 and RX2430 are all different grades of FDA approved polycarbonate. Lexan is manufactured by Sabic Innovative

Plastics while Makrolon RX2430 and RX2258 are manufactured by Bayer AG. All the PC grades are amorphous material with excellent melt flow index and added release agents to improve ejection. They were dried at 120ºC for 4 hours before moulding. PEEK LT-3 is FDA approved semi crystalline biomaterial launched by Victrex (Invibio Inc) in 1998 and is widely used for medical use. The main feature of PEEK LT-3 include its wide processing window, excellent processability and dimensional stability, high mechanical performance and resilient to repeated gamma radiation. PEEK was dried at 140ºC for 4 hours prior to moulding.

3.1.5. Design of experiments

The objective of the design of experiments (DOE) was to design and conduct experiments to determine the controlling factors and their best settings to get the best possible MNs. A two level four factor, full factorial DOE were carried out to optimise the filling of the MNs. The factors selected to be studied within DOE were (A) injection speed, (B) melt temperature, (C) mould temperature and (D) switch over/hold pressure which were varied at two levels 1-low and 2-high. Lexan grade of polycarbonate and PEEK LT-3 were selected for the DOE studies. Table 3.3 and 3.6 shows the levels of four factors chosen for micromoulding of MN from PEEK and LEXAN respectively. The combination of controlled factors for LEXAN and PEEK are shown in Table 3.5. Table 3.4 and 3.7 shows the experiment worksheet with all the 16 design orders (DO) for PEEK and Lexan respectively. The other optimised processing parameters which were kept constant for all the DO is shown in Table 3.12.

FACTORS AND LEVEL SETTINGS (PEEK)			
FACTORS	NAME	LEVEL 1	LEVEL 2
A	Injection Speed (mm/s)	200	600
B	Melt Temperature (°C)	400	420
C	Mould Temperature (°C)	200	220
D	Switchover/Hold Pressure (bars)	500	900
Interactions	Factor 1 x Factor 2		
AxB	Injection Speed	Melt Temperature	
AxC	Injection Speed	Mould Temperature	
AxD	Injection Speed	Switchover/Hold Pressure	
BxC	Melt Temperature	Mould Temperature	
BxD	Melt Temperature	Switchover/Hold Pressure	
CxD	Mould Temperature	Switchover/Hold Pressure	

Table 3.3 Factor and level settings for the DOE of PEEK.

EXPERIMENT WORKSHEET (PEEK)				
DESIGN ORDER (DO)	Injection Speed	Melt Temperature	Mould Temperature	Switchover/Hold Pressure
	A	B	C	D
1	200	420	200	500
2	600	420	200	500
3	200	420	200	900
4	600	420	200	900
5	200	400	220	500
6	600	400	220	500
7	200	400	220	900
8	600	400	220	900
9	600	420	220	900
10	200	420	220	500
11	600	420	220	500
12	200	420	220	900
13	600	420	220	900
14	600	420	220	900
15	600	420	220	900
16	600	420	220	900

Table 3.4 Experimental worksheet showing the design order for PEEK (DO-4 is low /DO-1 is intermediate/D0-13 high level settings).

EXPERIMENT DESIGN (PEEK and LEXAN)										
Full Factorial - 4 Factors and All Interactions										
Runs	A	B	C	D	AXB	AXC	AXD	BXC	BXD	CXD
1	1	1	1	2	2	2	1	2	1	1
2	2	1	1	1	1	1	1	2	2	2
3	2	1	1	2	1	1	2	2	1	1
4	1	1	1	1	2	2	2	2	2	2
5	1	2	1	1	1	2	2	1	1	2
6	2	2	1	1	2	1	1	1	1	2
7	1	2	1	2	1	2	1	1	2	1
8	2	2	1	2	2	1	2	1	2	1
9	1	1	2	1	2	1	2	1	2	1
10	2	1	2	1	1	2	1	1	2	1
11	1	1	2	2	2	1	1	1	1	2
12	2	1	2	2	1	2	2	1	1	2
13	2	2	2	2	2	2	2	2	2	2
14	1	2	2	1	1	1	2	2	1	1
15	2	2	2	1	2	2	1	2	1	1
16	1	2	2	2	1	1	1	2	2	2

Table 3.5 16 run full factorial design, allowing the experimenter to study 4 factors, each at two levels, and all of their 6 Interactions (AxB, AxC, AxD, BxC, BxD, and CxD) for LEXAN and PEEK.

FACTORS AND LEVEL SETTINGS (PEEK)			
FACTORS	NAME	LEVEL 1	LEVEL 2
A	Injection Speed (mm/s)	200	600
B	Melt Temperature (°C)	300	320
C	Mould Temperature (°C)	100	120
D	Switchover/Hold Pressure (bars)	500	900
Interactions	Factor 1 x Factor 2		
AxB	Injection Speed	Melt Temperature	
AxC	Injection Speed	Mould Temperature	
AxD	Injection Speed	Switchover/Hold Pressure	
BxC	Melt Temperature	Mould Temperature	
BxD	Melt Temperature	Switchover/Hold Pressure	
CxD	Mould Temperature	Switchover/Hold Pressure	

Table 3.6 Factor and level settings for the DOE of LEXAN.

EXPERIMENT WORKSHEET(LEXAN)				
DESIGN ORDER (DO)	Injection Speed	Melt Temperature	Mould Temperature	Switchover/Hold pressure
	A	B	C	D

1	200	320	100	500
2	600	320	100	500
3	200	320	100	900
4	600	320	100	900
5	200	300	120	500
6	600	300	120	500
7	200	300	120	900
8	600	300	120	900
9	600	320	120	900
10	200	320	120	500
11	600	320	120	500
12	200	320	120	900
13	600	320	120	900
14	600	320	120	900
15	600	320	120	900
16	600	320	120	900

Table 3.7 Experimental worksheet showing the design order for Lexan (DO-4 is low /DO-1 is intermediate/D0-13 high level settings).

For each experiment, the parts produced in the first 20 cycles were discarded in order to stabilise the process, then the following 10 parts were collected and the average masses, cavity pressure and temperature were measured.

3.1.6. Data acquisition

A Kistler 6189A piezoelectric pressure/temperature (p/T) sensor was flush mounted with the cavity wall of the fixed part of the mould (Figure 3.12 and 3.16a). It was used to monitor and optimises cavity pressure and temperature during the MN manufacturing. The cavity p/T sensor specifications are provided in Table 3.8. The small features and physical size of the MN component make implementation of an actual cavity pressure/temperature measurement extremely challenging. This sensor is a single wire solution with a diameter of 2.5 mm and was connected to the Kistler charge amplifiers (Figure 3.16b) supplied with the Micropower 15 machine.

Technical Data	
Range (bar)	0to 2000
Overload (bar)	2500
Sensitivity (pC/bar)	-6.5
K- type thermocouple	NiCr-Ni
Operating temperature range of the sensor, cable and connector box(ºC)	0 to 200 (allowed to rise to 240
Melt temperature at the front of the sensor (ºC)	<450

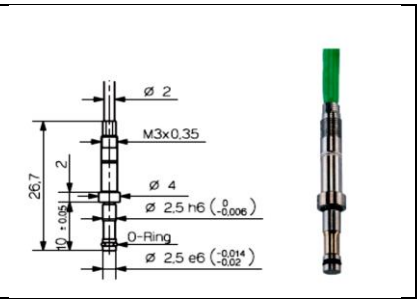

Table 3.8 Showing the Kistler 6189A p/T sensor specifications (Kistler, 2011).

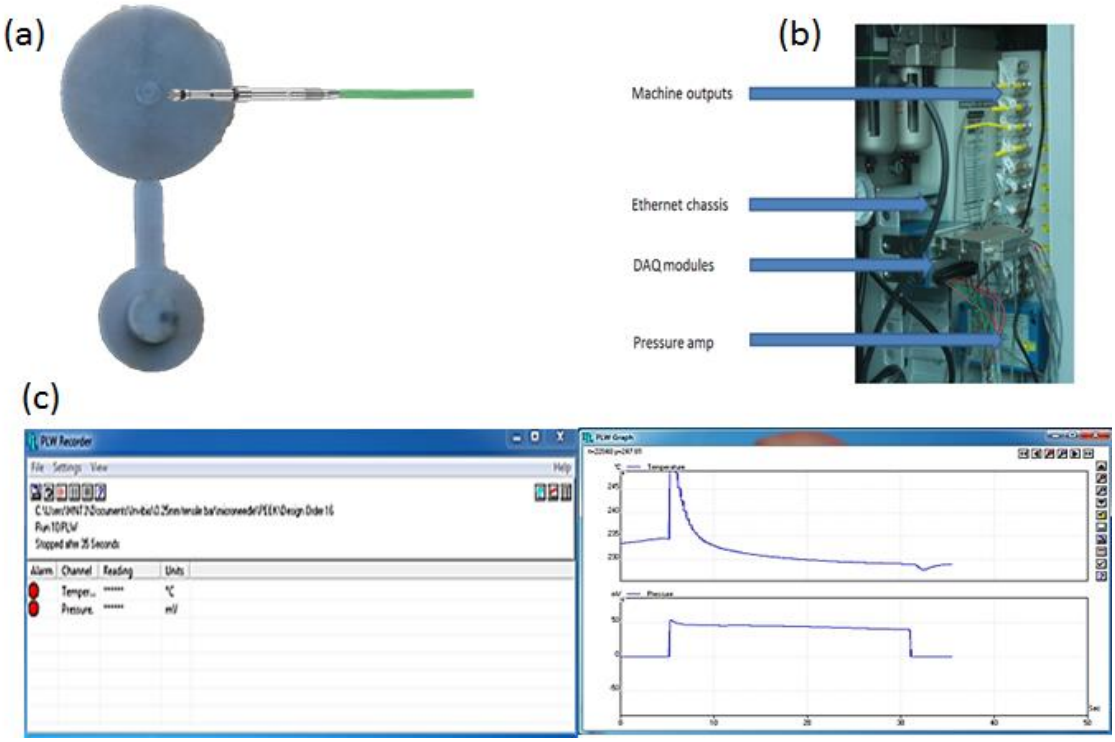

Figure 3.16 (a) Image showing the location of the p/T sensor for measuring cavity pressure and temperature (b) DAQ installation (c) acquisition software user interface

The MicroPower 15 has an optional output module which supplies a variety of process information in the form of 0-10 V analogue and 24 V digital outputs. The data is acquired by USB –Pico TC-08 and processed using Picolog recorder 6. The output from the pressure amp (Figure 3.16b) is then connected

to the channel 2 of the Pico TC-08 and temperature is connected to the channel 1. Figure 3.16c shows the acquisition software interface.

The Pico-TC 80 has a maximum input value of 70 mV, so the output from the pressure amp was scaled down using resistors. Temperature was recorded in °C while pressure was in mV. The recorded pressure value in mV was converted to bar using the Equation 3.1 and 3.2 for PEEK and Lexan respectively.

$$P\ (bar) = V\ (mV) \times 31.01 \quad (3.1)$$

$$P\ (bar) = V\ (mV) \times 15.63 \quad (3.2)$$

The acquisition is triggered using the injection start digital input and data is recorded at a sampling rate and duration specified by the operator. Typically this is chosen to be 2000 Hz and 4 seconds for micromoulding acquisition. Because the moulded part removal and data acquisition were done manually all the experiments were carried out in the semi-automatic mode. Once collected, the data is archived and then specific quality criteria are extracted for statistical analysis.

3.1.7. Microneedle dimensional evaluation

3.1.7.1. Scanning electron microscope

A Hitachi TM-3000 Table-top Scanning Electron Microscope was used for analysis of the MN insert and needle geometry. The Hitachi TM-300 has a magnification from 15X to 30000X, sample chamber of 700 mm diameter and 50 mm thickness. It features 5 kV, 15 kV and analysis observation modes. Because of the high aspect ratio and low contrast

of the MNs, analysis mode was used for imaging. The major advantage of using TM 3000 SEM was it works under low vacuum and does not need specimen coating.

3.1.7.2. Confocal laser microscope

It is very important to measure the tip radius and height of the MNs and the most common methods used are optical or electron microscopy. Because of its steep and complex structures, a 3D image analysis gives a better measurement of the needle geometry and quality control. In this study an Olympus vertical scanning laser confocal microscope LEXT OLS 4000 was used to accurately measure the tip radius and height of MN arrays.

The device offers a broad magnification range from 108X to 17280X and the exact 3D reconstruction of the MNs. The confocal laser microscope LEXT scans the surfaces with a laser beam with the wavelength of 405 nm thus allowing submicron visualization of material and component surfaces with the resolution of down to 0.10 µm. Measurements were taken with the 20X lens using the wide range stitching feature with 20 percent overlap to produce a measurement area of 5mm x 5mm. A five level brightness switch (Table 3.9) was enabled to accurately illuminate the specimen.

Position(µm)	Brightness
600	49
550	47.1
520	49.1
20	75.5
0	48.4

Table 3.9 Brightness switch settings used for the confocal measurements.

3.1.7.3. Atomic force microscope

The most important feature of the MN is that the tip has to be sharp in order to effectively pierce the skin. So as to confirm the measurements made from confocal laser microscope, AFM (MFP-3D Asylum Research Santa Barbara, USA) was used to measure the tip radius of the MNs.

3.1.7.4. Generation of PDMS microneedles for insert characterisation

Figure 3.17 Photograph of the holder with the MN insert used for PDMS replication.

To validate the geometry of MN insert created using an EDM process, a non-destructive casting method was performed using polydimethylsiloxane (PDMS). PDMS is an organosilicon compound most commonly used as stamp resin during soft lithography and more over it is a low modulus elastomer, inert and hydrophobic. The MN insert was cleaned and degreased with acetone in a sonication bath for 10 mins and rinsed with deionised water and later dried using nitrogen gas. The MN insert was then pushed into an insert holder as

shown in the Figure 3.17. Mixing of the PDMS and curing agent was done at a proportion of 10:1 respectively and mixed thoroughly and poured on the insert. The curing was carried under vacuum at 25°C for 2 days and finally the PDMS replicated MNs were carefully pushed out from the insert holder**.**

3.2. Results and discussion

3.2.1. High shear rheometry

Measured shear viscosities of three grades of polycarbonate across the shear strain rate range of 10^4 to 10^6 at melt temperatures of 280°C 300°C and 320°C are shown in Figure 3.18 a; b and c respectively. Shear viscosity of Makrolon 2258 and 2430 at 280°C and 300°C decreased from around 60 Pa.s at low strain rates to less than 2 Pa.s at the highest strain rates and the melts exhibited a pseudo-plastic shear thinning behaviour. At 320°C viscosity curves of Makrolon 2258 and 2430 almost overlapped indicating the shear viscosities almost similar and whereas Lexan showed two distinct regions of strain dependant behaviour. Lexan at 320°C showed a Newtonian behaviour at low strain rates and pseudo-plastic shear thinning behaviour at strain rates above 3 x 10^4 s^{-1}.

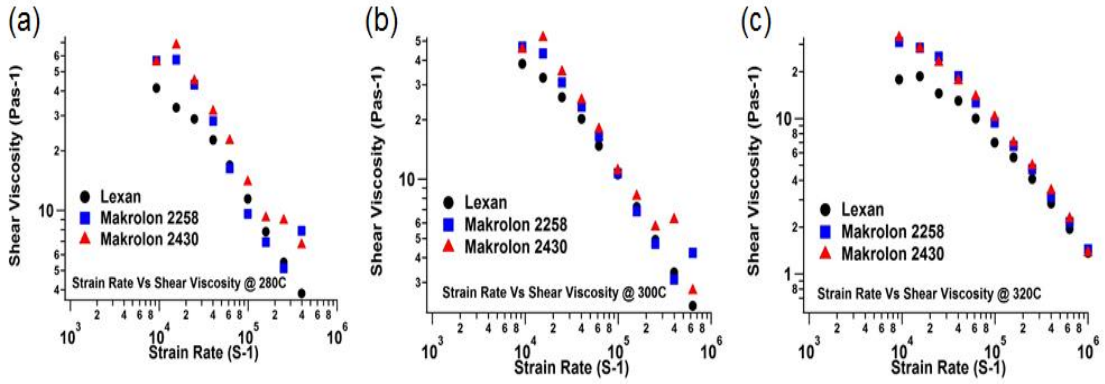

Figure 3.18 Shear viscosity of Lexan, RX2258 and RX2430 at (a) 280 (b) 300 and (c) 320°C.

The observation made from this results are as strain rates increased, the viscosities decrease linearly and maximum decrease in viscosity values was evident at 320°C.

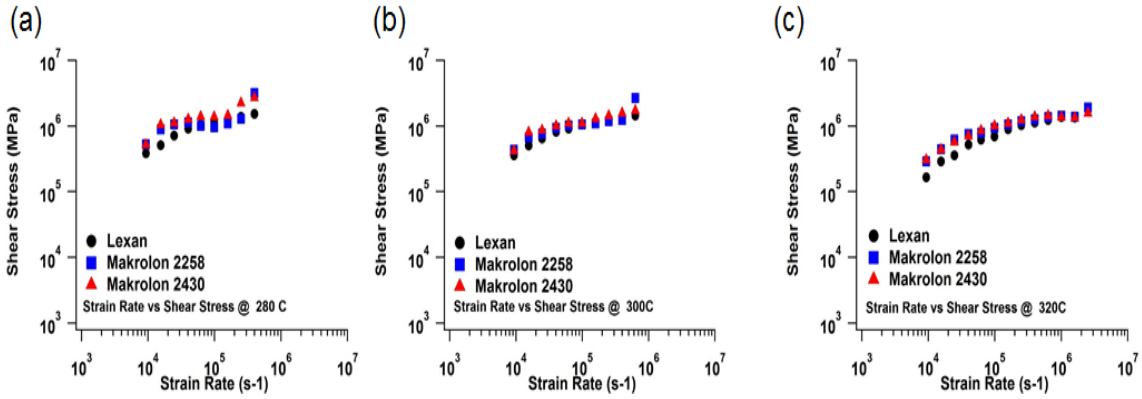

Figure 3.19 Shear stress of Lexan, RX2258 and RX2430 at (a) 280, (b) 300 and (c) 320°C.

At high strain rate the back bone stretch with in the polymer chains are high. To understand this plots of shear stress versus strain rate for the all three grades of polycarbonate and PEEK at various temperatures were studied and are presented in Figure 3.19 and 3.20b respectively. It was observed that the shear thinning behaviour at rates above $10^6 s^{-1}$ and maximum shear strain rate was limited below $10^7 s^{-1}$ before the upper pressure limit of machine barrel was reached.

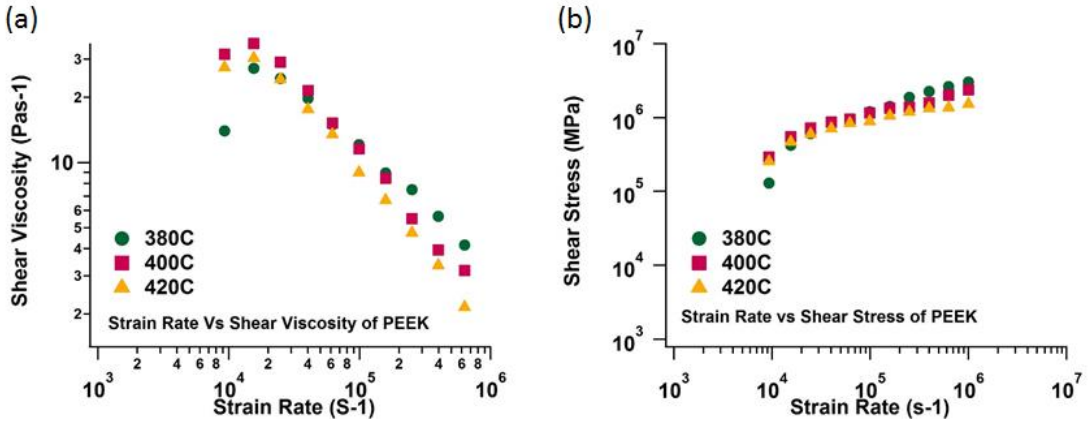

Figure 3.20 (a) shear viscosity and (b) shear stress of PEEK at various temperatures.

The plots of viscosity versus strain rate for the PEEK at 300, 320 and 340°C are presented in Figure 3.20a. Rheological behaviour of PEEK was predictable and exhibited decreasing viscosity with increasing strain rate (shear thinning behaviour). At logarithmic scale (Figure 3.20) the viscosity curves are almost straight lines for PEEK at 380, 400 and 420°C. PEEK shows a rapid and sharp shear thinning and maximum shear thinning was observed at 420°C.

3.2.2. Modelling and simulation of the micro-injection moulding process

One of the major disadvantage in µIM is the cost involved in the manufacturing of mould and mould inserts and to have modifications in the mould and re-design the inserts is again cost consuming (Menges *et al*., 2000 and Rannar, 2008). So to avoid the risks of re-engineering and to decrease the development time, the manufacturing steps like filling, packing and cooling stage and the properties of the µ-injection moulded products like shrinkage and warpage, can be simulated using computer aided engineering (CAE) software (Chu, 2009). Using these techniques, the moulding process could be simulated in a virtual environment and any alterations in tool design and process settings can be tested many times before the actual fabrication of the tool. In this study a three dimensional solver model was used.

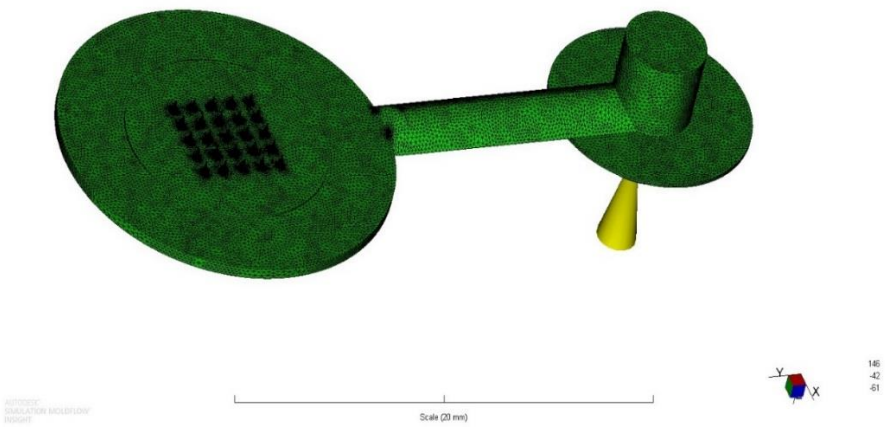

Figure 3.21 3D mesh model of microneedle.

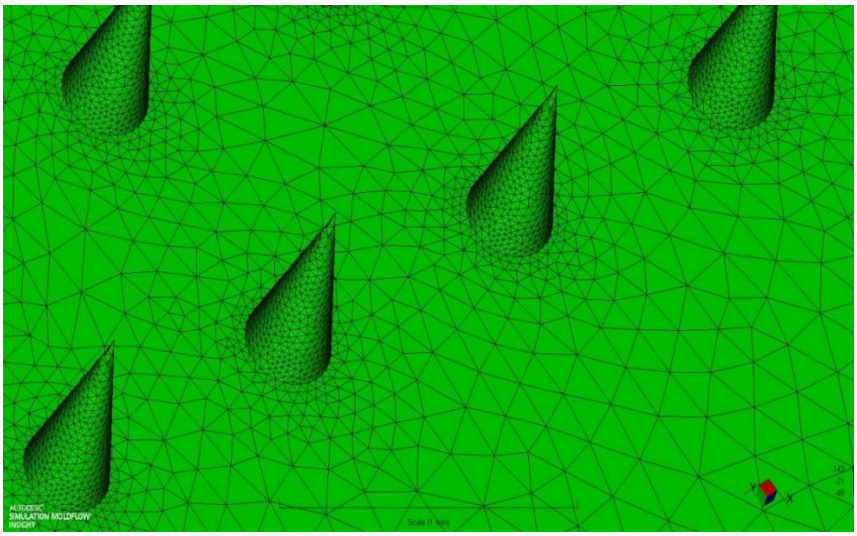

Figure 3.22 Partial enlarged view of the mesh grids.

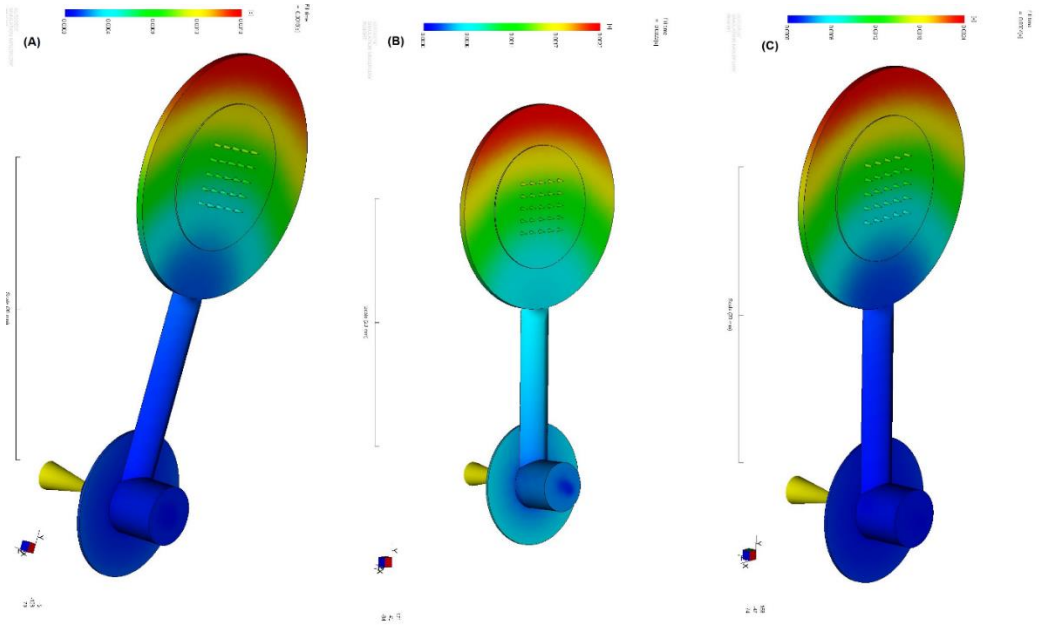

Figure 3.23 Fill time and fill pattern of PEEK at different flow rate.

The goal of the simulation studies was to analyse the filling pattern of the polymer melts into the microneedle cavities. Figure 3.21 shows a 3-Dimensional mesh model of microneedle and Figure 3.22 shows the enlarged view of the mesh. Previous studies conducted by Steglich *et al* reveals that the filling of the microneedles can be influenced by numerous injection moulding parameters like mould temperature and injection rates and as well as the microneedle geometry. The main aim of this simulation experiment was to focus on the effect of melt temperature and injection speed in filling MN cavities. An excerpt of the applied factors is listed in Table 3.2. From the initial moulding simulations (Figure 3.23) shows that the tips of the microneedles are the last places to fill. This suggests that there is a need for a combination of high holding pressures and high mould temperatures.

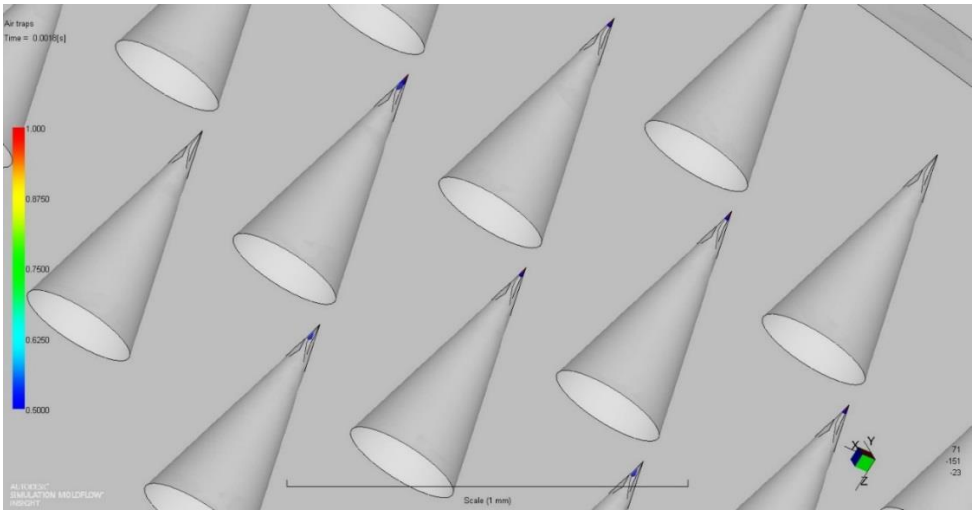

Figure 3.24 Enlarged view of the results from simulation indicating the possibility of air traps while moulding.

It was also observed that high injection speed and high melt temperature reduces the filling time moreover from Figure 3.24 it was understood that the problem of air entrapment at the tip of the cavities could lead to partial filling at the tip suggesting the need for venting to achieve a successful replication of the cavity.

3.2.3. Nanoindentation

The ultimate aim of the injection moulded polymeric microneedle is insertion to the skin without failure for effective transdermal drug delivery. Therefore it is of paramount importance to check the mechanical properties of the polymer material used for injection moulded microneedles. A depth-sensing nanoindentation devices allow the amount of penetration of an indenter into a material to be measured as a function of applied load. Nanoindentation test are capable of measuring the load at micro newton and displacement at nanometer

resolution. This ability allows the local interrogation of mechanical properties and the determination of the variation of these properties over a very small area. It has therefore, emerged as a new technique to study the mechanical properties of ceramics, soft tissues, bones, cartilages, fused silica, silicon and various other semiconductors at nano scale (Debra *et al*., 2005). Recently, considerable research is given to composites and polymers. (Hodzic, 2001 and Stachurski, 2000). As it was discussed in the Chapter 2, the method used to derive the hardness and modulus from the nanoindentation is based on the Oliver and Pharr model which takes into account the elastic recovery during the unloading segment of indentation. For metals and ceramics which are elastic-plastic materials the hardness and modulus are measured using this model but for viscoelastic materials like polymers, rate and time dependent properties should be considered.

Briscoe *et al* studied the influence of geometry of a rigid indenter upon the measured contact depth of a perfectly smoothed elastic space. They also performed a series contact compliance nanoindentation on polymeric materials and found out that the indentation depth increases immediately after the unloading segment begins to the creep effect of the viscoelastic nature of the materials. In cases where creep behaviour dominates the elastic response of the material, a 'nose' is observed on the indentation unloading curve. This phenomenon results in a negative and changing slope in the initial unloading region making it impossible to use the compliance method to measure modulus. They eliminated this noise during the test by holding the indenter at the maximum indentation load for some period of time. For the present study a 5 seconds holding time to eliminate noise was used. Vanlandingham *et a*l

reviewed and determined the uncertain issues during the indentation of polymeric materials and found out that modulus and hardness are dependent on the holding time and maximum force. In addition they also suggested that many experimental factors like load resolution, initial contact load and system compliance also cause inaccuracy in the measurements. Cheng *et al* developed flat end punch and a spherical indenter using a three element kelvin-voigt model for linear viscoelastic material to get elastic modulus from load relaxation and creep testing.

Although nanoindentation studies have been extensively performed to characterise the mechanical properties of bone, cartilages, tissues, and ceramics only few studies have examined micro-injection moulded polymers to date. In this study nano-indentation technique was employed to study the material hardness and modulus of the samples produced by micro-injection moulding. The output from these studies will be able to measure the responses of microscopic regions which can be a key to understanding mechanical behaviour of the polymeric microneedles.

Two different load indenters were used for this experiment, a low load and a high load. Low load indenter was used to cover loads from 1 mN to 10 mN whereas the high load indenter was used to cover 100 mN to 1 N. This range was selected because it covers the entire possible indentation load up to the instruments maximum limits.

Figure 3.25a illustrates one example of 10 load-displacement curves for polycarbonate surface. It was observed that there is a load-hold variation which suggests the uneven features in the surface which might have been replicated during the micromoulding process. This kind of load-hold variation does not

occur if the surface is absolutely smooth, which can be explained during calibration of the nanoindenter is been carried out Figure 3.25b.

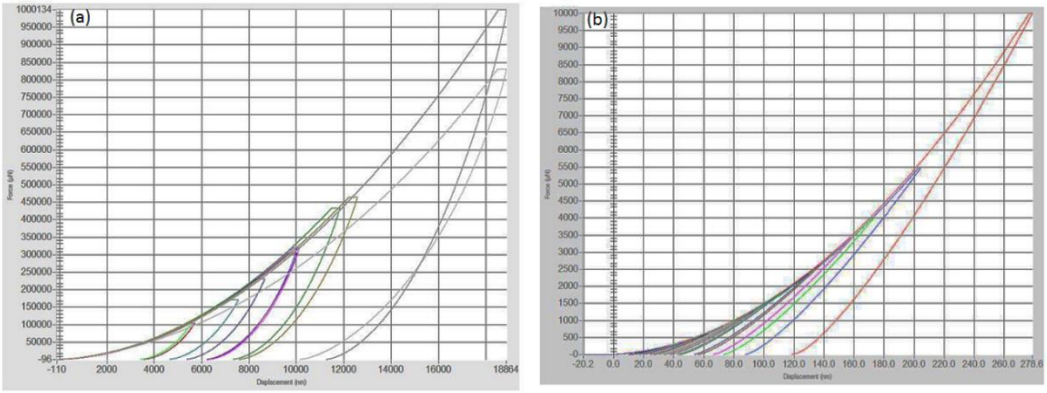

Figure 3.25 (a) representative load-indentation curves corresponding to a selection of 10 indentations on PC (b) reproducibility plot from indents performed in fused quartz.

The reduced modulus and hardness were calculated from force plots using equation 2.30 and equation 2.31 respectively and the values are shown in Table 3.10 and Table 3.11. This calculation is automatically done by the TriboScope® software. The reduced modulus results for the three polymer surfaces using low load and high load indenter are shown in Figure 3.26 and Figure 3.27 respectively.

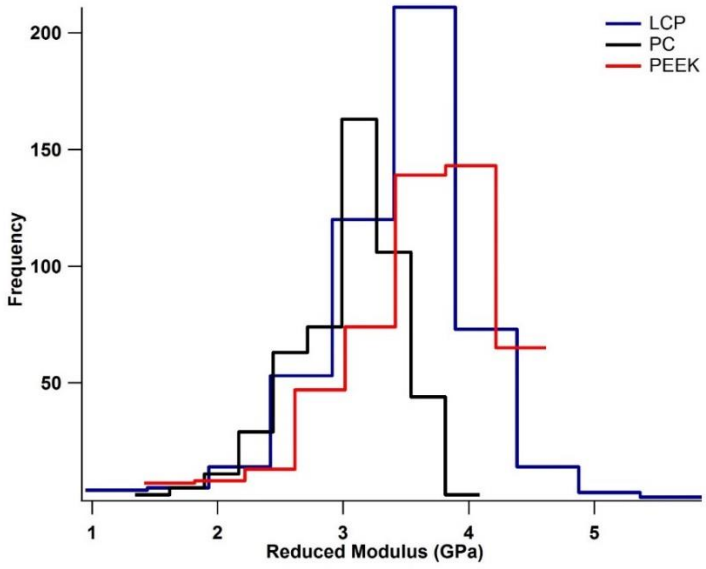

Figure 3.26 Histogram showing the distribution of all the low load indentations made for PEEK, LCP and PC for modulus (n= 500 for each polymer).

	Reduced Modulus(GPa)	Hardness (GPa)
PEEK	3.63±0.57	0.0469±0.015
LCP	3.46±0.59	0.0462±0.015
PC	3.03±0.43	0.0436±0.012

Table 3.10 Showing the nano-indentation results from the low load indenter (1mN to10mN) – mean ± st dev; (n=500 per polymer).

Low load indentation results showed highest modulus value of 3.63GPa for PEEK, while PC was the lowest at 3.03 GPa and for the high load LCP showed the highest modulus value of 5.12 GPa. To assess an overall picture of the each of the 500 indents made during low and high load, a distribution graph of modulus was plotted against applied load as shown in Figure 3.28. It is clearly evident that during low load indentation the modulus values for all three polymers were widely distributed in the range of 1-5 GPa. This was predominant in the case of LCP possibly because of the skin core effect (skin layer of the LCP is predominantly made of long fibrils) which is in agreement with the research carried out by *Kestenbatch and Rogausch* (2002) where they observed different molecular orientation at top skin region of injection moulded LCP. Other significant observation made from the high load distribution graph was that, as indented deeper into core region of LCP, it showed a linear distribution and higher modulus values. This is probably because as the indenter approaches the core part, where LCP mainly exists in spherical forms which gives more rigidity and hence giving good mechanical properties to the structure.

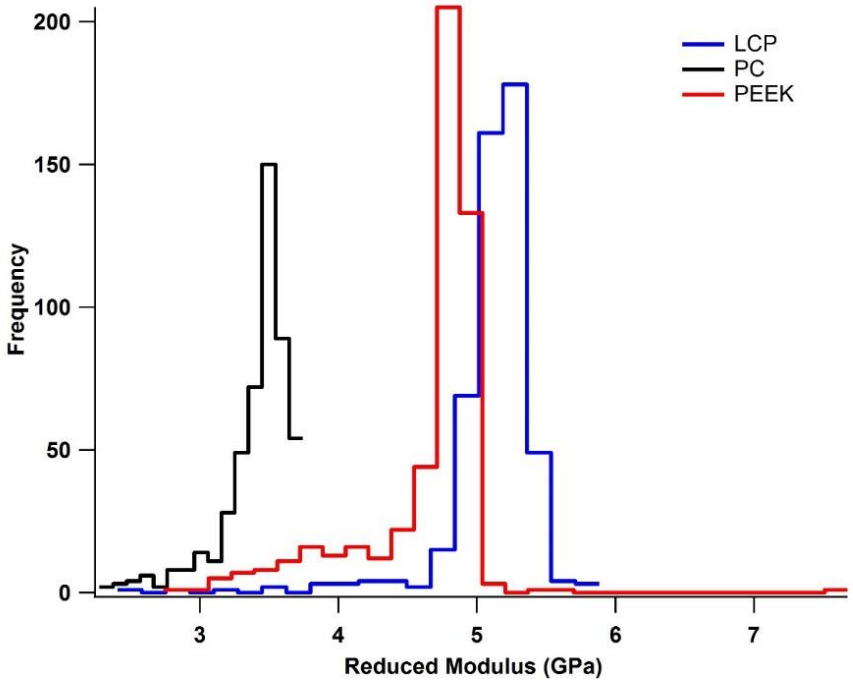

Figure 3.27 Histogram showing the distribution of all the high load indentations made for PEEK, LCP and PC for modulus (n= 500 for each polymer).

	Reduced Modulus(GPa)	Hardness (GPa)
PEEK	4.65±0.454	0.2709±0.0253
LCP	5.12±0.318	0.3422±0.0459
PC	3.41±0.249	0.1538±0.0084

Table 3.11 Nano-indentation results from the high load indenter (100mN to1N) – mean ± st dev; (n=500 per polymer).

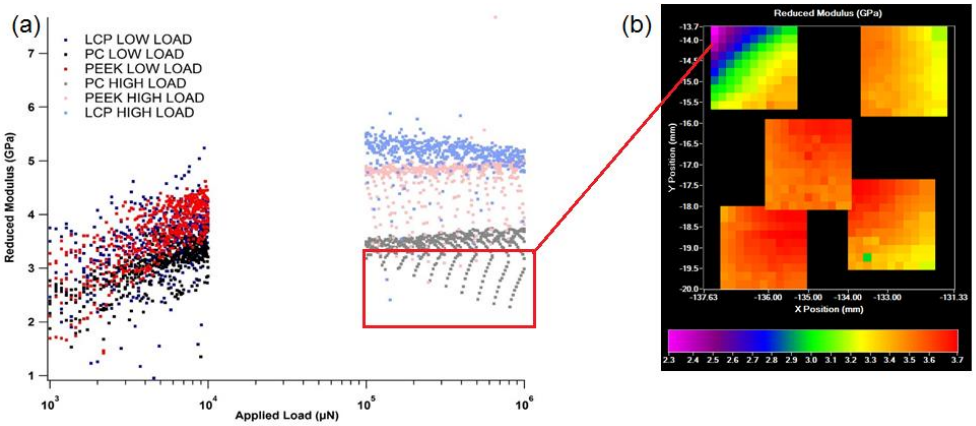

Figure 3.28 (a) distribution of modulus value for each indent vs applied load (low and high) (b) modulus mapping of the 100 indents made of 5 different locations on PC surface showing the edge effect.

The distribution of PEEK modulus value also follows a linear fit where maximum indents were in the range of 4.8-5 GPa. This was expected from PEEK as it is considered to be more resistant to penetration. This distribution also illustrates the harder nature of PEEK (semi crystalline) and LCP compared to amorphous PC. In the case of PC an unusual pattern of around 100 indents were observed with low modulus, this probably was due to edge effect (indents made of the edge of the PC surface) or may be due the sample not properly stuck to the sample holder. However, the remaining indents showed an average modulus value in the range of 3.2-3.5 GPa for PC.

3.2.4. Shot size optimisation

In the present study, the holding pressure option is selected as “Start Inj. Press. – Specific”, which means that the process is switched over to the packing stage when runner pressure reaches a specified pressure. The metering size is obtained by trial-and-error and initial trails (Figure 3.29) were performed for Lexan to study the filling patterns observed that process conditions like screw speed and back pressure was influencing the part filling and melt cushion as shown Figure 3.30 and 3.31. It was observed that at a combination of screw speed 20 mm/ sec and back pressure of 25 bar minimum melt cushion and full filling of part (part weight approx. 0.3 grams) was obtained and this setting (Table 3.12) was kept constant for rest of the experiments.

Parameters	Values
Shot Volume	3 mm
Screw Speed	20 mm/s

Back Pressure	25 bar
Clamping Force	120 kN
Cooling Time	10 secs

Table 3.12 Parameters obtained after shot size optimisation.

Figure 3.29 Parts produced during short shot optimisation (a) Lexan (b) PEEK.

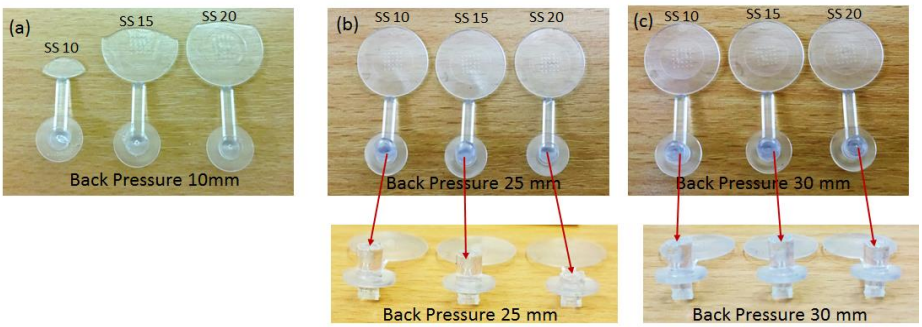

Figure 3.30 Parts produced with different back pressure.

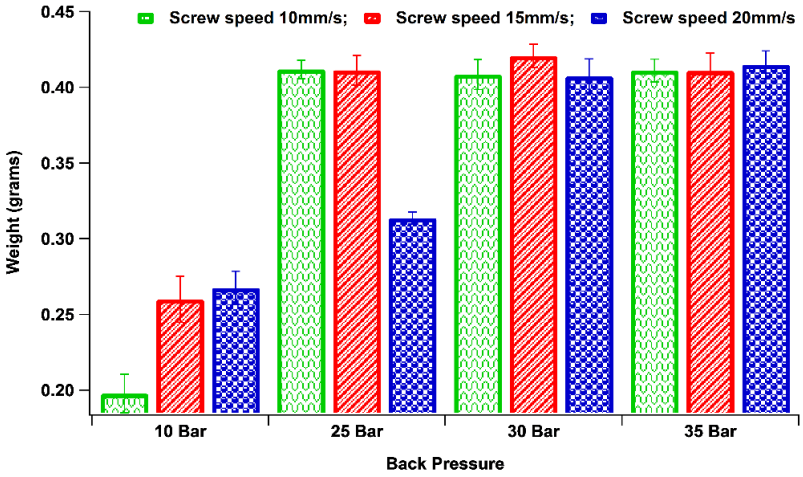

Figure 3.31 Weights of the parts produced with different combination of screw speed and back pressure.

3.2.5. Part weight analysis

Within each DO shot to shot variation was evaluated and observed that the weight of the parts produced from PEEK did not vary whereas in the case of Lexan there was significant variation between each DOE (Figure 3.32). This was because of the variation in melt cushion with each process settings for the DOE. Figure 3.33 (a) and (b) shows the variation of melt cushion for Lexan and PEEK respectively.

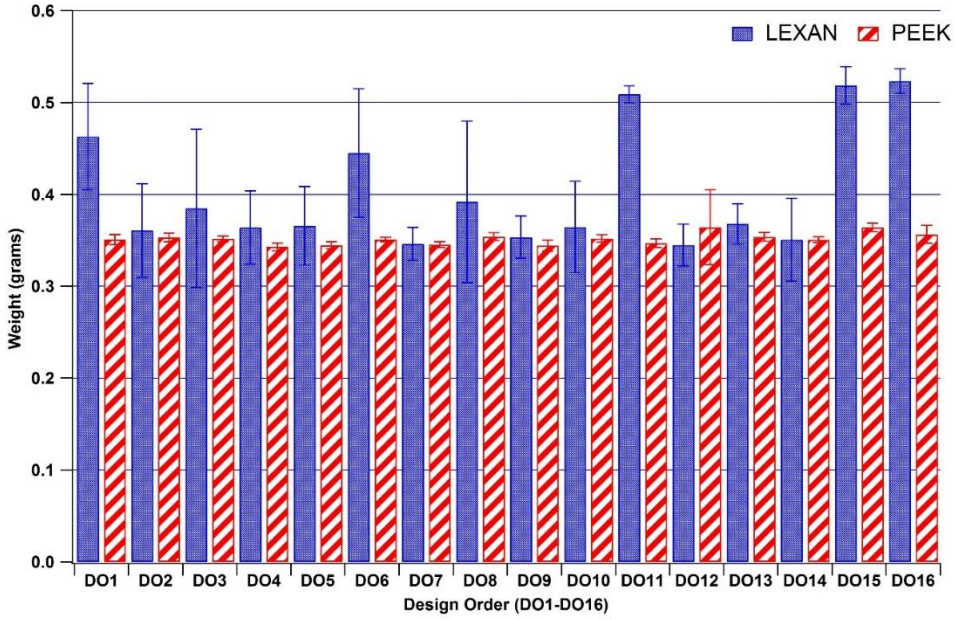

Figure 3.32 Weights of the parts obtained during each design order.

Figure 3.33 Photograph of the parts produced with different design order showing the variation in the melt cushion. (a) Lexan (b) PEEK.

3.2.6. Data acquisition

As micro-injection moulding is a relatively new technology, many researchers across the world are continuously conducting both theoretical and practical research to improve the quality of the miniature parts produced during the moulding process. The most important area is to develop a stable and optimised process monitoring method for identifying the process deviation and predicting the part quality.

Sometimes, poor mould design, un-optimised parameters or property of the material used for moulding may result in defects in the part produced (Zhang, 2004). In µIM process control, the mould cavity pressure is considered to be the most related to the final part quality than pressures measured at other locations. It provides direct indication of the condition of the polymer melt inside the mould cavity providing real time monitoring of each moulding cycle. So by obtaining the information from the cavity efficiently in conjunction with other machine

settings the fabrication process could be improved (Huang, 2002). Whiteside *et al* found that measuring cavity pressure is a better way of identifying part quality than injection pressure because cavity pressure is a direct measure of the changes of pressure within the cavity whereas injection pressure is the pressure value experienced by the injection piston.

With little research been conducted on behaviour of the cavity pressure curve in response to process variation a data acquisition suite was used to evaluate of injection piston dynamics, injection/cavity pressures and thermal properties of the tool platen. Figure 3.34 and 3.35 shows the cavity temperature results obtained from different design of experiments for Lexan and PEEK respectively. Variation in the temperature was because of the change in the mould and melt temperature. Measured melt temperature inside the cavity was 20-30ºC higher than the set mould temperature.

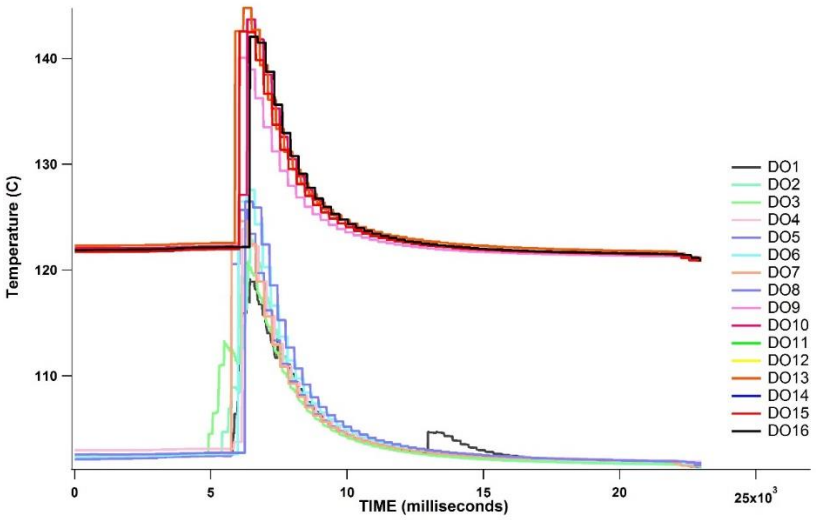

Figure 3.34 Graph showing the mould temperature measurements obtained using the data acquisition system for Lexan.

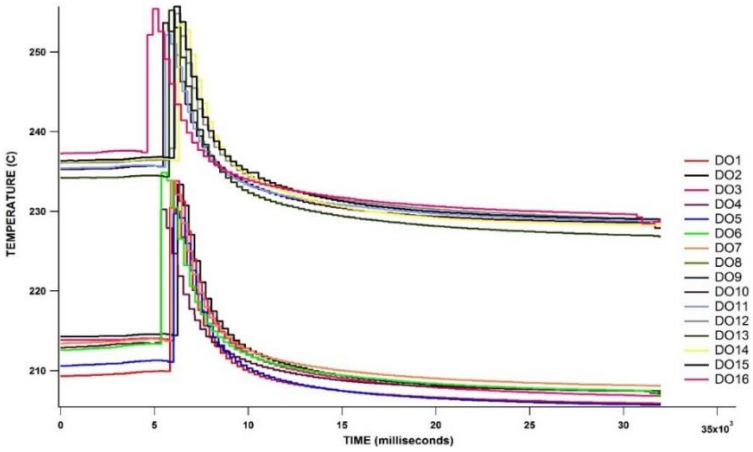

Figure 3.35 Graph showing the mould temperature measurements obtained using the data acquisition system for PEEK.

Figure 3.36 and 3.37 shows the cavity pressure results obtained from different design of experiments for Lexan and PEEK respectively. The results shows that with higher injection velocity and hold pressure a high cavity pressure was obtained. Difference in the measured cavity pressure between the DOE 1-16 is easily noticeable. With level 2 settings it was observed that the cavity pressure for Lexan to over 1100 bars and for PEEK it was over 1600 bars. The higher the cavity pressure better filling the polymer melts into cavities resulting in fully formed microneedles. The dimensional analysis parts produced with different DOE will be discussed in the later sections.

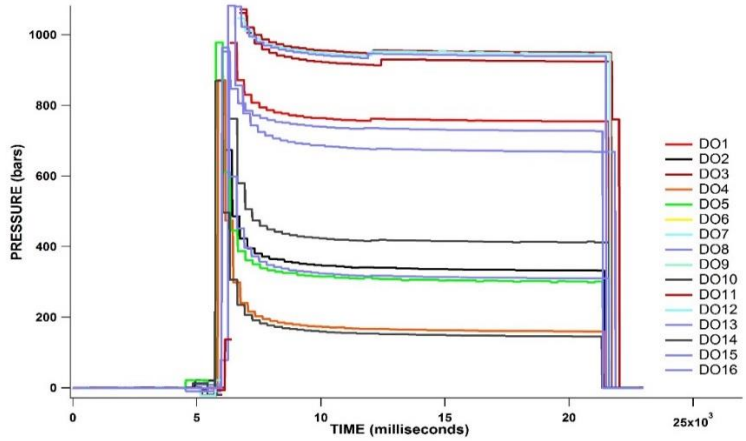

Figure 3.36 Graph showing the cavity pressure measurements obtained using the data acquisition system for Lexan.

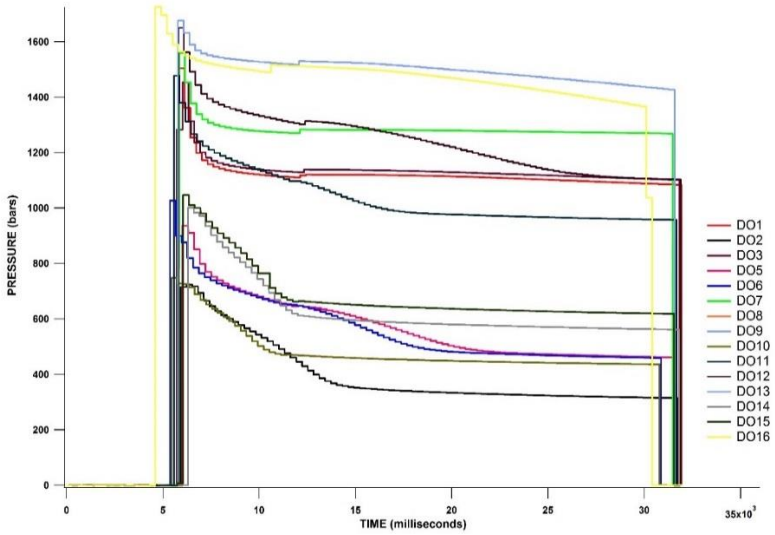

Figure 3.37 Graph showing the cavity pressure measurements obtained using the data acquisition system for PEEK.

In this study statistical experimentation was made to understand the effect of the independent variables or factors (A: injection speed B: melt temperature C: mould temperature D: hold pressure) on dependent variables or responses (part weight, cavity pressure and cavity temperature) at low and high level (represented by -1 and 1) of the process and a relation between them was calculated using a regression analysis. A response surface methodology (RSM) was used to find out the most significant parameter or combination of interaction which leads to the better microneedles. Analysis of Variance (ANOVA) was performed for Lexan and PEEK MNs and the significant factors that affect the response were calculated. Table 3.13 shows the experimental design matrix and results. Table 3.14 shows the ANOVA results for Lexan and it was very clear that from the coefficient of the R^2 value responses are insignificant. When R^2 values are high, close to 1, the better response model fits the actual data.

The R^2 values calculated in the table 3.14 for Lexan are less than 0.8 which is unacceptable.

	Factors				Interactions						PEEK			Lexan		
DO	X1	X2	X3	X4	X1X2	X1X3	X2X3	X1X4	X2X4	X3X4	TEMP	PRESSURE	WEIGHT	TEMP	PRESSURE	WEIGHT
1	-1	-1	-1	1	1	1	1	-1	-1	-1	230.48	1504.40	0.3508	119.10	977.26	0.46
2	1	-1	-1	-1	-1	-1	1	-1	1	1	233.37	722.83	0.3531	122.86	672.66	0.36
3	1	-1	-1	1	-1	-1	1	1	-1	-1	233.81	1453.20	0.3518	120.67	1061.59	0.39
4	-1	-1	-1	-1	1	1	1	1	1	1	230.24	638.33	0.343	123.88	871.68	0.36
5	-1	1	-1	-1	-1	1	-1	1	-1	1	229.7	936.22	0.3447	125.68	977.65	0.37
6	1	1	-1	-1	1	-1	-1	-1	-1	1	234.83	1027.02	0.351	127.56	962.96	0.45
7	-1	1	-1	1	-1	1	-1	-1	1	-1	233.88	1560.25	0.3453	124.64	951.89	0.35
8	1	1	-1	1	1	-1	-1	1	1	-1	254.81	1650.18	0.354	126.45	1082.20	0.39
9	-1	-1	1	-1	1	-1	-1	1	1	-1	253.34	1001.34	0.3443	140.06	868.74	0.35
10	1	-1	1	-1	-1	1	-1	-1	1	-1	253.65	747.18	0.352	143.69	761.66	0.36
11	-1	-1	1	1	1	-1	-1	-1	-1	1	252.17	1477.11	0.3468	142.06	1071.99	0.51
12	1	-1	1	1	-1	1	-1	1	-1	1	254.81	1650.18	0.3643	142.57	1046.79	0.34
13	1	1	1	1	1	1	1	1	1	1	255.24	1675.80	0.3536	144.77	1079.61	0.37
14	-1	1	1	-1	-1	-1	1	1	-1	-1	253.34	1001.34	0.3506	142.57	744.07	0.35
15	1	1	1	-1	1	1	1	-1	-1	-1	255.71	1046.49	0.3642	122.18	1035.65	0.52
16	-1	1	1	1	-1	-1	1	-1	1	1	255.38	1725.72	0.3565	123.45	1022.56	0.52

Table 3.13 Experimental design matrix and results (peak cavity pressure and temperature measured with average part weight) for PEEK and Lexan.

(a) ANNOVA for Lexan Temperature							
	df	SS	MS	F	Sig F	R^2	Pass/Fail
Regression	10	1087.54	108.75	1.6162	0.31033	0.76373	Fail
Residual	5	336.75	67.26				
Total	15	1423.25					

(b) ANNOVA for Lexan Pressure							
	df	SS	MS	F	Sig F	R^2	Pass/Fail
Regression	10	209399.73	20939.97	2.41	0.17	0.82837	Fail
Residual	5	43386.35	8677.27				
Total	15	252786.09					

(c) ANNOVA for Lexan Weight							
	df	SS	MS	F	Sig F	R^2	Pass/Fail
Regression	10	0.000454	4.54E-05	1.61	0.31	0.76273	Fail
Residual	5	0.000141	2.83E-05				
Total	15	0.000596					

df: degree of freedom, SS: Sum of squares, MS: Mean Square

Table 3.14 ANOVA results for Lexan (a) temperature (b) pressure (c) part weight.

(a) ANNOVA for PEEK Response Temperature							
	df	SS	MS	F	Sig F	R^2	Pass/Fail
Regression	2	1542.73	771.36	25.65	3.07E05	0.9563	Pass
Residual	13	391.01	30.08				
Total	15	1933.74					

(b) ANNOVA for PEEK Response Pressure							
	df	SS	MS	F	Sig F	R^2	Pass/Fail
Regression	3	2114169.69	704723.3	101.11	8.76E09	0.9619	Pass
Residual	12	83634.99	6969.58				
Total	15	2197804.69					

Table 3.15 ANOVA results for PEEK (a) temperature (b) pressure.

Table 3.15 shows the shows the ANOVA results for PEEK and it was very clear that from the coefficient of the R^2 value responses are significant. Table 3.16 shows the significant factors of PEEK (main and interaction factors) for the responses from the ANOVA analysis by selecting the backward elimination procedure where the factors with *p* value greater than 0.05 was deleted.

Response	Main factors and p value	Interaction factors
PEEK Temperature	Injection speed (A) *(p=0.0001)* and Mould temperature (C) *(p=0.033)*	None
PEEK Pressure	Mould temperature (C) *(p=0.0001)*	Melt temperature (B) *(p=0.02)* & Hold pressure(D) *(p=0.00001)*

Table 3.16 Significant factors effect for the responses for PEEK.

Considering the most significant terms and after the backward elimination a mathematical predicted model (equation in terms of actual factor) for cavity temperature and cavity pressure of PEEK was obtained.

$$\hat{Y} \text{ (cavity temperature)} = 244.67 + 2.356A + 9.533C \quad (3.3)$$

$$\hat{Y} \text{ (cavity pressure)} = 123.599 + 89.278B + 52.046C + 348.51D \quad (3.4)$$

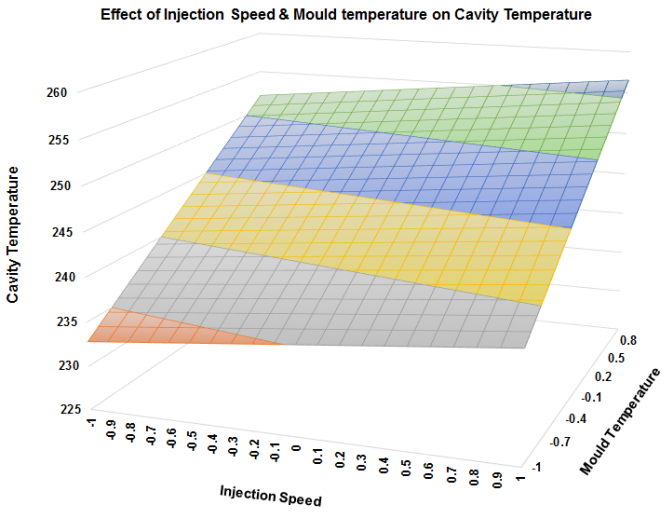

Figure 3.38 3D surface response graph for PEEK cavity temperature.

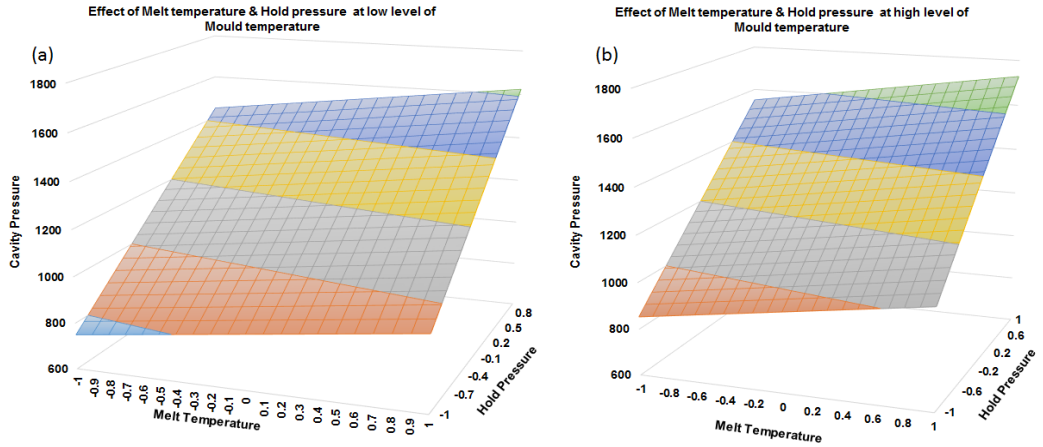

Figure 3.39 3D surface response graph B&D interaction for PEEK cavity pressure (a) at low level (b) at high level of mould temperature.

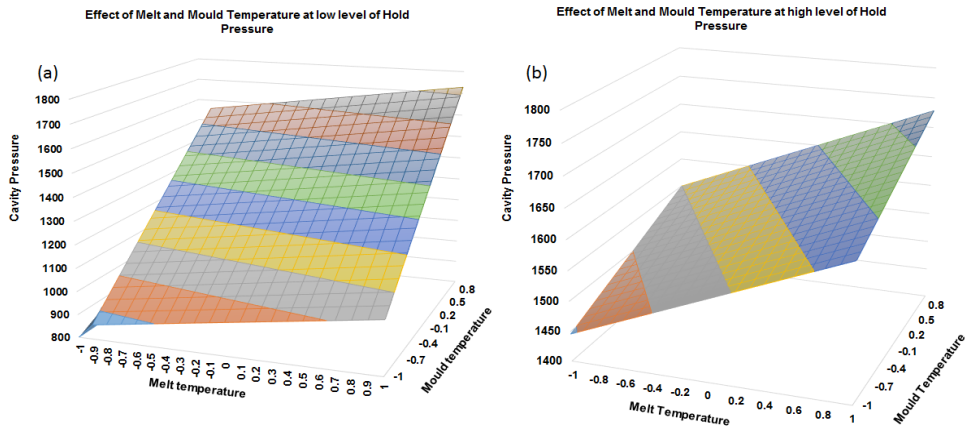

Figure 3.40 3D surface response graph B&C interaction for PEEK cavity pressure (a) at low level (b) at high level of hold pressure.

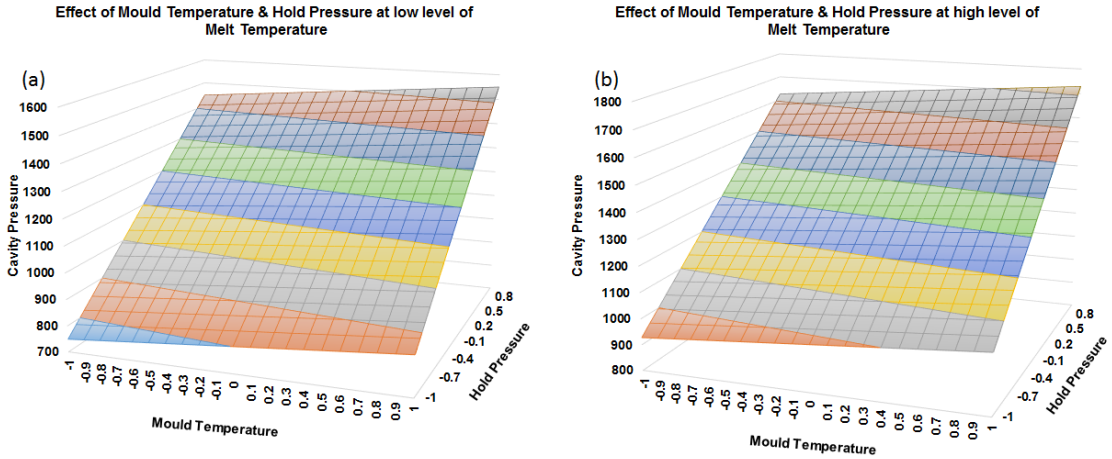

Figure 3.41 3D surface response graph C&D interaction for PEEK cavity pressure (a) at low level (b) at high level of melt temperature.

Figure 3.38 shows the factor effect of injection speed and mould temperature on cavity pressure response during moulding of PEEK microneedles. From the response graph it is evident that at higher level of mould temperature maximum cavity temperature was recorded. Figure 3.39 shows the effect of cavity pressure with various interactions of melt temperature and hold pressure at low and high level of mould temperature. Figure 3.40 shows the effect of cavity pressure with various interactions of melt temperature and mould temperature at low and high level of hold pressure, while Figure 3.41 shows the effect of cavity pressure with various interactions of mould temperature and hold pressure at low and high level of melt temperature. From these surface response graphs, by observing the gradient of each factors it is evident that the most significant factor that effects the cavity pressure is melt temperature and hold pressure. So from these interpretations, higher level of melt temperature and hold pressure was used to manufacture microneedles.

3.2.7. Microneedle dimensional analysis

Many established methods exist for creating MN cavity features like EDM, micro-milling, focused Ion beam and lithography. Electro-discharge machining is one of the most widely used tooling methods to generate deep and three-dimensional complex micro-features into the insert. EDM uses an electrode in the shape of the desired part made from carbon or copper to electrically vaporise (also called as spark erosion) the insert material and to create the micro features. But there are several concerns (Bigot *et al*., 2006) while using EDM that should be taken into account

1. The electrode would erode too quickly and needs replacement and if not replaced the resultant features made on the insert will not achieve the desired dimensions.
2. The resultant surface finish depends on pulse duration and voltage used during EDM process.
3. The rate at which the erosion takes place and effects on the tool steel.

Therefore it is off paramount importance that we validate the 3D-MN geometries produced on the insert obtained after EDM process. It is a challenging job to find a suitable measuring instrument for the characterisation of the insert. Contact measurements and optical measurement techniques can't be utilised due to the high surface slopes and poor reflectivity. Optical measurements of the MNs produced using these inserts was performed and as shown in the Figure 3.42 and it is very difficult to accurately measure the MN dimensions.

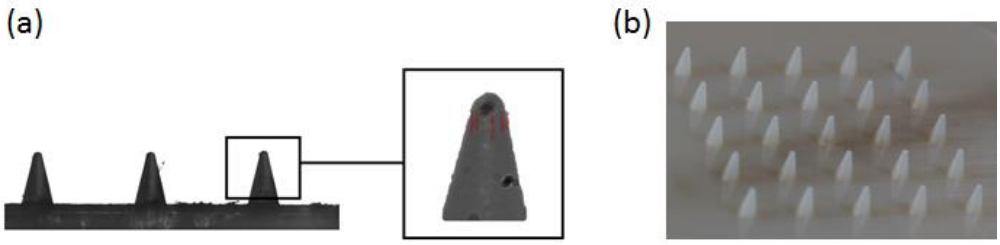

Figure 3.42 (a) optical microscopic image of the microneedles (b) macro photograph of the MN array.

Laser scan profilometers are generally used to validate the dimensions of the features in the insert, however a detailed and accurate characterisation of deep 3D micro cavities produced by EDM still poses a great challenge in terms of tooling validation.

A SEM image (Figure 3.43a) of the insert showing the all 5 x 5 arrays and single needle is shown in the Figure 3.43b, but it is very difficult to measure the exact dimensions of the shaft and tip. So the way to overcome these challenges is to reproduce the MNs using a PDMS casting method. This non-destructive techniques is extensively used for characterisation of micro-structured inserts and also to find out the surface finish of the insert. PDMS has no slimes and low shrinkage <0.1% (Jurischka *et al*., 2007) and an exact replicated model of the feature in PDMS could be obtained.

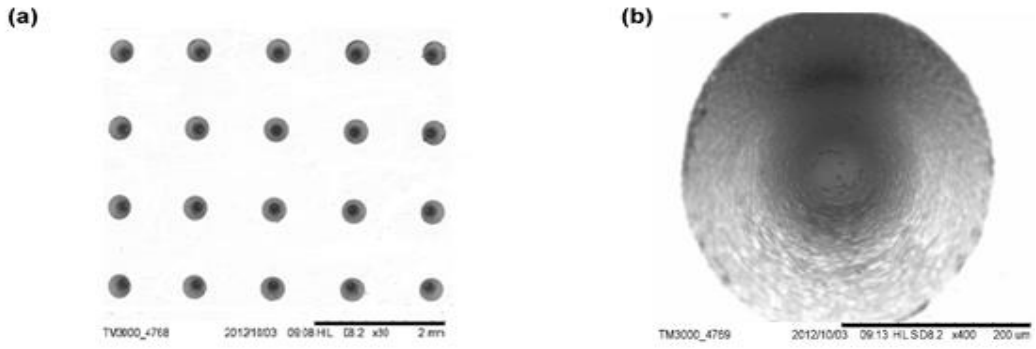

Figure 3.43 (a) SEM image of the MN insert (b) magnified SEM image of the single MN cavity in the insert showing the EDM machine surface finish and tip of the cavity.

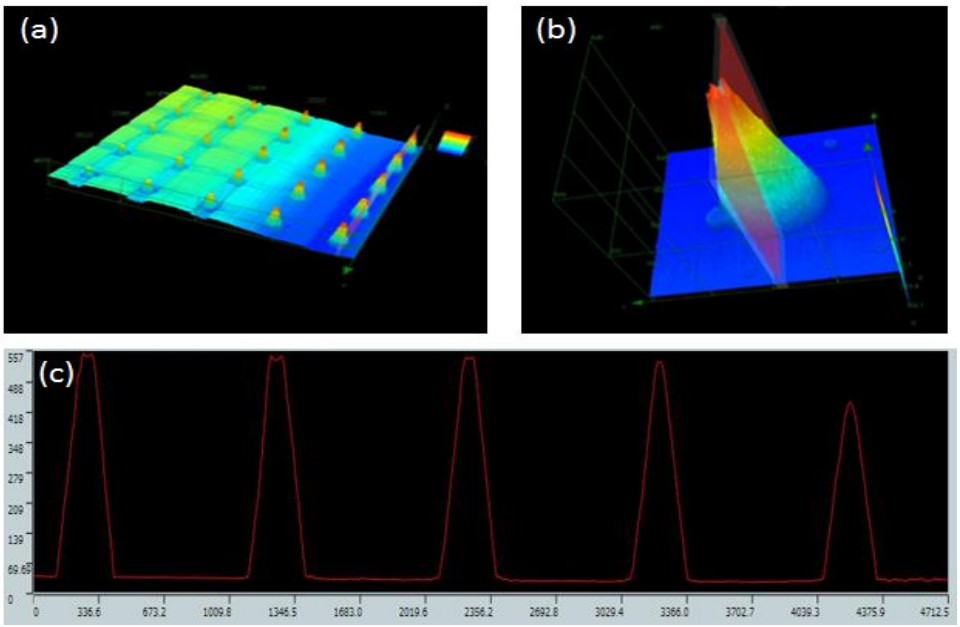

Figure 3.44 3D confocal image of the casted PDMS MNs (a) full 5x5 array (b) single needle (c) line measurement of the needle array.

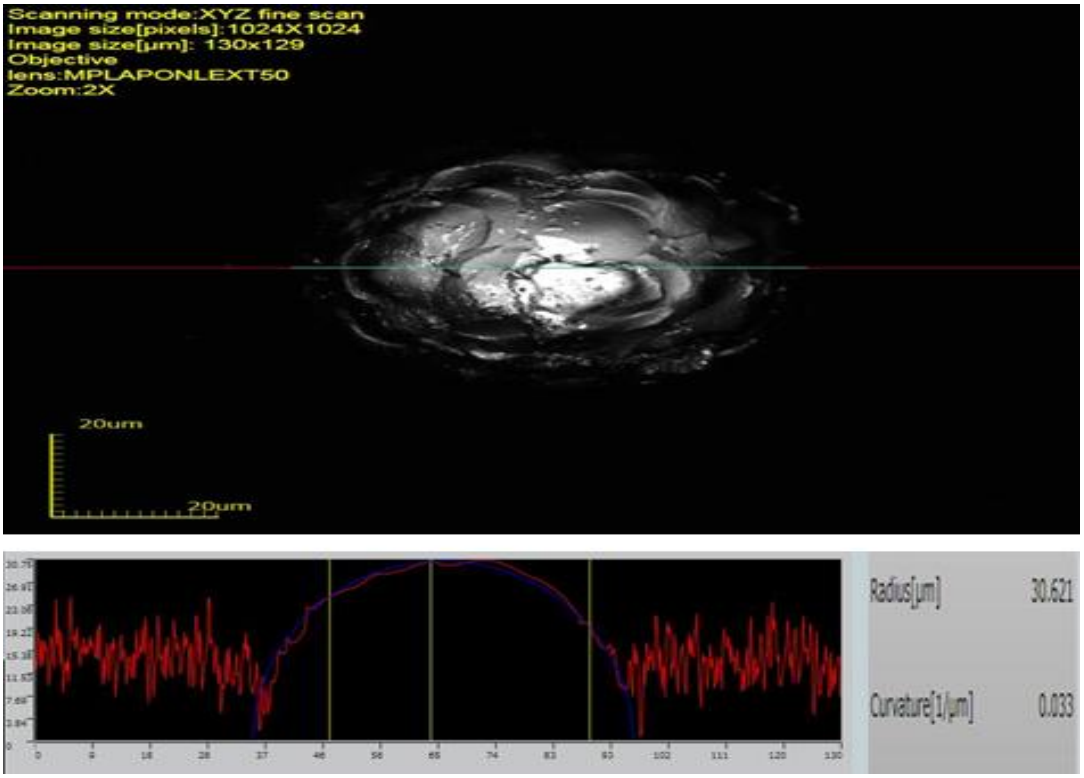

Figure 3.45 3D confocal image of the casted PDMS MNs showing the tip radius and EDM machine marking.

Heights of the PDMS casted MNs were measured using a confocal laser microscope (Figure 3.44). The height of the needles were found to be 556 ± 20 µm and tip radius 32 ± 8 µm . Confocal images (Figure 3.45) and SEM images (Figure 3.46) of the tip of the needles shows surface textures consistent with replication of EDM machined surfaces, indicating complete filling of the cavity. An AFM scan of the tip of the PDMS MN (Figure 3. 47) was also performed to confirm the tip radius obtained from confocal measurements. It was found that the tip radius was 31.62 µm and this confirms that the MN cavities manufactured by EDM is limited to a tip radius of approximately 32 µm.

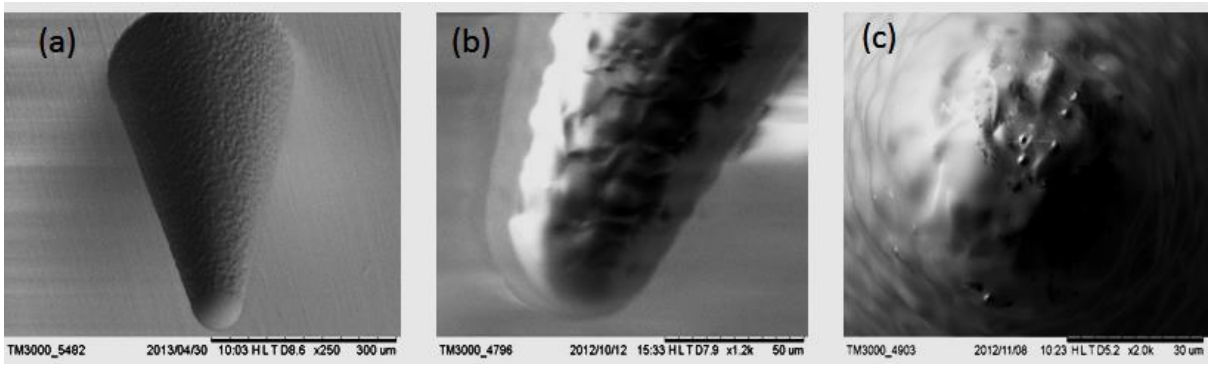

Figure 3.46 SEM image of the PDMS MNs (a) single needle 250X (b) single needle 1200x (c) single needle 2000x showing the EDM machine marking confirming the complete cavity filling.

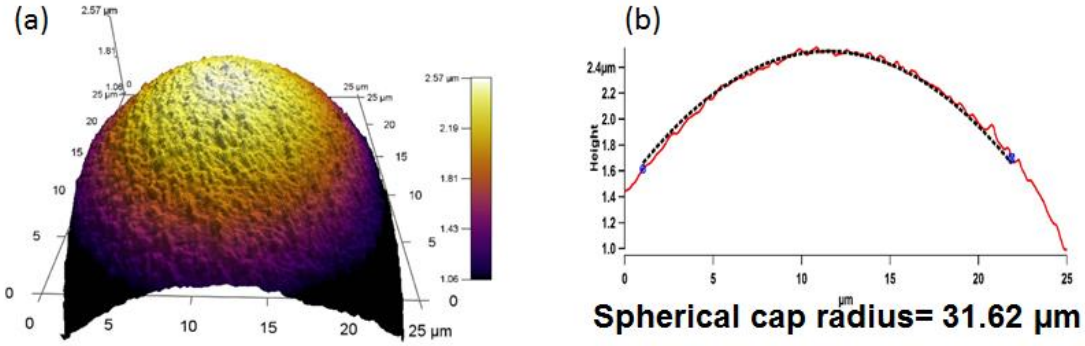

Figure 3.47 (a) AFM image of the PDMS MN tip (b) line graph showing the spherical cap radius of the needle

The following results focuses on the relationship between low, intermediate and high level process settings used during the DOE namely Design order 4, 2 and 13. In terms of part quality although weight is used as the quality indicator, a visual inspection can also be done to detect some obvious defects but as the features in the parts are micro in dimensions a confocal image analysis was carried out.

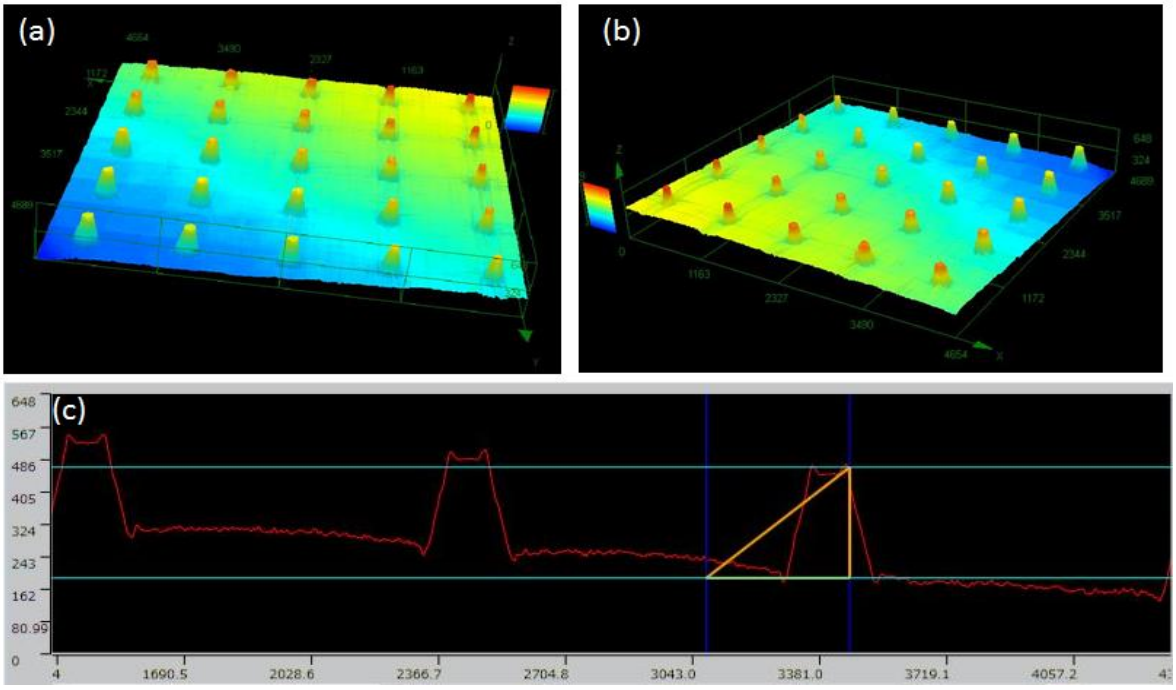

Figure 3.48 3D confocal image of Low level (DO-4) (a) front view of the PEEK MN array (b) side view of the PEEK MN array (c) line measurement of the needle array.

As shown in Figure 3.48 with the design order 4 the MNs produced are not completely formed. This is because during the DO-4 the injection speed and holding pressure was kept very low resulting in cavity pressure below 800 bars. The finest MNs were obtained from DO-13 but significant differences in MNs produced using DO-2 (Figure 3.49) and DO-13 (Figure 3.50) were not observed. A detailed graph showing the dimensions of the MNs manufactured using DO-4, 2 and 13 for Lexan and PEEK is shown in Figure 3.51.

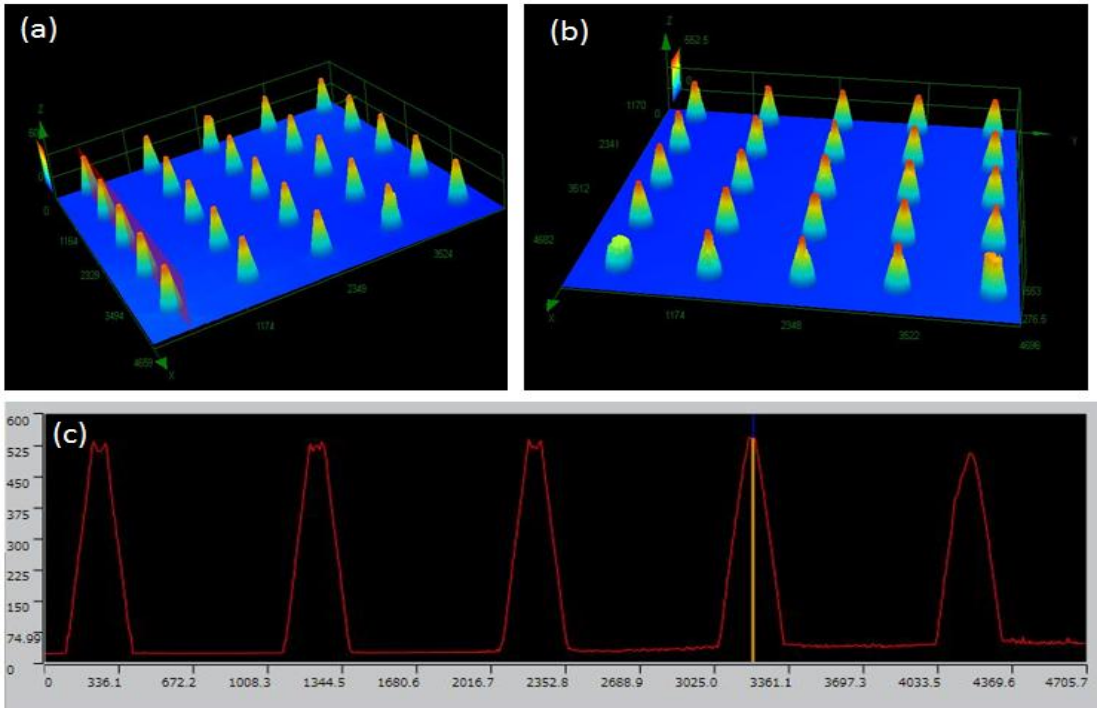

Figure 3.49 3D confocal image of Intermediate level (DO-2) (a) front view of the PEEK MN array (b) side view of the PEEK MN array (c) line measurement of the needle array.

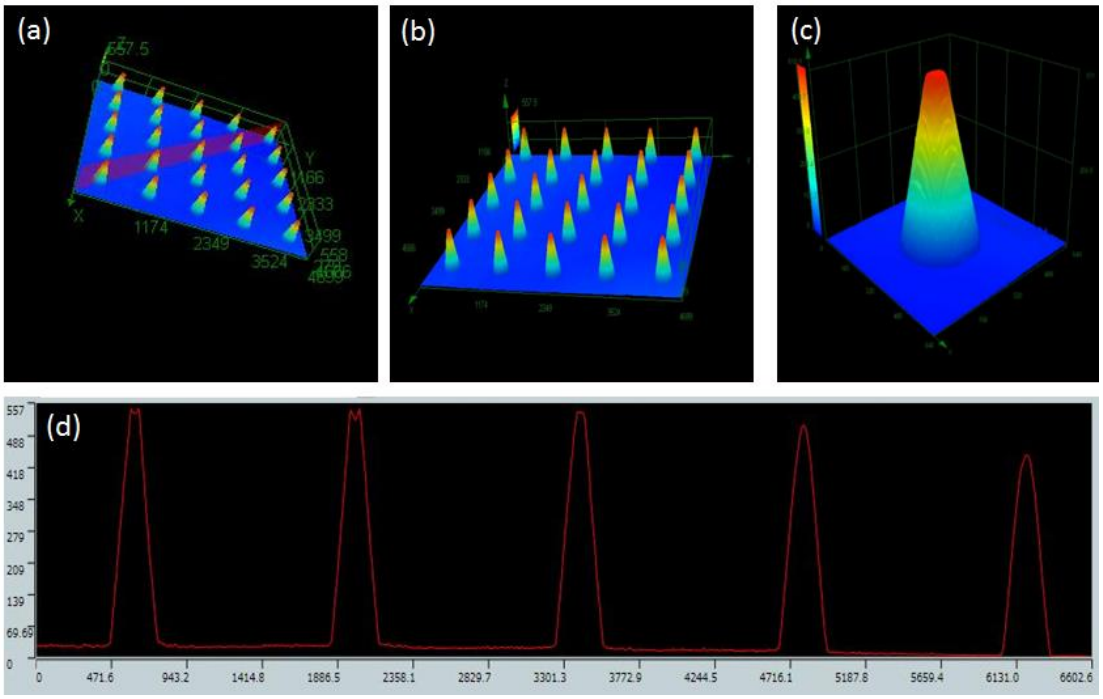

Figure 3.50 3D confocal image of High level (DO-13) (a) front view of the PEEK MN array (b) side view of the PEEK MN array (c) Single MN of PEEK (d) line measurement of the needle array.

These measurements suggests that the injection pressure along with the pack/hold pressure is the most important input parameter for getting sharp and fully formed MNs.

During the pack/hold stage extra polymer melt is fed into the mould cavity to compensate for shrinkage occurred during cooling. In micro-injection moulding the cooling cycle is short and the post filling stage requires a longer time, so understanding the cavity pressure during this post filling stage is very crucial.

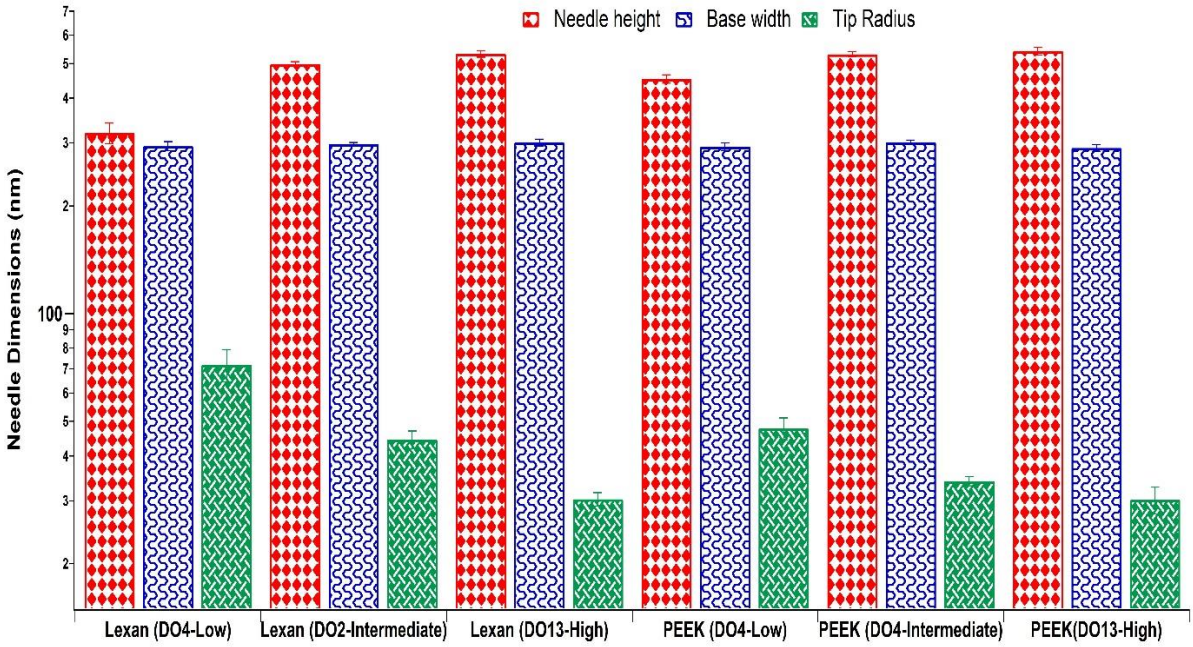

Figure 3.51 A bar graph showing the average needle height, base width and tip radius for Lexan and PEEK at D0-4(Low level) DO-2 (Intermediate level) DO-13 (high level).

From the images obtained from each design order it is very clear that with higher packing pressure and higher injection speed there was higher cavity pressure and hence better quality MNs were obtained.

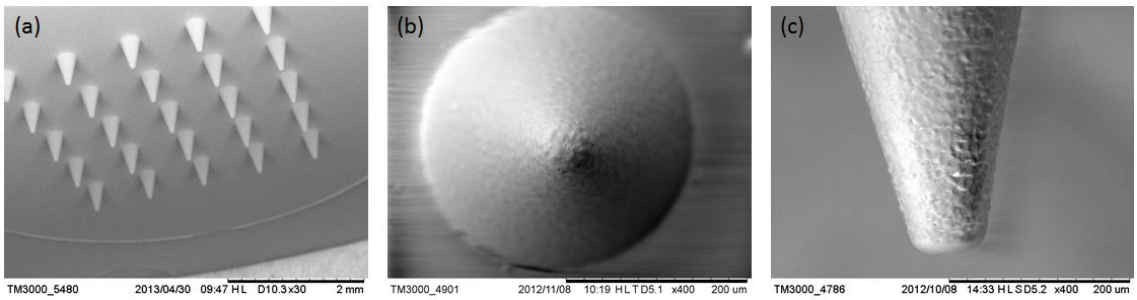

Figure 3.52 SEM image of High level (DO-13) (a) MN array of PEEK (b) top view of the needle (c) Single MN of PEEK.

It was also observed that the cavity pressure increases with increase in melt temperature because it increases the specific volume and decreases the viscosity of the polymer melt, hence increasing the fluidity of the polymer to enter into the microneedle cavities. These results are very well illustrated using the SEM image (Figure 3.52) showing the fully formed MNs at DO-13. From this experiment it is evident that MN geometry is affected by machine parameters and process conditions. Incorrect process parameters lead to decreased dimensional precision within MNs. From optimisation of all the earlier mentioned parameters like packing pressure, injection speed and cavity pressure it was found that design order 13 is the most suitable processing condition to obtain good quality MNs. Figure 3.53 shows the dimensional measurements of MNs manufactured using three different grades of polycarbonate and PEEK using DO-13.

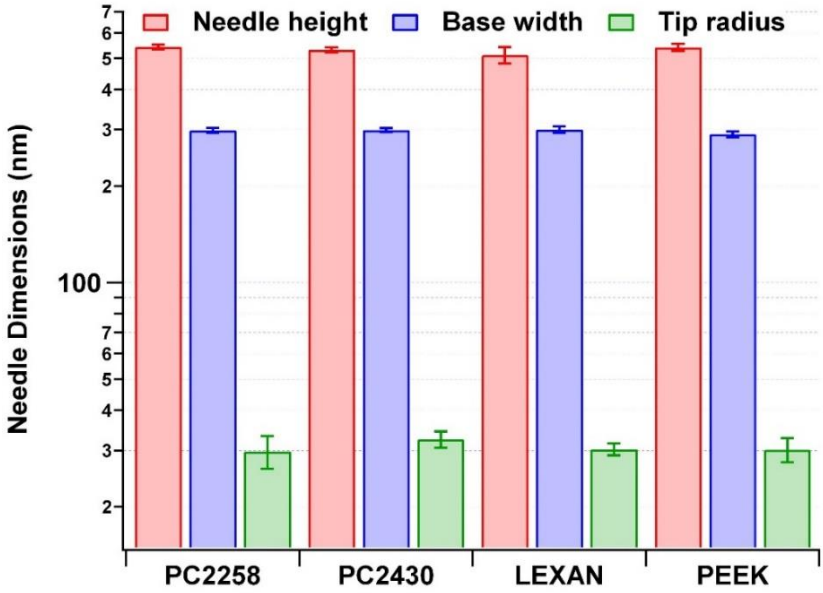

Figure 3.53 Bar graph showing the average needle height, base width and tip radius for all the polymers at DO-13 (high level).

3.3. Conclusions

In this work polymer melt rheology was measured under typical injection moulding conditions. The use of a conventional injection moulding machine for rheology purposes provided the establishment of viscosity curves of various grades of polycarbonate and PEEK at pressures higher than the ones obtained from rotational and capillary rheometers. All the polymers studied showed pseudo-plastic shear thinning behaviour and a dependence upon melt temperature. It was found that minimum viscosities were observed at 320^{o}C for polycarbonate grades and 420^{o}C for PEEK suggesting higher degree of the polymer filling into the microneedle cavities will be obtained at these temperatures.

Simulation of polymer filling into MN cavities were carried out using Moldflow software. Injection speed and melt temperature were the two different influencing moulding parameters used for simulation. It was evident that the

filling was achievable using the present MN cavity design with low injection speed and melt temperature but filling time could be decreased with higher injection speed. The simulation results also showed the necessity of vacuum venting and these information was further used while designing the microneedle tool and selecting the parameters for the design of experiments. With the feedback from the high shear rheology and simulation data injection, the mould and MN insert were manufactured.

Microneedle cavities were produced using an EDM process and these cavities were subsequently validated using a non-destructive PDMS casting method and found out that the maximum needle height and tip radius of MNs that could be achieved using this insert is 556 µm and 32.16 µm respectively. This work also presents the results of full factorial design of experiments to evaluate the influence of injection moulding process conditions upon the dimensional properties of resultant MNs. A data capture system capable of accurately measuring cavity temperature and pressure at high sampling rates has been presented along with the resulting experimental data suggesting that with higher cavity pressure produced better quality MNs. To accurately evaluate the dimensions of the high aspect ratio and complex geometry of MNs, techniques like SEM, AFM and confocal laser microscope were used to measure tip radius, base width and needle height from each design of experiments and the results suggests that the best MN geometry was obtained from higher hold pressure and melt temperature (design order-13).

3.4. References

1. Aho J, Moberg L, Syrjala S and Jarvela P. Injection moulding machine with height-adjustable slit die for rheological measurements of polymer melts under processing conditions. *Annual transactions of the rheology society* **19** (2011).

2. Bigot S, Valentincic J, Blatnik O and Junkar M. Micro EDM parameters optimisation, *Proceedings of the 2nd International Conference on Multi-Material Micro Manufacture 4M* (2006).

3. Briscoe BJ, Sebastian KS and Adams MJ. The effect of indenter geometry on the elastic response to indentation. *Journal of Physics D - Applied Physics*. **27** (1994) 1156-1162.

4. Chu J, Kamal MR, Derdouri A and Hrymak AN. Effects of Processing Conditions on Mechanical Properties and Crystallinity of Micro Injection Moulded Thermoplastics. ANTEC (2008) Milwaukee.

5. Chu J. Characterization of the Micro Injection Moulding Process and Its Products, A thesis submitted to the Faculty of Graduate Studies McGill University, (2009).

6. Cheng L, Xia X, Yu W, Scriven LE and Gerberich W. *J. Polym. Sci.Part B: Poly. Phys.* **38**(2000) 10-17.

7. Debra D, Charlesworth W, Miller DM, Miskioglu I and King JA. Nanoindentation of injection moulded PLA and self-reinforced composite PLA after *in vitro* conditioning for three months. *Journal of Biomedical Materials Research Part A* **74** (2005).

8. Hassan H. An experimental work on the effect of injection moulding parameters on the cavity pressure and product weight *Int J Adv Manuf Technol* **67**(2013) 675-686.

9. Huang HT and Cheng SC. Study of injection moulding pressure sensor with low cost and small probe. *Sensors and Actuators A* **101** (2002) 269–274.

10. Hodzic A, Kalyanasundaram S, Kim JK, Lowe AE and Stachurski ZH. Application of nano-indentation, nano-scratch and single fibre tests in investigation of interphases in composite materials. *Micron* **32** (2001) 765-775.

11. Jurischka R, Schoth A, Muller C, Baggi C, Gallera R and Reinecke H. Rapid Hybrid Tooling based on CNC- and µEDM-milling to fabricate Lab-on-a-Chip Systems. *Proceedings of the 3rd International Conference on Multi-Material Micro Manufacture*, 4M (2007).

12. Jeng M.C. Chen SC and Minh PS. Rapid mould temperature control in injection moulding by using steam heating. *International Communications in Heat and Mass Transfer* **37** (2010) 1295–1304.

13. Kelly A, Paradkar A, Coates P and York P**.** Shear and extensional rheology of hydroxypropyl cellulose melt using capillary Rheometry. *Journal of Pharmaceutical and Biomedical Analysis* **49** (2009) 304-310.

14. Kestenbach HJ and Rogausch KD. Molecular orientation of individual LCP particles in injection-moulded PPS/LCP blends. *Materials Research* **6** (2002) 75-83

15. Moon JS and Lee JM. Shear viscosity measurement of highly filled polycarbonate melts using a slit-die rheometer. *Rheology Journal* **25** (2013) 129-135

16. Menges G, Michaeli W and Mohren P. *How to make injection moulds*, Hanser Publishers, (2000).

17. Pirskanen J, Immonen J, Kalima V, Pietarinen J, Siitonen S, Kuittinen M, Monkkonen K, Pakkanen T, Suvanto, M and Paakkonen EJ. Replication of sub-micrometre features using microsystems technology. *Plastics, Rubber and Composites* **34** (2005) 222-226.

18. Oliver WC and Pharr GM. An improved technique for determining hardness and elastic modulus using load and displacement sensing indentation experiments. *J Mater Res* **7**(1992) 1564-83

19. Piotter V. Micro-injection moulding for the manufacturing of medical devices, Medical *device manufacturing & technology* (2006) 23-27.

20. Rannar LE. On Optimization of Injection Moulding Cooling Thesis submitted to Norwegian University of Science and Technology Faculty of Engineering Science and Technology **113** (2008).

21. Sha B, Dimov S, Griffiths C, and Packianather M.S. Investigation of micro injection moulding: Factors affecting the replication quality. Journal of Materials Processing Technology (2007) **183** 284-296.

22. Su YC, Shah J and Lin L. Implementation and analysis of polymeric microstructure replication by micro injection moulding. *Journal of Micromechanics and Micro engineering* **14** (2004) 415.

23. Shen YK and Wu WY. An analysis of the three-dimensional micro-injection moulding. *International Communications in Heat and Mass Transfer* **29** (2002) 423.

24. Shek KT and Lam DC. Insertion behaviour of microneedles for drug delivery *Advanced Materials Research* **50** (2008) 1442-1445.

25. Steglich D, Lacan F, Dessors S, Eigenbrod H, Moguedet M and Bambury E. Optimising the replication quality of polymer injection-moulded microneedles on the IMPRESS platform (2012)

26. Stachurski ZH and Kim JK. Nano-indentation of polymer–glass interfaces Part I. Experimental and mechanical analysis. *Polymer* **41** (2000) 6895-6905.

27. Vasco JC, Maia JM, and Pouzada AS. Thermo-rheological behaviour of polymer melts in microinjection moulding. *J. Micromech. Microeng* **19** (2009) 105-112.

28. VanLandingham MR, Villarrubia JS, Guthrie WF, Meyers GF. *Macromol.Symp.* **15** (2001) 167-170.

29. Whiteside BR, Brown EC, Ono Y, Jen CK and Coates PD. Polymer degradation and filling incompletion monitoring for micromoulding using ultrasound. *Society of Plastics Engineers* (2005) 200-204, United States.

30. Xue L, Zhou G, Zhang Y, Zhuang J, and Wu D. Micro injection Moulding and Strength Check of Polymer Micro-needle. *Advanced Materials Research*, (2013) 3136-3140.

31. Zhang L and Theurer BC. A Self-Energized Sensor for Wireless Injection Mould Cavity Pressure Measurement: Design and Evaluation. *Journal of dynamic systems, measurement, and control* **126** (2004).

32. Zhao J, Mayes RH, Chen G, Xie H and Chan PS. Effects of Process Parameters on the Micro Moulding Process. Polymer Engineering and Science **43** (2003) 1542.

33. Zhang N and Gilchrist MD. Characterization of thermo-rheological behaviour of polymer melts during the micro injection moulding process. *Polymer Testing* **31** (2012) 748–758.

Chapter 4 Influence of surface modification of polymer surfaces and protein adsorption

Graphical abstract

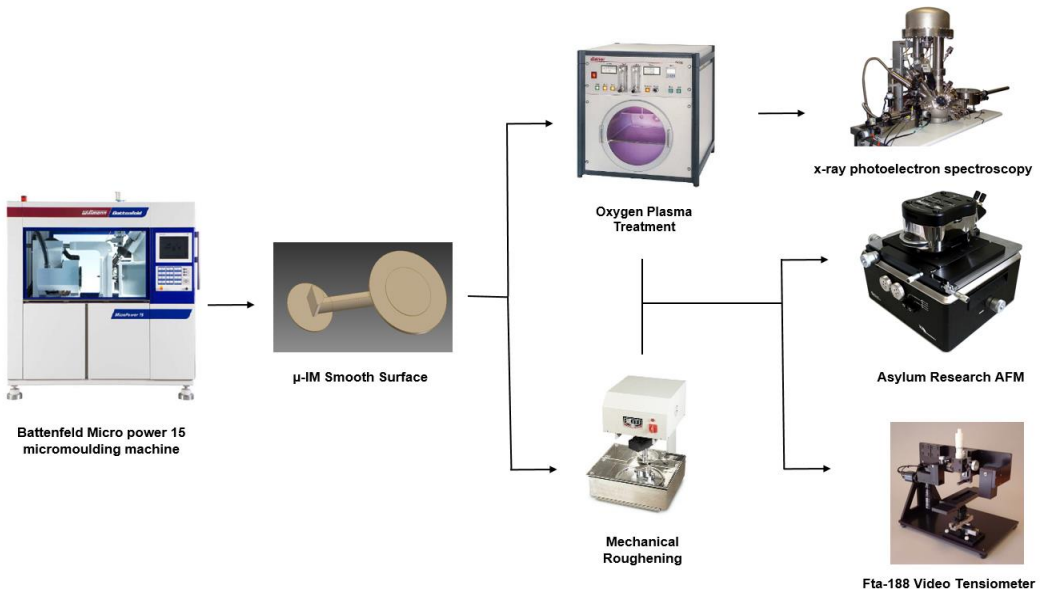

Figure 4.1 Schematic representation of the Chapter 4.

4.0. Introduction

Despite the extraordinary versatility of most polymers for solid MN manufacturing, there is one property that markedly reduces its application- a highly hydrophobic surface (Khan and Mahmoud, 2009). This property makes it difficult to wet and coat the polymeric MN surfaces with proteins, vaccines and active pharmaceutical ingredients (APIs). These problems arise because the plastic surfaces have relatively poor wetting and adhesion properties, which are due to their low surface energy (absence of polar surface groups) (Hildebrand *et al*., 2006; Khan and Azman, 2007; Finn, 2007). Hence, surface modification of polymeric materials plays an important role to improve surface properties such as wetting and adhesion for coatings, inking and printing processes, biomaterials, and APIs. Therefore, various modification techniques such as plasma treatment, UV irradiation, laser, chemical oxidation, flame and grafting have attracted much attention (Ma and Tang, 2005). Plasma treatment provides manifold possibilities to refine a polymer surface (Subedi *et al*., 2003). The plasma used for these applications, although not fully ionized, are composed of ions, free electrons, photons, neutral atoms and molecules in ground and excited electronic states (Vijayalakshmi *et al*., 2011). Each of these components has the potential for interaction with surfaces with which they come in contact.

The surface wetting and adhesion properties of plasma modified polymers are the subject of many studies and much work has been devoted to the enhancement of polymer-polymer, metal-polymer adhesion as well as dyeing and printing on the polymers (Garcia, 2009). A good understanding of the surface properties of a solid surface may be obtained relatively inexpensively from the measurement of surface contact angle (Heimenz, 1997). Therefore,

contact angle measurements have been performed to study the surface free energy, wettability and adhesion of low surface energy materials. The surface free energy of a solid is an important parameter, playing a vital role in the phenomena that occurs at solid-liquid and solid-gas interfaces. Hence, a knowledge of this parameter is useful in studies of adsorption and wettability processes, which play important role in coated drug delivery using polymeric microneedle devices. Measurement of the contact angle of the liquid with the solid surface permits a rapid and qualitative evaluation of surface free energy of the polymers (Rulison, 2003). In this chapter PEEK, LCP and PC surfaces created using µIM were treated with RF (radio frequency) oxygen plasma under different exposure times and mechanical abrasion treatment with the intention of improving the intrinsic low-surface properties. The differences in hydrophilicity of mechanically abraded and plasma-modified micro-injection moulded polymer discs were characterised by measuring the contact angle as a function of treatment time. The surface morphologies of the treated and untreated surfaces were analysed using AFM. The chemical bonding on the surface of the disc and functional groups was quantified using XPS analysis. In this chapter the role that oxygen plasma treatment and mechanical abrasion have on moulded polymer surfaces and their influence on protein absorption for microneedle drug delivery was also explored.

4.1. Experimental

4.1.1. Generation of moulded specimens for surface evaluation

4.1.1.1. Mould tool fabrication

The mould used for MN manufacture was used to produce specimen for surface evaluation but instead of using the MN insert described in Chapter 3, a flat mould insert and a polished sapphire window (Optical grade C-plane Orientation +/-0.5 degrees, 26.5mm dia +/-0.1 x 4mm thick +/-0.1 mm and with 1.5 nm roughness) was used on the moving side of the mould.

4.1.1.2. Moulding flat polymer samples

The moulding of the specimens was performed on a Battenfeld Microsystem 50 micro-injection moulding machine as shown in Figure 4.2 using the parameters mentioned in the Table 4.1.This machine differs from a regular injection moulding machine by combining an extrusion screw with plunger-based metering and injection systems. A 14 mm diameter extrusion screw mounted at an angle of 45 degrees to the injection axis feeds into metering chamber containing a servo-driven piston to accurately prepare a dose of material. A second servo-driven injection piston is then used to inject the shot with a velocity up to 1000mm/s directly to the split plane of the mould. The machine has a custom mould design with a thermoelectric heating system allowing the tool temperature control over the range 30-250 ^{o}C. A data acquisition suite allows evaluation of injection piston dynamics, injection/cavity pressures and thermal properties of the tool platen. A tempsonic RH series magnetostrictive position transducer was used to measure injection piston displacement and velocity.

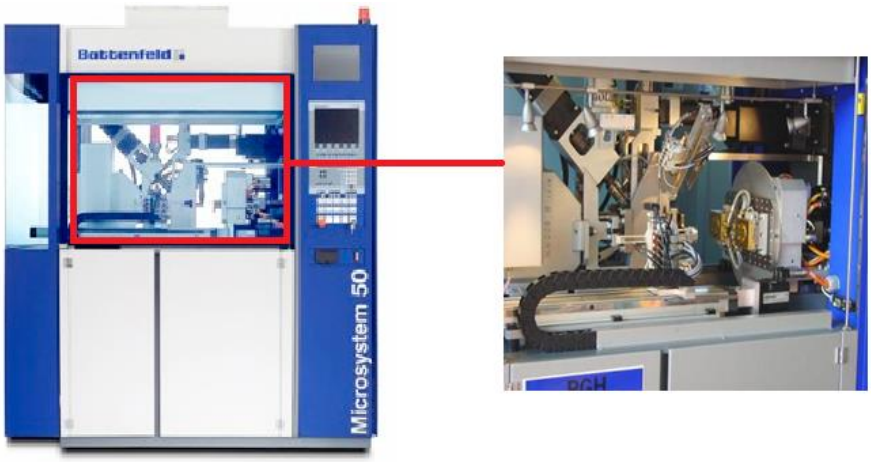

Figure 4.2 Battenfeld Microsystem 50 micro-injection moulding machine.

Injection moulding parameters

Parameter	PEEK	LCP	PC
Melt temperature(°C)	420	350	320
Maximum injection velocity(cm^3/s)	11.8	8.8	7.5
Clamping force (kN)	50	50	50
Time of holding pressure (s)	3.8	4	4
Mould base temperature(°C)	200	120	120

Table 4.1 Injection moulding parameters.

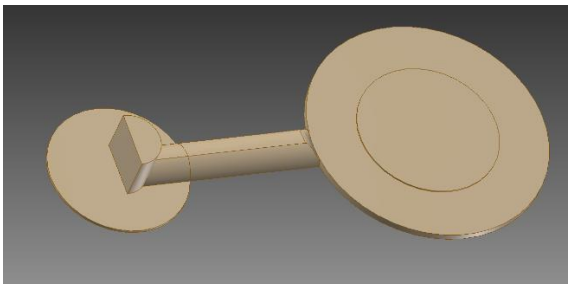

Figure 4.3 Schematic of the injection moulded samples for surface analysis.

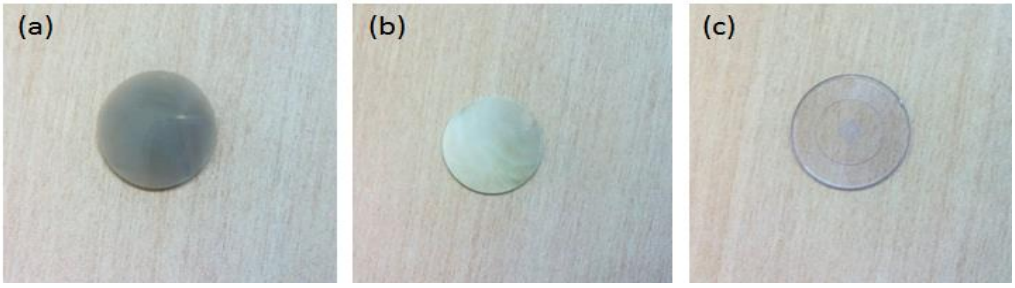

Figure 4.4 Photographic images of micro-injection moulded specimen used for characterisation (a) PEEK (b) LCP and (c) PC.

Figure 4.3 shows the schematic of the complete moulded part and Figure 4.4 shows the top view of each specimen used for surface analysis. Moulded specimens of each material manufactured using a µIM process was of 17 mm diameter and 0.5 mm thickness which was ideal for the surface characterisation. A data acquisition site in the moulding hardware allows evaluation of injection piston dynamics, injection/cavity pressures and thermal properties. However the process data was not recorded as the focus of the work was only to generate a reasonably flat surface with a pre-existing mould insert.

4.1.2. Mechanical abrasion

Three different Micro-mould inserts were ultra-fine grinded by a Buehler Motopol automatic grinder to obtain a low (≈5µm), intermediate (≈10µm) and high (≈15µm) surface roughness. These inserts were then used to replicate polymer surfaces with different roughness values for analysis.

4.1.3. Surface oxygen plasma activation

PEEK, LCP and PC moulded discs were utilized to evaluate the effectiveness of the plasma activation process. The plasma treatment system (nano series plasma surface machine by Diener electronic, Jettingen, Germany) with a cylindrical chamber with capacity of 24 litres was used for this study. The generator works with radio-frequency signal of 40 kHz and maximum power of 300 W fully variable. Figure 4.5 shows the schematic of the plasma treatment process.

A pump (Pfeiffer Duo), with 1.8 m^3/h and pressure of 3×10^{-2} mbar was used to evacuate the plasma chamber. Samples of polymers which needed plasma activation were placed in the plasma chamber, and the vacuum pump was utilized to reduce the pressure to 0.1 mbar and at that pressure of the process gas (i.e. oxygen 99% of purity) was fed into the chamber. When this working pressure was achieved the generator was switched on and process gas in the recipient was ionised

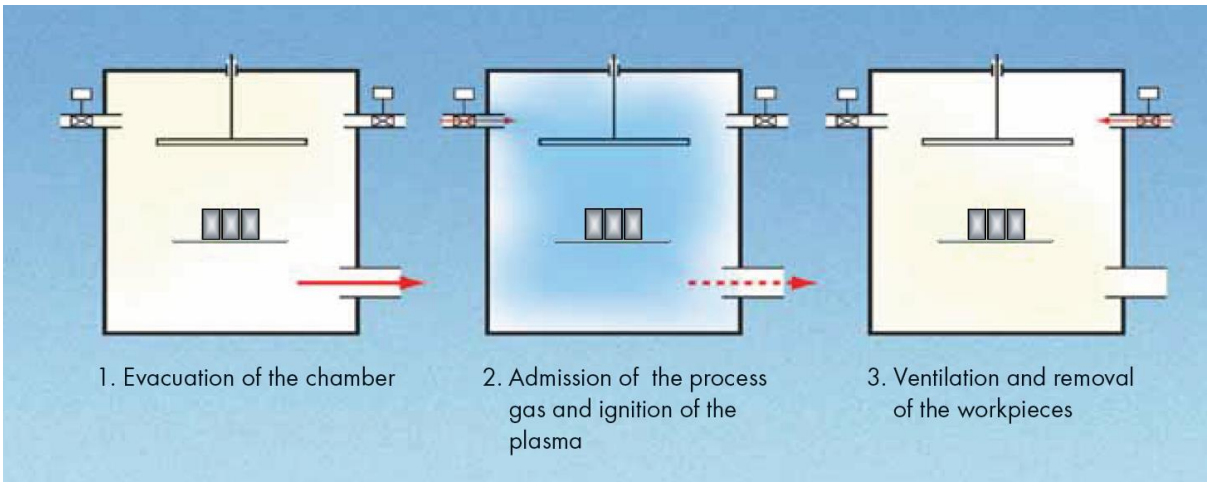

Figure 4.5 Process sequence of plasma treatment.

4.1.4. Contact angle measurements

Each disc produced from the µIM was washed and subsequent experimental procedures were performed under clean conditions. Dynamic contact angle studies were performed using various set of probe liquids (n-octanol, n-hexane, n-octane, n-heptane, cyclohexane, toluene, benzyl alcohol, ethylene glycol, glycerol and double distilled water). Practically, a droplet (~0.7µl of probe liquid) was released on the surface to be measured, positioned on a levelled horizontal plan. An optical system (source, optics and CCD camera) was used to analyse the drop profile. The θ value was calculated using image analysis software. Contact angle measurement on the polymeric surface was measured using dynamic sessile drop method. This procedure was carried out using FTA 188 video tensiometer (Figure 4.6a).

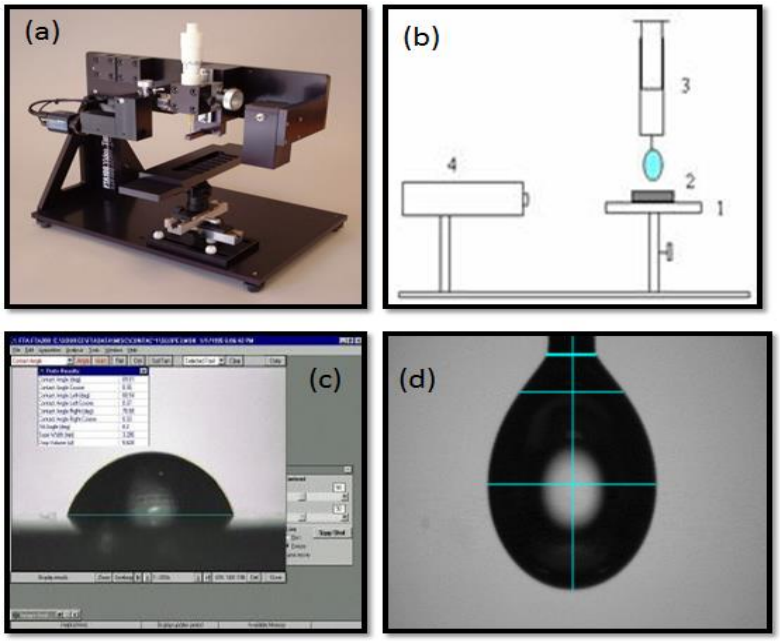

Figure 4.6 (a) picture of a video tensiometer FTA188 (b) schematic representation of experimental rig (c) Fta32 video software interface and (d) interfacial tension measurements made using Fta32 video software interface.

4.1.4.1. Process operation

A simplified system (schematised in Figure 4.6b) consists of an adjustable horizontal plate (marked as 1) to host the test substrate (marked as 2) and a syringe (marked as 3) to deliver liquid drops on the solid surface.

The contact angle and interfacial tension measurements of the liquid drop was captured using a high-speed video camera (marked as 4) mounted parallel to the drop. All measurements were carried out at room temperature (21°C). Images of spreading drops were analysed for contact angle, drop base area, and drop height, volume and maximum diameter in correlation with time by the built-in Fta32 Video software package in the computer system. Figure 4.6 c & d shows how the contact angle and interfacial measurements were taken on the Fta32 software. Each experiment was repeated three times and the results presented here are the averaged data for each experiment. Once all the contact angle data for a set of probe liquids on a polymers was obtained total surface free energy of the polymer surfaces were calculated using Owens/Wendt theory.

4.1.5. Surface characterisation using AFM

4.1.5.1. Measurements on untreated and treated surface

AFM was used to examine the changes in the polymer surface before and after the treatment process. All AFM scans were made using an MFP-3D scanner from Asylum Research, Santa Barbara, USA. Silicon nitride cantilever tips (Applied Nanostructures, Santa Clara, USA) with a tip radius of 15 nm and spring constant of 0.3 Nm were used. The scans were made on 10 µm × 10 µm scale and repeated five different times on five different area of the polymer film

at a resolution of 512 x 512 pixels. Images were interpreted using integrated MFP-3D™ Igor software (USA). Errors in the piezo-linearity were corrected for by using zero and first order flattening. The scans were made on 10 µm × 10 µm scale and repeated five different times on five different area of the polymer film.

4.1.5.2. Surface morphology after protein adsorption

Protein solution of 50 µg/ml was prepared with lyophilized powder of Bovine Serum Albumin (Sigma-Aldrich, UK) in a Phosphate Buffer Solution (PBS) of pH 7.4. Plasma treated and untreated polymer samples were immersed in 5 ml protein solution and allowed to incubate at 37°C. After 2 hours samples were removed from the incubator and rinsed with Milli-Q water to remove unbounded protein. All the sample polymers were then allowed to dry at room temperature. AFM analysis was performed as soon as all the samples were dried after protein adsorption. The scans were made on 10 µm × 10 µm scale and repeated five different times on five different area of the polymer film. Single high resolution scans was also made on 1.5 µm × 1.5 µm scale.

4.1.6. Protein quantification after surface treatment

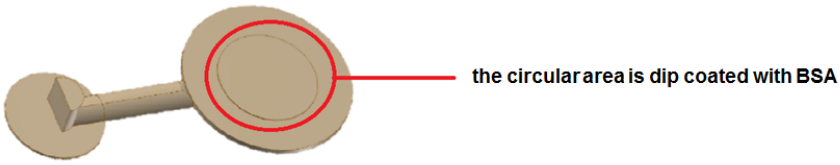

Figure 4.7 Schematic showing the area of the moulded sample where the protein coating has been carried out.

In order to study the influence of surface treatment on protein adsorption, BSA quantification studies were carried out on the plasma treated and mechanically abraded polymer samples. The selected area as shown in the Figure 4.7 of the surface modified (plasma and mechanical abraded) PEEK, LCP and PC polymer disc were dip coated with 500 µg/ml BSA for 15 mins. After the coating these disc were put into a vial containing 1 ml of PBS and ultra sonicated to remove all the BSA bound to the polymer surface and subsequently analysed for the BSA content using HPLC.

4.1.7. Analysis of BSA in solution by HPLC

BSA analysis was performed using reversed phase HPLC method which consists of a gradient system of 0.1% trifluoroacetic acid (TFA) in water (A) and 0.08% TFA in acetonitrile (B) with initial A/B ratio of 80/20, which changed linearly to the final ratio of 35/65 (A/B) within 15 min. The flow rate was 1ml/min throughout and BSA separation was carried out using a Symmetry 300® C4 protein analysis column (50 x 4.6 mm 5 µm particle size, Waters, USA). A UV

detector (model 746, Waters, USA) was used in a wavelength of 220 nm for BSA detection. The injection was made using a loop injector equipped by a 50 µl loop. A stock solution of BSA of concentration 100 µg/ml was prepared in phosphate buffer (pH=7.4) and various concentrations of 1, 2, 4, 8, 10 and 25 µg/ml were prepared by serial diluting the stock solution. These samples were then injected into the HPLC and then linear regression analysis was out on known concentration and corresponding peak heights. The regression coefficient (r) slope and intercept of the resulting calibration curves were determined.

4.1.8. XPS analysis

Changes to the surface chemistry induced by plasma treatment and the adsorption of BSA onto to the polymer surfaces were determined by X-ray photoelectron spectroscopy (XPS) using a Kratos Axis Ultra DLD spectrometer (Kratos, UK). A monochromated AlKa X-ray (1486.6 eV) source operating with an anode voltage of 15 kV and a 10 mA current was utilised throughout. The chamber pressure was maintained at $<5 \times 10^{-8}$ mbar during spectral analysis. Wide energy survey scans (1–1300 eV), with a step size of 0.5 eV was used to identify all the elements in the samples. When the convoluting XPS peaks the energy scale was calibrated with the 284.4 eV low energy component of the C1s peak. The XPS spectra were obtained (C1s, O1s and N1s) for injection moulded samples for PEEK, LCP and PC and named as follows

(a) Untreated

(b) Plasma Treated

(c) Untreated + BSA

(d) Plasma Treated + BSA

4.2. Results and discussion

4.2.1. Plasma treatment

4.2.1.1. Contact angle and surface energy

Analysis of the surface free energy of PEEK, PC and LCP surfaces has been made on the basis of dispersive and non-dispersive components. Surface free energy (γ_s) and its polar (γ_{sp}) and dispersion (γ_{sd}) components of the samples were determined from sets of contact angles made by the probe liquids (n-octanol, n-hexane, n-octane, n-heptane, cyclohexane, toluene, benzyl alcohol, ethylene glycol, glycerol and double distilled water) according to Owens-Wendt-Equation (2.7). The dispersive and polar surface tension components of the probe liquids used to obtain the components of surface free energy of the different polymers and the contact angles for each liquid on the polymer surfaces are shown in Figure 4.8.

Contact angle data for a set of probe liquids on a the untreated polymer surfaces was obtained and the surface tension values (overall, polar and dispersive) for the liquid used provides all the information necessary to plot contact angle data on Owens/Wendt format.

(1) Liquid	PTFE (θ)	Rad	Cos(θ)	PEEK (θ)	Rad	Cos(θ)	σ_L	σ_L^D	$(\sigma_L)^2$	σ_L^P	X	Y
n-octanol	59.00	1.03	0.51	16.71	0.29	0.96	25.48	20.70	649.46	4.78	0.48	5.48
n-hexane	12.86	0.22	0.97	0.00	0.00	1.00	18.84	19.24	355.12	-0.39	0.00	4.30
n-octane	29.00	0.51	0.87	0.00	0.00	1.00	21.30	22.14	453.61	-0.84	0.00	4.53
n-heptane	22.00	0.38	0.93	0.00	0.00	1.00	19.90	20.43	395.97	-0.53	0.00	4.40
cyclohexane	45.00	0.79	0.71	8.82	0.15	0.99	29.65	35.58	879.13	0.00	0.00	4.94
toluene	51.00	0.89	0.63	0.00	0.00	1.00	34.28	43.31	1174.79	0.00	0.00	5.21
Benzyl alcohol	75.00	1.31	0.26	6.68	0.12	0.99	38.70	32.96	1497.83	5.75	0.42	6.72
ethylene glycol	89.00	1.55	0.02	12.75	0.22	0.98	47.80	32.83	2284.38	14.96	0.68	8.24
Glycerol	96.00	1.68	-0.10	11.32	0.20	0.98	56.17	35.12	3154.88	21.05	0.77	9.39
Water	107.00	1.87	-0.29	16.66	0.29	0.96	72.80	36.83	5299.77	35.97	0.99	11.74

(2) Liquid	PTFE (θ)	Rad	Cos(θ)	LCP (θ)	Rad	Cos(θ)	σ_L	σ_L^D	$(\sigma_L)^2$	σ_L^P	X	Y
n-octanol	59.00	1.03	0.51	21.46	0.37	0.93	25.48	20.70	649.46	4.78	0.48	5.41
n-hexane	12.86	0.22	0.97	0.00	0.00	1.00	18.84	19.24	355.12	-0.39	0.00	4.30
n-octane	29.00	0.51	0.87	0.00	0.00	1.00	21.30	22.14	453.61	-0.84	0.00	4.53
n-heptane	22.00	0.38	0.93	0.00	0.00	1.00	19.90	20.43	395.97	-0.53	0.00	4.40
cyclohexane	45.00	0.79	0.71	11.44	0.20	0.98	29.65	35.58	879.13	0.00	0.00	4.92
toluene	51.00	0.89	0.63	0.00	0.00	1.00	34.28	43.31	1174.79	0.00	0.00	5.21
Benzyl alcohol	75.00	1.31	0.26	5.74	0.10	0.99	38.70	32.96	1497.83	5.75	0.42	6.72
ethylene glycol	89.00	1.55	0.02	13.90	0.24	0.97	47.80	32.83	2284.38	14.96	0.68	8.22
Glycerol	96.00	1.68	-0.10	23.96	0.42	0.91	56.17	35.12	3154.88	21.05	0.77	9.07
Water	107.00	1.87	-0.29	16.00	0.28	0.96	72.80	36.83	5299.77	35.97	0.99	11.76

(3) Liquid	PTFE (θ)	Rad	Cos(θ)	PC (θ)	Rad	Cos(θ)	σ_L	σ_L^D	$(\sigma_L)^2$	σ_L^P	X	Y
n-octanol	59.00	1.03	0.51	19.10	0.33	0.94	25.48	20.70	649.46	4.78	0.48	5.45
n-hexane	12.86	0.22	0.97	0.00	0.00	1.00	18.84	19.24	355.12	-0.39	0.00	4.30
n-octane	29.00	0.51	0.87	0.00	0.00	1.00	21.30	22.14	453.61	-0.84	0.00	4.53
n-heptane	22.00	0.38	0.93	0.00	0.00	1.00	19.90	20.43	395.97	-0.53	0.00	4.40
cyclohexane	45.00	0.79	0.71	12.68	0.22	0.98	29.65	35.58	879.13	0.00	0.00	4.91
toluene	51.00	0.89	0.63	0.00	0.00	1.00	34.28	43.31	1174.79	0.00	0.00	5.21
Benzyl alcohol	75.00	1.31	0.26	8.12	0.14	0.99	38.70	32.96	1497.83	5.75	0.42	6.71
ethylene glycol	89.00	1.55	0.02	13.25	0.23	0.97	47.80	32.83	2284.38	14.96	0.68	8.23
Glycerol	96.00	1.68	-0.10	24.34	0.42	0.91	56.17	35.12	3154.88	21.05	0.77	9.06
Water	107.00	1.87	-0.29	14.30	0.25	0.97	72.80	36.83	5299.77	35.97	0.99	11.81

Figure 4.8 Results for the probe liquids used to test on (1) PEEK (2) LCP (3) PC.

Once the graph was plotted the slope of the line was used (shown in Figure 4.9) to calculate the dispersive component of the surface energy of the solid using equation (2.6).

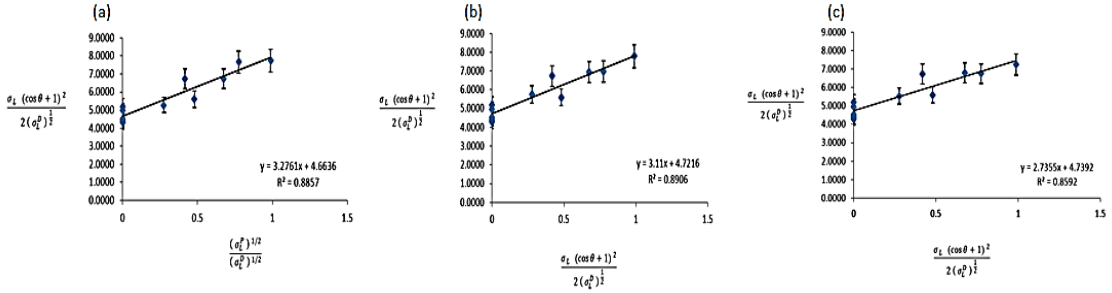

Figure 4.9 Graph showing the Owens/Wendt plot for (a) PEEK (b) LCP and (c) PC.

Surface tension data of all the probe liquids mentioned in Figure 4.8 clearly shows that surface tension of the straight chain alkanes and cyclic alkanes (cyclohexane) contribute to the dispersive forces. None of these liquids have any polar component to the overall surface energy and as dispersive forces are no-site specific Van-der Waals type forces, and that these are the only type of molecular interactions possible for alkanes (Rulison, 2003 and Roger, 2001). The remainder of the liquids in the list (except toluene) contains hetero-atoms (the term is used to indicate that non-carbon atoms have replaced carbon in the backbone of the molecular structure or any atom that is not carbon or hydrogen) in the form of hydroxyl, carbonyl, amide or nitrate functionally. These causes the liquids to be capable of polar type interactions with surfaces to which they are applied. That capability is reflected in the fact that they all have substantial polar components to the overall surface tensions. Now the dispersive and polar components of the overall surface tension for the probe liquids is known, consequently the magnitude of the dispersion force contribution to the surface energy, of the polymer surface can be determined by measuring interfacial tension and contact angles, using the set of probe liquids as the primary reference phase.

As expected, the water contact angles made on all three untreated polymers (Figure 4.11) are larger (above 71°) because of the low-energy and hydrophobic nature of the polymer surfaces. The surface used for testing contact angle was made by µIM having a sapphire window on one side of the mould resulting a very smooth surface. The AFM image of the sapphire window (Figure 4.12) reveals the surface roughness of 1.5 nm so it is expected that the surface generated will also be off similar roughness. The total surface free energy (polar

and dispersive component) of the polymers are shown in the Figure 4.10. The values of polar and dispersive component of the polymer according Owens/Wendt model equation shows that molecular interactions are mainly dispersive. The fit confidence of the Owens/wendt plot for PEEK/LCP and PC were r^2=0.885; 0.890 and 0.859 respectively.

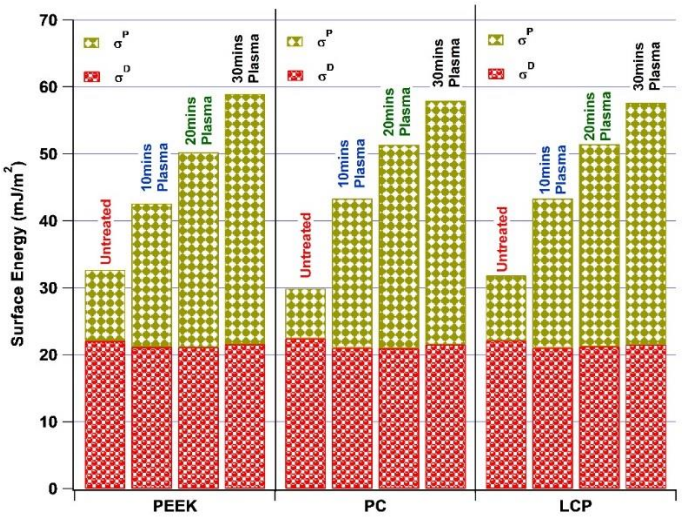

Figure 4.10 Bar graph showing the polar (σ^P) and dispersive (σ^D) component of the surface energy of the three polymers before and after plasma treatment calculated using Owens/Wendt theory.

The wetting behaviour of the polymer samples were dramatically changed after oxygen plasma treatment. It was observed that for all three polymers oxygen plasma treatment lowers the contact angle as compared to the untreated samples. Figure 4.11 shows the water contact angle values for untreated and plasma treated polymer samples.

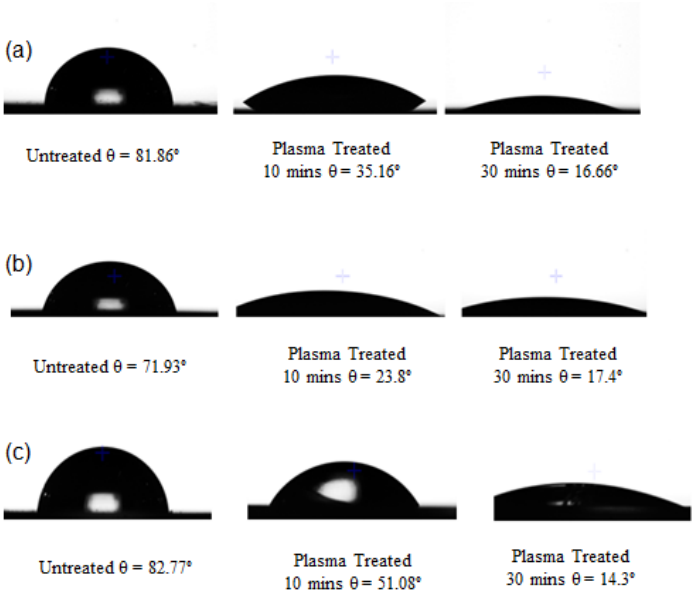

Figure 4.11 Water contact angle for (a) PEEK (b) LCP (c) PC before and after 10 and 30 mins of oxygen plasma treatment.

This was expected, since the plasma activation process more oxygen-containing functional groups of the polymers are generated on the polymer surface caused by the reactions between the polymer and active species from the oxygen plasma thus increasing the hydrophilicity. Another important factor which increases the wettability is the surface modification mechanism by UV (VUV) radiation emitted by plasma, the exposure to the oxygen plasma discharge is sufficient to break chemical bonds (C-C, C-H), (Pelagade *et al*., 2010) and leaves free radicals at or near the surface (Rochford, 2002 and Kim, 2004). These radicals can react only with other surface radicals or by chain transfer reaction. If the polymer surface is flexible, or if the radicals can migrate along it, then recombination, unsaturation or cross-linking can occur (Mcintyre and Walzak, 1995). Moreover, the plasma removes low molecular weight species or converts them to high molecular weight species by cross-linking reaction (Finson *et al*., 1995). In summation the oxygen plasma treatment

causes the cross-linking at PEEK, LCP and PC surfaces as well as the sputtering of the material.

4.2.1.2. Plasma treatment and surface topography

The effect of plasma treatment depends on internal and external parameters like type of plasma (DC, RF, or microwave), the discharge power density, pressure, and flow rate of the gas or gas mixture and exposure time (Powles, 2007). The surface of the polymer is activated during plasma treatment, which brings about the chain session of the existing groups on the surface of the polymer and creates new functional groups such as –OH and –OOH. Oxygen plasma is used to increase polar functional groups (hydroxyl, carboxyl, ether, carbonyl, etc) (Labay *et al*., 2010 and Vasilev, 2013) which can successfully increase the surface free energy of the polymer (Rochford, 2002). In the recent years the surface treatment of polymers was performed by many researchers to make suitable for adhesion (Liu and Lu, 2006; D'Sa *et al*., 2010; Yeo *et al*., 2006 and Kuzuya *et al*., 2005).

The morphologies of the three experimental untreated polymeric surfaces are shown in Figure 4.13, as viewed by the AFM. This is a local probe technique that reveals local structural features, which are not necessarily representative for the whole sample surface. Because of this reason an appropriate way to record and process many images from different areas of the surface were used. This furnishes local structure information with high resolution but also enables to determine an average behaviour. Figure 4.12 shows the AFM image of the sapphire window used to mould flat surfaces. Figure 4.13 contains the representative AFM images of untreated polymer surfaces and scans were made on 10µm x 10 µm scale and repeated 5 times and average surface

roughness was used. All the evaluations that are described in the following have, thus been carried out quantitatively and averaged over a large number of pictures recorded in different areas of the samples. The average surface roughness R_a of untreated PEEK/LCP and PC were 1.51, 2.79 and 1.61 nm respectively. This confirms that the surfaces were relatively smooth for all polymers which is important for surface characterisation.

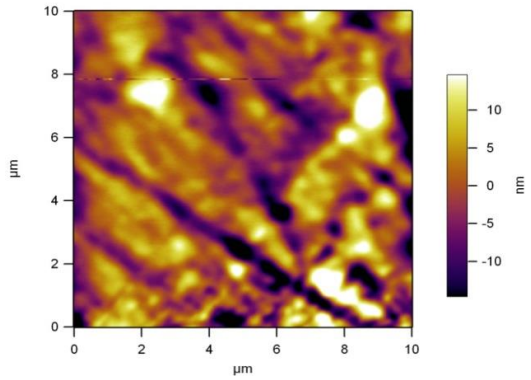

Figure 4.12 AFM scan of the sapphire window used in the manufacturing of the moulded specimen.

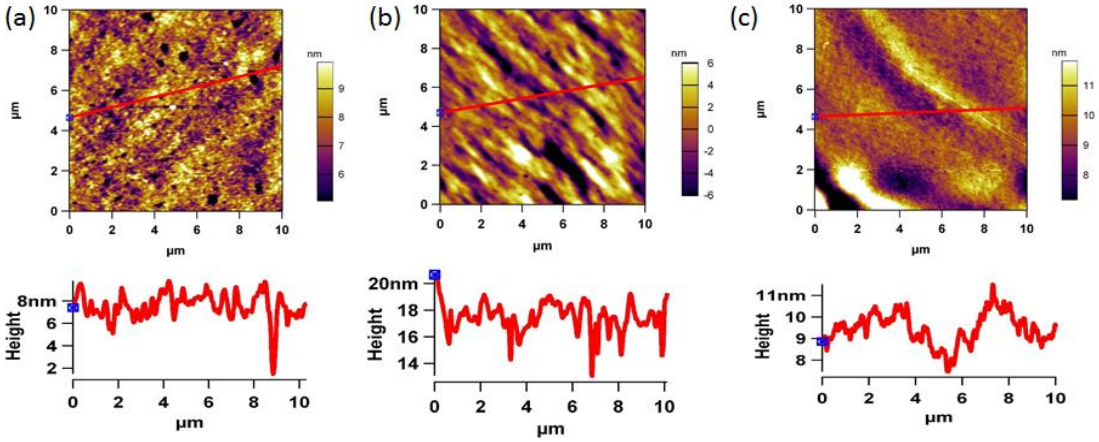

Figure 4.13 Representative 2D tapping mode AFM images (10µm x 10µm) and line profiles for UNTREATED (a) PEEK (b) LCP (c) PC.

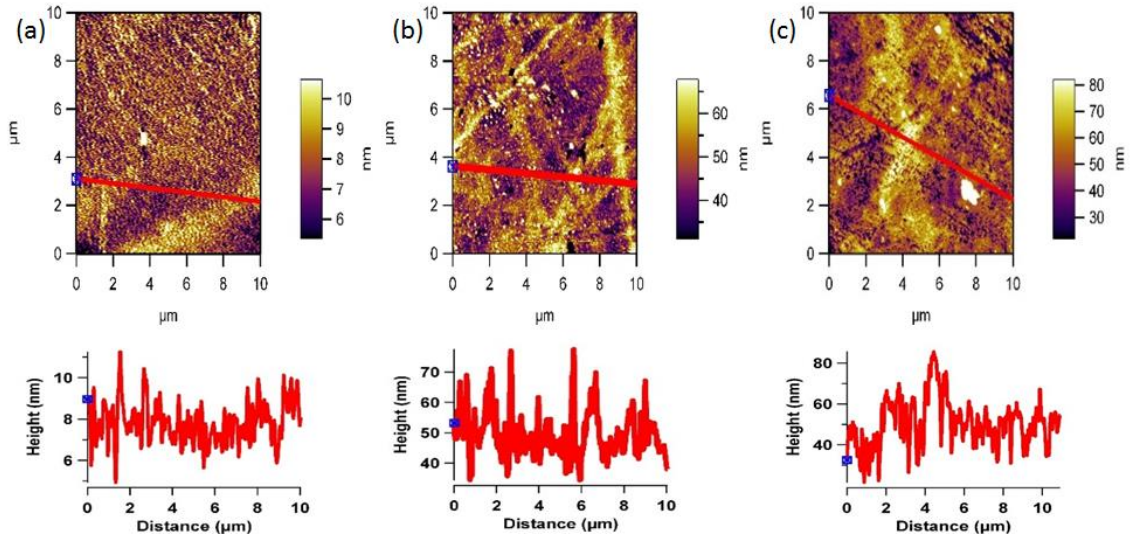

Figure 4.14 Representative 2D tapping mode AFM images (10µm x 10µm) and line profiles for PEEK after (a) 10 (b) 20 (c) 30 mins of oxygen plasma treatment.

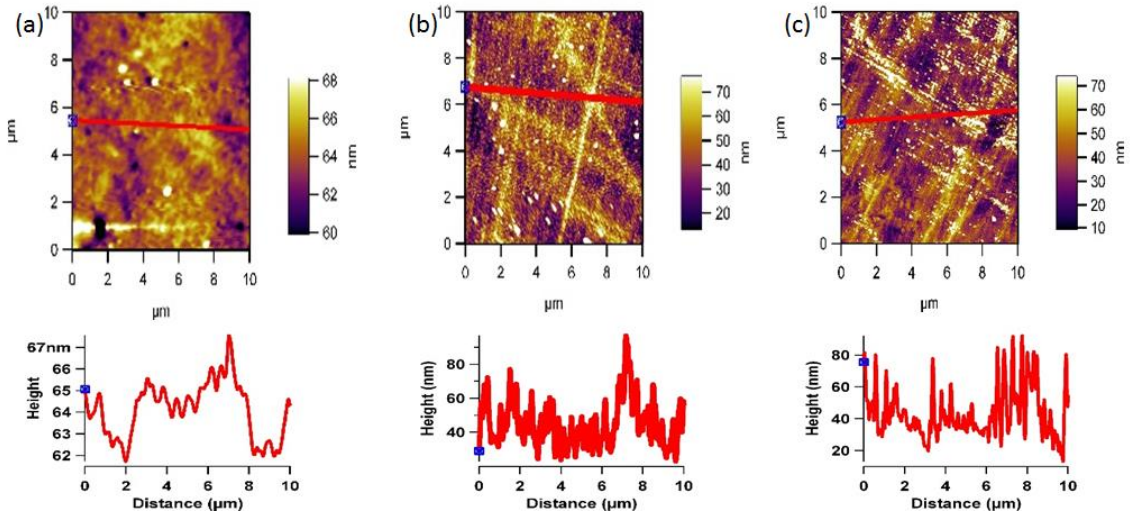

Figure 4.15 Representative 2D tapping mode AFM images (10µm x 10µm) and line profiles for LCP after (a) 10 (b) 20 (c) 30 mins of oxygen plasma treatment.

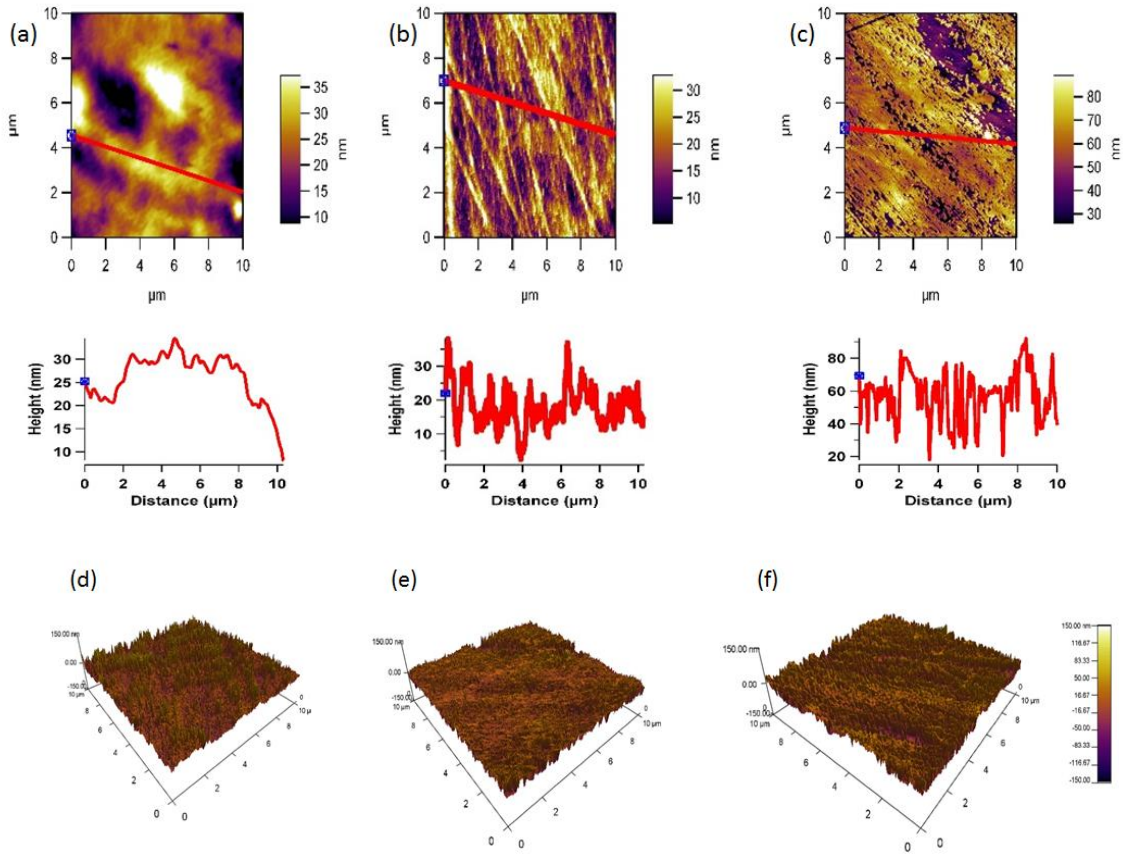

Figure 4.16 Representative 2D tapping mode AFM images (10µm x 10µm) and line profiles for PC after (a) 10 (b) 20 (c) 30 mins of oxygen plasma treatment (d-f) 3D tapping mode AFM images of 30 mins of oxygen plasma treatment surfaces of PEEK, LCP and PC respectively.

The AFM images Figure 4.14, 4.15 and 4.16 reveal the surface morphology and the line profiles of the polymer surfaces after plasma treatment for 10, 20 and 30 minutes respectively. It is well known that the wettability of a polymer surface is affected by the surface morphology, especially the surface roughness. AFM scans to examine the changes in the surface morphology induced before and after oxygen plasma treatment was performed. After the plasma treatment for 30 minutes showed the presence of aggregate structure (sign of patchiness or inhomogeneities) with various sizes on the surface. The different sizes of the aggregate indicate the uneven effect of the surface etching by plasma treatment. The plasma treatment time can be optimised by comparing the

contact angle and AFM data. The AFM scans showed that after 30 mins, further exposure can simply etch away the material that was previously modified by the plasma. This can also be the reason for minima and maxima properties as function of time, and highlights the importance of optimising the treatment period and to optimise the plasma treatment time, contact angle vs plasma treatment time was measured and found out that after 30 minutes of plasma there is no significant decrease in the contact angle, as shown in Figure 4.17.

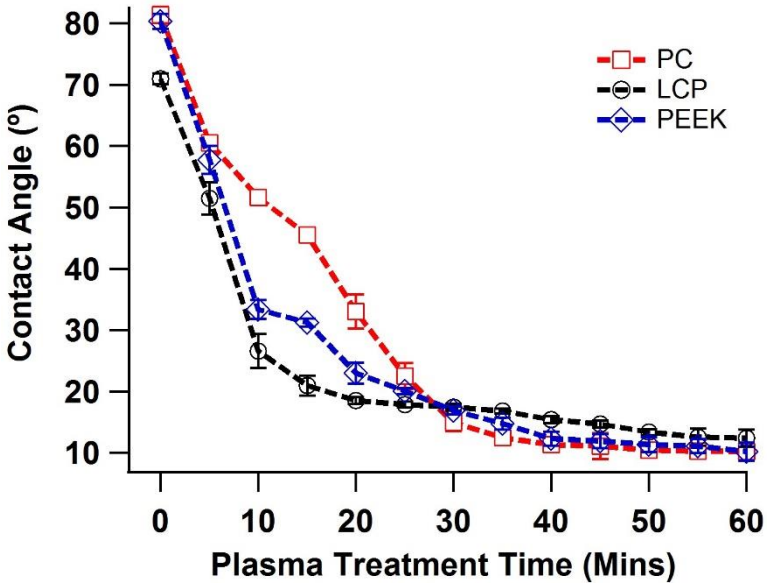

Figure 4.17 Water contact angle with plasma treatment time for PEEK, LCP and PC.

The plasma treated surfaces of all three polymers also showed the formation of the pit-like structures, probably because of sputtering effects of plasma which was predominantly observed on the PC surface. The AFM images of treated LCP samples showed much more etched or bumpy features on surface than that of PEEK and PC. Changes in the surface roughness of the oxygen plasma treated polymer samples were quantified by root-mean square (rms) values to highlight the surface modifications due to oxygen plasma treatment at 30 mins. Figure 4.18 shows average roughness values of untreated and plasma treated

samples. The average surface roughness increases from 1.51, 2.79 and 1.61 nm for the untreated PEEK, LCP and PC, reaching a value of 13.34, 15.48 and 15.05 nm after 30 mins of plasma treatment respectively.

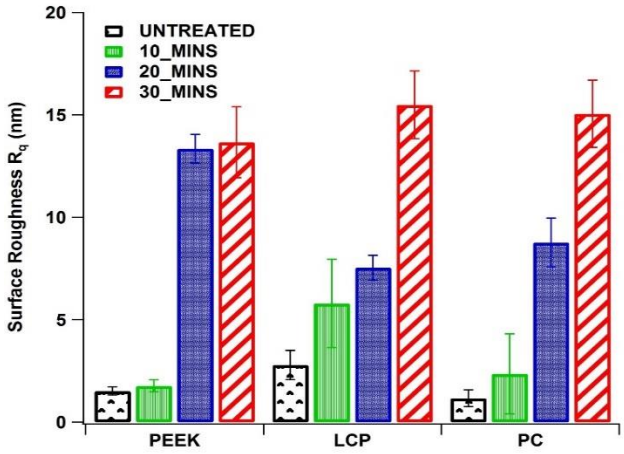

Figure 4.18 Bar graph showing the average root mean square (RMS) roughness of untreated and plasma treated samples.

This indicates that LCP and PC's surface roughness has slightly increased more than that of PEEK suggesting PEEK to be more resistant to plasma treatment as compared to LCP and PC (Comyn *et al*., 1996). These results also support the idea that the effects of oxygen plasma treatment on the polymer surface observed by AFM are due to plasma bombardment of the surface and scission of the polymeric chains, which in turn rearrange themselves to give rise to a new surface morphology (Finson *et al*., 1995). In general, the higher the plasma treatment time, the greater roughness observed.

Protein adsorption studies to understand the adhesion of BSA on to both treated and untreated polymer surfaces were conducted. Figure 4.19a-c shows the effects of adsorbing BSA from solution containing 50 µg/ml on untreated surfaces. The scans were made on 10 µm × 10 µm areas and repeated five different times on five different area of the polymer film. Single high resolution scans were also made on 1.5 µm × 1.5µm areas (Figure 4.19 d-f). Protein

adsorption on polymer surface did not substantially increase the roughness indicating the poor adhesion of the polymer and suggesting the need for surface treatment to increase the wettability. The higher resolution image reveals presence of protein which is irregularly spread on the surface.

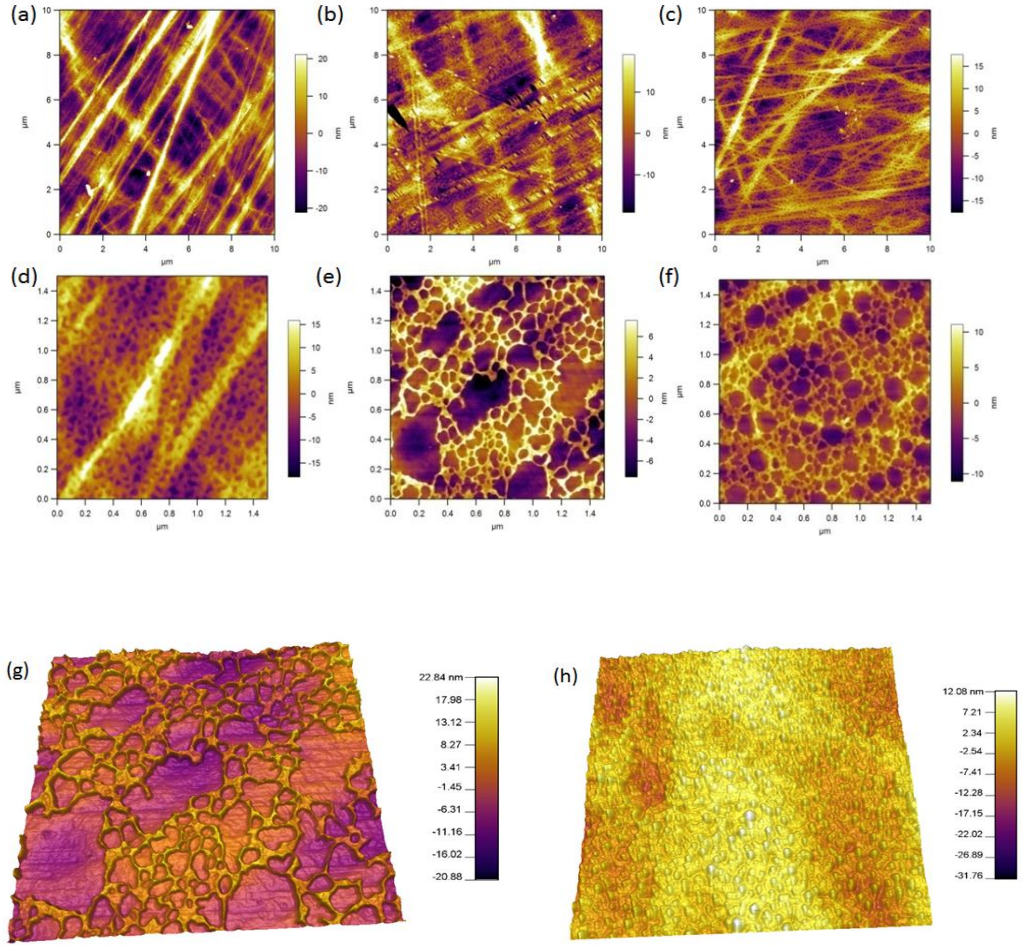

Figure 4.19 Representative 2D tapping mode AFM scans of untreated (a) PEEK (b) LCP (c) PC surface after 50µg/ml BSA adsorption. (d-f) shows a higher resolution 1.5 µm scan after protein adsorption for the corresponding polymers and (g) representative 3D tapping mode AFM scans of untreated PC+ BSA showing how the BSA is adsorbed on a hydrophobic polymer surface (h) representative 3D tapping mode AFM scans of plasma treated PC + BSA showing how the BSA is adsorbed on a surface modified polymer surface.

The 3D AFM image (Figure 4.19g and h) of both the untreated and treated PC samples gives a clear understanding of the BSA adsorption at the polymer surfaces. In the case of untreated samples a patchy pattern of BSA was

observed whereas, for plasma treated the BSA was uniformly spread over the entire polymer surface, indicating better adsorption.

4.2.1.3. XPS

The effect that plasma treatment had on the moulded polymer samples were examined using XPS and resulting curve fitted data for O1s and C1s are graphically shown in Figure 4.20.

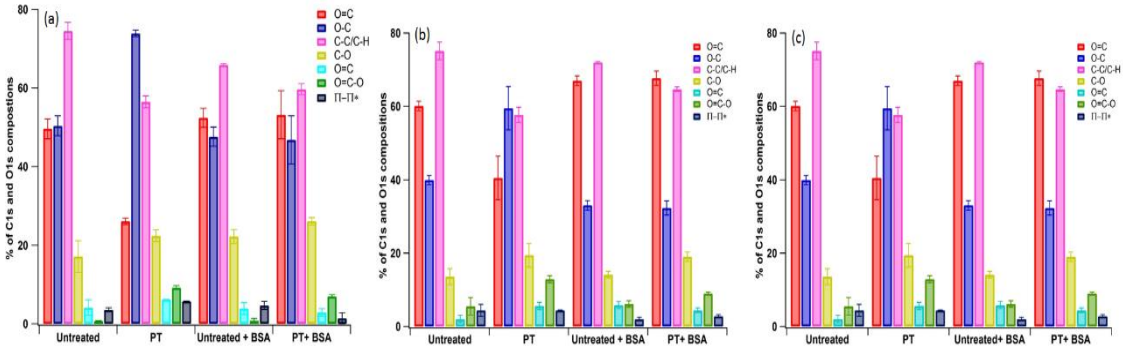

Figure 4.20 Curve fitted data for O1 and C1s peaks for (a) PEEK (b) LCP and (c) PC.

The XPS data indicates in the case of untreated and plasma treated PEEK and PC samples lack of nitrogen, thus N-peak is only expected to appear just on the BSA treated samples. LCP on the other hand, have nitrogen in its chemical composition and the variation of N-peak with the BSA treatment makes the spectra difficult to understand.

After plasma treatment, a broader O1s peak and an increase of the CPS (counts per second) of all the peaks convoluted for all three polymer samples were observed. An increase in C1s peak as well as the peak shape compared to the untreated samples was also seen. After plasma treatment there was a change from a two peak-like envelope in the O1s peak to a bell like envelope. The highest variation due to the oxidation process was recorded for the O-C peak (533.9 eV), the aromatic and aliphatic components C-C/ C-H (284.9 eV)

and –O-(C=O) - (289.2 eV). This trends were observed previously in the literature (D'Sa *et al*., 2010). The C1s peak was de-convoluted after plasma treatment into 5 components at the following binding energies 285 eV (C-C/C-H); 286 eV (C-C=O); 287 eV (O=C); 291.8 eV (π-π* satellite peak) and 289.5 eV (O-C=O).

The O1s envelope can be fitted with two peaks 532.1ev (O=C) and 533.8 eV (O-C). The plasma treatment produces an increases alkyl components (C-C/C-H) with a concomitant increase of the oxidation components at 286.6 eV and 289.5 eV.

The presence of N1s peak is evident for the PEEK and PC +BSA samples whereas, for LCP sample the peak becomes more significant (CPS double). In the case of the plasma treated+BSA samples N1s do not suffer significant modifications with plasma treatment.

The de-convolution of the C1s spectra for both untreated+BSA and plasma treated+BSA samples show a change of the C-C/C-H peak which can be due to the C-N component and a contribution of polar groups such as: C-O/C-N, O=C-O/O=C-N (reduced for the PT+BSA and higher for UT+BSA treated sample and this is in accordance with the results obtained by D'Sa *et al*). Differences appear as well for the components at 286 eV and 289 eV where both components increases in the case of plasma treated sample. From the XPS data it was evident that the O_2 plasma treatment is an efficient way of modifying the surface of LCP, PC, PEEK polymer surfaces. This statement is not supported only by the XPS data (polar group's percentage modification) but as well by the contact angle and surface energy calculations. The contact angle measurement indicates an increase of approximately 7 times from the untreated sample to O_2

plasma treated samples for all 3 polymers – this indicating an increase in wettability of the surface. The O_2 plasma treatment creates species which are transferred during this process to the polymer sample surface making this surface more adherent to different materials.

From the XPS data and the AFM scans (Figure 4.19g-h) it was observed that when BSA approaches the hydrophobic (untreated) surface it randomly spreads over non-uniformly, forming a patchy network of protein. Where as in the case of plasma treated surface BSA forms a hydrogen bond with the surface and this way creating a well ordered and uniform protein layer. To illustrate this proposed mechanism a schematic is shown in Figure 4. 21.

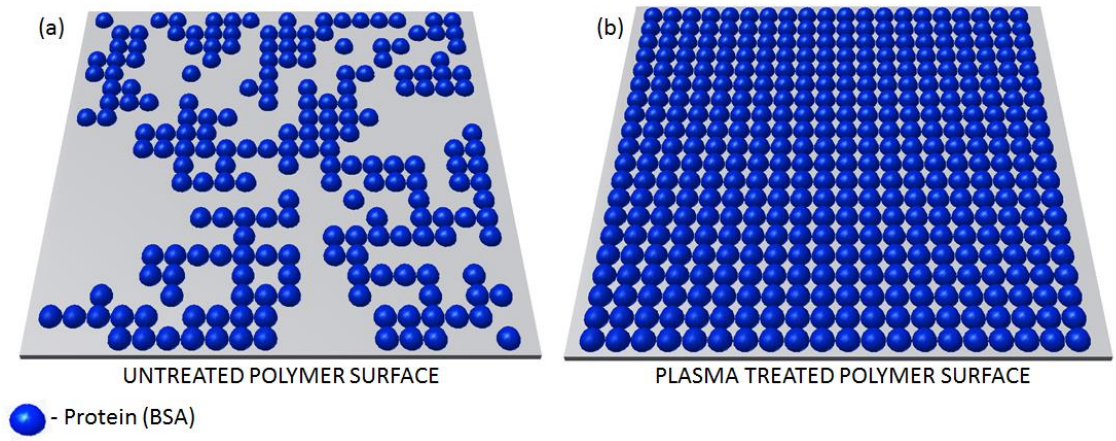

Figure 4.21 Proposed mechanism of BSA adsorption onto (a) untreated and (b) plasma treated polymer surfaces.

4.2.1.4. HPLC

A high performance liquid chromatography method was used to quantify the BSA adsorbed on the polymer surfaces. A calibration curve was obtained for BSA standard solutions of (1, 2, 4, 8, 10 and 25 µg/ml) (r^2=0.9985). Figure 4.22 shows the chromatogram of BSA and Figure 4.23 shows the calibration curve, the equation for the best fit line and the regression values for BSA.

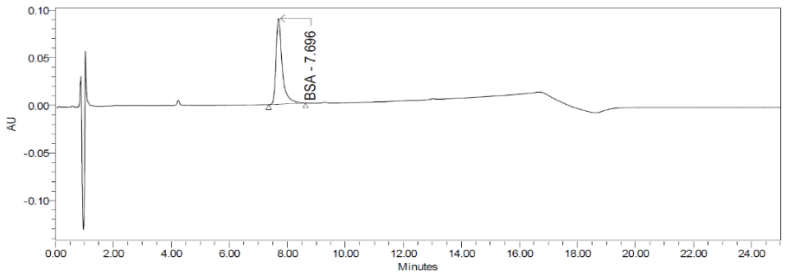

	Peak Name	RT	Area	% Area	Height
1	BSA	7.696	1344660	100.00	90055

Figure 4.22 Chromatogram of BSA containing PBS samples (10 µg/ml) showing the BSA has the retention time of 7.69 mins.

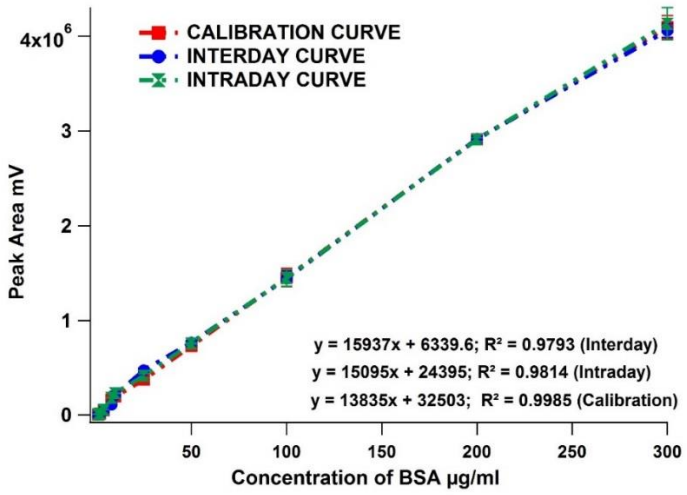

Figure 4.23 Calibration curve showing a plot of peak area versus concentration for BSA. The mean peak area determined from the calibrations obtained on 3 different days are plotted against nominal concentration values. Error bars denoting standard deviation are displayed for each point. Calibration curve were constructed by plotting mean peak area calculated from triplicate inter-day values for three different days.

Selected concentration µg/ml	Mean concentration found µg/ml	SD	Accuracy (%)
Inter-day			
1(low)	0.9862	0.024	98.62
50(medium)	46.45	4.67	92.9
300 (high)	297.57	1.92	99.19
Intra-day			
1 (low)	1.034	0.103	96.6
50(medium)	48.9	6.84	97.8
300(high)	295.13	7.41	98.37

Table 4.2 Accuracy and precision of the HPLC method (n=3).

Table 4.2 describes the accuracy and precision of the inter-day and intra-day analyses of three different concentration (low, medium and high) of BSA. The values obtained from the assay procedure showed good reproducibility with similar intra-day and inter-day results. This calibration curve was used to determine the unknown concentration of BSA adsorbed on to the surface modified polymer samples.

4.2.1.5. Protein quantification after plasma treatment

In this study PEEK, LCP and PC polymer samples were treated by oxygen plasma, to modify their surface properties in order to study the influence of plasma treatment on protein adsorption on polymer samples. BSA was the model drug used in this experiment and 500 µg/ml BSA solution was dip coated to the surface of the plasma treated polymer samples. Figure 4.24 shows the amount of BSA adsorbed on various polymer sample at different plasma treatment times.

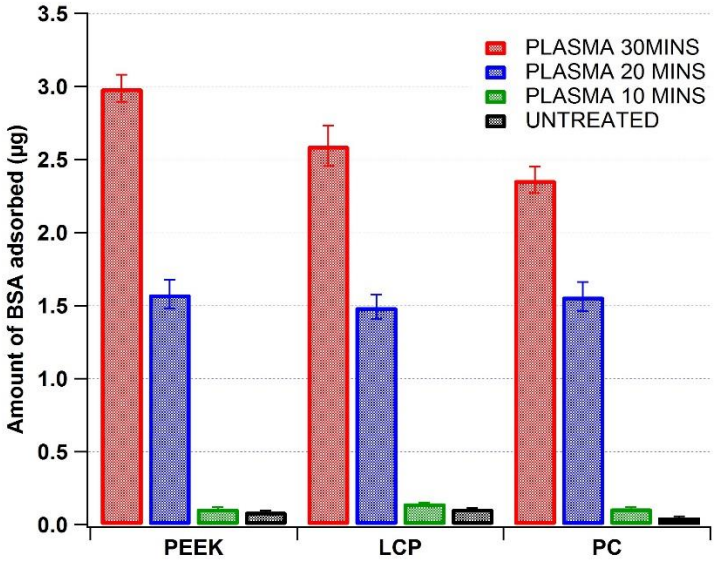

Figure 4.24 Amount of BSA adsorbed at different plasma treatment time.

The maximum amount of BSA adsorbed was achieved for all three polymer samples were at 30 minutes of plasma treatment. BSA adsorbed on to the plasma treated sample was 30 times more as compared to the untreated sample. This effectiveness is because plasma treatment creates wettable polar surfaces on which the BSA could spread uniformly and thus provides extensive interfacial contact (Hammer and Tirrel, 1996; Yeo *et al*., 2006). More over treatment of polymer samples in plasma environment incorporates hydrophilic groups which contribute to an increase in wettability and form a weak Van der Waal's force between the protein layer and the polymer surface (D'Sa *et al*., 2010 and Kasemo, 2002). Contact angle data and the AFM images also reveals the increase in wettability due to the increase in surface roughness.

4.2.2. Mechanical abrasion

Surface roughening using mechanical abrasion method is the simple and inexpensive modification method. In this study, inserts for micro moulding were abraded using silica carbide paper. Three different levels of roughness: low (5 µm), intermediate (10 µm) and high (15 µm) were created on to each insert and subsequently moulded using PEEK, LCP and PC. All these moulded polymer samples were then characterised in terms of surface energy, surface topography and protein adsorption.

4.2.2.1. Contact angle and surface energy

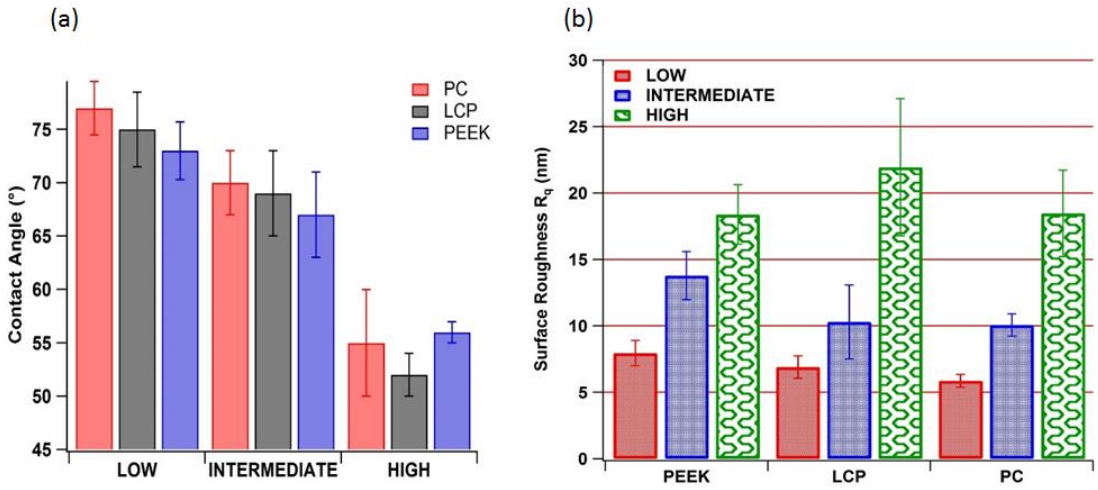

Figure 4.25 (a) water contact angle with different levels of mechanical abrasion for PEEK, LCP and PC (b) bar graph showing the surface roughness of each polymer vs mechanical abrasion level.

Figure 4.25a shows the water contact angle data for different levels of mechanical abrasion and it was observed that there was no significant reduction in the contact angle even with high level of mechanical abrasion when compared to 30 minutes of plasma treatment. Mechanical abrasion could only lower the contact angle to 52° in the case of LCP, where as in plasma treatment

a significant reduction in contact angle was achieved. The surface roughness of the different levels of mechanically abraded polymer samples were quantified by root-mean square (rms) values. Figure 4.25b shows average roughness values of each level of abrasion.

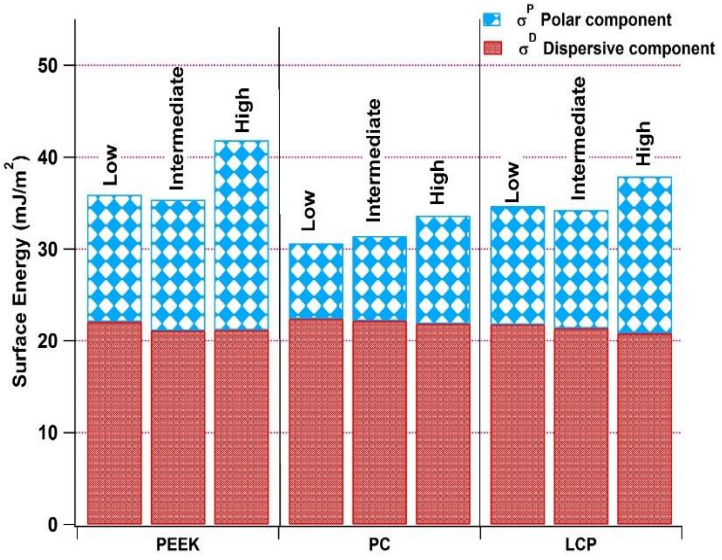

Figure 4.26 Bar graph showing the polar (σ^P) and dispersive (σ^D) component of the surface energy of the three polymers after different levels of mechanical roughening calculated using Owens/Wendt theory.

The wetting behaviour of the polymer samples did not change significantly after mechanical abrasion. It was observed that for all three polymers oxygen plasma treatment lowers the contact angle as compared to the mechanically abraded samples. Figure 4.26 shows the surface energy of the different levels of abrasion and observed no change in the dispersive component of the surface energy but there was slight change in the polar component in the high level of abrasion. This kind of result was expected because unlike plasma treatment mechanical abrasion causes bulk modification of the surface by creating random scratches, whereas plasma treatment restrict the surface modifications

to depth of several nanometers of the specimen while maintaining its bulk properties and desired surface polarities can be achieved even with low temperature to avoid sample destruction. A maximum surface energy of 42 mJ/m^2 was obtained using mechanical abrasion whereas using plasma treatment a maximum surface energy of 58.42 mJ/m^2 was achieved, suggesting plasma treatment a better and efficient way of surface modification.

4.2.2.2. Mechanical abrasion and surface topography

The surface morphologies and line profiles of all the three levels of mechanically abraded polymer surfaces are shown in Figure 4.27-4.29 as viewed by the AFM. A significant observation from AFM measurement was the presence of parallel and longish structures forming a fibril or filament pattern on all three polymer surfaces made from low level abrasion. This might due to the features formed on to the insert during the grinding process. The fibril pattern was also evident on PEEK samples for intermediate and high levels of abrasion. In general the surface roughness values were found to change with each level of abrasion as indicated by the AFM data.

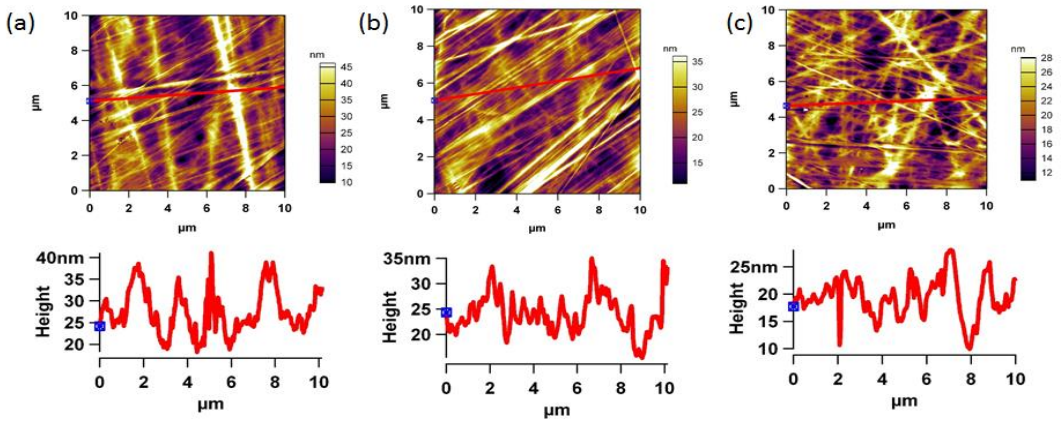

Figure 4.27 Representative 2D tapping mode AFM images (10µm x 10µm) and line profiles for LOW level (a) PEEK (b) LCP (c) PC.

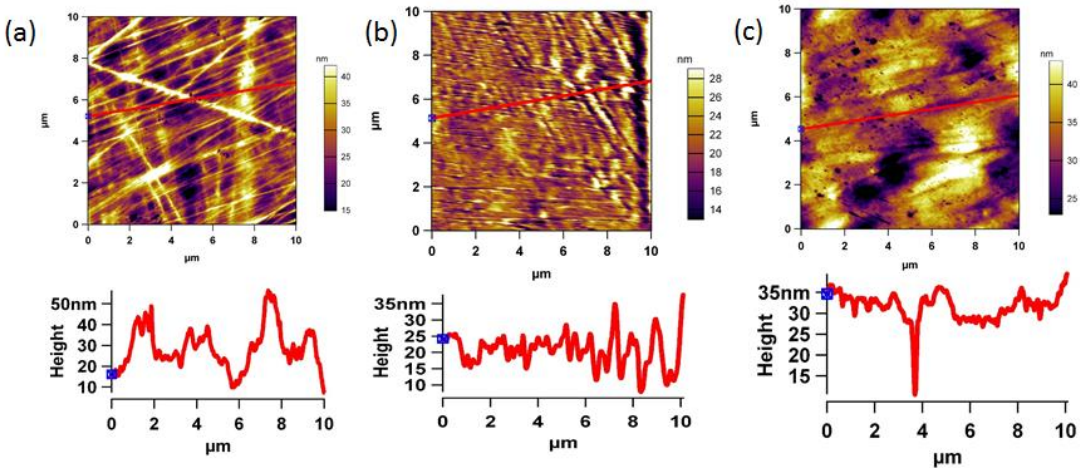

Figure 4.28 Representative 2D tapping mode AFM images (10µm x 10µm) and line profiles for INTERMEDIATE level (a) PEEK (b) LCP (c) PC.

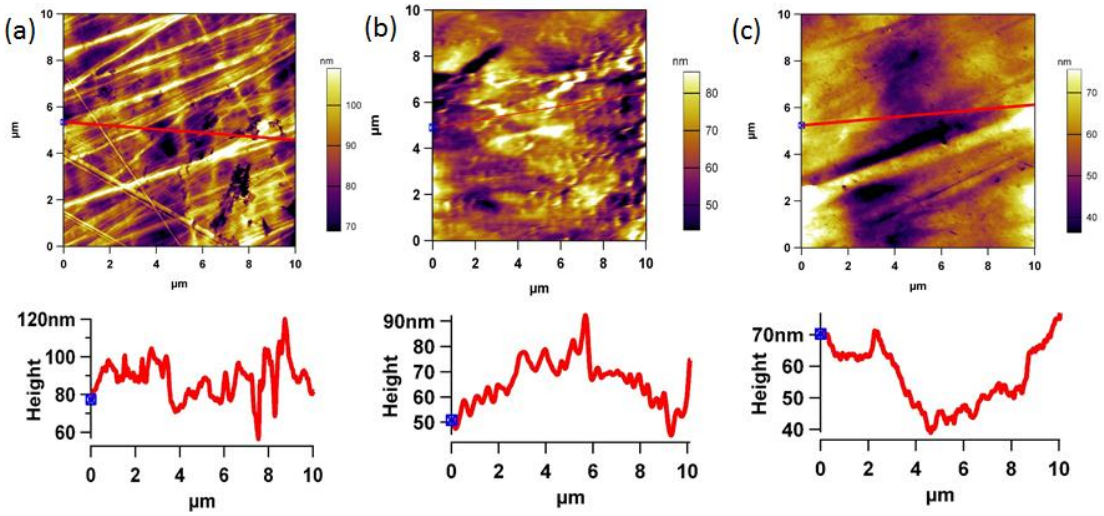

Figure 4.29 Representative 2D tapping mode AFM images (10µm x 10µm) and line profiles for HIGH level (a) PEEK (b) LCP (c) PC.

4.2.2.3. Protein quantification after mechanical abrasion

Following the protein quantification after plasma treatment a comparison study is carried out using the mechanically abraded samples. Figure 4.30 shows the amount of BSA adsorbed on various polymer sample at different levels of

abrasion. The maximum amount of BSA adsorbed was achieved at high level of abrasion for all three polymer samples.

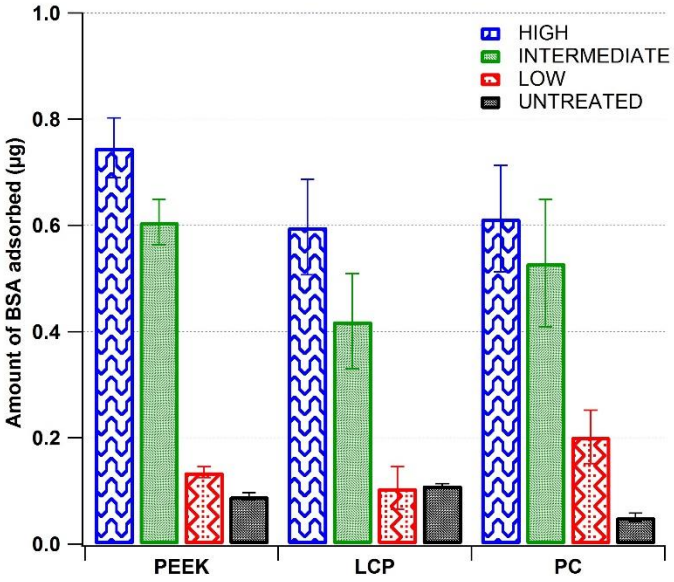

Figure 4.30 Amount of BSA adsorbed at different with different levels of mechanical abrasion for PEEK, LCP and PC.

Amount of BSA adsorbed on to the mechanically abraded surface was 8 times more as compared to the untreated sample. The maximum amount of BSA adsorbed on mechanical abraded surface was 0.78 µg as compared to 3 µg obtained from plasma treatment. This study clearly indicates that oxygen plasma treatment is an effective method for modifying the surfaces of injection moulded PEEK, LCP and PC samples. Only 30 minutes of plasma treatment at high power settings were required to significantly alter the water contact angle and surface oxygen content. Another observation made was that plasma treatment did not significantly affect the surface roughness for relatively short exposure times (determined by AFM). This indicates that the change in water contact angle on polymer surface for 10 minutes plasma treatment was mainly a consequence of plasma induced changes in surface chemistry. However the increase in surface roughness for 30 minutes plasma treatment was due to

chain scission reaction that occurred in the polymer surface region (Ma and Tang, 2014). Hence it could be confirmed that the change in wettability induced by plasma treatment was due to the combination of oxidative surface chemistry and moderate surface roughening, whereas in the case of mechanical abrasion this is only due to surface roughening caused by abrasion.

4.3. Conclusions

Oxygen plasma and mechanical abrasion has been used to modify the surface of the micro-injection moulded polymer samples. It was found that plasma treatment modified the surfaces both in chemical composition and morphology whereas mechanical abrasion just changed the surface roughness values. The plasma treatment increased the polar component of the surface energy of polymer samples causing in decrease in contact angle and increase in total surface energy. The XPS analysis confirmed the increase in the polar groups in the plasma treated polymer surfaces.

The AFM images showed the increase in surface roughness for both plasma as well as mechanical abraded surfaces. A HPLC method was used to determine the amount of BSA adsorbed after surface modification and showed that plasma treatment is a much more efficient way to increase the adsorption of the BSA onto the polymer surface as compared to the mechanically treated counterparts. This proves that increase in the adsorption of BSA onto the polymer samples could be improved by plasma treatment which will be highly beneficial to coat the shafts of the solid microneedles.

4.4. References

1. Burton ZT, Surface characterization, adhesion, and friction properties of hydrophobic leaf surfaces and nano patterned polymers for super hydrophobic surfaces. Thesis submitted to Ohio State University (2005).

2. Bauman BD, Surface-modified polymer particles: performance additives for epoxy and cast polyurethane. *Thermoset Technology/Epoxy Resin Formulators Division Technology Conference*, (2002) Florida.

3. Comyn J, Mascia L, Xiao G and Parker BM, Plasma-treatment of polyetheretherketone (PEEK) for adhesive bonding, *International Journal of Adhesion and Adhesives* **16** (1996) 97-104.

4. D'Sa RA, Burke G.A and Meenan BJ, Protein adhesion and cell response on atmospheric pressure dielectric barrier discharge-modified polymer surfaces, *Acta Biomaterialia* **6** (2010) 2609–2620.

5. Davies P, Courty C, Xanthopoulos N and Mathieu HJ, Surface treatment for adhesive bonding on carbon fibre-poly(etherether ketone) composites, *Journal of Materials Science Letters* **10** (1991) 335-338.

6. Finn KH, The Measurement of surface energy of polymer by means of contact angles of liquids on solid surfaces, Thesis Submitted University of Oslo (2007).

7. Finson E, Kaplan SL and Wood L, Plasma Treatment of Webs and Films in 38th *Annual Technical Conference Proceedings for the Society of Vacuum Coaters*, Chicago, (1995).

8. Garcia T, Plasma Processes as a Cleaner Alternative for Cleaning, Corrosion Resistance, and Functionalization of Metallic Surfaces. *2nd International Workshop Advances in Cleaner Production* (2009) 21-27.

9. Hanke L.E, Handbook of Analytical Methods for Materials*. Materials Evaluation and Engineering, Inc*. (2001) Plymouth.

10. Heimenz P, Principles of Colloid and Surface Chemistry (Undergraduate Chemistry: A Series of Textbooks) Marcel Dekker, New York (1997)

11. Hildebrand HF, Blanchemain N, Mayer G, Chai F, Lefebvre M, and Boschin F, Surface coatings for biological activation and functionalization of medical devices, *Surface & Coatings Technology* **200** (2006) 6318–6324.

12. Hammer DA and Tirrell M, Biological ahesion at interfaces, *Annual Review Mater Science* **26** (1996) 651–691.

13. Introduction to plasma technology published by *Diener electronic* GmbH Co. KG Germany (2007).

14. Kurtz SM and Devine JN, *Biomaterials* **28** (2007) 4845.

15. Kim S, Polyetheretherketone Surface Functionalization by Low-Energy Ion-Beam Irradiation under a Reactive O_2 Environment and Its Effect on the PEEK/Copper Adhesives, *Langmuir* **20** (2004)157-163.

16. Kuzuya M, Kondo S and Sasai Y, Recent advances in plasma techniques for biomedical and drug engineering, *Pure Applied Chemistry* **77** (2005) 667–682.

17. Khan MI and Hassan A Wetting characteristics of photographic base solid polymeric substrates. *In: VIIth National Symposium on Polymeric Materials,* (2007) 23-25.

18. Kasemo B, Biological surface science, *Surface Science* **500** (2002) 656–677.

19. Kuzuya M, Kondo S and Sasai Y, Plasma Techniques for Preparation of Controlled Drug Release System, *Plasmas and Polymers* **6** (2001) 145-162.

20. Labay C, Canal C and Garcı´a-Celma MJ, Influence of Corona Plasma Treatment on Polypropylene and Polyamide 6.6 on the Release of a Model Drug, *Plasma Chem Plasma Process* **30** (2010) 885–896.

21. Liu YC and Lu DN, Surface Energy and Wettability of Plasma-treated Polyacrylonitrile Fibers, *Plasma Chem Plasma Process* **26** (2006) 119–126.

22. Lyklema J and Norde W, Protein adsorption and bacterial adhesion to solid surfaces: A colloid-chemical approach, *Colloids Surf* **38** (1989) 1–13.

23. Norde W, The behavior of proteins at interfaces, with special attention to the role of the structure stability of the protein molecule, *Clin Mater* **11** (1992) 85-91.

24. Mittal KL, Contact Angle, Wettability, and Adhesion, VSP International Science Publishers (1993) ISBN 90-6764-157-X.

25. Ma R and Tang T, Current Strategies to Improve the Bioactivity of PEEK, *International Journal of Molecular Science* **15** (2014) 5426-5445.

26. Mcintyre NS and Walzak MJ, New UV/Ozone Treatment Improves Adhesiveness of Polymer Surfaces, *Modern Plastics* (1995) 79-81.

27. Mohammad IK and Mohamed MN, Spreading behaviour of silicone oil and glycerol drops on coated papers, *Leonardo Journal of Sciences* **8** (2009) 18 - 30.

28. Pelagade S, Singh NL, Shahb S, Qureshi A, Rane RS, Mukherjee S, Deshpande UP, Ganesan V and Shripathi T.Surface free energy analysis for bipolar pulsed argon plasma treated polymer films Journal of Physics: Conference Series (2010)

29. Powles RC, Nanoindentation response of PEEK modified by mesh-assisted plasma immersion ion implantation, *Surface & Coatings Technology* **201** (2007) 7961–7969.

30. Roger P, Surface Tension Measurements Using the Drop Shape Method First Ten Angstroms, Portsmouth (2001).

31. Rochford ETJ, Effect of Plasma Treatment of PEEK on Bacterial Adhesion, *56th Annual Meeting of the Orthopaedic Research Society* (2002)

32. Rulison C. So you what to measure surface energy? Technical Note 306 (2003) Kruss GmbH, Hamburg. 1-16.

33. Subedi D, Zajickova L, Bursikova V and Janca J, Surface modification of polycarbonate (bisphenol A) by low pressure of plasma, *Himalayan Journal of Sciences* **1** (2003) 115-118.

34. Vijayalakshmi KA, Mekala M, Yoganand CP and Pandiyaraj KN, Studies on Modification of Surface Properties in Polycarbonate (PC) Film Induced by DC Glow Discharge Plasma, *International Journal of Polymer Science* (2011)

35. Vasilev K, Nano engineered Plasma Polymer Films for Biomaterial Applications, *Plasma Chem Plasma Process* **34** (2014) 545-558.

36. Yeo SH, Choi CR and Jung D, Investigation of Protein Adsorption Using Plasma Treatment for Protein Chips, *Journal of the Korean Physical Society* **48** (2006) 1325-1328.

Chapter 5 Performance and prediction of penetration forces and drug delivery of polymeric solid microneedles

Graphical abstract

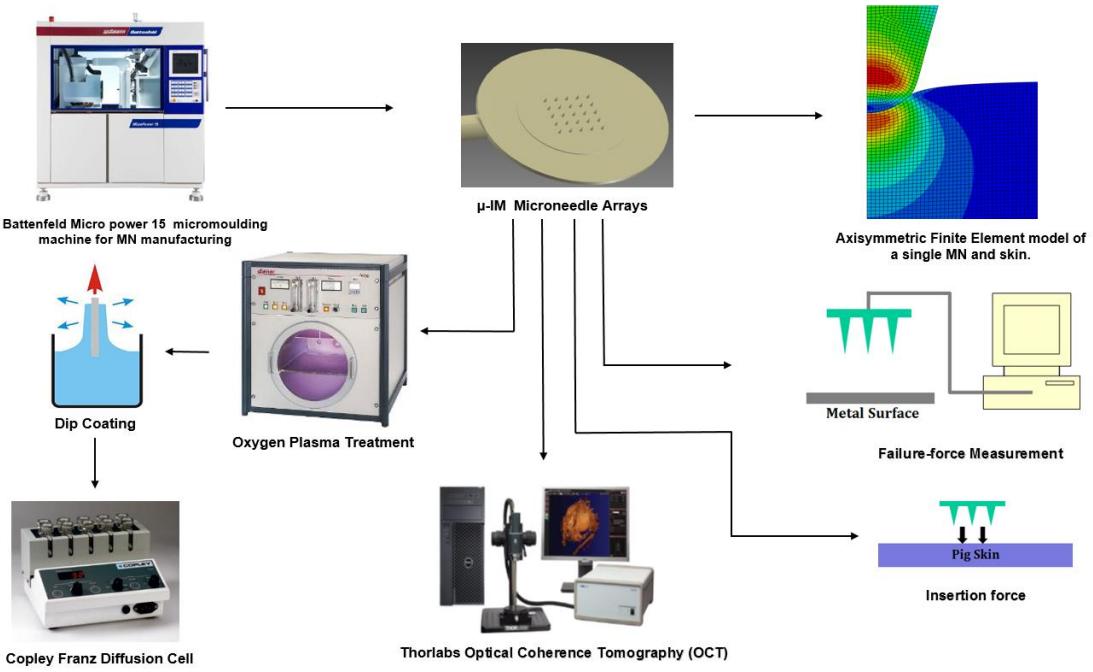

Figure 5.1 Schematic representation of the Chapter 5.

5.0. Introduction

It is of paramount importance to understand the penetration behaviour of microneedle arrays but it can be challenging to perform detailed experimental studies of the microneedle's interaction with skin tissue. In particular, the forces required to insert microneedles into the skin have to be quantified and related to the microneedle design. Knowledge of the mechanical properties, understanding the origin of insertion forces and behaviour of skin is a prerequisite to optimise microneedle design. A high insertion force can lead to breaking of individual needles, limiting the number of microneedles in an array (Davis, 2004 and Aggarwal *et al.,* 2004). Also, the insertion force directly relates to pain during the application process (Gill *et al*., 2008). 3D image analysis and simulation studies in addition to the skin penetration studies will shed insight into the most influential parameters that determine penetration performance which can be used to optimise needle designs. In addition, this data can be used to evaluate the impact of variation in needle forms produced during a real manufacturing process.

Skin, being a multilayer composite, exhibits highly non-linear, viscoelastic, anisotropic material properties during MN insertion where large tissue displacements and deformations are involved; consequently large local strains in the skin tissue can occur. In this chapter, methods to characterise the interaction between microneedles and porcine skin are introduced. Using these methods a careful and systematic experimental analysis of the needle-tissue interaction force curve was obtained. Here, we also describe the utility of OCT in studying MN insertion depth and position in porcine skin *in-vitro*.

The experimental studies are performed with different µIM-MN manufactured from polycarbonate (PC) and poly ether ether ketone (PEEK) under different insertion conditions, demonstrating the versatility of the approach. Furthermore, a finite element model of skin was established to understand the effect of tip geometry on penetration. Finally adsorption performance and BSA release kinetics for each sample set was assessed using Franz diffusion cell.

5.1. Experimental

5.1.1. Measurement of fracture force of the microneedles

To investigate the fracture force of the micro-injection moulded MNs, a series of experiments were conducted by compression of the MNs on a steel plate. All the compression tests were performed using a Bose Electroforce 3100 instrument with a 225 N load cell and Wintest® software (Bose, MN, USA), this instrument provides 1 mN force resolution and 0.001 mm displacement resolution. MNs made from PEEK and PC were compressed to the loads of 4, 8, 16 and 32 N in a load controlled mode at a rate of 1 N/s. Load and displacement were recorded during compression of the MNs to the steel plate. Videos during the compression test were captured with Pixelink PL-A776 3.1 mega pixel CMOS colour camera coupled with a 2X telecentric lens and a LED fibre optic telecentric illuminator and these videos were converted to sequences of still images using Image J® software.

5.1.2. Measurement of MN insertion force into neonatal porcine skin

To measure the actual force required to puncture the porcine skin, moulded MNs were mounted to the load cell of the Bose electro force instrument as shown in the Figure 5.2 (a). A bi-axial skin stretcher was used to hold the dermatomed abdominal neonatal porcine skin specimen under tension as shown in the Figure 5.2 (b). The MNs made from PEEK and PC were attached to the load cell and slowly driven towards the skin and MN-skin penetration were carried out using a load controlled mode at the rate of 1 N/s and a total of 8 N were utilised for this study.

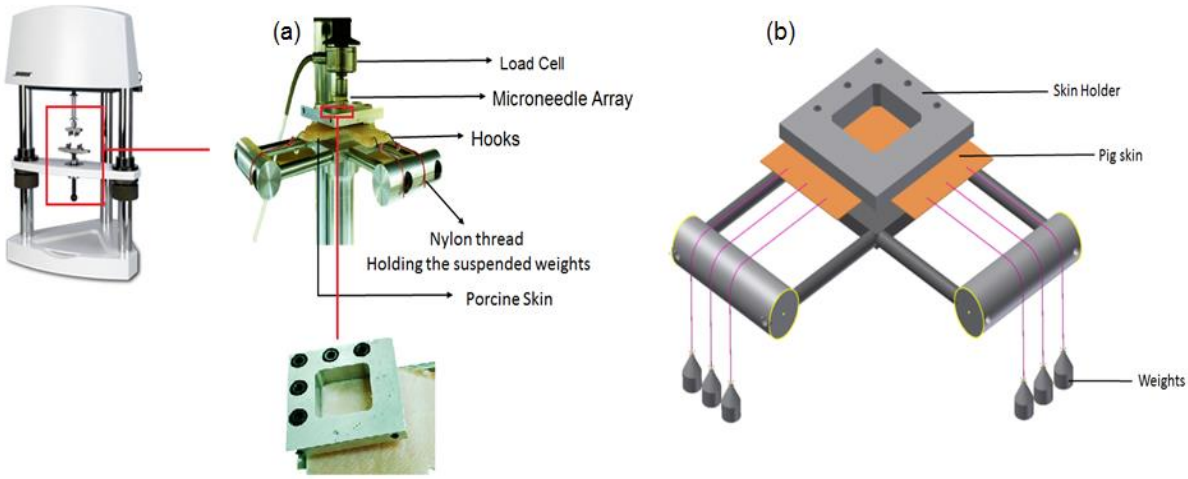

Figure 5.2 Schematic of the skin holding device for MN insertion (a) skin holding device and (b) schematic of the experimental setup.

5.1.3. Optical coherence tomography

Optical coherence tomography was used to visualise MN insertion into porcine skin *in vitro* in 2D and 3D. MN arrays were inserted into porcine abdominal skin using gentle finger pressure. Images were then obtained using high resolution swept source Telesto-II (shown in Figure 5.3) with LSM03 objective OCT

Imaging Systems from Thorlabs (Ely, UK). The spectral wavelength operates at 1325 nm with 10 mW of laser output facilitating real time high resolution imaging of the upper skin layers (7 µm lateral 12 µm vertical resolution). The skin was scanned at a frame rate of up to 76 kHz (A-Scan rate) per second (scan width=5 mm). 2D images were converted into a 3D representation using the imaging software ImageJ®.

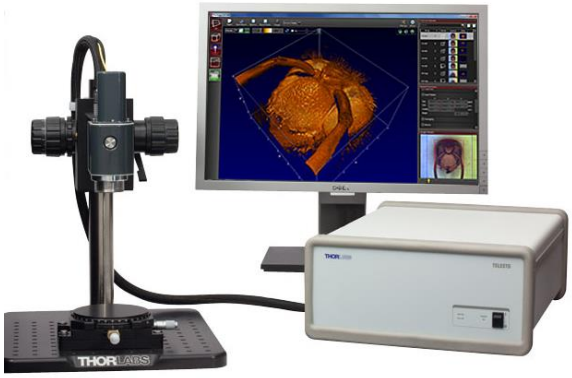

Figure 5.3 Image of the Thorlabs Optical coherence tomography.

5.1.4. Coating rows of microneedles

In-plane rows of microneedles were dip coated using an in-house designed coating device. The coating device consisted of two parts: (1) the micro-positioning dip coater and (2) the coating solution reservoir.

Micro-positioning dip coater: was designed to restrict access of the coating liquid only to the microneedle shaft to prevent contamination of the base, to provide sufficient time to the microneedle inside the BSA reservoir and to slowly retract the MNs from the reservoir. To enable three-dimensional alignment and dipping of microneedle arrays into the reservoir, a piezoelectric nano-positioner (PZA12) was assembled on a cross-roller linear stage which holds the MN arrays (Figure 5.4b). To view the whole dipping process a Pixelink PL-A776 3.1

mega pixel CMOS colour camera coupled with a 2X telecentric lens and a LED fibre optic telecentric illuminator were used (Figure 5.4b-f). The coating was performed automatically by custom software authored using Lab View software (National Instruments). A schematic of the dip coating setup is shown in Figure 5.4a.

Coating solution reservoir: The reservoir was custom made of specific dimension from quartz (Figure 5.4c). The BSA solution used for dip coating was of concentration 10 mg/ml solution.

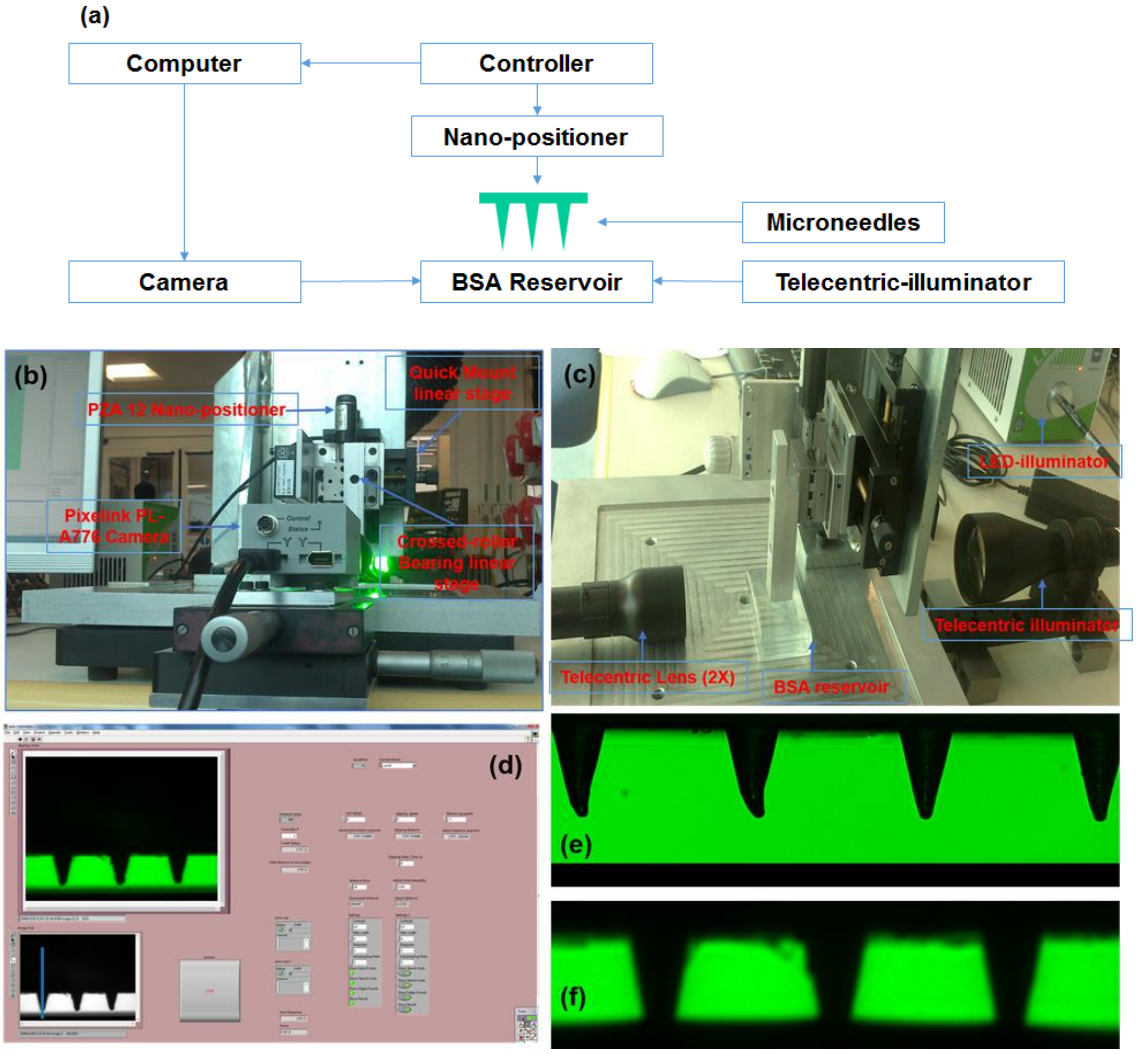

Figure 5.4 (a) schematic of the nano-positioner dip coating set up (b) photograph of dip coating apparatus showing individual components (c) side view showing the lens and the BSA reservoir (d) interface of the Lab-view software used to control the dip coating procedure (e) MN array as seen from the software before dip coating (f) while coating.

5.1.5. *In vitro* delivery of BSA across the neonatal porcine skin

Passive diffusion of BSA (a water soluble protein with MW 69 KDa) from the polymeric MN arrays across dermatomed abdominal neonatal porcine skin was investigated *in vitro* using Franz diffusion cells (FDC) (Copley, UK). Neonatal porcine skin samples were shaved and excess fat was removed and pre-equilibrated in phosphate buffer (PBS, pH 7.4) for 2 hours before the experiments. BSA coated MNs were inserted into the circular specimen of skin which was secured to the donor compartment of the FDC. It was then placed on top of the receptor cell which was filled with 7ml of PBS. This complete unit was then mounted on to the Franz cell with synchronously stirred using magnetic teflon stir bars at constant speed of 400 rpm and thermostabilised at 37±1ºC. A schematic of the experimental setup is shown in Figure 5.5. At different time points, aliquots from the receptor medium was withdrawn from the sampling arm and replaced with fresh preheated phosphate buffer pH 7.4 (at 37ºC) . The sink condition was maintained throughout the experiment and concentration of BSA in the receptor medium was determined using HPLC (the HPLC method was the same as that mentioned in Chapter 4.1.7). The cumulative amount of BSA permeated was calculated using PCP disso Software.

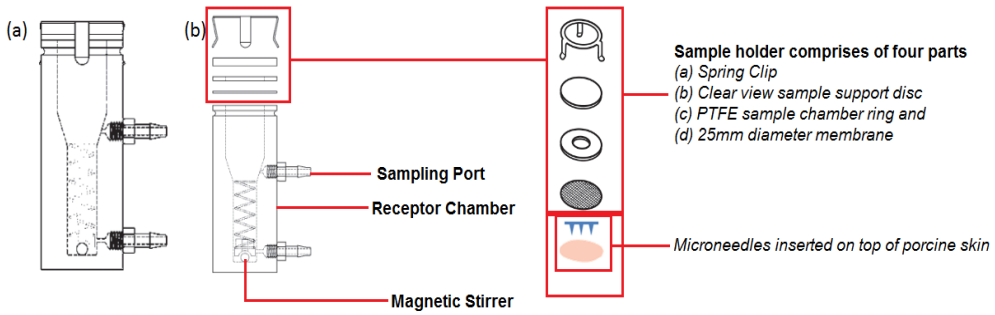

Figure 5.5 Schematic of the Franz diffusion experimental setup (a) vertical diffusion cell (b) exploded view of the cell and sample holder.

5.1.6. Quantification of the residual BSA from the MN shaft after insertion.

Untreated and plasma treated MNs were dip coated with 10 mg/ml of BSA for 10 minutes. These MNs were then inserted into the porcine skin using the thumb pressure and removed after 15 mins. The MNs after the insertion were transferred to a vial containing 2.5 ml of PBS solution and ultra sonicated to remove the residual BSA on the MNs and the amount of the residual BSA was then quantified using the HPLC method.

5.1.7. Finite element analysis

Finite element analysis was modelled using the Abaqus Explicit commercial software package. The skin and tip of the microneedles were meshed separately and the skin was modelled using the Ogden material model. (Ogden, 1972). The size of the modelled skin volume was a cylinder of 100 μm radius and 100 μm depth with 1225 linear quadrilateral elements and 1296 nodes. The number of linear quadrilateral elements and nodes in the needle model were 1303 and 1399 respectively.

After meshing the following material properties were assigned to the model.

Material of needle (PEEK): Linear elastic; Young's Modulus=3600 MPa, Poisson's Ratio=0.36 (Density=1.32e-9 tonnes/mm^3).

Material of skin (porcine): Single layer. Linear elastic; Young's Modulus=57.7 MPa, Poisson's Ratio=0.48 (Density=1.05e-9 tonnes/mm^3).Contact interaction: Coulomb friction with mu=0.1.

5.2. Results and discussion

5.2.1. Nano-dip coating microneedles

Solid microneedles are generally used for drug delivery by coating the drug or protein onto the MN shaft and then inserted into the skin, but there are no detailed

studies of the coating process itself. Therefore it is very important to identify a rational basis of coating strategies, which will enable uniform coating of therapeutics. Although dip-coating is a simple process which is able to coat complex geometries, special considerations should be taken while coating micron-scale microneedle shafts. This is mainly because of the effects of surface tension and capillary forces which become more prominent at these micron scales. Therefore in this study a novel nano-dip coating process was developed that will

1. Make a uniform coating of BSA possible.
2. Limit the BSA deposition only to the microneedle shaft and not to the base plate.
3. Use an aqueous solution preventing denaturing of BSA.

4. Provide sufficient time for the microneedle shaft inside the BSA reservoir for the coating process to occur.

Using the nano-positioner dip coating device as mentioned in the material method section (5.1.4) it was possible to move the MN array and simultaneously visualise the dipping process, restricting the coating solution to MN shaft. This physical masking eliminated BSA contact with the MN base plate and overcame issues with surface tension and capillary forces.

5.2.2. Delivery of BSA from coated MNs

Figure 5.6 shows the comparative passive permeation of BSA across neonatal porcine skin when released from PEEK untreated and plasma treated microneedles. The results indicate that the BSA delivery from the plasma treated MNs was found to be more efficient than that from untreated MNs. Although plasma treated MNs were able to receive a higher amount of the BSA during coating than untreated samples, the total amount of the BSA that could be delivered was limited because of relatively small surface area of the MNs. Using BSA as a model drug a maximum of 1 µg of BSA (totally loading amount) was coated on 25 plasma treated MNs (550 µm long and 300 µm wide). The plasma treated and untreated MNs showed similar release for the initial 6 hours and during the 24 hours it was found that more than 60% of BSA permeated from plasma treated MNs. This is because plasma treatment increases the surface energy and enhances BSA adsorption onto the needle shaft. (detailed mechanism of BSA adsorption before and after plasma treatment discussed in Chapter 4.2.1).

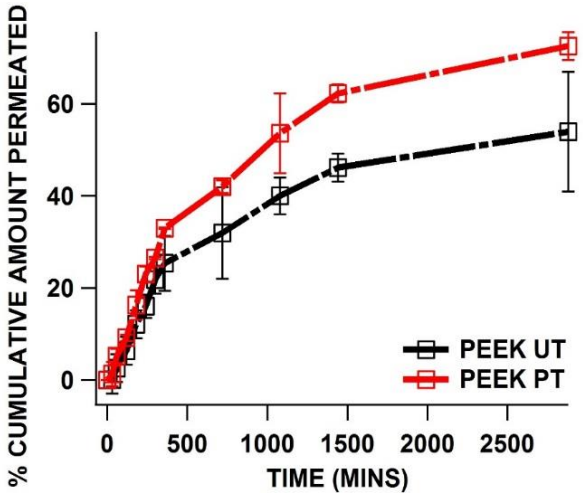

Figure 5.6 Permeation comparison of BSA coated untreated and plasma treated PEEK microneedles.

In theory, the skin limits diffusion of any molecules larger than 500 Da (Brown *et al*., 2006 and Han, 2013) with a partition coefficient between 1-5 while passing through the stratum corneum. (Kushner, 2006 and Kalia *et al*., 2001). BSA has a molecular weight in the range of 66 to 69 kDa (Hamidi, 2009) which is significantly higher than 500 Da, so delivery of these kind of proteins is very difficult using transdermal patches. Devin *et al* studied permeability of BSA using 150 µm long MNs and found permeability to be 0.02 µm/s and suggested the use of longer needles for better permeability. In this study MNs of 550 µm in length were used and pre-treating these MNs using plasma we were able to permeate over 600 ng of BSA across the porcine skin in 24 hours which is a reasonable amount considering the large size of the BSA molecule. This suggests the potential for using MNs for transporting large molecules through human skin. Molecules like insulin which is smaller than BSA should have better permeability if a MN delivery method was to be used. The primary reason for selecting BSA as the model drug for this study was because BSA is a hydrophilic molecule with molecular weight range between the size of peptide and vaccines and it is less prone for skin metabolism.

5.2.3. Quantification of the residual BSA from the MN shaft after insertion

Solid MNs are generally used for proteins and vaccine delivery and the efficiency of these MNs depends on how quick the coated formulation is released from MNs to the skin. In this study we quantify and compare the residual BSA that is left in the untreated and plasma treated MN shaft after insertion onto porcine skin for 15 mins. Figure 5.7 shows the amount of BSA loaded (assay) and residual (after insertion) to untreated and treated MNs of PEEK and PC.

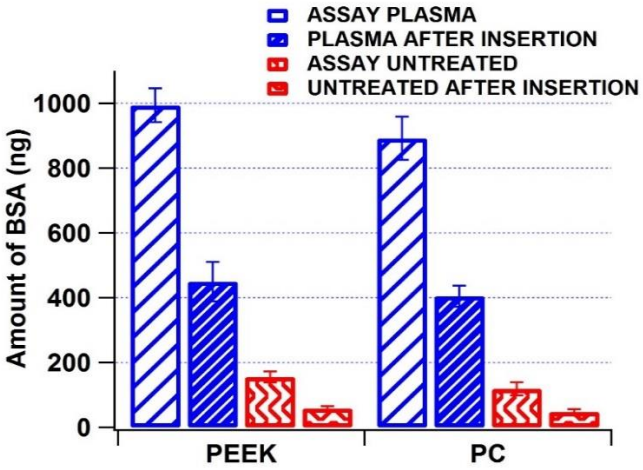

Figure 5.7 showing the comparison of amount of BSA coated on to the plasma and untreated PEEK and PC microneedles and residual BSA from the needle after insertion.

It is evident that the plasma treated MNs could load up to 1 µg of BSA and the residual amount after insertion was found to be 428 ng that means 572 ng of BSA was been delivered into the skin in first 15 mins whereas in the case of untreated MNs could only load 183 ng and the residual amount after insertion was found to be 64 ng which means 119 ng of BSA was delivered into skin from the untreated MNs. From this it was observed that the amount of BSA loaded was more in the case of plasma treated MNs and just over half the amount was

released but the in the case of the untreated MNs even though the initial loading was 5.7 times over than the plasma treated MNs the proportion of the original amount which was delivered to the skin was slightly higher (65% vs 57.2%). This is because plasma along with increasing the surface energy of the polymer surfaces it also increases the adhesion of BSA to the MN shafts resulting in a reduced release rate.

5.2.4. Fracture force determination

Skin exhibits viscoelastic behaviour and bending of the microneedles could occur if the MNs are not strong enough during insertion (Gittard *et al*., 2013). Moreover the skin is not uniform throughout the body which can affect the MN insertion force so it is of paramount importance to experimentally measure the effect of the MN geometry on the force required to insert MNs into skin and the forces the needles can withstand before fracturing. In this study, the mechanical property (measurement of fracture force) of the injection moulded microneedles was examined. The MN arrays of PEEK and PC were compressed on to a steel plate and force versus displacement was measured along with video data. The MNs underwent compression forces ranging from 4 N to 32 N. Figure 5.8 (a) shows all the events occurred at different load during the experiment whereas Figure 5.8. (b) shows the PEEK MN fracture mechanism.

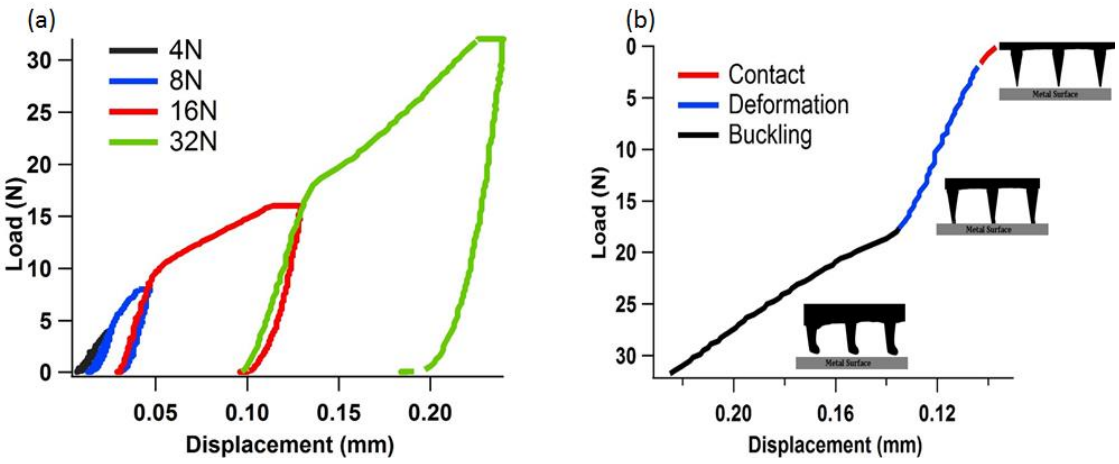

Figure 5.8 MN failure force results (a) graph showing all the events of PEEK MN failure at different load during the experiment (b) characteristic force vs displacement plots showing the PEEK MN fracture mechanism.

SEM images of the microneedles after compression with a 32 N force are provided in Figure 5.9. Both the MNs made from PEEK and PC were able to sustain forces up to 8 N without any visual signs of plastic deformation. At forces above 16 N a slight plastic deformation of the tip was seen (Figure 5.8 a) and with 32 N of force a complete plastic deformation of the needle tip was observed.

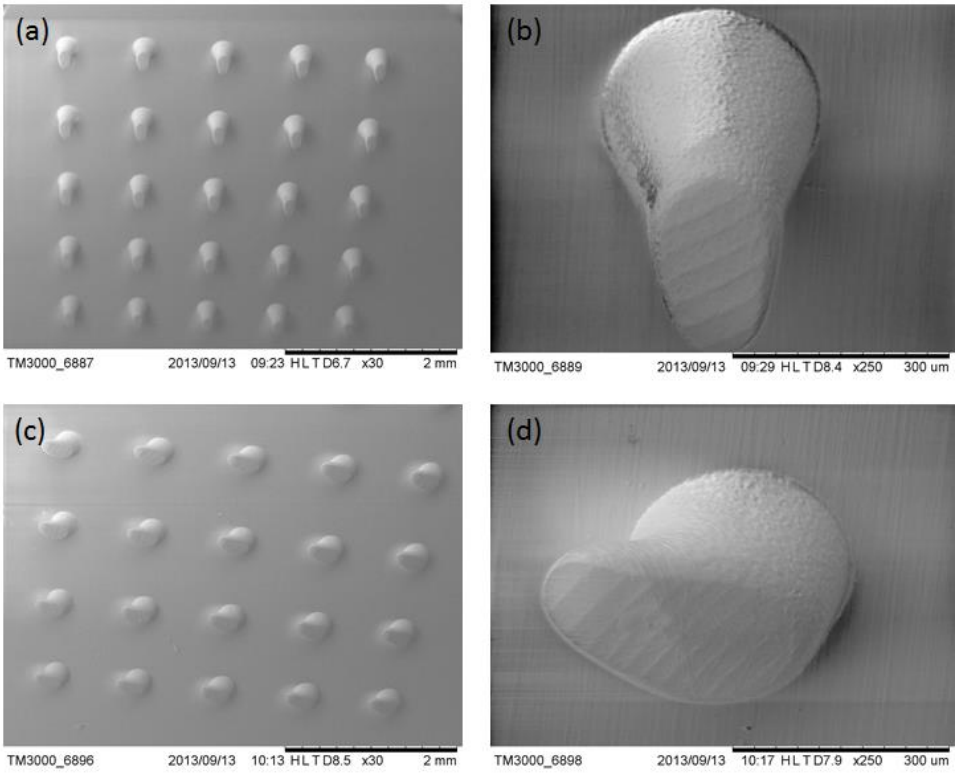

Figure 5.9 (a) SEM image of PEEK MN array after compression test (b) single PEEK MN (c) PC MN array (d) PC single MN.

Another significant observation is that none of the MNs showed fracture near the tip, rather bending of the needles at forces greater than 16 N was seen. These results shows that the polymeric moulded MN arrays could withstand high insertion forces without breaking the tip into the skin, which is very important factor considering the risk associated with tip breakage during MN application.

5.2.5. Force of insertion

Although many MN designs have been proposed, not all of them are capable of penetrating into the skin and there is very limited knowledge available regarding MN design for skin penetration (Davis *et al*., 2004). Recently many researchers

started using OCT imaging to visualise microneedle penetration, but the mechanics involved are not clearly understood (Coulman *et al*., 2011 and Groves *et al*., 2012). Park *et al* carried out experiments to find out the relationship between MN geometric factors and skin penetration and observed that the sharper the tip, lesser the insertion force however they also noticed sharper tips are susceptible to breakage. Aoyagi *et al* examined the effects of tip angle on insertion force for poly lactic acid MNs. From the literature available we could understand that most of the common techniques used for measuring the MN skin penetration are transepidermal water loss (TEWL), (Verbaan *et al*., 2007; Vemulapalli *et al*., 2008 and Sivamani *et al*., 2009) electrical resistance and post penetration staining methods. (Choi *et al*., 2006 and Park *et al*., 2007). More over in some studies MN penetration was carried out using thick rubber sheets (Shek, 2008). In this study force required for MN skin penetration was determined using force displacement behaviour. Injection moulded polymeric microneedles of PEEK and PC were brought in contact to the porcine (details as mentioned in the experimental section 5.1.2) while continuously measuring the needle force and displacement. Figure 5.10 shows the representative graph showing all the events of PEEK MN penetration.

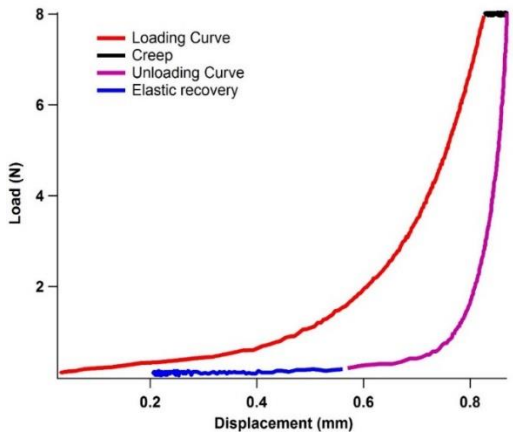

Figure 5.10 Graph showing all the events of MN penetration.

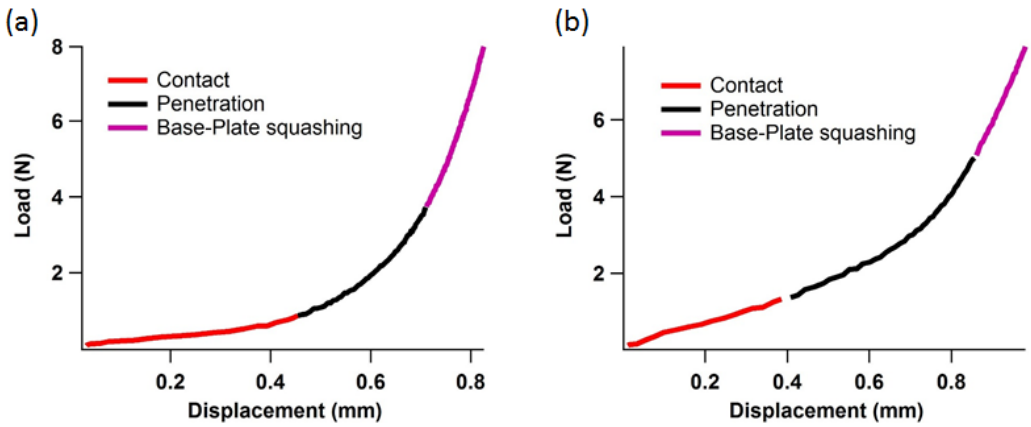

Figure 5.11 Skin penetration force vs displacement for MN penetration of full thickness porcine skin in load control mode (a) PEEK (b) PC.

Figure 5.11 shows force vs displacement for PEEK and PC MNs and it reveals that the force required to press the needle against the porcine skin increased with displacement, it also showed three separate sections the initial one being all the MN arrays coming in contact with the skin followed by the actual penetration and finally a steep slope after insertion which was due to base plate quashing against the skin. From these experiment it was found that the actual insertion force for PEEK and PC MNs were 1.2 and 1.5 N respectively. These insertion forces are well within the deformation force calculated suggesting that the injection moulded polymeric MNs are mechanically strong enough to penetrate porcine skin for MN drug delivery.

5.2.6. Optical coherence tomography (OCT)

Microneedle insertion behaviour and the morphology of the channels created into the skin are usually characterised by traditional histological methods and

relies on the biopsy of the MN treated skin area and subsequent histological analysis (fixation and sectioning) (Coulman *et al*., 2011). These kind of experiments could alter the skin structure and may produce artefacts. (Godin *et al*., 2007 and Welzel, 2001). Although these experiments could confirm if the stratum corneum has been comprised, but they do not reveal the true depth of penetration (Donnelly *et al*., 2010).

Limitations of analytical instruments and experimental procedures have prevented the exact measurement of micro channels in skin following MN insertion. Significant advancements have been made in last decade on optical imaging techniques and optical coherence tomography is one among them. OCT is a non-invasive interferometric technique which enables imaging skin architecture *in vivo* and in real time with high resolution up to a depth of 2-2.5 mm (Huang *et al*., 1991). In this study a state of the art OCT imaging system was used *in vitro* to visualise the penetration of the polymeric MNs in real time while it was inserted into the porcine skin *in-vitro*. The OCT system generates real time data as a sequence of images in x-z plane and therefore can create 2D and 3D images of the skin. For representational clarity most of the data are shown in 3D (Figure 5.12 a-d)

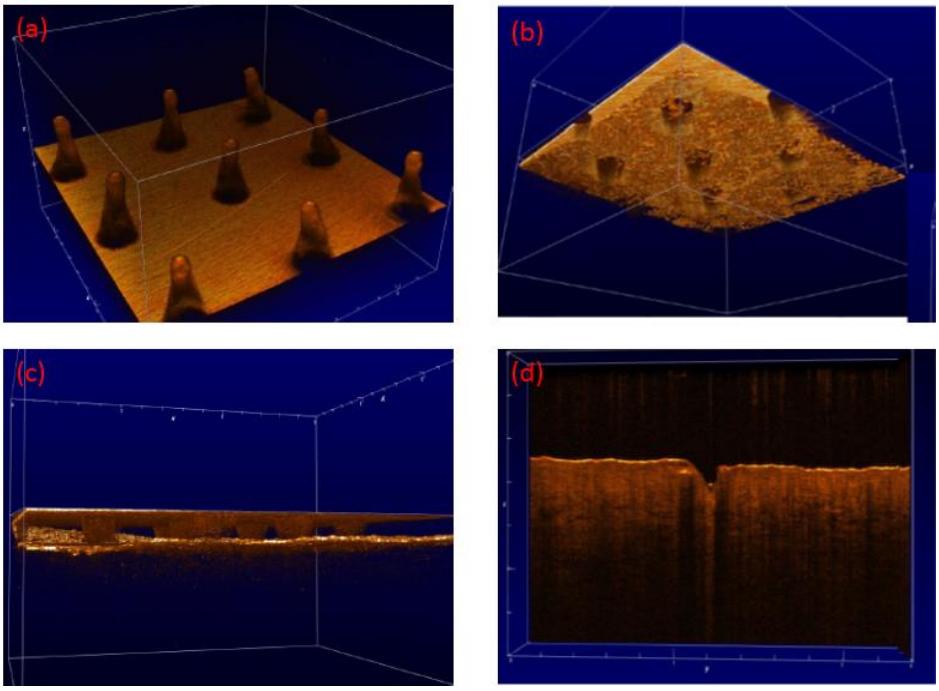

Figure 5.12 (a) OCT 3D volume data of PEEK before insertion (b) 3D volume data of PEEK MN array while inserted in pig skin view from below the skin (c) view through the air gap between the base-plate and skin (d) resealing of the skin.

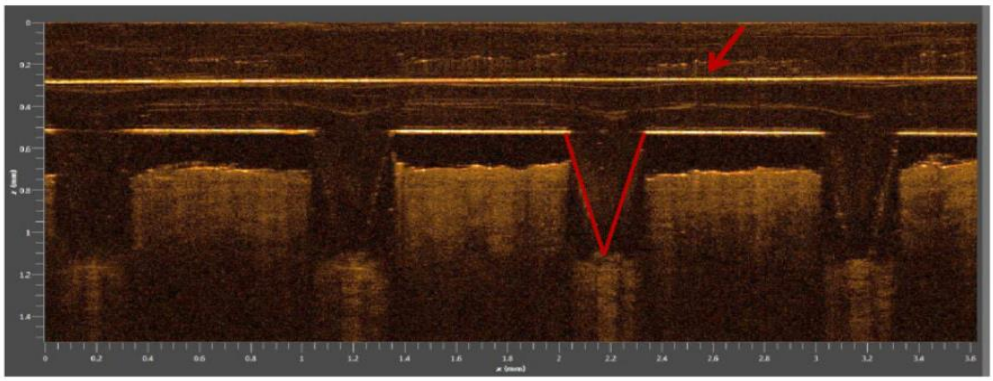

Figure 5.13 OCT Cross-section images acquired during PEEK MN insertion into porcine skin. The red lines indicate the borders of the MN cone. The first line (indicated by arrow) corresponds to the base plate of the MN array.

From Figure 5.12 (c) and Figure 5.13 it was observed that around 80% of the MN shaft penetrated into the skin, leaving a clear gap between the stratum corneum and MN base-plate. It was also found out that approximately 70 minutes was required for the skin to reseal after the removal of the inserted microneedles. The response of human skin to MN insertion is dictated by the biomechanical properties of the tissue. OCT images of the porcine skin

punctured by PEEK MNs shows that around 440 µm (from the total length of 550 µm) of the needle shaft was able to penetrate the skin and this is because of the elastic behaviour of the skin.

In this study the OCT has been successfully used to capture images of the MNs penetration *in situ in vitro* demonstrating the performance of the microneedles. This imaging technique recently have made a significant implication in the microneedle research community and generating bio-mechanical response of skin to MN insertion and how different designs could alter the penetration performance in real time. Additionally OCT could also be used for to extract useful information relating to the deposition of the drug upon insertion from the coated solid microneedles.

5.2.7. Finite element analysis

To enable predictive design of the MNs, a greater understanding of the biomechanical properties of stratified human skin and the mechanics of skin penetration is essential. A computational model of skin and MNs could quantify and predict the micro-scale deformation that takes place during insertion.

Anatomically skin comprises of three layers, namely: epidermis, dermis and the underlying hypodermis. The outer most sub layer of the epidermis is stratum corneum which is responsible for resistance to microneedle insertion. (Groves *et al*., 2012). The dermis is made up of matrix of collagen and elastin fibres, and is responsible for strength and flexibility. When load is applied to the skin, these elastin fibres align and increase the stiffness to endure the deformation (Brown, 1973). The hypodermis (sub cutaneous fat), is a soft structure which gives the cushioning to the overlaying tissue. All these layers, with different material

properties, give the skin very complex bio-mechanical attributes. Moreover skin is considered to be an anisotropic and viscoelastic material, which can withstand large deformations. The skin's bio mechanical properties could significantly vary with age, race and location within the body. Due to the skin's complexity, creating an accurate model of the human skin is challenging.

In this study an axisymmetric finite element model of the MN and skin was used to create a predictive model to find the effect of microneedle tip size on penetration.

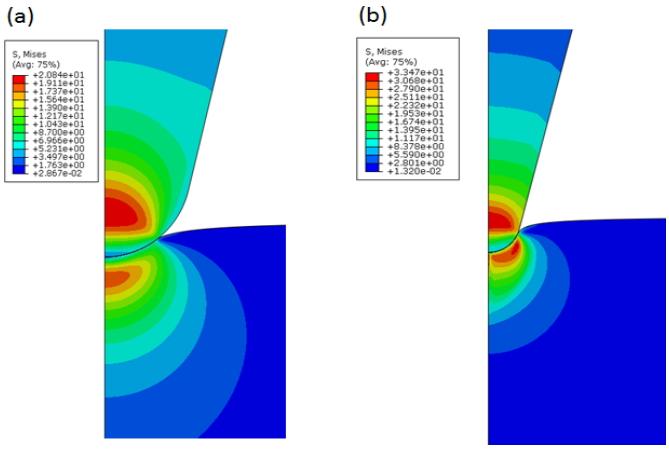

Figure 5.14 Axisymmetric Finite Element model results showing Von Mises stress contours for a single MN indenting skin with tip radius (a) 30 μm and (b) 10 μm.

Figure 5.14 shows images of the FE model of microneedle with two different tip radii, 30 μm and 10 μm, indenting porcine skin. From this simulation it was observed that, higher stress in the skin using MN with 30 μm tip radius as compared to 10 μm suggesting that a sharper tip will result in need of less penetration force. An axisymmetric model was used in this study, as it requires less computation however, in an event like buckling of the MNs this model won't be able to show the simulation which is drawback of this model.

5.3. Conclusions

Microneedles manufactured from PEEK and PC using micro-injection process were shown to possess appropriate material properties for transdermal drug delivery. Both the investigated polymers with their geometries were able to penetrate porcine skin; the forces for the skin penetration were 10 times less than the forces at which microneedle fracture took place. Skin penetration observation revealed that microneedle piercing of the skin is not a single event instead it is a series of event before the MNs could progressively penetrate deep into the skin. In this study a unique MN dip coating system was developed which allows to successfully coat the BSA to the MN shaft without contaminating the base plate and these coated needles were subsequently tested for skin diffusion studies and results confirmed that plasma treated MNs could adsorb and deliver the protein more effectively than untreated MNs. Furthermore we have shown the utility of OCT in an effective determination of the location and the true depth of the MNs while penetration. Finally a finite element model of the skin and needle was established to understand the effect of tip geometry on penetration.

5.4. References

1. Aggarwal P and Johnston CR, Geometrical effects in mechanical characterizing of microneedle for biomedical applications, *Sensors and Actuators B: Chemical* **102** (2004) 226-234.

2. Aoyagi S, Izumi H and Fukuda M, Biodegradable polymer needle with various tip angles and consideration on insertion mechanism of mosquito's proboscis, *Sensors and Actuators* **143** (2008) 20-28.

3. Choi JW, Park IB, Ha YM, Jung MG, Lee SD and Lee SH, Insertion force estimation of various microneedle array types structures fabricated by micro steriolithography apparatus, SICE-ICASE International Joint Conference, Busan, South Korea, (2006) 3678–3681.

4. Brown MB, Martin GP and Jones SA, Akomeah FK, Dermal and transdermal drug delivery systems: Current and future prospects, *Drug Delivery* **13** (2006) 175–187.

5. Brown IA, Scanning electron-microscope study of effects of uniaxial tension on human skin, *British Journal of Dermatology* **89** (1973) 383–393.

6. Coulman SA, Birchall JC, Alex A, Pearton M, Hofer B, O'Mahony C, Drexler W and Povaz˘ay B, In vivo, in situ imaging of microneedle insertion into the skin of human volunteers using optical coherence tomography, *Pharmaceutical Research* **28** (2011) 66–81

7. Devin V, Ping MW, Shawn PD, Jung HP, Paul JC, Mark GA and Mark RP, Microfabricated needles for transdermal delivery of macromolecules and nanoparticles: Fabrication methods and transport studies, *PNAS* **100** (2001) 13755–13760.

8. Davis SP, Landis BJ, Adams ZH, Allen MG and Prausnitz MR, Insertion of microneedles into skin: measurement and prediction of insertion force and needle fracture force, *Journal of Biomechanics* **37** (2004) 11551163.

9. Donnelly R.F, Majithiya R, Singh TR, Morrow DI, Garland MJ, Demir YK, Migalska K, Ryan E, Gillen D, Scott CJ and Woolfson AD, Design, optimisation and characterisation of polymeric microneedle arrays prepared by novel laser-based micromoulding technique, *Pharmaceutical Research* **2** (2010) 169-178.

10. Groves RB, Coulman SA, Birchall JC and Evans SL, Quantifying the mechanical properties of human skin to optimise future microneedle device design, *Computer Methods in Biomechanics and Biomedical Engineering* **15** (2012) 73–82.

11. Godin B and Touitou E, Transdermal skin delivery: predictions for humans from in vivo, ex vivo and animal models, *Advanced Drug Delivery Reviews* **59** (2007) 59(11) 1152–1161.

12. Gittard SD, Chen B, Xu H, Ovsianikov A, Chichkov BN, Monteiro-Riviere NA and Narayan RJ, The effects of geometry on skin penetration and failure of polymer microneedles, *Journal of Adhesion Science and Technology* **27** (2013) 227-243.

13. Gill HS, Denson D, Burris BA and Prausnitz MR, Effect of microneedle design on pain in human subjects, *Clinical Journal of Pain* **24** (2008) 585–594.

14. Han T and Das DB, Permeability enhancement for transdermal delivery of large molecule using low-frequency sonophoresis combined with microneedles, *Journal of Pharmaceutical Sciences* **102** (2013) 3614–3622.

15. Huang D, Swanson E, Lin C, Schuman J, Stinson W and Chang W, Optical coherence tomography, *Science* **254** (1991) 1178–1181.

16. Hamidi M and Zarei N, A reversed-phase high-performance liquid chromatography method for bovine serum albumin assay in pharmaceutical dosage forms and protein/antigen delivery systems, *Drug Testing and Analysis* **1** (2009) 214–218.

17. Kushner J, Theoretical and experimental investigations of passive and ultrasound-enhanced transdermal drug delivery, PhD Thesis, Cambridge: Massachusetts Institute of Technology (2006).

18. Kalia YN and Guy RH, Modeling transdermal drug release, *Advanced Drug Delivery Reviews* **48** (2001) 159–172.

19. Ogden RW, Large deformation isotropic elasticity - on the correlation of theory and experiment for incompressible rubber like solids, *Proceedings Royal Society of London A mathematical, physical and engineering Science*, **326** (1972) 565–584.

20. Park JH, Yoon YK, Choi SO, Prausnitz MR, Allen MG, Tapered conical polymer microneedles fabricated using an integrated lens technique for transdermal drug delivery, *IEEE Transactions on Biomedical Engineering* **54** (2007) 903-913.

21. Sivamani RK, Stoeber B, Liepmann D and Maibach HI, Microneedle penetration and injection past the stratum corneum in humans, *Journal of Dermatological Treatment* **20** (2009) 156-159.

22. Shek KT and Lam DCC, Insertion behaviour of microneedles for drug delivery, *Advanced Materials Research* **47-50** (2008) 1442-1445.

23. Verbaan FJ, Bal SM, van den Berg DJ, Groenink WHH, Verpoorten H, Luttge R and Bouwstra JA, *Journal of Controlled Release* **117** (2007) 238-245.

24. Vemulapalli V, Yang Y, Friden PM and Banga AK, Synergistic effect of iontophoresis and soluble microneedles for transdermal delivery of methotrexate, *Journal of Pharmacy and Pharmacology* **60** (2008) 27-33.

25. Welzel J, Optical coherence tomography in dermatology: a review, *Skin Research and Technology* **7** (2001) 1–9.

Chapter 6 Micro-injection moulding of hollow microneedles

Graphical abstract

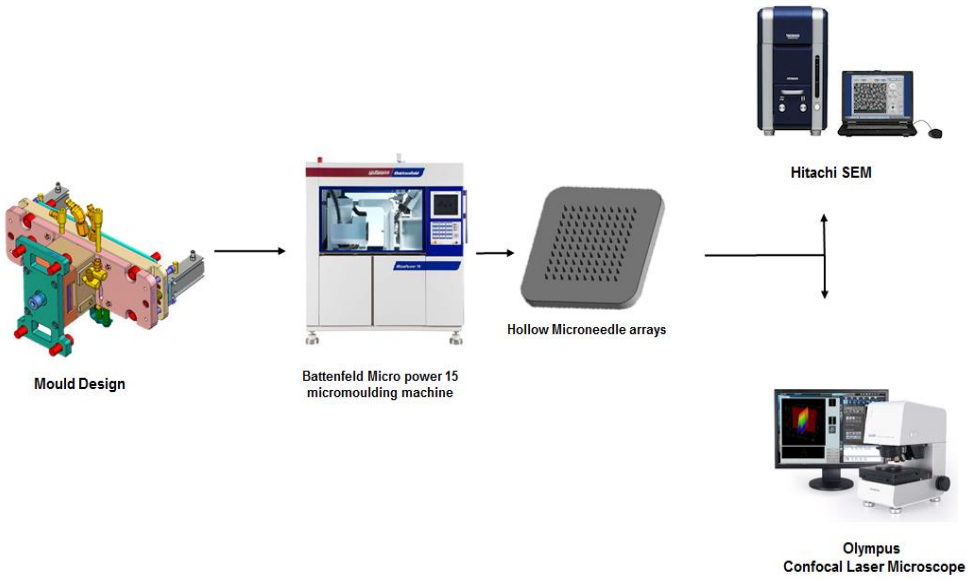

Figure 6.1 Schematic representation of the Chapter 6.

4.0. Introduction

Drug delivery using solid microneedles is generally achieved by pre-coating the surface of the MNs with active pharmaceutical ingredients (APIs) and then inserted into the skin for the drug to be absorbed and diffused into the dermis (Wang, 2009; Prausnitz, 2004 and Banga, 2009). However the major limitation of this method is that the amount of the drug released and time of the delivery are all constrained by limited surface area of the solid needles and limitation of the coating techniques (Bal *et al*., 2010). An array of hollow MNs offer lots of advantages compared to their solid counterpart (Roxhed *et al*., 2008). Hollow MNs can facilitate a pressure driven fluid flow thereby enabling faster rates and higher volume of drug delivery in a similar fashion to conventional hypodermic needles. Furthermore, the dose of the desired API can be controlled with the needs of the patient (Maaden *et al*., 2012). This can be achieved via passive or active diffusion through the bore of the MN (Nuxoll *et al*., 2009).

Hollow MNs are most commonly used for drug delivery but recently significant research is carried out in biological fluid withdrawal from the body for bio-chemical sensing which include blood and interstitial fluid. This has got potential application of hollow microneedles to be used with patients with renal dysfunction. Patients with renal failure carry excess of fluid volumes and because of the limited capability of the intravascular and intracellular compartments to expand it is found that the most of the accumulated fluid is in the interstitial compartment (Ebah, 2012). This results in several of the waste products due the malfunctioning kidney to accumulate within body fluids and become toxic to cells and metabolic process (uremic toxins). Blood studies are carried out to understand the physiological and pathophysiological composition

of the extracellular fluids and measurement of this in clinical practice is used for diagnosis and monitoring of renal disease and assessment of the renal therapies like dialysis. This demands frequent blood sampling from the patients with inconvenience of repeated venipuncture and also this method does not give enough information about the interstitial composition (Nahas and Bello, 2005). A direct and minimally invasive or non-invasive technique of extracting interstitial fluid using hollow MNs will become a key tool to help bridge the knowledge gap of interstitial fluid composition and will potentially simplify and improve renal patient monitoring (Ebah, 2012).

Despite the several advantages which hollow MNs offer, it is extremely difficult and expensive to manufacture the micron-sized needle arrays. The main aim of the work described in this Chapter was to design, optimise and manufacture hollow polymeric biocompatible MN array system using micro-injection moulding for extraction and analysis of interstitial fluid during renal disease.

6.1. Experimental

6.1.1. Mould design and fabrication

A three plate mould was designed which has key features required for electrical heating, (as oil heating is not ideal for medical device manufacture) venting and vacuum. This customised tool was sourced from Isometric tool and design in Wisconsin, USA, who are a leading provider of micro featured injection-mould tools worldwide.

Figure 6.2 shows the photograph of the mould and magnified photographs of the mould inserts. A technical 3D drawing of the mould showing each part is shown in Figure 6.3-6.5.

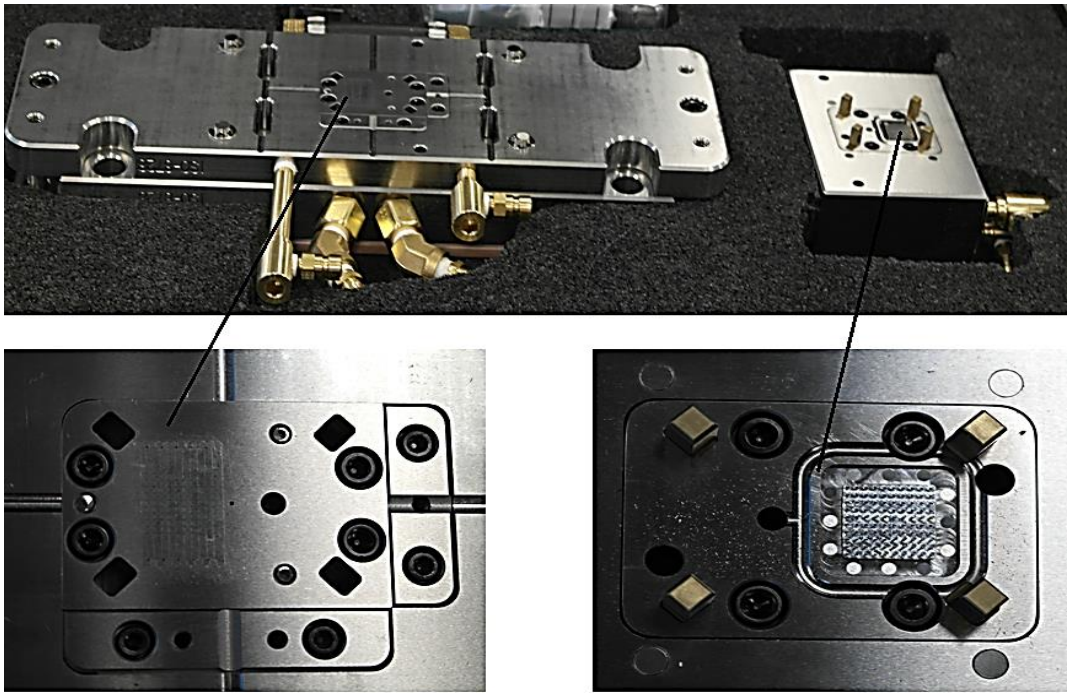

Figure 6.2 Photograph of the mould assembly showing the magnified picture of the A and B side of microneedle insert.

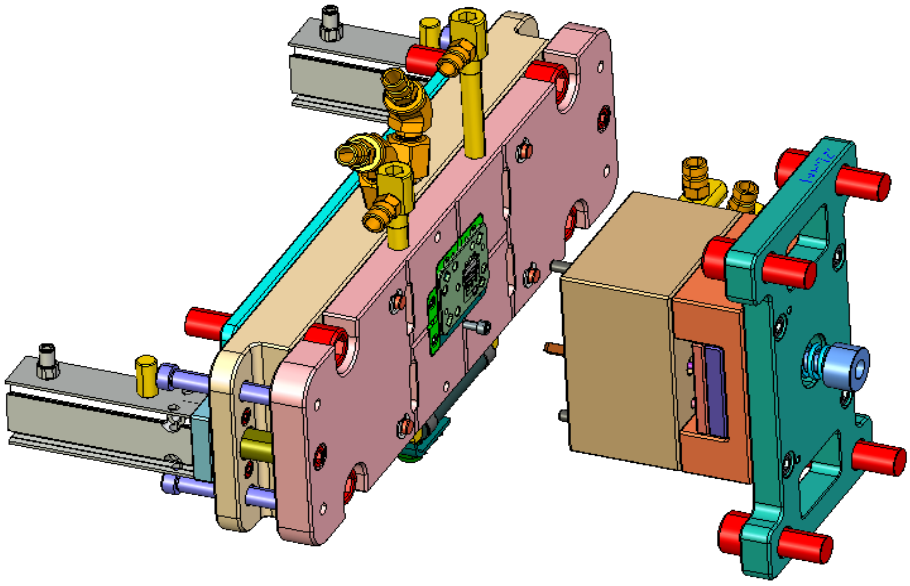

Figure 6.3 3D drawing of the mould assembly.

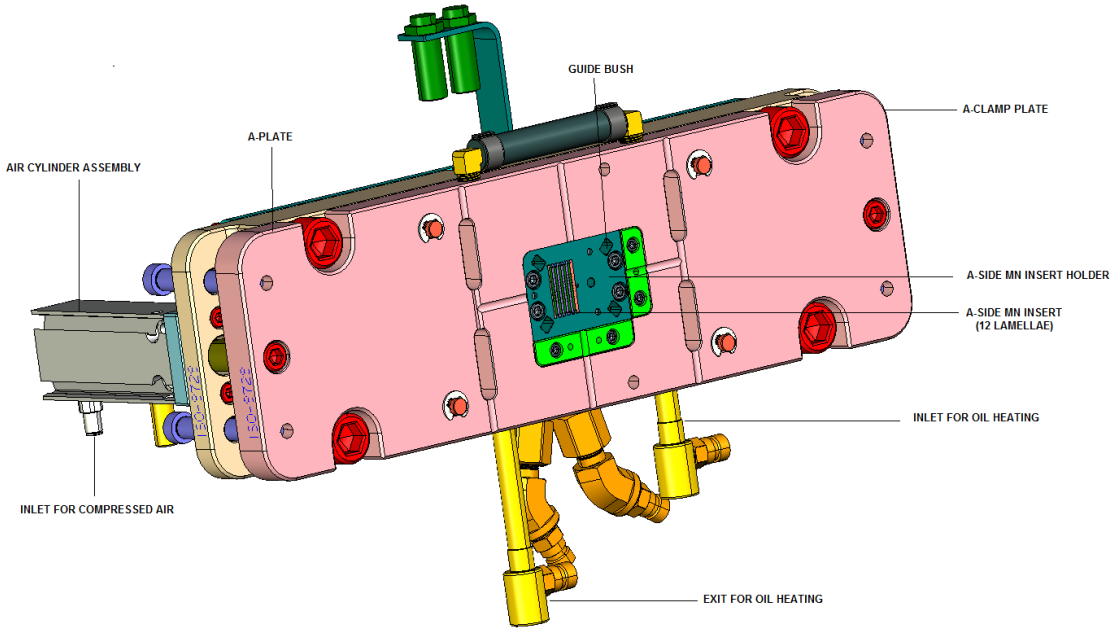

Figure 6.4 Labelled 3D technical drawing of A-side of the mould assembly showing various components of the mould.

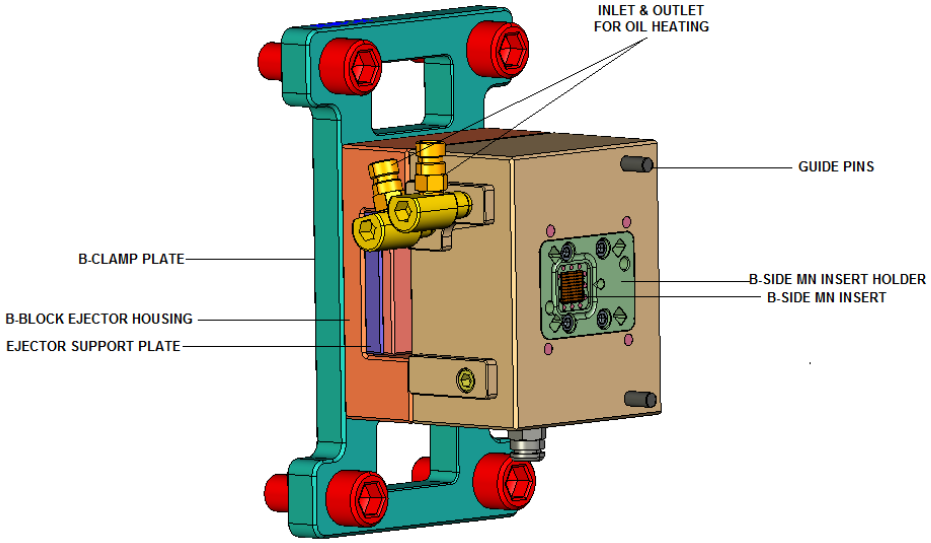

Figure 6.5 Labelled 3D technical drawing showing various components of the B-side of the mould assembly.

4.1.2. MN mould inserts and part geometry

The MN mould inserts which form the microneedles comprises of 2 separate insert units: (1) A-side MN insert (Figure 6.4) and (2) B side MN insert (Figure 6.5), where the first insert is located in the A side of the mould and second is located in the B side of the mould. Both the MN inserts were fabricated by Isometric tool and design using a low voltage EDM process. A 420 stainless steel plate with surface roughness approximately 0.3 µm was used to create the MN insert. The A-side insert consists of 11 stacked laminates with each laminate containing plurality of cavities and core on each side of the laminate. All 11 laminates are held together by a MN insert holder as shown in Figure 6.6a. Each laminate is numbered L1 to L11 for reference. 10 negative cavities having the shape of a half pyramid or (V) shaped groove as shown in Figure 6.6b were machined into the top surface of each laminate with exception of L11.

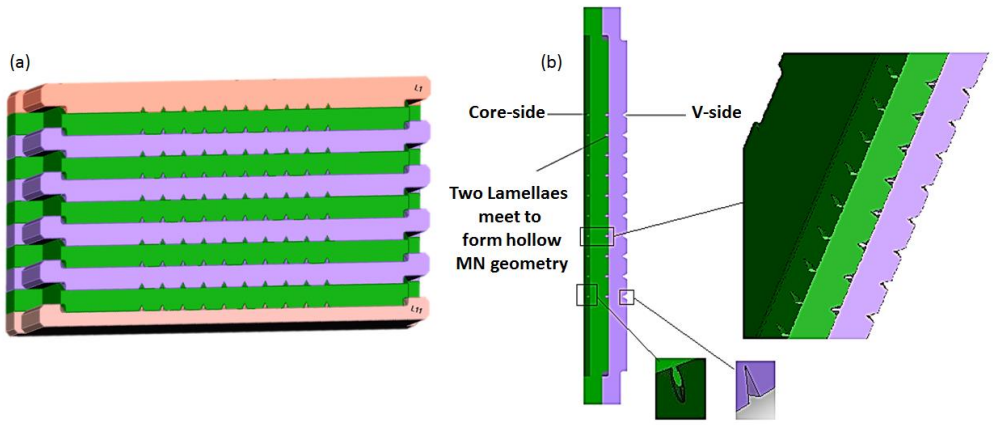

Figure 6.6 (a) Showing the stacked laminate assembly (b) depicts a side view of the laminate showing v-side and core side.

Another 10 structured cavities with an ellipsoidal shape (core side) was made on the exact opposite V-side of the laminate Figure 6.6b with exception of

laminate 1. All 11 laminates are stacked together such that laminate with the core side slides between the laminate having the V-side as shown in Figure 6.6a. This assembly was held together with the help of MN insert holder shown in Figure 6.4. An additional submicron venting between the laminates were provided which helps in the high fidelity replication of the microstructures.

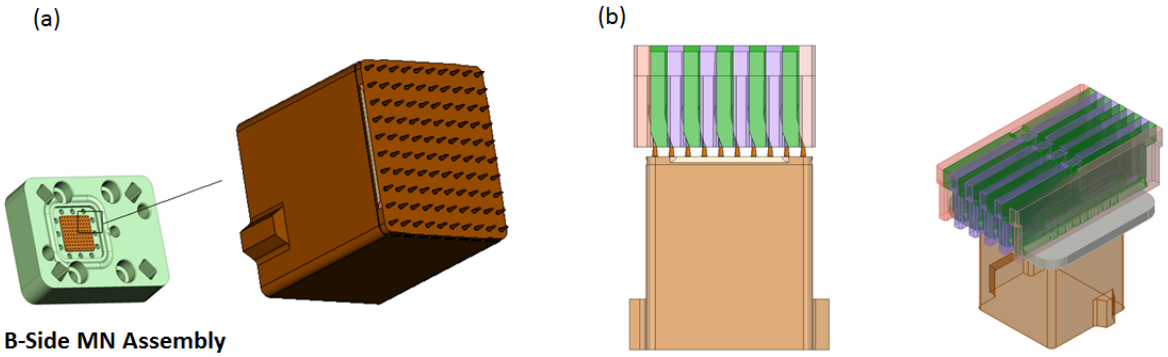

Figure 6.7 (a) Showing the B-side MN insert with insert holder (b) depicts a side view when both A and B-side of MN insert during mould closing.

The B-side of the MN insert comprises of 100 projections fabricated by EDM into a S7 steel plate of dimensions 18 mm in length, 18 mm in width and 30 mm thickness. The projection were arranged in a 10x10 array so that it overlaps the core side of laminate in the A side of the MN insert. These projection are held together in a steel plate holder as shown in the Figure 6.7a which also houses a total of 12 ejector pins and was used to enable ejection of the resulting hollow MN. Details of the MN part geometry is shown in the Figure 6.8.

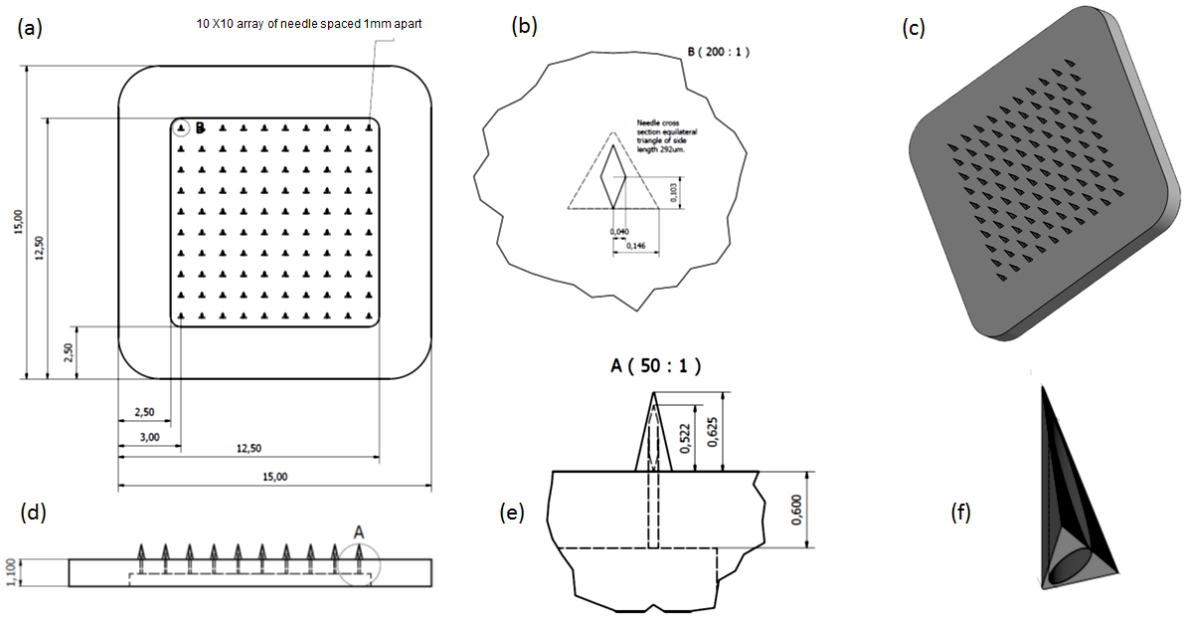

Figure 6.8 (a) 2D-view of the hollow MN part with dimensions (b) top-view of the single MN with dimensions (c) 3D schematic representation of a microneedle array (d) and (e) schematic representation of a microneedle array showing its geometrical parameters like height of MNs in array, lumen dimensions and width of the base plate (f) single hollow MN showing the lumen.

4.1.3. Micro-injection moulding hardware

Microneedle moulding trails were performed on a Battenfeld MicroPower 15 micromoulding machine at the University of Bradford. The hollow MN mould assembly as shown in Figure 6.2 was installed on to the moulding machine. Lexan and PEEK were chosen as two polymers used for the study. The PEEK pellets were dried at 140ºC for 4 hours before loading into the hopper from where it is fed into the rotating screw to achieve the processing temperature to get the polymer into the melt state. Both sides of the mould were heated to a specified temperature and the moulding cycle was initiated by the closing of A-side towards the B -side of the MN insert. After injecting the first shot of polymer, the process was switched from injection specific to pack pressure (900 bars). The moulding parameters and design of experiments were the same used for manufacturing the solid MNs except for the shot volume, which was optimised at 5 mm. Details of the machine and DOE are discussed in the

Chapter 3. All the MNs produced from these experiments were subsequently characterised for the dimensional properties using SEM and confocal laser microscope.

6.2. Results and discussion

6.2.1. Moulding performance

The hollow MN products were micro-injection moulded using a Battenfeld Micro-Power 15 micro-injection moulding machine. The actual part geometry is shown in Figure 6.8 with the needle height (625 µm) and lumen width (80 µm). During the moulding process it was evident that filling was achievable but not consistent. A representative image of the partially filled MNs are shown in Figure 6.9.

During the initial experiments it was concluded that incomplete filling defects are caused by wrong melt temperature, insufficient shot volume, low holding pressure and injection speed. But as higher processing parameters were used a better filling was achieved as shown in Figure 6.10 and realised the main reason for inferior microneedles was breakage during demoulding. When a replicated part solidifies in the mould cavity the mould opens and the part is forcibly demoulded or ejected from the replication tool typically using a series of ejector pins (Delaney *et al*., 2011 and Gravea *et al*., 2007). These ejector pins apply some force to overcome the retarding forces which develop at the moulded part and cavity interface due to friction and adhesion.

Demoulding of micro-replicated parts is challenging as the features are comparatively weak and can be easily damaged by the forces required to overcome the frictional forces at surface (which are comparatively high due to the high surface area to volume ratio of the micro components). Micro moulding

also introduces challenges for achieving adequate structural strength of the tool features, for example, the micro cores required for high aspect ratio parts (Hopkinson and Dickens, 2000). During cooling, dimensional shrinkage occurs which can cause the material to contract around any upstanding core features in the mould cavity, which creates a risk of part breakage during ejection/demoulding (Gravea *et al*., 2007). Additional problem may arise if there is no draft angle (Delaney *et al*., 2011).

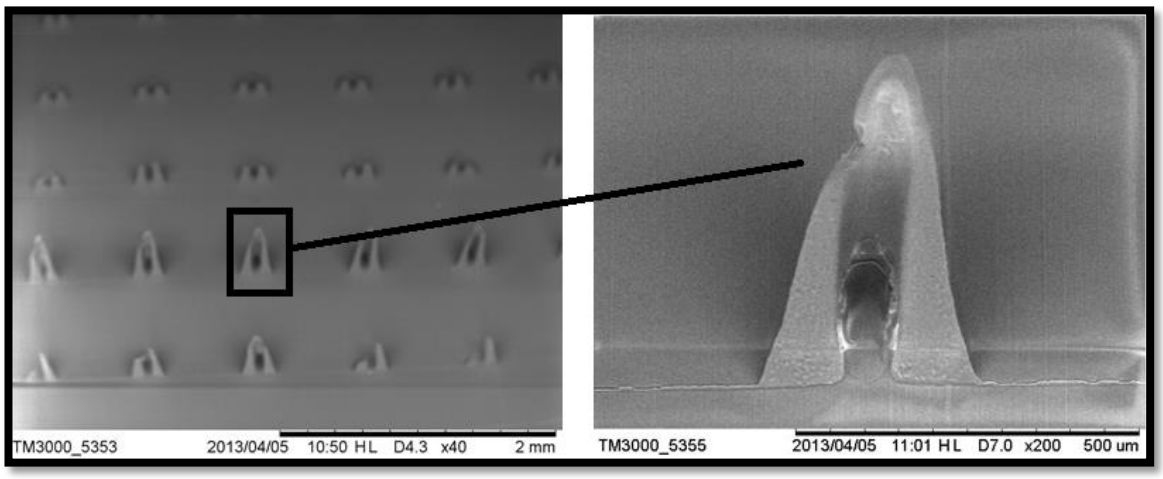

Figure 6.9 SEM image of the inconsistent filling of the MNs.

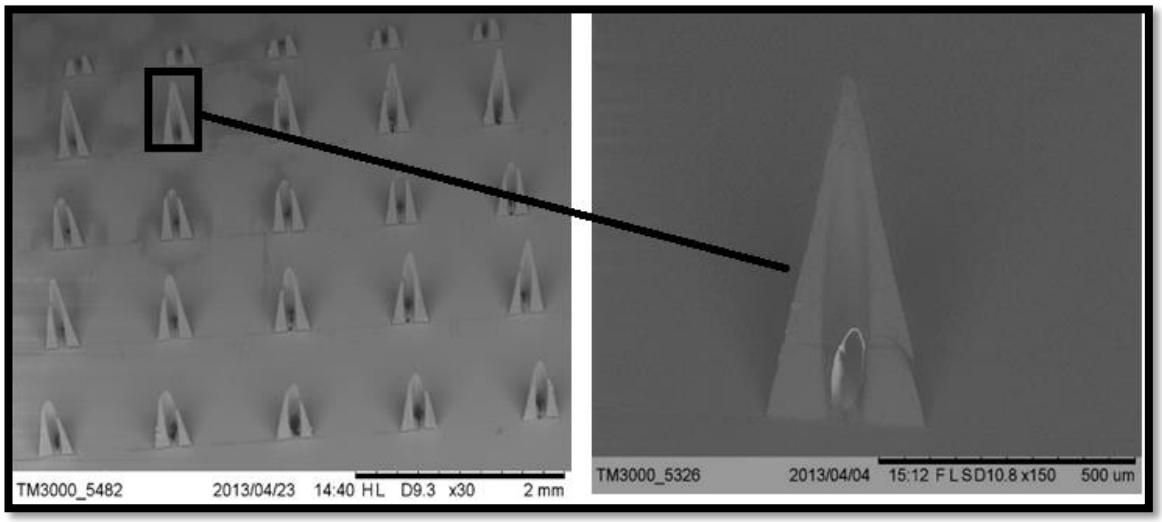

Figure 6.10 SEM image showing the complete filling of the MNs.

From this it was identified that the filling of the MN Figure 6.10 was not the main issue, rather release of the microneedles from the MN insert cavities was a problem as they were fracturing as the mould opened. To investigate this phenomenon A-side of the MN needle insert was carefully stripped and each laminate was observed under SEM to confirm if any remaining part of broken needles was present. Figure 6.11a and b shows the core side of the laminate and Figure 6.11 c and d shows v-side of the laminate before and after moulding.

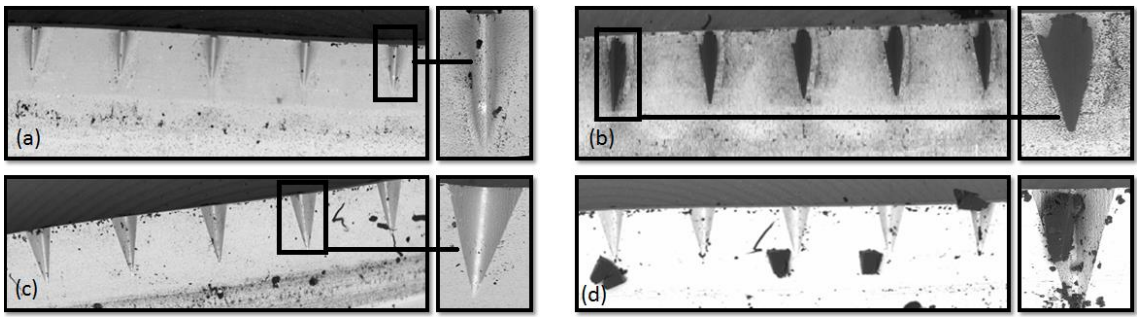

Figure 6.11 SEM image of laminate (a) core side before moulding (b) core side after moulding showing the breakage during ejection (c) V-side of the laminate before moulding (d) V-side after moulding showing fragments of polymer sticking into the cavity.

A-side of MN insert without stripping the individual laminate was also imaged and Figure 6.12 and 6.13 shows the SEM image of the insert before and after moulding respectively. Figure 6.14 shows a 3D confocal image of MN array. All these images gives us clear evidence of MNs sticking within the cavity and hence gets broken while the mould open. Demoulding of micro parts is a complex process and is influenced by many factors.

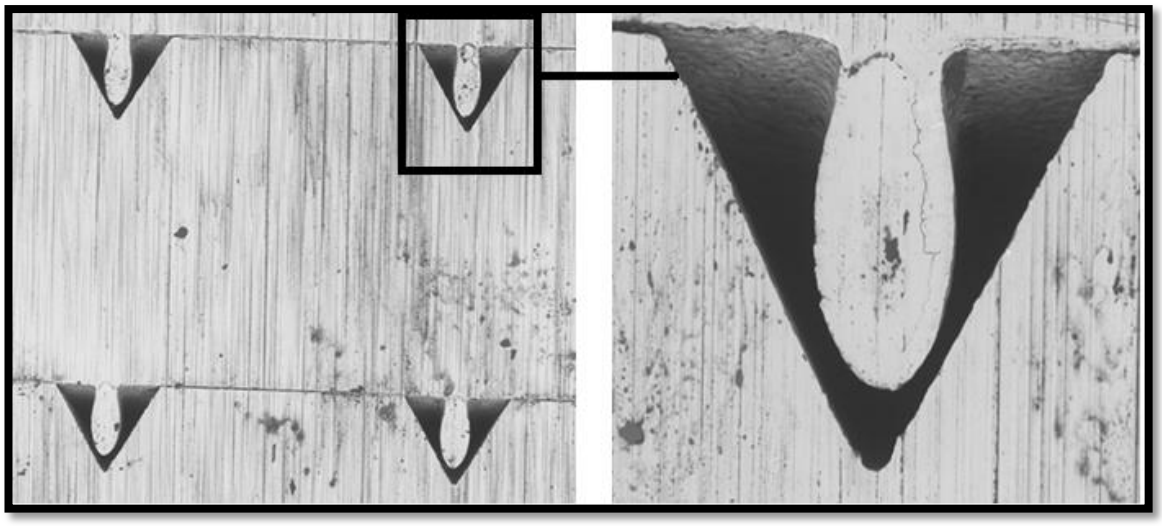

Figure 6.12 SEM image of the A-side of the MN insert before moulding.

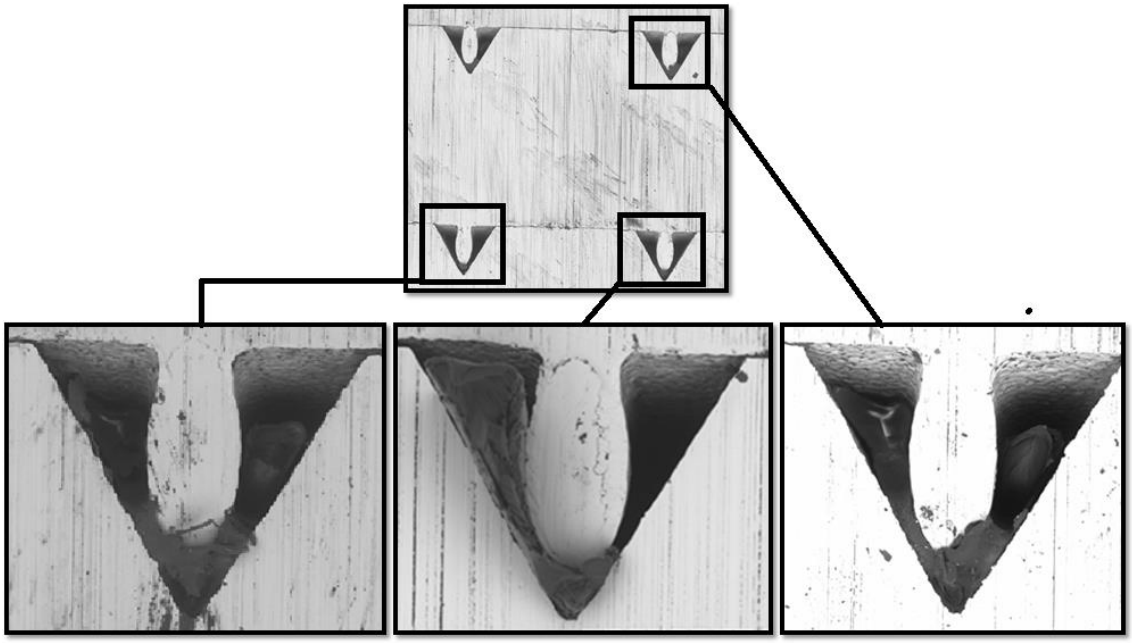

Figure 6.13 SEM image of the A-side of the MN insert after moulding giving the evidence of the MN part stuck between the core and the wall of the cavities.

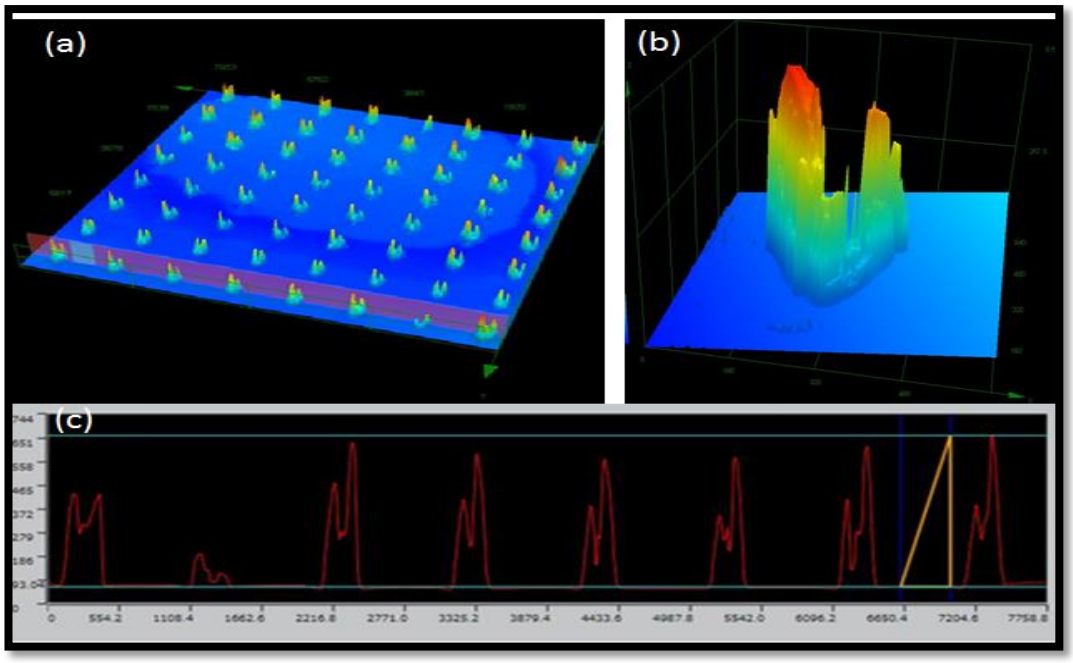

Figure 6.14 3D confocal image of the (a) MN array (b) single MN (c) dimensions of the poorly formed needles.

Burke *et al* (1991) identified that understanding coefficient of friction and contact pressure could help to reduce the demoulding force. Research carried out by Sasaki *et al* (2000) confirms that optimum roughness of the tool reduces adhesion thereby minimising the ejection forces. Worgull *et al* (2006) highlights the importance of surface finishing could give an extremely smooth side walls to avoid friction during demoulding.

6.2.2. Causes of MN breakage

It was identified that the following three mould insert design factors for MN needle breakage while demoulding.

Draft Angle: the injection moulded parts have an outside wall and internal ribs that are formed by opposing surfaces of tool metal inside a closed mould. To enhance proper release of the part during demoulding, the side walls of the mould are tapered in the same direction that the mould opens. This tapering is called as draft (Figure 6.15). Draft angle is generally added to the cavity side of

the mould because it assist part release from the cavity as the mould opens. This also reduces the effects of undercuts and facilitate air movements. Draft angles vary from a fraction to several degrees and depends upon material rigidity, shrinkage and mould surface roughness (Malloy, 1994 and Griffiths *et al*., 2010).

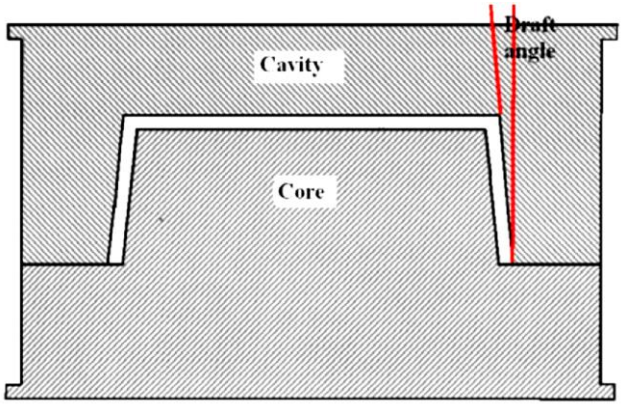

Figure 6.15 Significance of cavity draft angles during parts ejection from the mould (Malloy 1994).

During the demoulding process when the part is ejected from the cavity it is ejected from the core. Polymer material usually shrinks and builds pressure and grip tightly onto the core resulting in need of higher ejection forces which might break the part. Higher core angles reduce the initial ejection forces and simplifies the ejection system design (Malloy 1994). Examination of the inserts Figure 6.11, 6.12 and 6.13 suggested that most forces resulting from the part shrinkage would be concentrated around the core side of the mould and in the mould used for MN for this work had no draft angle resulting in high frictional forces between the core and the part leading to MN breakage.

Surface Finish: The micro features on the MN insert have been manufactured using EDM technology. It is a well-established method technique to produce

high precision machining on materials of any hardness and shape. However this method creates machined surfaces with micro cracks and pores caused by the high temperature gradient during the EDM process which reduces the surface finish quality (Boujelbene *et al*., 2009 and Griffiths *et al*., 2010). It was observed that the surface roughness value of 1.5 microns on the MN insert which causes extra adhesion for the polymer to grip onto the core and to the cavity wall and hence needle breakage while demoulding.

Wall Thickness: The wall thickness depends on the size and geometry of the part. In the present study, because of the core ellipsoidal shape (which create the lumen in the hollow MN) there was minimum wall thickness at the tip of the microneedle, creating a weak spot to break while demoulding. Figure 6.16a shows a confocal image unfilled cavity before moulding Figure 6.16b shows a confocal image of the cavity respectively after demoulding and clearly visualise the MN stuck between the cavity wall and the core. Figure 6.16c shows the evidence of insufficient wall thickness at the tip to provide adequate strength to the MN part for ejection.

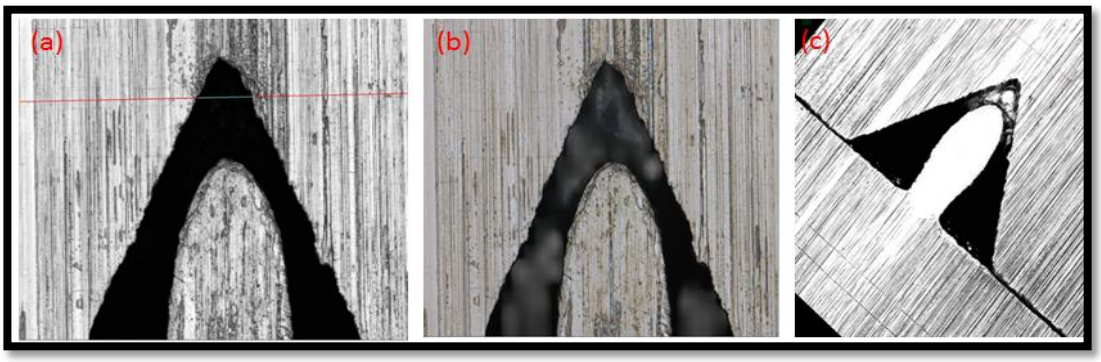

Figure 6.16 (a) confocal image of the A-side of the MN insert before moulding (b) after ejection (c) MN part stuck between the core and tip of the cavity wall.

Core step: due to high clamping forces involved in the moulding process (120 kN) the point where the projections from the B-side of the MN insert meet the A side has been damaged. A confocal image of that area showed a step Figure 6.17a resulting in formation of flash across split core interface Figure 6.17b.

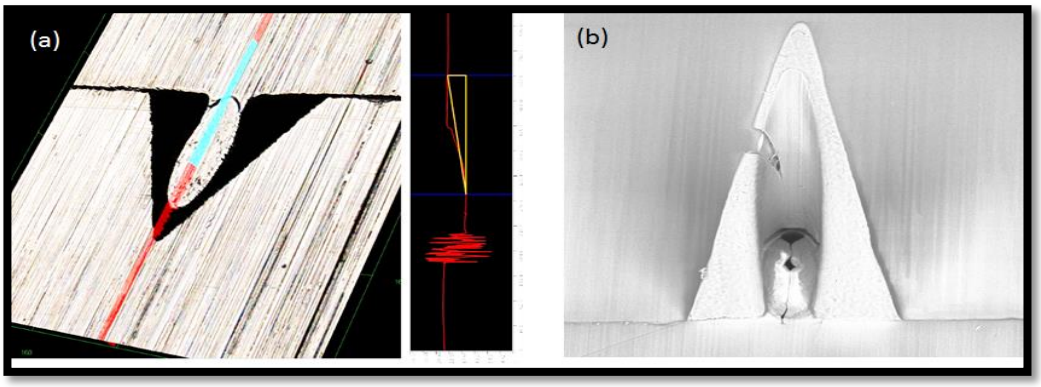

Figure 6.17 (a) confocal image of the MN insert showing the step across the split core interface (b) SEM of the MN with flash at the lumen.

6.2.3. Recommendations

Redesign: it was identified that the minimum wall thickness is one of the reasons for the MN breakage while demoulding and to prevent that happening redesign the core with the major axis and minor axis of the core needs to be reduced as shown in the Figure 6.18b. It is also recommended to re-machine the core with some draft angle Figure 6.18a. All these changes to the initial design will give following mentioned advantages

1. Hole-size at the external needle surface remains unchanged.
2. Provides thicker sections to aid flow to form the needle tip.
3. Provides a more suitable filling profile and reduces weld line formation.
4. Provides thicker sections to provide greater needle strength.
5. Provides a draft to reduce the force required to release the needle.

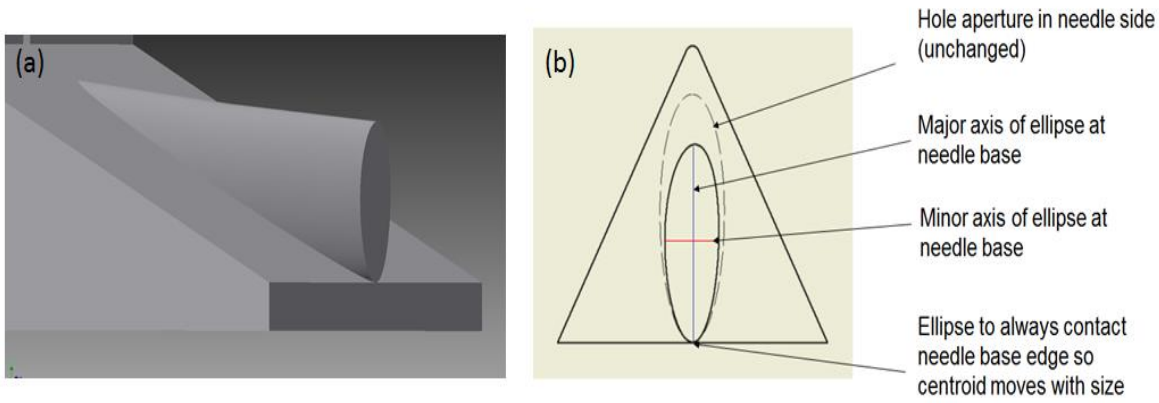

Figure 6.18 (a) 3D drawing of the redesigned core with increase in the draft angle (b) top view sketch of the redesigned core with reduced major axis of ellipse at the needle base which will increase the core-cavity wall thickness and improves the ejection of MNS.

Surface coating: The surface roughness of the mould cavity depends upon machining process involved. A typical EDM process used to create a micro feature will result in a 250-2500 µm in roughness (Brye, 1998). Ideally, the smoother the cavity finish, the lower force is required for ejection (if suitably vented and no vacuum effect occurs). This could be achieved by reducing the hills and valleys during the machining process. Figure 6.19 shows the degree of roughness of the cavity surface after EDM process and after polishing.

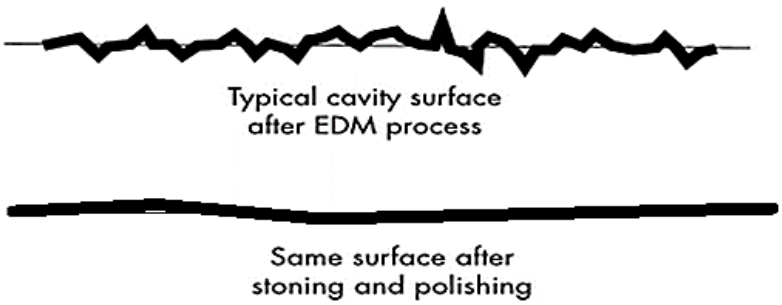

Figure 6.19 Schematic of the surface finish before and after polishing of the EDM processed cavity part (Brye, 1998).

To reduce the surface roughness of the MN cavities titanium nitride (TiN) or diamond like carbon (DLC) coating are recommended. The study carried out by Tosello *et al* (2012) proves that use of TiN reduced the surface roughness of EDM cavities to 3 nm and they also found out that TiN coating reduced the wear and tear during the injection moulding process. Many researchers also suggests the use of DLC coating to improve the surface finish (Pham *et al*., 2004; Gangopadhyay *et al*., 2011 and Griffiths *et al*., 2010).

6.3. Conclusions

The intended purpose of this study was to manufacture a micro-injection moulded hollow microneedle array for interstitial fluid extraction. A three plate mould with MN insert was fabricated using an EDM process. A DOE was carried out to optimise the injection moulding parameters. The moulded parts were primarily checked for filling and dimensional accuracy using SEM and confocal microscopy. The results obtained confirmed that filling was achievable but not consistent. It was also confirmed that main reason contributing for the MN breakage during demoulding was due to less draft angle in the core part and surface finish of the mould. Various recommendations for modifications to the initial tool design were suggested.

6.4. References

1. Bal, SM, Ding Z, Riet EV, Jiskoot W and Bouwstra J, Advances in transcutaneous vaccine delivery: do all ways lead to Rome? *J. Control. Release* **148** (2010) 266–282.

2. Brye DM., Plastic Injection Moulding: Mould Design and Construction Fundamentals (Fundamentals of Injection Moulding) Volume 3 Published by Society of manufacturing Engineers, Michigan USA. 1998.

3. Banga, AK, Microporation applications for enhancing drug delivery, Expert Opin. *Drug Deliv.* **6** (2009) 343–354.

4. Burke C. and Malloy R, An Experimental Study of the Ejection Forces Encountered during Injection Moulding, *ANTEC* (1991) 1781-7.

5. Boujelbene M, Bayraktar E, Tebni W and Salem SB, Influence of machining parameters on the surface integrity in electrical discharge machining*. Archives of materials Science and engineering,* **37** (2009)11-116.

6. Davis SP, Martanto W, Allen MG and Prausnitz MR, Hollow metal microneedles for insulin delivery to diabetic rats, *IEEE Trans. Biomed. Eng.* **52** (2005) 909–915.

7. Delaney K., Bissacco G and Kennedy D, Demoulding Force Prediction for Micro Polymer Replication: A Review of Relevant Literature. *Proceedings of the 7th. International Conference on Multi-Material Micro Manufacture* (2011).

8. Ebah LM, Extraction and Analysis of Interstitial Fluid, and Characterisation of the Interstitial Compartment in Kidney Disease. A Thesis submitted to the University of Manchester for the degree of Doctor of Philosophy in the Faculty of Medical and Human Sciences (2012).

9. Gangopadhyay A, Sinha K, Dairene UY, Mcwatt DG, Zdrodowski RJ, and Simko SJ. Friction, Wear, and Surface Film Formation Characteristics of Diamond-Like Carbon Thin Coating in Valvetrain Application, *Tribology Transactions*, **54** (2011) 104-114.

10. Griffiths CA, Dimov SS, Brousseau EB, Chouquet C, Gavillet J and Bigot S, Investigation of surface treatment effects in micro-injection-moulding, *Int J Adv Manuf Technol* **47** (2010) 99–110.

11. Gravea AD, Erikssona T and Hansena HN, Demouldability of microstructures in polymer moulding 3rd International Conference on Multi-Material Micro Manufacture (2007).

12. Hopkinson N and Dickens PM, Using stereolithography tools for injection moulding: research into tensile tool failure and unexpected benefits of the process, *Proceedings of the IMechE, Part B*, (2000) 891-899.

13. Nuxoll E and Siegel R, BioMEMS devices for drug delivery, *IEEE Engineering in Medicine and Biology*, **28** (2009) 31-39

14. Nahas AM and Bello AK, Chronic kidney disease: the global challenge. *The Lancet,* **365** (2005)331-40.

15. Maaden KV, Jiskoot W and Bouwstra J, Microneedle technologies for transdermal drug and vaccine delivery Journal of Controlled Release **161** (2012) 645–655

16. Malloy, Plastic Part Design for Injection Molding, Hanser Publishers, 1994.

17. Prausnitz, M.R. Microneedles for transdermal drug delivery, *Adv. Drug Deliv.Rev.* **56** (2004) 581–587.

18. Prausnitz MR, Gill HS and Park HJ, Modified Release Drug Delivery, Vol. 2nd ed, Healthcare, New York, (2008) 295–309.

19. Pham DT, Dimov SS, Bigot S, Ivanov A and Popov K. Micro-EDM – Recent Developments and Research Issues. *J. of Materials Processing Technology*, **50** (2004) 149-152

20. Roxhed N, Samel B, Nordquist L, Griss P and Stemme G, Painless drug delivery through microneedle-based transdermal patches featuring active infusion, *IEEE Trans. Biomed. Eng*. **55** (2008) 1063–1071.

21. Shin H and Park E, Analysis of Incomplete Filling Defect for Injection-Moulded Air Cleaner Cover Using Moldflow, *Journal of Polymers* **14** (2013) 1131-42

22. Sasaki T, Koga N, Shirai K, Kobayashi Y and Toyoshima A, An experimental study on ejection forces of injection moulding. *Precision Eng*, **24**, (2000) 270-273.

23. Tosello G, Hansen HN, Gasparin S, Albajez JA and Esmoris I, Surface wear of TiN coated nickel tool during the injection moulding of polymer micro Fresnel lenses, *Annals of CIRP*, **61** (2012)535-538

24. Wang P, Brock A, Rajaraman S, Paik SJ, Kim SH, and Allen MG, Hollow Polymer Microneedle Array Fabricated by Photolithography Process Combined with Micromoulding Technique, 31st Annual International Conference, USA (2009).

25. Worgull M, Heckele M, Hetu JF and Kabanemi KK. Friction during the Demolding of Microstructures Moulded by Hot Embossing, *Journal of Microlithography, Microfabrication, and Microsystems*, 5 (2006).

Chapter 7 Conclusions and Recommendations

7.0 Conclusions

A substantial amount of academic and patent literature is available on a wide range of MN designs for effective transdermal drug delivery. However, there are many issues that need to be addressed before MNs find widespread use. The ultimate commercial success of MN based delivery and monitoring devices will depend on how cost effective these products are and also their overall acceptability with health care professionals and regulatory bodies. Currently MNs are manufactured using variety of MEMS techniques which require multiple manufacturing steps and pharmaceutical companies wishing to commercialise MNs would need to invest significant capital to design, optimise and characterise a cost effective reproducible method for bulk manufacturing of MNs. Therefore a great opportunity exist to develop a cost effective manufacturing process that could be easily implemented by pharmaceutical companies.

Micro-injection moulding process could achieve this need but being a complex process, a better understanding is required. In this study, MNs were successfully manufactured using µIM processes with a range of high performance engineering thermoplastics with high volume outputs. High shear rheology of these selected materials and simulation of polymer filling into MN cavities were carried out to understand the material behaviour at high shear rates experienced during µIM. Feedback from these data were used to design the mould and MN insert. The MN cavity was created on the insert using an EDM process and this mould insert was validated using a PDMS casting method, which showed that the maximum needle height and

tip radius of MNs that could be achieved using this insert is 556 µm and 32.16 µm respectively.

MNs were manufactured using the Battenfeld Micropower 15 micro-moulding machine and parameters such as injection pressure, injection speed, melt temperature, filling time and mould cavity temperature are key parameters that were measured. Various design of experiments along with in-line data acquisition measurements were performed to optimise the fabrication process. SEM, AFM and CLM were used to accurately measure the dimensions of the moulded MNs. From the statistical analysis it was observed that a combination of higher cavity pressure and injection speed produced better quality MNs.

With the knowledge gained while manufacturing solid MNs, a strategy for the manufacture of hollow MNs was implemented. A DOE was carried out to optimise the injection moulding parameters and observed that filling was achievable but MNs were fractured during ejection process. The main reason contributing for the MN breakage during demoulding was due to insufficient draft angle in the core part, thin wall strength and high surface roughness of the mould. Based on these results further modifications to the initial tool design were suggested.

Surface modification studies revealed that plasma treatment modified the surfaces both in chemical composition and morphology whereas mechanical abrasion just changed the surface roughness values. The plasma treatment increased the polar component of the surface energy of polymer samples causing a decrease in the contact angle and an increase in the total surface energy. The XPS analysis confirmed the increase in the polar groups in the

plasma treated polymer surfaces. A HPLC method was used to determine the amount of BSA adsorbed after surface modification and showed that plasma treatment is a much more efficient way to increase the adsorption of the BSA onto the polymer surface than mechanical treatment methods. This surface modification can be implemented in a real manufacturing process to improve the drug loading on the solid MN shaft.

To assess the performance of the micro-injection moulded MNs, porcine skin penetration and buckling experiments were carried out and it was found out that the MNs buckled at forces above the forces required to pierce the skin which assures that MN tip will not break in the skin during insertion. In addition use of OCT has revealed the exact location and true depth of the MN during penetration. It was observed that around 80% of the MN shaft penetrated into the skin, leaving a clear gap between the stratum corneum and MN base-plate. OCT results also revealed that approximately 70 minutes was required for the skin to reseal after the removal of the inserted microneedles.

A computerised MN dip coating system was developed which allowed successful coating of the BSA to the MN shaft without contaminating the base plate. These coated needles were subsequently tested for skin diffusion studies and results confirmed that plasma treated MNs could permeate BSA across the porcine skin.

All these findings demonstrate the feasibility of MNs manufactured using µIM for effective transdermal drug delivery. With a bright future for the microneedle sector, micro-injection moulded MNs have the potential to

capture a significant portion of the drug delivery market when compared to MNs manufactured using alternative techniques.

7.1. Recommendations

Based on the outcomes of this research, further studies would be recommended on the following areas

(a) Needle design and manufacture

Solid MN geometry was kept constant throughout the study due to the cost involved in manufacturing MN inserts with different geometries. It would have been ideal to study the effects of different geometry and tip size on manufacturing, drug delivery and penetration. The techniques developed for in-line data acquisition requires significant improvement and a better system with higher acquisition rate needs to be used for measuring the cavity pressure. Micro-CT method would have been a better way to validate the microneedle insert manufactured by EDM process than PDMS method. The use of micro-CT could have given a higher resolution of the skin penetration experiments as compared to the OCT technique.

(b) Drug delivery

This study has investigated the performance of MNs using BSA as the model drug and demonstrated the capability of MNs to deliver hydrophilic-high molecular weight molecules. Similar studies should have been carried out using drugs with different molecular weights and hydrophilicity. All the MN penetration and BSA delivery experiments were performed *in vitro* using porcine skin. *In vivo* testing using human skin is the only way to obtain the real MN penetration ability so utilisation of human skin is recommended to

enhance the understanding of the relationship between drug delivery and skin penetration mechanics.

(c) Computational

Development of a universal skin model which represents all skin types of all race, age and body location should be considered. This would help to get a robust microneedle penetration simulation data which could be used for generating an optimal MN design.

Appendix

List of publications

1. Korde S, Pagire S, *Nair K*, Whiteside B, Kelly A and Paradkar A, Composition containing Chitin, (GB Patent filed, 2014).

2. Coates P, Whiteside B, Kelly A and *Nair K*, High strain rate rheometry of polymer melts and nano-composites, The 29th International Conference of The Polymer Processing Society (PPS-29) 2013.

3. *Nair K*, Grant C, Whiteside B, Patel R, Norris K & Paradkar A, *Preformulation studies of polymers for microneedle design*; Microneedle 2012, Cork, Ireland.

4. *Nair K*, Whiteside B, Bobe C, Twigg P, Norris K & Paradkar A, Novel characterisation methods of microneedles manufactured by micro-injection moulding, 4M 2015, Milan, Italy.

5. *Nair K*, Grant C, Whiteside B, Bobe C, Patel R, Norris K & Paradkar A, Investigation of plasma treatment on polymeric micro-injection moulded microneedle for protein drug delivery, *Journal of material science,* (manuscript under preparation).